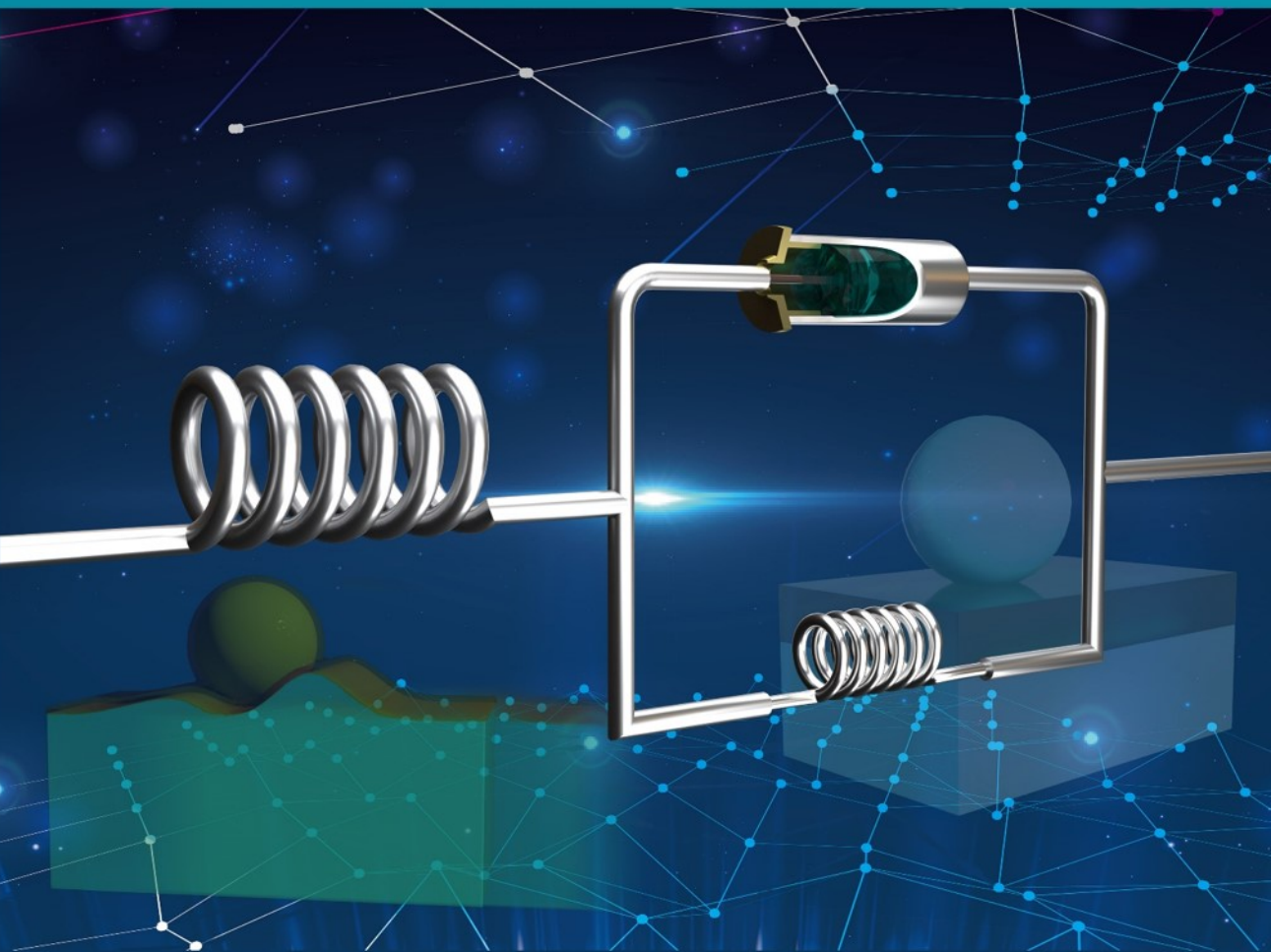


SOLID VISCOELASTICITY IN CONTACT MECHANICS AND ELASTOHYDRODYNAMIC LUBRICATION



Yan Zhao

**SOLID VISCOELASTICITY IN CONTACT
MECHANICS AND ELASTOHYDRODYNAMIC
LUBRICATION**

Yan Zhao

SOLID VISCOELASTICITY IN CONTACT MECHANICS AND ELASTOHYDRODYNAMIC LUBRICATION

DISSERTATION

to obtain
the degree of doctor at the University of Twente,
on the authority of the rector magnificus,
Prof. dr. ir. A. Veldkamp,
on account of the decision of the Doctorate Board
to be publicly defended
on Friday 26 August 2022 at 12.45 hours

by

Yan Zhao

born on 10th of September 1993
in Hebei, China

This dissertation has been approved by:

Promotor:

Prof. dr. ir. C.H. Venner

The presented research is carried out in the Engineering Fluid Dynamics group, Faculty of Engineering Technology, University of Twente, The Netherlands.

The research has been financed by the China Scholarship Council (CSC) and SKF Research and Technology Development (RTD) in Houten, the Netherlands.

ISBN : 978-90-365-5426-8
DOI : 10.3990/1.9789036554268
Printed by : IPSKAMP Printing

Copyright © 2022 by Yan Zhao, The Netherlands. All rights reserved. No parts of this thesis may be reproduced, stored in a retrieval system or transmitted in any form or by any means without permission of the author. Alle rechten voorbehouden. Niets uit deze uitgave mag worden vermenigvuldigd, in enige vorm of op enige wijze, zonder voorafgaande schriftelijke toestemming van de auteur.

Graduation Committee

Chair/secretary: Prof. dr. ir. H.F.J.M. Koopman

Supervisor: Prof. dr. ir. C.H. Venner

Co-supervisors: Prof. dr. G.E. Morales-Espejel

Dr. ir. C.W. Visser

Committee members: Prof. dr-ing. G. Poll

Prof. dr. ir. P.M. Lugt

Prof. dr. A. Blume

Prof. dr. J. Wang

Dr. ir. R.A.J. van Ostayen

Contents

Summary	xi
Samenvatting	xv
Nomenclature	xix
1 Introduction	1
1.1 Tribology	1
1.2 EHL	3
1.2.1 Development of EHL Theory	4
1.2.2 Regimes of EHL	7
1.3 Solid Viscoelasticity	8
1.3.1 Viscoelastic Half-Space Contact	8
1.3.2 Viscoelastic Layer vs. "Hard" EHL Film.	9
1.4 Objective.	10
1.5 Outline.	11
2 Fundamentals of Viscoelasticity	13
2.1 Viscoelastic Behavior.	13
2.1.1 Creep	14
2.1.2 Stress Relaxation	15
2.1.3 Linear Viscoelastic Material	16
2.1.4 Dynamic Loading	16
2.2 Rheological Models.	18
2.2.1 Linear Elements	18
2.2.2 The Maxwell Model	19
2.2.3 The Kelvin-Voigt Model	20
2.2.4 The Standard Linear Solid (SLS) Model	22
2.3 Boltzmann Superposition Principle.	25
2.4 Elastic-Viscoelastic Correspondence Principle	26
2.4.1 Viscoelastic Half-Space Deformation	28
2.4.2 Deformation in Steady-State Rolling Contacts	29
3 Viscoelastic Dry Contact	33
3.1 Introduction	33
3.2 Viscoelastic Modeling	35
3.2.1 Static Contact	37
3.2.2 Rolling Contact Problem	38

3.3	Numerical Solution.	40
3.3.1	Static Contact	41
3.3.2	Rolling Contact	42
3.3.3	Multi-Relaxation Times	44
3.4	Results and Discussion.	46
3.4.1	Static Contact Results	46
3.4.2	Rolling Contact Results.	48
3.4.3	Rolling/Sliding Viscoelastic-on-Viscoelastic Contacts.	54
3.4.4	Multiple-Relaxation Times	56
3.5	Conclusion.	57
4	Viscoelastic Lubricated Contact	59
4.1	Introduction	59
4.2	Theory and Numerical Methods	61
4.2.1	Viscoelastic Deformation.	62
4.2.2	EHL Equations	64
4.2.3	Numerical Solution.	67
4.3	Experimental Approach	68
4.3.1	Test Setup and Materials	69
4.3.2	Optical Interferometry Methods	71
4.4	Results and Discussion.	73
4.4.1	Dimensionless Parameter Variation	73
4.4.2	Experimental Results.	82
4.4.3	Film Thickness Scaling and Self Similarity	87
4.5	Conclusion.	93
4.6	Appendixes to Chapter 4.	94
A	Relations between Dimensionless Parameters for EHL Point Contact.	94
B	Discrete Equations	95
C	VEHL Model Validation	97
D	Elastic Modulus Determination of PMMA	99
5	Viscoelastic Layer Modeling	101
5.1	Introduction	101
5.2	Viscoelastic Modeling and Formulation	103
5.2.1	Viscoelastic Rheological Model.	104
5.2.2	Modeling Formulation	105
5.3	Foundation Approach	106
5.3.1	Deformation Equation	107
5.3.2	Numerical Methods	107
5.4	Papkovich-Neuber (PN) Approach	108
5.4.1	3D Elastic Half-Space and Elastic Layered Solution.	109
5.4.2	Correspondence Principle and Viscoelastic Layered Solution.	111

5.5	Model Verification	113
5.5.1	Elastic Layer-Elastic Substrate System	113
5.5.2	Viscoelastic Half-Space.	114
5.5.3	Viscoelastic Layer-Elastic Substrate System	115
5.5.4	Foundation Approach vs PN Approach.	115
5.6	Results and Discussion	117
5.6.1	Elastic Layered Elastic Half-Space	117
5.6.2	Viscoelastic Layer on Elastic Half-Space	122
5.7	Towards EHL Film Behavior Modeling	129
5.8	Conclusion.	132
5.9	Appendixes to Chapter 5.	133
A	Viscoelastic Properties	133
B	Frequency Response of Elastic Layered Half-Space	135
C	Green's Function Analysis	140
6	Conclusion and Recommendations	143
6.1	Conclusion.	143
6.2	Recommendations for Future Work	144
	Bibliography	147
	List of Publications	159
	Acknowledgments	161

Summary

Driven by the urgent need for transition to new sustainable technology in terms of use of resources and generated waste products, optimal efficiency is of crucial importance. Energy losses at any scale in machines of old (transitional) and new technology and processes need be minimized and performance and service life maximized. In many applications, the service life increasingly depends on the interfaces in which power and forces are transmitted, i.e. in machine parts in relative motion. Also reducing the energy losses (friction) in these contacts directly contributes to increased efficiency. Therefore, detailed understanding of the underlying mechanisms of contact and lubrication at rolling/sliding interfaces plays an essential role towards more sustainable technology.

Lubricated concentrated contacts are common in engineering applications, mostly between "hard" materials (steel) as in rolling bearings, cam-followers, and gears, but also between a hard and a soft part as in the case of a steel shaft and an elastomeric seal. In recent decades, soft materials are increasingly used in mechanical engineering, in aviation industry, and in various processes in physics, and bio-(fluid) mechanics, due to advantages such as light weight, good recyclability, and controllable design-performance capability. For "hard" materials, the deformation of the contacting elements is predominantly elastic. The understanding of the physical mechanisms governing the lubrication film formation and the associated pressure generation has reached a very high level of predictability. However, soft materials exhibit viscoelastic behavior in contacts, and, in spite of the excellent work that has been done regarding the elastomeric seal contacts, the current understanding of the effect of solid viscoelasticity on the lubrication of soft contacts, particularly for point contacts, is less advanced than the understanding of the purely elastic contacts. This limits the design and performance optimization of the related tribological contacts and systems. To advance the understanding of the effects of solid viscoelasticity in dry and lubricated contacts, in this thesis fundamental aspects of the modeling and efficient numerical simulation of viscoelastic point contact problems are studied.

1. Viscoelastic dry (VED) contact problem

In the literature models and equations for viscoelastic contact problems are scattered in different research disciplines such as contact mechanics, physics, and bio-mechanics. As a starting point the modeling of concentrated contacts between viscoelastic solids, and the approaches to obtain numerical solutions are revisited for static creep and dynamic rolling conditions. A new viscoelastic deformation modeling equation is derived for the standard linear solid (SLS) viscoelastic half-space so that the efficiency of computation of the viscoelastic deformation remains close to that of the elastic case, rather than being much more expensive owing to its time varying nature. This is achieved by rewriting the viscoelastic deformation equation from an integral form into a differential form by applying the Leibniz integral theorem. The developed approach generalizes with equal efficiency to more complex (realistic) viscoelastic material behavior with multiple relaxation times. An advantage of the approach is further that it can straightforwardly be implemented as

add-on in any existing (EHL) contact solver regardless of the numerical method used, e.g. such as the multigrid methods used in this work. Detailed results of a parameter study on contact behavior are presented and discussed, such as the effect of the Deborah number, and the relation between the two extreme cases of dry contacts: the rolling problem and the static problem. Finally, in addition to the case of a rigid sphere against a viscoelastic half-space, also the case of contact between two viscoelastic bodies is considered.

2. The Visco-elastohydrodynamically lubricated (VEHL) contact problem

An efficient multigrid based algorithm is presented for the numerical simulation of the effects of solid viscoelasticity on elastohydrodynamic lubrication (EHL). The algorithm is based on the viscoelastic half-space deformation evaluation method developed in the first part of the thesis. The dimensionless parameters governing the VEHL problem are identified and a parametric study is presented showing the effect of solid viscoelasticity on the pressure and film thickness in the conjunction. In addition to this theoretical research, experiments have been carried out measuring the lubricating film thickness as a function of operating conditions using optical interferometry in configurations where viscoelastic behavior was expected to be of significance, i.e. a soft PMMA ball rolling against a glass disc. Experimental and theoretical results are compared showing that the degree of viscoelastic behavior of PMMA is much smaller than expected. Finally the scaling of the pressure and film profiles in the inlet and outlet regions to the contact have been studied for soft contacts, investigating the self-similarity of the pressure and film solution in these regions.

3. Viscoelastic layered dry contact problem

The three dimensional quasi-static (point) contact problem of a rigid sphere rolling on a viscoelastic layered elastic half-space is studied. Two different modeling and numerical approaches have been used, i.e. a simplified foundation approach which relies on the thin layer assumption, and a full numerical solution based on the complete Navier-Cauchy equations accounting for viscoelastic behavior. Results are presented to study the effects of the layer viscoelasticity on the contact pressure, subsurface stresses and layer deformation. The foundation approach is realized by implementing the constitutive equation of the viscoelastic model into the multigrid method based elastic solver, calculating the layer and substrate deformations separately. The approach for the viscoelastic Navier-Cauchy equations is based on Papkovitch-Neuber potentials and the solution is obtained by solving the equations in the Fourier domain according to the elastic-viscoelastic correspondence principle. The comparison of the results obtained with the two models clearly demonstrates that the simplified foundation approach can well be used to predict the layer deformation of very thin layers qualitatively, but also that under some conditions the stresses are significantly influenced by bending effects which are not accounted for in the foundation based model. As a next step, the layer thickness after deformation is investigated at different conditions. The aim here is to explore the capability of representing a conventional "hard" EHL film with an ultra-thin viscoelastic layer. This approach may give a new model method for EHL and mixed lubrication. It is shown that by considering the piezoviscosity effect of the dashpot in the SLS viscoelastic layer using the foundation approach typical EHL film features including the outlet constriction and the two side-lobes can be observed. This offers promising modeling options for mixed lubrication models based on visco-elastic layers. However, the results need to be seen as a remarkable coincidence, and not representative for all contact configurations.

In this thesis, a detailed description and a systematic numerical simulation for the above three viscoelastic contact problems are provided. The results presented provide a good framework for the understanding and interpretation of viscoelastic solid effects in highly deformed (soft) dry and lubricated contacts. The methodology proposed in this work may have spin-off to polymer elastic layer lubrication, to soft meta-material design for lubricated contacts, tomography based computational diagnostics, and to biomedical applications.

Samenvatting

Onder invloed van de dreigende gevolgen van de wereldwijde klimaatverandering is er een sterke noodzaak tot de ontwikkeling van nieuwe duurzame technologie waarbij minder gebruik gemaakt wordt van natuurlijke hulpbronnen, de invloed op de omgeving wat betreft gegenereerde afvalproducten kleiner is, en zo min mogelijk energieverliezen optreden.

Energieverliezen doen zich voor op elke schaal in machines zowel met oude (overgangs) en met nieuwe technologie. Ten eerste door functionele inefficiëntie, zoals bijvoorbeeld loslating van stroming rondom een windturbineblad. Ten tweede door wrijvingsverliezen tussen bewegende machineonderdelen, zoals gegenereerd in de gesmeerde contacten in (kogel)lagers en tussen tandwielen. Daarnaast is het van belang de levensduur te maximaliseren zodat de gebruikte grondstoffen en de geïnvesteerde energie bij het maken van het product of apparaat optimaal tot hun recht komen. In veel toepassingen hangt de levensduur in toenemende mate af van wat zich afspeelt in de gesmeerde contacten. Gedetailleerd begrip van de onderliggende mechanismen van contact en smering is daarom ook essentieel voor de ontwikkeling van duurzamere technologie. Gesmeerde geconcentreerde contacten komen veel voor in technische toepassingen, meestal tussen "harde"materialen (staal) zoals in wentellagers, nok-stoter mechanismen en tussen de tanden van tandwielen, maar ook tussen een hard en een zacht onderdeel zoals in het geval van een stalen as en een rubber afdichting. In de afgelopen decennia is het gebruik van relatief zachte materialen in de techniek toegenomen bijvoorbeeld in toepassingen in de luchtvaart- en automobiël-industrie, in specifieke toepassingen of processen in de natuurkunde zoals interactie tussen zachte deeltjes in een stroming, en op het gebied van de biomedische stromingsleer, met name kunstmatige gewrichten, maar ook de interactie tussen bloedcellen onderling en tussen bloedcellen en de wanden van bloedvaten. Zachte materialen kunnen specifieke voordelen hebben zoals een laag gewicht, lage productiekosten en prijs, goed te recycleren te zijn, of voordelen bieden vanwege het vermogen slijtagedeeltjes op te nemen in de zachte matrix. Bij "harde"materialen is de vervorming van de contactelementen overwegend elastisch. Het begrip van de fysische mechanismen die in dat geval de vorming van de smeerfilm en de daarmee gepaard gaande drukverdeling in het contact bepalen, is met de huidige modellen zeer goed te voorspellen. Zachte materialen vertonen in veel gevallen visco-elastisch gedrag, en ondanks het uitstekende werk dat is gedaan op het gebied van rubber (elastomere) afdichtingen en band-weg contacten, is het huidige begrip van het effect van visco-elasticiteit van de contactelementen op de smering en levensduur van het contact, in het bijzonder voor de puntcontact configuratie, nog lang niet compleet. Dit heeft uiteraard zijn weerslag op het ontwerp en de prestatie-optimalisatie van de gerelateerde tribologische contacten en systemen. Om het begrip van de effecten van het visco-elastische gedrag van de contact-elementen op het gedrag van droge en gesmeerde contacten te vergroten, worden in dit proefschrift fundamentele aspecten van de modellering en efficiënte numerieke simulatie van visco-elastische puntcontactproblemen bestudeerd.

1. Visco-elastisch droog (VED) contact

In de literatuur zijn beschrijvingen van modellen en vergelijkingen voor visco-elastische contactproblemen verspreid over de vakliteratuur van verschillende disciplines zoals contactmechanica, toegepaste/technische natuurkunde, en biomechanica. Als startpunt wordt daarom in dit proefschrift eerst een recapitulatie gegeven van de modellering van geconcentreerde contacten tussen visco-elastische vaste stoffen en worden de diverse methodes om numerieke oplossingen te verkrijgen beschreven voor het geval van een contact in een toestand van statische kruip, en voor een contact in de dynamische rollende contactsituatie. Een nieuwe modelvergelijking voor de visco-elastische vervorming wordt gepresenteerd voor het geval van half oneindig materiaal dat zich gedraagt als een "Standard Linear Solid". De vergelijking maakt numerieke evaluatie van de visco-elastische vervorming mogelijk met een efficiëntie vergelijkbaar met die van het elastische geval, in tegenstelling tot de veel reken intensievere manier die nodig is wanneer tijdsafhankelijke variatie specifiek via een discretisatie in de tijd wordt meegenomen. Het voordeel wordt bereikt door de visco-elastische vervormingsvergelijking te herschrijven van een integraalvorm in een differentiaalvorm door de Leibniz-integraalstelling toe te passen. De ontwikkelde aanpak generaliseert met gelijkblijvende efficiëntie naar meer complex (realistisch) visco-elastisch materiaalgedrag met meerdere relaxatietijden. Een voordeel van de aanpak is verder dat het eenvoudig kan worden geïmplementeerd als add-on in elke bestaande (EHL) contactoplosser, ongeacht de gebruikte numerieke methode, zoals bijvoorbeeld de multigrid-methoden die in dit werk worden gebruikt. Gedetailleerde resultaten van een parameterstudie naar het contactgedrag worden gepresenteerd en besproken, zoals het effect van het Deborahgetal, en de relatie tussen de twee extreme gevallen van droge contacten: het dynamische rollende contact probleem, en het statische probleem. Tenslotte wordt naast het geval van een star bolvormig lichaam tegen een visco-elastische half oneindig lichaam ook het geval van contact tussen twee visco-elastische lichamen beschouwd.

2. Het visco-elastohydrodynamisch gesmeerde (VEHL) puntcontact

Een efficiënt algoritme is ontwikkeld voor de berekening van de smeerfilm en drukverdeling in het contact op basis van multigrid technieken. Het ontwikkelde algoritme is vervolgens gebruikt in een parameter studie. Het algoritme maakt gebruik van de evaluatiemethode voor de visco-elastische deformatie die in het eerste deel van het proefschrift is beschreven. De dimensieloze parameters die het gedrag van de oplossing van het VEHL-probleem bepalen worden geïdentificeerd en de effecten van het visco-elastische gedrag op de drukverdeling en smeerfilmdikte in het contact wordt geanalyseerd in relatie tot de operationele condities van het contact. Naast het theoretische/numerieke onderzoek zijn experimenten uitgevoerd ter validatie, met name betreffende meting van de smeerfilmdikte in het contact tussen een PMMA kogel en een glazen schijf met behulp van optische interferometrie. Uit de vergelijking van de experimentele en theoretische resultaten wordt geconcludeerd dat onder de gegeven condities, de mate van visco-elastisch gedrag van PMMA veel kleiner is dan verwacht op basis van de literatuur. Ten slotte is de schaling van de druk- en film-profielen in de inlaat- en uitlaat-gebieden naar het contact bestudeerd voor zachte contacten, waarbij met name de gelijkvormigheid van de druk- en filmplossing in deze gebieden is onderzocht.

3. Droog contact met visco-elastische laag.

Tot slot is het driedimensionale quasi-statische (punt)contactprobleem van een onvervormbare bol die rolt over een visco-elastische gelaagd materiaal onderzocht. Twee ver-

schillende modellen zijn gebruikt voor de visco-elastische laag. Ten eerste de zogenaamde “foundation approach” die gebaseerd is op de gereduceerde modelvergelijkingen voor het geval van een zeer dunne laag. Ten tweede de resultaten van een volledig model gebaseerd op de Navier-Cauchy vergelijkingen rekening houdend met het visco-elastisch gedrag. Resultaten worden gepresenteerd met betrekking tot de effecten van de visco-elastische laag op de contactdruk, de vervorming van de viscoelastische laag, en de spanningen onder het oppervlak. Het model gebaseerd op de “foundation approach” is opgelost met behulp van multigrid technieken, waarbij de vervorming van de visco-elastische laag wordt berekend door de constitutieve vergelijking van het visco-elastische model te implementeren in de eerder ontwikkelde multigrid methode voor het elastische probleem, waarbij de vervorming van substraat en van de visco-elastische laag beiden afzonderlijk worden berekend. De benadering voor de visco-elastische Navier-Cauchy-vergelijkingen is gebaseerd op Papkovich-Neuber-potentialen en de oplossing wordt verkregen door de getransformeerde vergelijkingen in het Fourier-domein op te lossen volgens het elastisch-visco-elastische correspondentie principe. De vergelijking van de verkregen resultaten met de twee modellen toont aan dat het vereenvoudigde model goed geschikt is om de het contactgedrag in het geval van zeer dunne lagen kwalitatief te voorspellen, maar ook dat onder sommige omstandigheden de spanningen aanzienlijk worden beïnvloed door buigefecten die niet worden meegenomen in het vereenvoudigde model. Als volgende stap wordt de laagdikte na vervorming onderzocht onder verschillende omstandigheden. Het doel hiervan is om de mogelijkheid te onderzoeken of een gesmeerd conventioneel “hard” EHL contact gemodelleerd kan worden als een droog contact met een dunne visco-elastische laag. Het wordt aangetoond dat bij gebruik van het “foundation approach” model, wanneer piezo-visceuze effecten meegenomen worden in het gedrag van de visceuze demper in het SLS visco-elastische model voor de laag, typische kenmerken van een EHL-film optreden, waaronder de restrictie van de film in de uitlaat, en de twee zijlobben aan beide zijden van het contact. Dit biedt veelbelovende modelleringsopties voor modellen met gemengde smering op basis van visco-elastische lagen. Echter, het wordt ook aangetoond dat de resultaten moeten worden gezien als opmerkelijke (en misschien uitzonderlijke) resultaat in specifieke omstandigheden, die niet zonder meer representatief zijn voor alle contactconfiguraties.

In dit proefschrift wordt een gedetailleerde beschrijving gegeven van een systematische modellering, en analyse door middel van numerieke simulaties, van het gedrag van drie visco-elastische contactproblemen. De gepresenteerde resultaten bieden een goed raamwerk voor het begrijpen en interpreteren van visco-elastische vaste stof effecten in sterk vervormde (zachte) droge en gesmeerde contacten. De ontwikkelde methodes kunnen ook gebruikt worden voor de analyse van het effect van een dunne polymeerlaag op het oppervlak, zoals in een vetgesmeerd EHL contact kan voorkomen, bij het ontwerp van zachte meta-materialen voor gesmeerde contacten, en bij de analyse en diagnostiek van contacten op basis van tomografische informatie bijvoorbeeld in biomedische toepassingen.

Nomenclature

Notation

- a Contact radius, [m]
- a_0 Radius of elastic Hertzian contact, [m]
- \bar{a} Dimensionless contact radius, $\bar{a} = a/a_0$, [-]
- \bar{a}_{\max} Dimensionless maximum contact radius, $\bar{a}_{\max} = a_{\max}/a_0$, [-]
- D_{inlet} Deborah number based on inlet length, $D_{\text{inlet}} = \tau/\frac{e}{v_2}$, [-]
- $D_{\text{Hertz}}(De)$ Deborah number based on Hertzian radius, $D_{\text{Hertz}} = De = \tau/\frac{a_0}{v_m}$, [-]
- e Inlet length under elastic conditions with effective modulus E_0 , $e = a_0\lambda^{\frac{2}{5}}$, [m]
- E_f, E_s Modulus of the linear springs in the SLS model, [Pa]
- E_0 Effective modulus at an extremely low speed, $1/E_0 = 1/E_f + 1/E_s$, [Pa]
- E_∞ Effective modulus at an extremely high speed, $1/E_\infty = 1/E_f$, [Pa]
- \bar{E}_0 Dimensionless effective modulus at an extremely low speed, $\bar{E}_0 = E_0/p_H$, [-]
- \bar{E}_∞ Dimensionless effective modulus at an extremely high speed, $\bar{E}_\infty = E_\infty/p_H$, [-]
- E' Storage modulus of viscoelastic materials, [Pa]
- E'' Loss modulus of viscoelastic materials, [Pa]
- E^* Complex modulus of viscoelastic models, [Pa]
- F_r Friction force, [N]
- \bar{F}_r Dimensionless friction force, $\bar{F}_r = F_r/\frac{3W_0a_0}{2\pi R_0}$, [-]
- h Gap height, [m]
- h_0 Penetration displacement for an undeformed contact, [m]
- h_{\min} Minimum film thickness on the central line along x direction, [m]
- h_{cen} Central film thickness, [m]
- h_{cens} Central film thickness under an extremely low speed, elastic conditions with effective modulus of E_0 , [m]

h_{pmax}	Film thickness at the maximum pressure, [m]
h_x	Uniform mesh size in x direction, [m]
h_y	Uniform mesh size in y direction, [m]
H	Dimensionless gap height, $H = h/\delta$, [-]
H_0	Dimensionless penetration displacement for an undeformed contact, $H_0 = h_0/\delta$, [-]
H_{cen}	Dimensionless central film thickness, $H_{\text{cen}} = h_{\text{cen}}/\delta$, [-]
H_{cens}	Dimensionless central film thickness at an extremely low speed, elastic conditons with effective modulus of E_0 , $H_{\text{cens}} = h_{\text{cens}}/\delta$, [-]
H_{pmax}	Dimensionless film thickness at the maximum pressure, $H_{\text{pmax}} = h_{\text{pmax}}/\delta$, [-]
H^*	Scaled film thickness, $H^* = \frac{\pi}{4} H \lambda^{-3/5}$, [-]
l	Layer thickness, [m]
l_0	Initial layer thickness, [m]
\bar{l}	Dimensionless layer thickness, $\bar{l} = l/\delta$, [-]
\bar{l}_0	Dimensionless initial layer thickness, $\bar{l}_0 = l_0/\delta$, [-]
L	Moes lubricant parameter, $L = \alpha E' ((2\eta_0 v_m)/(E' R_0))^{1/4}$, [-]
M	Moes load parameter for point contact, $M = W_0/(E' R_0^2)((2\eta_0 v_m)/(E' R_0))^{-3/4}$, [-]
N_t	Number of time steps in time domain, [-]
p	Pressure, [Pa]
p_0	Atmospheric pressure, [Pa]
p_{H}	Maximum Hertzian pressure, $p_{\text{H}} = 3W_0/(2\pi a_0^2)$, [Pa]
p_{cen}	Central pressure, [Pa]
p_{max}	Maximum pressure, [Pa]
P	Dimensionless pressure, $P = p/p_{\text{H}}$, [-]
P_{cen}	Dimensionless central pressure, $P_{\text{cen}} = p_{\text{cen}}/p_{\text{H}}$, [-]
P_{max}	Dimensionless maximum pressure, $P_{\text{max}} = p_{\text{max}}/p_{\text{H}}$, [-]
R_0	Radius of sphere, [m]
R_e	Elasticity ratio, $R_e = E_f/E_s$, [-]
t	Time, [s]

T	Dimensionless time, $T = t/\tau$, [-]
u	Viscoelastic deformation, [m]
u_e	Elastic deformation, [m]
U	Dimensionless viscoelastic deformation, $U = u/\delta$, [-]
U_e	Dimensionless elastic deformation, $U_e = u_e/\delta$, [-]
v_1	Moving velocity of the sphere, [m/s]
v_2	Moving velocity of the (layered) substrate, [m/s]
v_m	Entrainment (mean) velocity, $v_m = (v_1 + v_2)/2$, [m/s]
v_s	Sum velocity, $v_s = (v_1 + v_2) = 2v_m$, [m/s]
V_x	Sliding velocity, [m/s]
W_0	Normal load, [N]
x, y	Coordinate, [m]
x_a	Contact limit at inlet side, [m]
x_b	Contact limit at outlet side, [m]
X, Y	Dimensionless coordinate, $X = x/a_0$, $Y = y/a_0$, [-]
X_a	Dimensionless contact limit at inlet side, $X_a = x_a/a_0$, [-]
X_b	Dimensionless contact limit at outlet side, $X_b = x_b/a_0$, [-]
X^*	Scaled coordinate in x direction, [-] $X^* = (X + 1)\lambda^{-2/5}$ for inlet film, $X^* = (X - 1)\lambda^{-2/5}$ for outlet film
α	Pressure-viscosity coefficient, [Pa^{-1}]
$\bar{\alpha}$	Dimensionless viscosity index, $\bar{\alpha} = \alpha p_H$, [-]
β	Retardation time of viscoelastic SLS model, [$\beta = \tau/(1 + R_e)$]
δ	Maximum Hertzian displacement, $\delta = a_0^2/R_0$, [m]
ϵ	Strain, [-]
ϵ_0	Imposed constant strain, [-]
η	Dynamic viscosity of lubricant, [$\text{Pa}\cdot\text{s}$]
η_0	Ambient viscosity, [$\text{Pa}\cdot\text{s}$]
η_s	Viscosity of the dashpot in the SLS model, [$\text{Pa}\cdot\text{s}$]

$\bar{\eta}$	Dimensionless viscosity, $\bar{\eta} = \eta/\eta_0$, [-]
λ	Lame parameter, $\lambda = 12\eta_0 v_m / (a_0^3 p_H)$, [-]
μ	Friction coefficient, $\mu = F_r/W_0$, [-]
ν	Poisson ratio, [-]
ρ	Density, [kg/m ³]
ρ_0	Ambient density, [kg/m ³]
$\bar{\rho}$	Dimensionless density, $\bar{\rho} = \rho/\rho_0$, [-]
σ	Stress, [N/m ²]
σ_0	Imposed constant stress, [N/m ²]
τ	Relaxation time of viscoelastic material, $\tau = \eta_s/E_s$, [s]
$\bar{\tau}$	Dimensionless rolling velocity, $\bar{\tau} = V_x/(a_0/\tau)$, [-]
φ_c	Creep compliance operator of viscoelastic material, [-]
ψ_r	Relaxation operator of viscoelastic material, [-]
Δ_t	Dimensionless uniform time step, [-]

Subscripts

1, 2	Surface 1, surface 2
c, s	Coating, (layered) substrate

Abbreviation

EHL	Elasto-hydrodynamic lubrication
GDS	Grid dependent solution
GIDS	Grid independent solution
MG	Multigrid
MLMI	Multilevel multi-integration
SLS	Standard linear solid model
VED	Viscoelastic dry contact
VEHL	Visco-elastohydrodynamic lubrication

Chapter 1

Introduction

1.1 Tribology

Current technologies are pushed to their limits by increasingly strict efficiency demands, required reduction of material use, and required reduction of environmental impact, e.g. noise and pollution. The transition to new sustainable technology in terms of use of resources, generated waste products, and optimal efficiency is of crucial importance. With an increasingly fraction of the global energy usage originating from tribological contacts to overcome friction [64], energy losses at any scale in machines need be minimized and performance and service life maximized. In many applications the service life increasingly depends on the contact interfaces at which power and forces are transmitted, e.g. in machine elements in relative motion such as bearings and gears. Detailed understanding of the underlying mechanisms of contact and lubrication at rubbing interfaces plays an essential role towards more sustainable technology.

Tribology is the study of the phenomena that occur between interacting surfaces in relative motion including but not limited to friction, wear and lubrication. The term was coined by Peter Jost [77] in 1966, even though tribological activities date back thousands of years, e.g. grinding wood to make fire and the invention of the wheel to reduce sliding friction. Tribology is almost everywhere, in nature, industry, and everyday life, and it contributes, e.g. to improve the energy efficiency of engines, to enable fast read/write operation in hard discs, and to protect artificial joints against wear of the surfaces. It is also crucial for the operation of many microfluidic devices and governs the interaction of particles dry or in a flow on the smallest scale.

As a subject, tribology is highly interdisciplinary. To solve a tribological problem, taking the famous experiments of sliding friction measurements carried out by Leonardo da Vinci as an example, requires the knowledge of many disciplines such as mathematics, physics, chemistry, materials science, continuum mechanics (contact mechanics, fluid mechanics, thermodynamics), mechanical and surface engineering, and even nano technology. In general, contact and lubrication are two fundamental aspects of tribology. Contact behavior represents characteristics of deformable interacting bodies, and lubrication is the effective way to reduce friction and wear by forming a (low shear stress separation) protective interfacial film.

According to the nature and the continuity of the formed lubricating film, four lubrication regimes are classified to indicate the lubrication status at rubbing interfaces under different operating conditions: boundary lubrication, mixed lubrication, elastohydrodynamic lubrication (EHL) and hydrodynamic lubrication (HL). They are usually depicted by the so called Stribeck curve [128], schematically shown in Fig.1.1. For boundary lubrication,

a continuous fluid lubrication film cannot be formed in the contact zone, and the applied load is mainly carried by the solid asperities of the rubbing surfaces. This asperity contact behavior leads to a relatively large friction coefficient and often elevated wear of the surfaces. In EHL and hydrodynamic lubrication regimes, a continuous thin hydrodynamic film is formed to fully separate the rubbing surfaces and the load is entirely carried by this lubricating film. In hydrodynamic lubrication, film formation is governed by entrainment speed and gap geometry. In EHL, the film formation is augmented by the deformation of the surfaces due to the high pressures. The EHL film thickness typically ranges from 20nm to 1~2 μ m. The mixed lubrication regime is characterized by a partial film lubrication, in which the load is carried by both the noncontinuous lubricant film and the solid asperities.

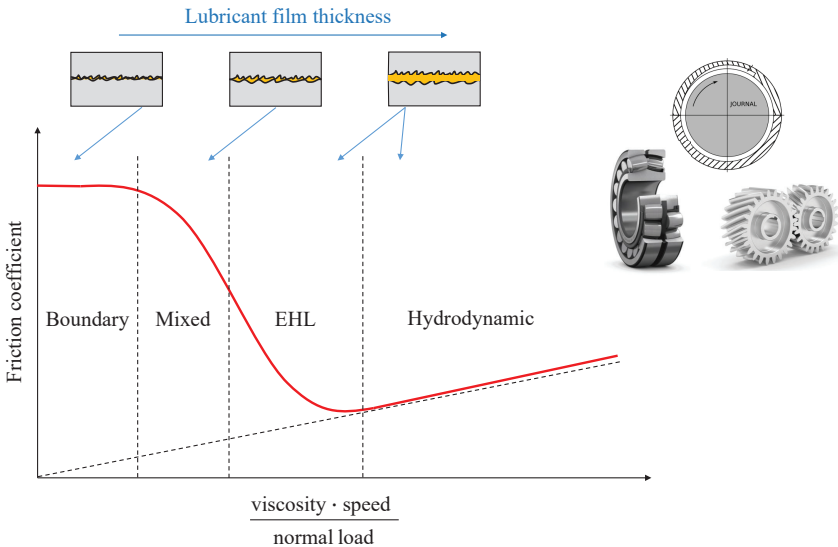


Figure 1.1: Schematic of Stribeck curve and lubrication regimes for elastic tribo-contacts.

EHL is the fundamental lubrication mechanism of non-conformal contacts, which exist widely in machine elements such as rolling bearings and gears in automotive, industrial and aerospace applications. These tribo-pairs are usually made of steel or alloy, and the deformation upon applied load is predominantly elastic. For these classical applications in engineering, the understanding of the physical mechanisms governing the lubrication film formation and the associated pressure generation has reached a very high level of predictability as a result of extensive theoretical/numerical and experimental research in the last 70 years. Nowadays even the effect of material heterogeneity and anisotropy of bearing steels on the contact pressure, the contact stresses and the fatigue life in dry and EHL lubricated conditions can be modelled and calculated [153–155]. Apart from the above-mentioned elastic hard metals, soft materials such as polymers are increasingly used in modern industry due to a range of outstanding properties in terms of corrosion and chemical-resistance, low cost, less noise generation and light weight. These materials behave mostly viscoelastically rather than purely elastically. However, the current under-

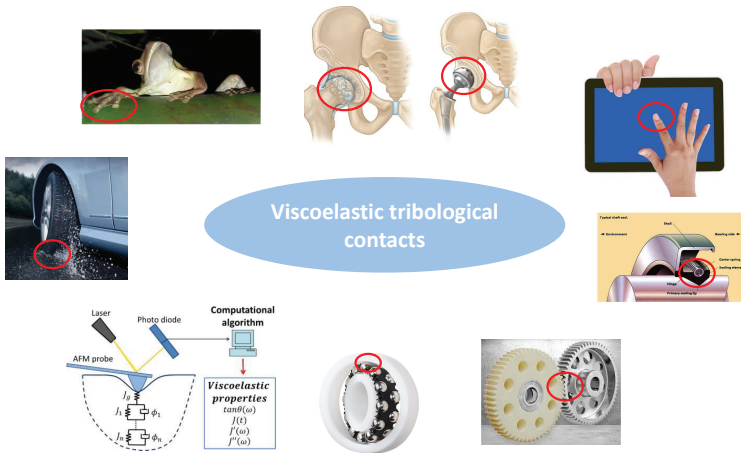


Figure 1.2: Examples of viscoelastic dry and lubricated tribological contacts.

standing of viscoelastic dry and lubricated contacts is less advanced compared to that of elastic tribological contacts. Viscoelasticity is mainly accounted for when studying seals [28, 40, 121, 122, 125, 136].

Fig.1.2 gives some examples of viscoelastic tribological contacts including bio-lubrication of natural/artificial hip joints with synovial fluids, adhesive contact behavior of tree frog's feet/skin on a wet lotus leaf, grease/oil lubricated steel-plastic hybrid rolling bearings, plastic gears and seals in automotive industry, and so on. The need to understand aspects of solid viscoelasticity is even more clear in the physics of soft matter and bio-(fluid) mechanics [6, 79, 89, 133], since many biomaterials respond viscoelastically, for example, heart tissue, muscle tissue and cartilage. Compared to elastic materials, viscoelastic materials exhibit time-dependent deformation behavior and dissipate energy under dynamic contact conditions [17, 25, 110]. Detailed fundamental knowledge of viscoelastic contacts is essential to increase predictability and reliability, and for the optimization of the tribological performance of these soft contacts. By carrying out numerical simulations and experimental investigations, this thesis explores the effect of solid viscoelasticity on both dry and EHL lubricated point contacts.

In principle, an (lubricated) elastic contact problem can be treated as a special case of a viscoelastic one when the viscous part of the material is negligible. Numerically, it will be shown later that the solution of a viscoelastic contact problem can be obtained based on the corresponding elastic solution [3]. Therefore, the development of the lubricated elastic contact problems, EHL, lays the foundation for viscoelastic contact problems.

1.2 EHL

EHL is a hydrodynamic lubrication regime, in which the film thickness is enhanced by effects of solid (elastic) deformation and lubricant piezoviscosity. In the following sec-

tion, the development of the classical "hard" EHL theory and the different EHL regimes distinguished are briefly introduced.

1.2.1 Development of EHL Theory

Motivated by Tower's experiments on sliding bearings [132], Reynolds [117] derived the nowadays well-known Reynolds equation to describe the pressure generation of thin film flow in a narrow gap. This equation together with the contact theory of elastically deformable bodies proposed by Hertz [63] laid foundation for the development of the EHL theory. Two effects that benefit the formation of an EHL lubricant film were revealed: the elastic deformation of contacting surfaces due to high contact pressure and the increase of lubricant viscosity with increasing pressure in the inlet region. Combining these two aspects, Ertel [36, 111], but firstly published by Grubin [52] in 1949, made pioneering progress in the development of the EHL theory through inlet analysis.

Due to the strong interaction between the pressurized lubricant and the elastically deformed solids, the governing equations of an EHL problem cannot be solved analytically. In 1951, Petrusevich [108] achieved the first numerical solution of an EHL line contact problem showing the characteristics that are widely known today, i.e. a nearly constant film in the contact zone with a local constriction at the outlet. The pressure is a near Hertzian pressure with a gradual inlet sweep and near the outlet a pressure spike. With the development of numerical methods and computers, empirical film thickness equations based on the curve fits of numerical results were developed for EHL line [32] and point [55] contacts by Dowson and coworkers. Even though more advanced function fits based on the asymptotic solutions and numerical results were developed since [99, 102], these Dowson equations are still widely used in engineering design of gears and rolling element bearings today. Unfortunately due to the need to simultaneously solve the elastic deformation and fluid flow, solving EHL problems computationally very expensive by direct solution as well as by iterative methods. As a result, most studies only considered the steady 1D (infinite wide) line contact, or point contacts with low resolution.

In the early 1970's, multigrid numerical methods were introduced by Brandt [15] as an efficient method to solve partial differential equations. In their standard conceptual approach multigrid techniques exploit multiple coarse grids (hence the name) to accelerate convergence of iterative schemes to obtain a grid independent convergence speed on the target grid. This methodology was introduced to solve the EHL problems by Lubrecht [90, 91]. Further development by Venner [138] led to optimally efficient Multigrid/Multilevel solvers [141], which opened the way to simulation of many transient effects of lubricated contacts, e.g. EHL film behavior under dynamic load or speed conditions, and effect of surface roughness moving through pressurized EHL contacts even on small scale computers. The algorithms are still widely used in the field today. Recent developments involve full 3D solution of the elastic problem for grain structured material using actual measured topology, see Fig.1.3 from [156].

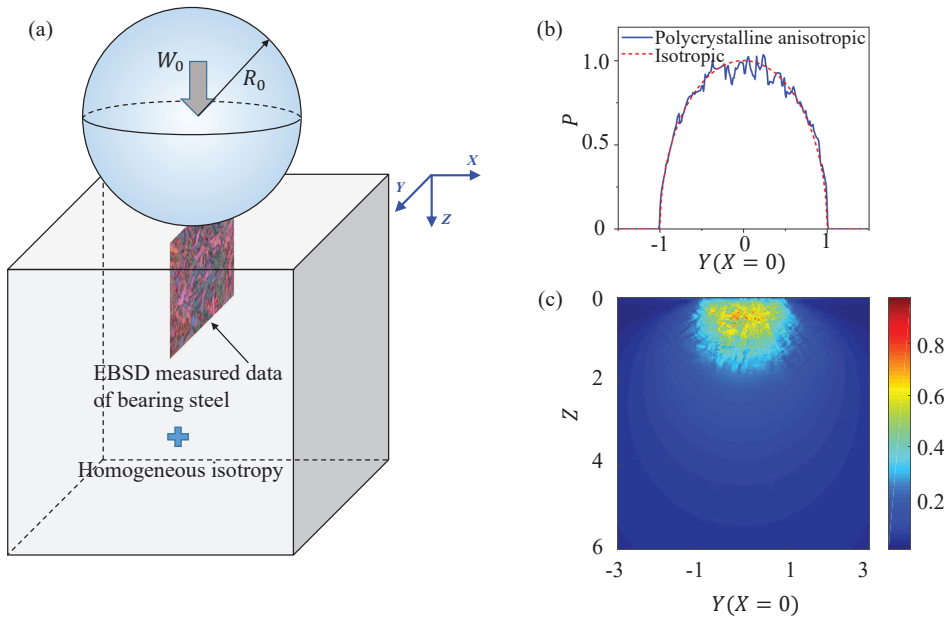


Figure 1.3: 3D solution of elastic contact problems for heterogeneous and anisotropic material from [156]: (a) schematic of the 3D contact problem with EBSD measured data of a bearing steel; (b) calculated pressure distribution in the central YZ plane; (c) calculated stress field in the central YZ plane.

Experimentally, the optical interferometry technique introduced by Cameron and Gohar in 1950s [43] has been widely used to validate the EHL theory by measuring the thin film thickness formed between a transparent glass disc and a steel ball. This method has advantages of high precision (as high as 1 nm) and the detailed visualization of the shape of the dynamic lubricating film. Fig.1.4 shows a sketch of a typical ball-on-disc test rig (EHD2, PCS Instruments, UK), which has also been used in the present work. The local EHL film thickness can be obtained by detecting the coherent wavelength [76], by matching the color [20, 59], or by analyzing the intensity of the interference fringes [53, 92] depending on the used light source and hardware.

Fig.1.5 compares the measured EHL central film thickness in a ball-on-disc contact as a function of entrainment speed for a mineral oil with theoretical results from both multigrid numerical simulations [141] and the empirical Hamrock-Dowson equation [55] on a double log scale. Also displayed are the typically observed interferograms at a number of speeds. A good agreement is observed between experimental and theoretical results. The optical interferometry technique has also been used to study the EHL film behavior under conditions of starvation [129, 143] and transient status caused by effects of surface roughness [24], non-steady speeds [42, 147], impact squeeze motion [120] and so on. These experiments and the associated numerical analysis demonstrate the mature development of the EHL theory for the film thickness of "hard" EHL.

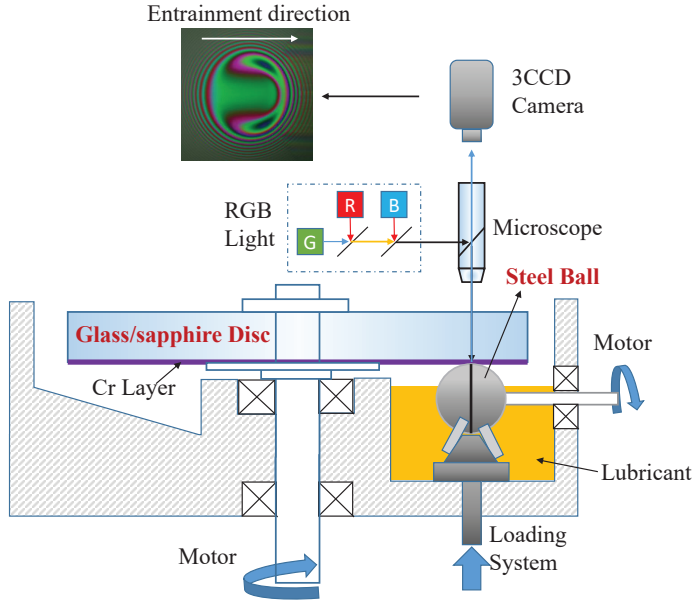


Figure 1.4: Schematic of the optical ball-on-disc test rig for EHL film thickness measurement.

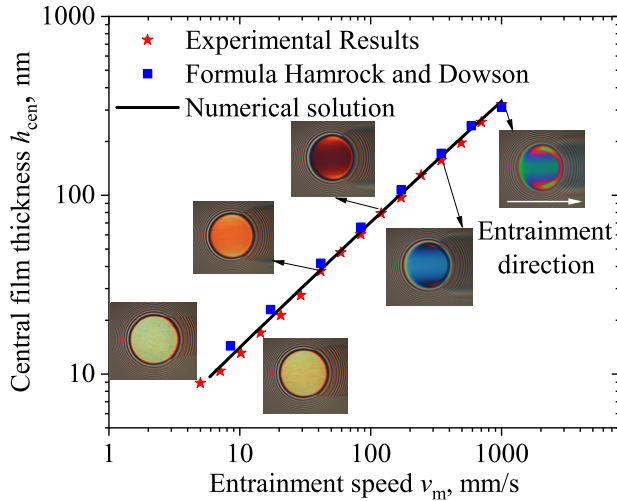


Figure 1.5: Comparison of the central film thickness of an EHL lubricated elastic contact as a function of entrainment speed between experimental and simulation results. (Operating conditions: pure rolling. HVI60 oil with viscosity 0.0447Pa·s; load, 20N; ball radius, 9.525mm; temperature, 23°C; pressure-viscosity index 22.5GPa⁻¹; glass disc-steel ball with reduced modulus 111.2GPa). The left hand side is the flow entrainment direction for the interferograms.

1.2.2 Regimes of EHL

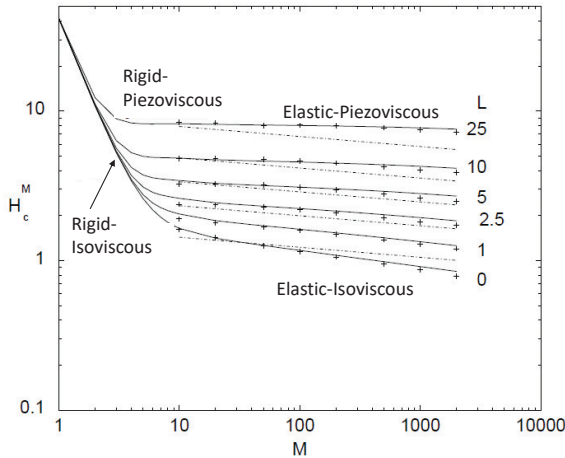


Figure 1.6: Calculated central film thickness H_c^M as a function of M and L for an elastic lubricated circle contact under fully flooded conditions, taken from [141]. M and L in the figure are dimensionless parameters proposed by Moes and Bosma [100] and further details can refer to Chapter 4.

For (EHL) lubricated contacts, four lubrication regimes have been classified [74] according to the extent of solid elastic deformation and the lubricant piezoviscosity. These are the isoviscous-rigid, piezoviscous-rigid, piezoviscous-elastic and isoviscous-elastic regimes. Being a typical example, Fig.1.6 from [141] shows a design graph of the central film thickness in a circular contact based on the dimensionless parameters representing material, load and speed operating conditions and lubricant piezoviscosity. In this chart, different regimes are indicated.

The isoviscous-rigid regime is in fact hydrodynamic lubrication, and occurs usually in lubricated conformal contacts where the two surfaces have similar matching shapes (conformal contact), such as in journal and thrust sliding bearings. Compared to non-conformal contacts, the high degree of local conformity results in a relatively low contact pressure, which is typically in the range of 1~50MPa. Such pressures are usually not high enough to significantly increase the lubricant viscosity in the contact or to lead to significant deformation of the surfaces.

The piezoviscous-rigid lubrication regime presents rarely in practical applications but it has been suggested that it may exist in the contacts of roller end-guide flange in moderately loaded cylindrical tapered roller bearings [73]. In these situations, the contacting solids are very stiff and show negligible elastic deformation, but the lubricant viscosity increases with local pressure.

The piezoviscous-elastic hydrodynamic lubrication, or "hard" EHL, or often simply EHL, exists widely in metallic and ceramic/hybrid rolling element bearings and gears. The high elastic modulus of these materials result in high contact pressures, which are typically in the range of 0.5~4GPa [157]. Such high local pressures result in a local elastic deformation of the solid surfaces to form a small region of conformity and also produce a large increase in

the lubricant viscosity in the EHL contact. These two aspects, i.e. solid elastic deformation and piezoviscous effect of the lubricant, have profound effects on the formation of an EHL film and affect its shape. For these "hard" EHL contacts, the surface deformation is usually much larger than the EHL film thickness and the contact area (contact half-width) is typically thousand times larger than the central film thickness, $a_{\text{Hertz}} = h_{\text{cen}} \cdot O(10^3)$.

The isoviscous-elastic hydrodynamic lubrication regime is known as "soft" EHL. It exists in many lubricated non-conforming contacts in engineering and in nature where one or both of the solid surfaces are made of materials with relatively low elastic modulus. In nature, soft tissues are almost everywhere, and typical engineering examples are found in windscreen wipers, tyres, seals, rolling-bearings with polymer cages and plastic rolling bearings and gears assuming elastic material. For these cases there is significant deformation of the material upon loads, which produces a large region of local conformity. This leads to contact pressures in the range of 1~50MPa, which, are high enough to (elastically) deform or even change the shape of the contact, but not sufficient to produce a significant rise in viscosity of the lubricant. For this lubrication regime, Snoeijer et al [124] showed that the EHL problem is a singular perturbation on the Hertzian dry contact problem. For both line and point contact the EHL film profiles at the inlet and outlet exhibit self similarity and can be scaled in terms of a similarity solution allowing for a detailed description of the film thickness with speed and/or load.

It should be noted that the developed EHL theory is mainly for elastic materials and cannot meet the needs of viscoelastic materials [122], e.g. for polymers and polymer-based composites. In this thesis, the built "hard" and "soft" EHL solutions are taken as the starting point for the modeling of viscoelastic contact problems. The effect of solid viscoelasticity will be studied including viscoelastic half-space and viscoelastic layered contact problems.

1.3 Solid Viscoelasticity

1.3.1 Viscoelastic Half-Space Contact

Viscoelastic materials have a time-varying response to mechanical loads. The main difference between elastic and viscoelastic contact problems lies in the deformation response to external loads as a result of the rheological behavior in both static and dynamic rolling/sliding contacts. Elastic materials deform instantaneously in response to an applied load without showing any time delay. The resulting contact parameters of an elastic half-space in dry contacts, e.g. the deformation depth, the contact area and the contact pressure, can be calculated analytically according to the Hertzian contact theory.

Numerically, the solution of an elastic half-space dry contact problem can be obtained by solving the 3D Navier-Cauchy equation such as in Ref. [153, 154] or by solving the simplified 2D Boussinesq equation with efficient numerical methods such as the discrete convolution fast Fourier transform (DC-FFT) method [88] or the multilevel multi-integration (MLMI) method [141]. Analytical solutions and efficient numerical methods are available for idealized elastic contacts. However, this is not yet the case for viscoelastic contact problems. The most challenging part of solving a viscoelastic dry and/or lubricated contact problem is the efficient evaluation of the viscoelastic deformation. In principle, to know the deformation of a viscoelastic half-space, a time integration should be added to the elastic

Boussinesq deformation equation to take the history effect into account. This is expensive from a computation point of view, and therefore a new scheme to evaluate the viscoelastic deformation is highly needed.

1.3.2 Viscoelastic Layer vs. "Hard" EHL Film

In classical EHL theory, the Reynolds equation, obtained from the Navier Stokes equation in the regime of thin layer flow $h/L \ll 1$ (lubrication assumption), is used to describe the viscous lubricant flow. It relates the pressure in the lubricant film to the gap geometry and the velocities of the moving surfaces. In highly loaded contacts, inside the contact area, the lubricant, owing to the high viscosity, hardly exhibits any pressure driven flow, and it behaves as a near solid layer. This may provide a new way of modeling lubrication in the very thin film regime, i.e. not from the viewpoint of a continuous film but from the viewpoint of a viscoelastic material with a very local support.

This approach may have another advantage. Regarding the lubricant film prediction most models rely on the continuum based Reynolds equation, possibly augmented with a complementary condition to account for starvation [27] and/or a pragmatic incorporation of a minimum film threshold to allow local film breakdown in modeling mixed lubrication. However, by definition a continuum Reynolds based model is quite limited in the possibilities to model complex intermittent contact problems as well as possible variation of the rheological behavior. Some first steps towards an alternative approach of EHL contact modeling were pioneered by van Emden and Venner[134]. They developed a generic first model of this nature based on a standard dry contact between semi-infinite elastic bodies, e.g. using surface integral equations, covered with a viscoelastic oedometric layer aimed to represent a lubricant film.

It was demonstrated that with the dry-contact viscoelastic (oedometric) layer model, simulation results of the shape of separating film could be obtained that were strikingly similar to the well-known fully flooded fluid EHL film results obtained without solving the Reynolds equation. Note that dry contact problems are relatively easier to solve than the classical fluid-structure coupled way of modeling. Recently, experiments were carried out by the author with a solid thin PDMS (polydimethylsiloxane) layer between a steel ball and a glass disc under pure rolling and squeeze (creep) test conditions. The film profile (shape of the deformed PDMS layer) in the contact zone was measured by optical interferometry. It is interesting to see that essential elements of fluid film lubrication, e.g. the occurrence of the characteristic side lobes during a pure rolling test and the dimple during a squeeze (creep) test, were well represented by the viscoelastic layer, see Fig.1.7 (c) and (d). Note that there was no liquid lubricant except for the viscoelastic solid-like PDMS layer.

These results lead to the hypothesis that it may be possible to model a lubricant film as a possibly partitioned viscoelastic layer with specific local properties which can be modeled without the need of the continuum based Reynolds equation and would allow a much larger variety of constitutive behavior to be implemented. In this thesis, the possibility of modeling EHL and even mixed lubrication using the concept of viscoelastic layer will be further studied by carrying out numerical simulations of viscoelastic layered contact problems.

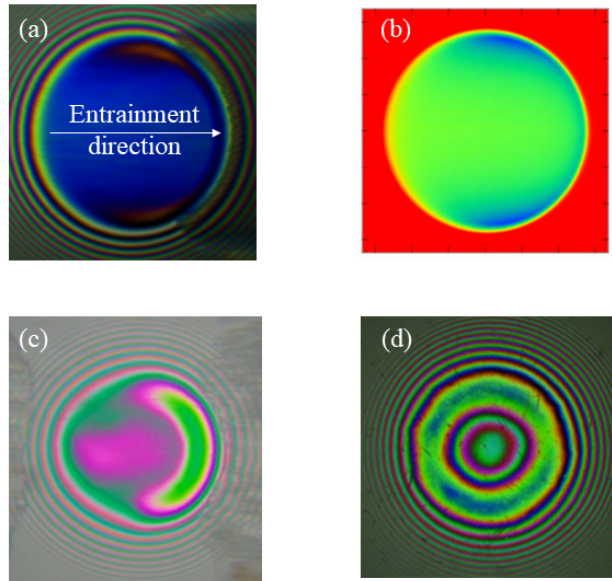


Figure 1.7: Concept of viscoelastic layer lubrication and interferograms of lubricating film in concentrated point contacts between a loaded steel ball and a glass disc. (a) experimental result: a typical horse-shoe shaped EHL film measured with oil lubrication, at pure rolling; (b) simulation results with viscoelastic layer model [134], based on dry contact; (c) experimental result: PDMS viscoelastic layer lubrication, no oil, at pure rolling; (d) experimental result: indentation of PDMS viscoelastic layer with an initial thickness of $20\mu\text{m}$, no oil.

1.4 Objective

To advance the understanding of solid and layered viscoelastic EHL, the following configurations are studied,

- **Viscoelastic dry (VED) contact problem;** in literature, the information regarding viscoelastic modeling with different models and equations is quite scattered. In this work, a concise description of modeling and numerical simulation will be provided. A novel and efficient modeling method for the deformation evaluation of a viscoelastic half-space will be developed.
- **Visco-elastohydrodynamically lubricated (VEHL) contact problem;** the classical EHL theory for elastic contacts will be extended to VEHL based on the viscoelastic deformation evaluation scheme developed in the first work, and the effect of solid viscoelasticity on the film profile and pressure distribution will be described in relation to the relevant dimensionless parameters.
- **Viscoelastic layered dry contact problem;** a 3D viscoelastic layered contact model will be presented, and the concept of using a viscoelastic layer to represent a "hard" EHL film will be discussed.

For each viscoelastic contact problem, the relevant viscoelastic deformation, contact size, and pressure distribution are investigated by comparing in close to the corresponding elastic cases.

1.5 Outline

The outline of this thesis is as follows.

Chapter 2 introduces the fundamentals of viscoelasticity. First, elementary mechanical models that describe the rheological properties of viscoelastic materials are introduced. These models present the relationship between stress and strain and the mathematical description of the phenomena of creep and relaxation behavior of viscoelastic materials. Second, the correspondence principle and the Boltzmann superposition principle are used to derive the viscoelastic deformation equation based on existing elastic solutions for viscoelastic contact problems.

In Chapter 3, modeling and numerical simulation of the VED point contact problems are presented. Different approaches to model the viscoelastic deformation are discussed for both static and dynamic rolling contacts. In particular a novel viscoelastic deformation equation is proposed so that the efficiency of computation of a viscoelastic contact problem remains close to that of an elastic problem. For the numerical simulation, multigrid methods have been used.

In Chapter 4, the VED contact problem studied in Chapter 3 is extended to the lubricated case, i.e. VEHL problem. A theoretical and experimental investigation is evaluated and validated. An efficient VEHL numerical algorithm has been developed by implementing the new viscoelastic deformation equation proposed in Chapter 3. This algorithm is used for a parametric study to investigate the effect of solid viscoelasticity on the pressure and film thickness. For model validation, lubricating film thickness measurements are carried out using optical interferometry in configurations of a soft PMMA ball rolling against a glass disc. The results provide a good framework for the understanding and interpretation of viscoelastic solid effects on the film and pressure behavior in highly deformed (soft) lubricated contacts.

Chapter 5 studies viscoelastic layered contact problems. The three dimensional (3D) quasi-static contact problem for a rigid sphere rolling on a viscoelastic layered elastic half-space is considered. The effects of the viscoelastic layer and its thickness on rolling contacts are investigated using both a simplified foundation approach as well as a full numerical method named as Navier-Cauchy stress analysis. A parametric study is carried out for a thin layer regarding contact stresses and layer deformation. The possibility of EHL modeling using the concept of viscoelastic layer contacts as suggested by von Emden [35] is discussed.

Finally, in Chapter 6 the conclusion of the present study and recommendations for the future research are given.

Chapter 2

Fundamentals of Viscoelasticity

Viscoelasticity is the study of materials with mechanical properties that have characteristics of both elastic solids and viscous fluids. In this chapter, some fundamentals of linear viscoelasticity are reiterated. First, typical viscoelastic behaviors including strain creep behavior and stress relaxation behavior are introduced in Sec.2.1. The basic rheological (mechanical) models of viscoelasticity are introduced in Sec.2.2, including the Maxwell model, the Kelvin-Voigt model and the Standard Linear Solid (SLS) model. The derivation of their constitutive equations, creep compliance and relaxation modulus functions are given. Subsequently in Sec.2.3, the Boltzmann superposition principle is used to characterize more general stress/strain-varying viscoelastic response, e.g. strain response for varying stress input. Finally, the elastic-viscoelastic correspondence principle used to solve viscoelastic contact problems is introduced. Its application in deriving the viscoelastic half-space deformation equations based on the elastic deformation equations is given in Sec.2.4.

2.1 Viscoelastic Behavior

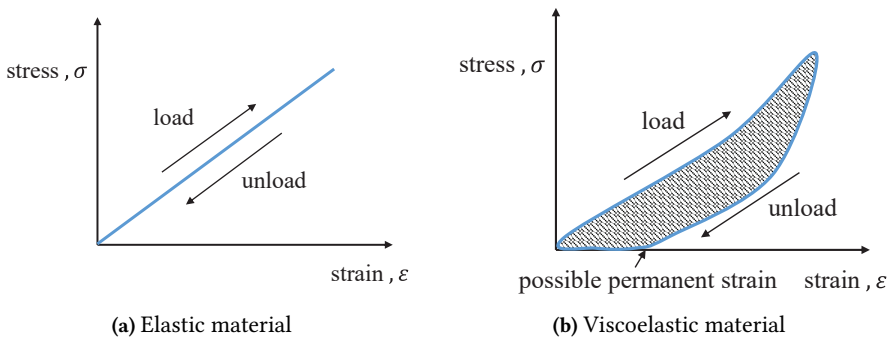


Figure 2.1: Stress-strain curves for a purely elastic material (a) and a viscoelastic material (b) obtained in a tension/compression test.

For viscoelastic materials, the mechanical characterization consists of performing uniaxial tensile/compressive tests as is common for elastic solids, see Fig.2.1. For purely elastic materials, the deformation due to an external load is completely and instantaneously reversible upon load removal. The loading and unloading curves coincide, as shown in

Fig.2.1 (a). No energy is dissipated in a loading-unloading cycle. A viscoelastic substance has both elastic and viscous components and dissipates energy during a loading-unloading cycle. A hysteresis loop is visible in the stress-strain curve, indicating the amount of energy lost in the process, see Fig.2.1 (b).

The viscosity of a viscoelastic material leads to a time-dependent strain rate of the material in a deformation process. To describe the time-dependent material response, specific tests are used in the studies of viscoelasticity. The three most common tests are strain creep, stress relaxation and dynamic (sinusoidal) loading [17, 80].

2.1.1 Creep

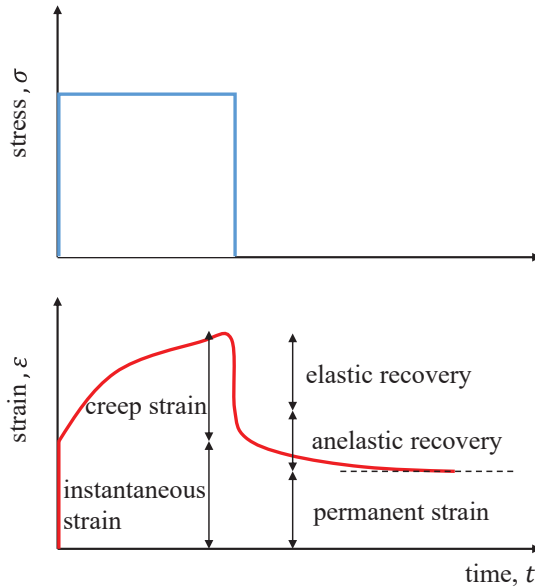


Figure 2.2: Schematic of strain response to the creep-recovery tests: stress imposed (top), strain response (bottom).

Fig.2.2 shows typical responses of a complex but close to real viscoelastic material to an imposed constant load during a specific period of time in a creep-recovery test. Firstly an instantaneous elastic strain occurs upon loading, followed by an increasing strain over time. This time-dependent response is known as *creep*, which is one of the fundamental characteristics of viscoelastic materials. The creep strain usually increases with a decreasing rate so that eventually a more-or-less constant-strain steady state is reached. Many materials do not reach such a noticeable steady-state, not even after a very long time [17]. When unloading, the elastic strain is recovered immediately followed by an anelastic recovery-strain recovered over time. At the end, a permanent strain may then be left in the material.

A test which focuses on the loading phase only is called a creep test. In a creep test, it is obvious that if the stress is constant and the strain is a function of time, the compliance

also varies with time. Analogous to the definition of the elastic compliance (the reciprocal of the elastic modulus), the compliance so obtained is defined as the creep compliance of viscoelasticity and is given by,

$$\varphi_c(t) = \frac{\epsilon(t)}{\sigma_0} \quad (2.1)$$

2

2.1.2 Stress Relaxation

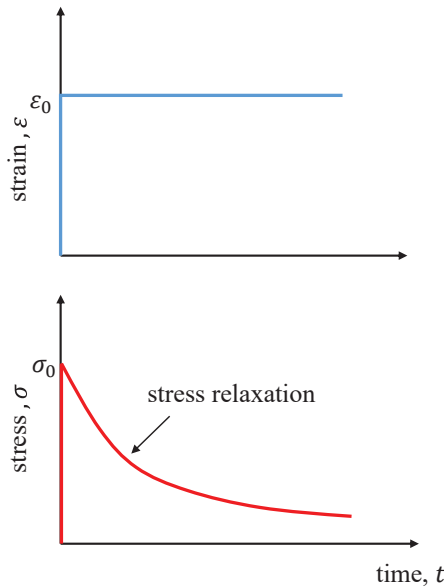


Figure 2.3: Schematic of stress response to an imposed strain: the imposed strain (top) resulting stress as a function of time (bottom).

The second fundamental test for viscoelastic materials is the stress relaxation test. Fig.2.3 shows the typical response of a viscoelastic material to a constant strain. The stress required to hold the viscoelastic material at a constant strain decreases over time. This phenomenon is called *stress relaxation*. It is due to re-arrangement of material on molecular- or micro-scale.

The stress relaxation test defines a new quantity called the relaxation modulus,

$$\psi_r(t) = \frac{\sigma(t)}{\epsilon_0} \quad (2.2)$$

Writing Eq.(2.2) as $\sigma(t) = \psi_r(t)\epsilon_0$ gives a stress-strain relation analogous to Hooke's law for materials that are time independent.

Summarizing, a relaxation test provides the equation for the material property identified as the relaxation modulus. Similarly, a creep test provides the equation for the creep compliance.

2.1.3 Linear Viscoelastic Material

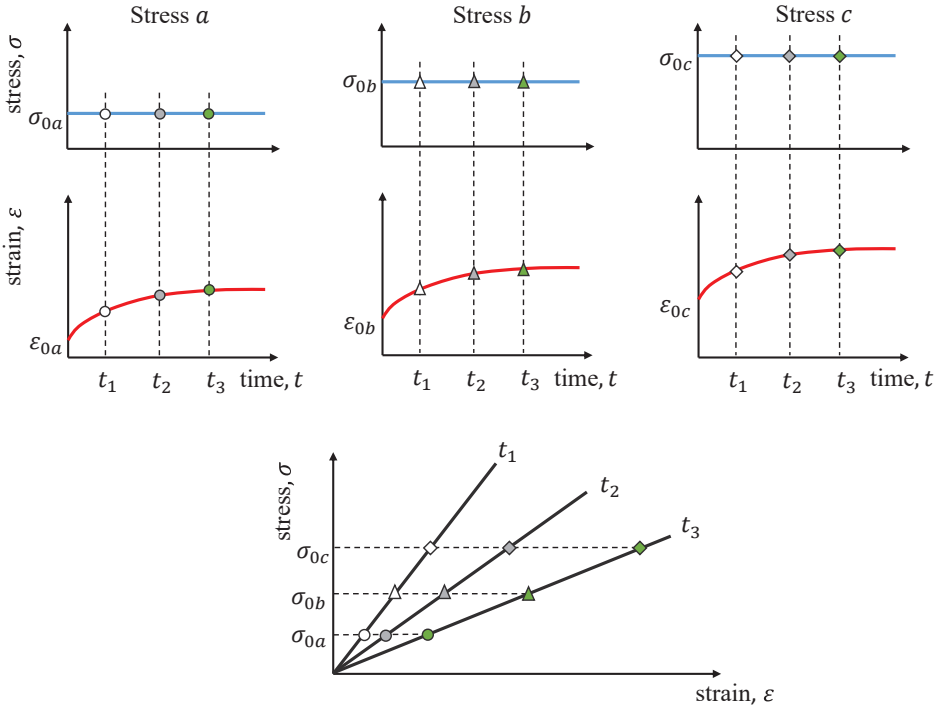


Figure 2.4: Schematic representation of linear viscoelastic material and its linear response to different stresses.

Linear viscoelastic materials are those for which there is a linear relation between stress and strain at any given time, see Fig.2.4. In other words, the above-mentioned creep compliance and relaxation modulus are functions of time only and do not depend on the levels of the applied stress/strain. In this thesis, the investigations are confined to this linear viscoelasticity assumption.

2.1.4 Dynamic Loading

Viscoelastic behavior normally occurs at different time scales in material. Creep and stress relaxation tests are convenient for studying material response at long times (minutes to days), but less accurate at shorter times (seconds and less). Dynamic tests, in which the stress (or strain) resulting from a harmonic strain (or stress) is measured, are often used to characterize the material response over short periods of times.

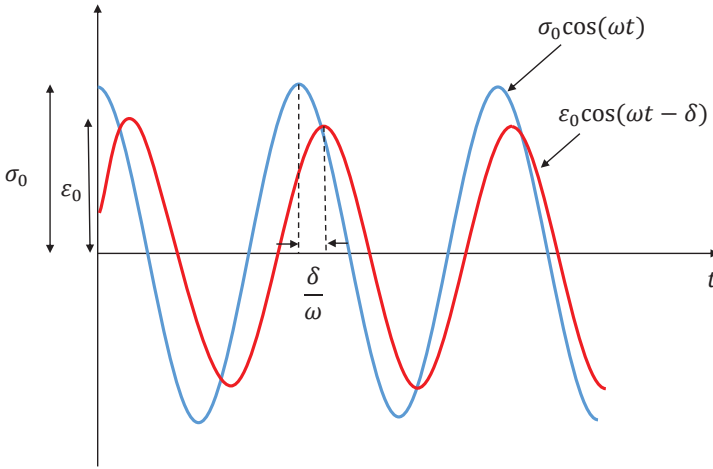


Figure 2.5: Strain response to an sinusoidal oscillating stress in a dynamic loading test.

When a viscoelastic material is subjected to a harmonically varying stress, a steady state will eventually be reached. The resulting strain is also harmonic with the same angular frequency but with a delay of phase angle δ , see Fig.2.5. This delayed response in strain is analogous to the delayed strain observed in creep tests. For a dynamic loading case with the origin along the time axis is chosen to coincide with a time at which the strain passes through its maximum. The strain and stress functions are:

$$\epsilon(t) = \epsilon_0 \cos(\omega t), \quad (2.3)$$

$$\sigma(t) = \sigma_0 \cos(\omega t + \delta). \quad (2.4)$$

The phase angle δ in Eq.(2.4) is usually referred to as the *loss angle* of the material [17]. Expanding the stress using trigonometric relations,

$$\sigma(t) = \sigma_0 \cos(\omega t) \cos(\delta) - \sigma_0 \sin(\omega t) \sin(\delta). \quad (2.5)$$

Defining:

$$E' = \frac{\sigma_0}{\epsilon_0} \cos(\delta), \quad E'' = \frac{\sigma_0}{\epsilon_0} \sin(\delta), \quad (2.6)$$

Eq.(2.5) can be written as:

$$\sigma(t) = \epsilon_0 \left(E' \cos(\omega t) - E'' \sin(\omega t) \right). \quad (2.7)$$

The quantities defined in Eq.(2.6) are a measure of how much the response is in phase with the input. E' , the ratio of the in-phase stress to the strain, is called the *storage modulus* and the E'' , the ratio of the out-of-phase stress to the strain, is called the *loss modulus*. They are usually written as the components of a complex modulus, E^* :

$$E^* = E' + iE'', \quad (2.8)$$

with $i = \sqrt{-1}$. The loss angle can be expressed as

$$\tan(\delta) = E' / E'' . \quad (2.9)$$

A convenient way to obtain the complex modulus is to express the stress and strain functions:

$$\sigma(t) = \sigma_0^* e^{i\omega t} , \quad (2.10)$$

$$\epsilon(t) = \epsilon_0^* e^{i\omega t} . \quad (2.11)$$

The complex modulus can now be written simply as

$$E^* = \sigma_0^* / \epsilon_0^* . \quad (2.12)$$

2.2 Rheological Models

Rheological-mechanical models and constitutive equations are essential to describe viscoelastic behavior of material quantitatively. In principle, at least phenomenologically, the stress-strain relation of linear viscoelastic materials can be modeled by two basic elements, i.e. an elastic (Hooke) spring and a viscous (Newtonian) dashpot, in various configurations. In this section, these two basic elements and the widely used rheological-mechanical models for viscoelastic materials are presented.

2.2.1 Linear Elements

Hooke spring: for ideal elastic solids in accordance with Hooke's law, the deformation behavior can be modeled with a spring. The stress σ is proportional to strain ϵ in a small deformation but independent of the rate of strain

$$\sigma = E\epsilon \quad (2.13)$$

where E is the stiffness of the spring.

Newtonian dashpot: for ideally viscous fluids in accordance with Newtonian fluid behavior, the deformation/flow behavior is usually modeled by a linear dashpot (damper). It responds with stress being proportional to strain-rate

$$\sigma = \eta \dot{\epsilon} \quad (2.14)$$

where η is the Newtonian viscosity of the fluid. Note that there is no deformation of the dashpot at the onset of stress, and it takes time for the strain to build up.

The deformation behavior of viscoelastic materials can now be modeled by combining basic elements of a Hooke spring and a Newtonian dashpot in various configurations. The two simplest viscoelastic models are the Maxwell model and the Kelvin-Voigt model. More complex models are combinations of multiples of the two basic elements in series and/or parallel. In the following section, the most widely used models, i.e. the Maxwell model, the Kelvin-Voigt model and the standard linear solid (SLS) model, are given and their creep compliance and relaxation modulus functions are derived.

2.2.2 The Maxwell Model

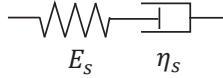


Figure 2.6: Schematic of the Maxwell viscoelastic model

The Maxwell model, schematically shown in Fig.2.6, is one of the simplest but widely used viscoelastic rheological models. It consists of a spring with stiffness E_s and a dashpot with viscosity η_s in series.

Let ϵ_1 be the strain of the spring part and ϵ_2 the strain associated with the dashpot. As the elements are in series, by definition the stress must be equal: $\sigma = \sigma_1 = \sigma_2$, and

$$\epsilon = \epsilon_1 + \epsilon_2 = \frac{\sigma}{E_s} + \epsilon_2. \quad (2.15)$$

Differentiation with respect to time gives:

$$\dot{\epsilon} = \frac{\dot{\sigma}}{E_s} + \dot{\epsilon}_2 = \frac{\dot{\sigma}}{E_s} + \frac{\sigma}{\eta_s}. \quad (2.16)$$

We can now write Eq.(2.16) in the so-called standard form, in which the constitutive equation is written with σ and $\dot{\sigma}$ on one side scaled such that σ appears with multiplication unity, and ϵ and $\dot{\epsilon}$ on the other side of the equality sign:

$$\sigma + \eta_s \frac{\dot{\sigma}}{E_s} = \eta_s \dot{\epsilon}. \quad (2.17)$$

To obtain the creep compliance function of the Maxwell model we apply a constant stress $\sigma(t) = \sigma_0$. In that case $\dot{\sigma} = 0$. Eq.(2.17) then reduces to:

$$\sigma_0 = \eta_s \dot{\epsilon}, \quad (2.18)$$

which can be solved for $\epsilon(t)$ giving

$$\epsilon(t) = \frac{\sigma_0}{\eta_s} t + C, \quad (2.19)$$

where the integration constant C follows the initial condition $\epsilon(0) = \frac{\sigma_0}{E_s}$, so that:

$$\epsilon(t) = \frac{\sigma_0}{\eta_s} t + \frac{\sigma_0}{E_s} = \varphi_c(t) \sigma_0, \quad (2.20)$$

where $\varphi_c(t)$ is the creep compliance function:

$$\varphi_c(t) = \frac{1}{E_s} + \frac{t}{\eta_s}. \quad (2.21)$$

Correspondingly, the relaxation modulus function can be obtained by solving the constitutive differential equation with a constant strain as input. The detailed derivation is not repeated here, interested readers are referred to [17]. The relaxation modulus of the Maxwell model is

$$\psi_r(t) = E_s e^{-t/\tau}, \quad (2.22)$$

where τ is the relaxation time, $\tau = \frac{\eta_s}{E_s}$.

Fig.2.7 shows the creep (and recovery) response of viscoelastic materials characterized by the Maxwell model (solid line). There is an instant increase in strain ϵ_0 when a constant stress σ_0 is applied. The Maxwell model, with a free dashpot, has continuously increasing strain in the loading phase and ends with a permanent strain when the load is removed, as shown in the figure. Compared to the response of a close to real viscoelastic material represented by the dashed line in the figure, there is creep but not of continuously decreasing strain-rate type and delayed elasticity. Hence, the Maxwell model, also called the Maxwell *fluid* model, can often not be used to describe the creep behavior of real viscoelastic materials.

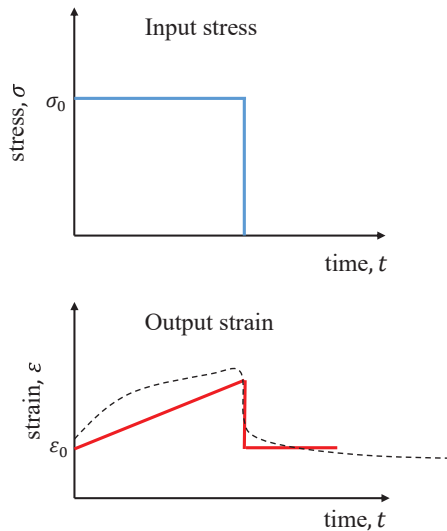


Figure 2.7: Creep behavior of a viscoelastic material characterized by the Maxwell model. The dashed line in the figure represents the response of a realistic viscoelastic material as given in Fig.2.2.

2.2.3 The Kelvin-Voigt Model

The Kelvin-Voigt model is another basic model for viscoelasticity. It consists of a spring element with modulus E_s and a dashpot element with viscosity η_s in parallel, see Fig.2.8.

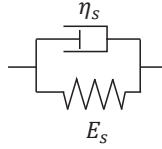


Figure 2.8: Schematic of the Kelvin-Voigt viscoelastic model.

Let ϵ_1 be the strain associated with the spring element and ϵ_2 the strain associated with the dashpot element. As the elements are in parallel, the strain must be equal: $\epsilon = \epsilon_1 = \epsilon_2$. The total stress is the sum of the stresses $\sigma = \sigma_1 + \sigma_2$. The relation between stress σ , stress rate $\dot{\sigma}$, strain ϵ and strain rate $\dot{\epsilon}$ is,

$$\sigma = \sigma_1 + \sigma_2 = E_s \epsilon + \eta_s \dot{\epsilon}. \quad (2.23)$$

The creep compliance function of the Kelvin-Voigt model follows from solving $\epsilon(t)$ from

$$E_s \epsilon + \eta_s \frac{d\epsilon}{dt} = \sigma_0. \quad (2.24)$$

This is done in two steps using standard methods. Let the solution be written as $\epsilon = \epsilon_p + \epsilon_h$. First we determine the solution ϵ_h of the homogeneous equation, and next find a particular solution ϵ_p of the inhomogeneous equation. ϵ_h satisfies:

$$E_s \epsilon + \eta_s \frac{d\epsilon}{dt} = 0. \quad (2.25)$$

Substitution of $\epsilon_h(t) = e^{\lambda t}$ gives $\lambda = -\frac{E_s}{\eta_s}$ so that the solution is

$$\epsilon_h(t) = C e^{-\frac{E_s}{\eta_s} t}. \quad (2.26)$$

A particular solution of the inhomogeneous equation is $\epsilon_p(t) = \frac{\sigma_0}{E_s}$. So the solution $\epsilon(t)$ is:

$$\epsilon(t) = \frac{\sigma_0}{E_s} + C e^{-\frac{E_s}{\eta_s} t}. \quad (2.27)$$

The constant C follows from the initial condition: $\epsilon(0) = 0$ as the response of the material to an applied constant stress is not immediate due to the dashpot and the spring in parallel. Substitution of $\epsilon(0) = 0$ in Eq.(2.26) gives $C = -\frac{\sigma_0}{E_s}$, so that

$$\epsilon(t) = \frac{\sigma_0}{E_s} + C e^{-\frac{E_s}{\eta_s} t} = \frac{\sigma_0}{E_s} (1 - e^{-\frac{t}{\tau}}), \quad (2.28)$$

the ratio $\tau = \eta_s/E_s$ is referred to as the retardation time. From the definition $\epsilon(t) = \sigma_0 \varphi_c(t)$, we find the creep compliance function for the Kelvin-Voigt model:

$$\varphi_c(t) = \frac{1}{E_s} (1 - e^{-t/\tau}). \quad (2.29)$$

Solving the constitutive equation of the Kelvin-Voigt model with a constant strain input gives the relaxation function,

$$\psi_r(t) = E_s + \eta_s \delta(t), \quad (2.30)$$

where $\delta(t)$ is the Dirac delta function.

The response of the Kelvin-Voigt model in a creep-recovery test given in Fig.2.9 shows that a time-delayed response occurs, as the dashpot connected in parallel with the spring prohibits a sudden increase in the output of strain. Again, the spring wants to recover but the dashpot holds it back when unloading. The creep-recovery response given in Fig.2.9 shows a transient-type creep and an anelastic recovery, but no instantaneous elastic strain compared to the response of a real viscoelastic material (the dashed line in the figure). Hence, the Kelvin-Voigt model, also called the Kelvin *solid* model, cannot be used to describe the relaxation behavior of real viscoelastic materials.

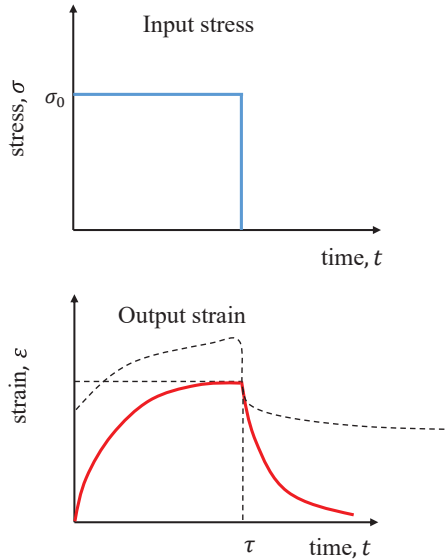


Figure 2.9: Creep behavior of viscoelastic materials characterized by the Kelvin-Voigt model. The dashed line in the figure represents the response of a real viscoelastic behavior as given in Fig.2.2.

2.2.4 The Standard Linear Solid (SLS) Model

A more complicated and representative rheological model, i.e. the three-element Standard Linear Solid (SLS) model in the Kelvin representation, is schematically shown in Fig.2.10. This model consists of two units (subscript 1 and 2): a linear spring of rigidity E_f , and a Kelvin-Voigt model of a spring E_s in parallel with a dashpot of viscosity η_s . Towards the modeling of real viscoelastic material behaviors, we expect the left-hand spring to deform immediately upon loading. The dash pot then takes up the stress, transferring the load to the second spring as it slowly creeps over time. Upon unloading we expect the left-hand spring to contract immediately and for the right-hand unit to slowly relax, being held back by the dashpot.

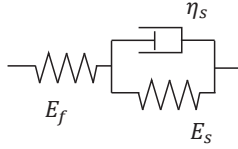


Figure 2.10: Schematic of the standard linear solid (SLS) viscoelastic model in the Kelvin representation.

As the left-hand spring and the Kelvin-Voigt unit are in series, by definition we have

$$\sigma = \sigma_1 = \sigma_2, \quad (2.31)$$

and

$$\epsilon = \epsilon_1 + \epsilon_2. \quad (2.32)$$

For the Kelvin-Voigt unit in the SLS model, we have $\sigma = \sigma_2 = E_s \epsilon_2 + \eta_s \dot{\epsilon}_2$. Using $\epsilon_1 = \frac{\sigma_1}{E_f} = \frac{\sigma}{E_f}$ and $\epsilon_2 = \epsilon - \epsilon_1$, we find

$$\sigma = E_s \left(\epsilon - \frac{\sigma}{E_f} \right) + \eta_s \left(\dot{\epsilon} - \frac{\dot{\sigma}}{E_f} \right), \quad (2.33)$$

as the differential equation which relates stress and strain. Written in a standard form, the constitutive equation of the SLS model is:

$$E_f (\epsilon + \tau \dot{\epsilon}) = (1 + R_e) \sigma + \tau \dot{\sigma}, \quad (2.34)$$

where τ is the constant (single) relaxation time $\tau = \eta_s / E_s$, and R_e is the elasticity ratio $R_e = E_f / E_s$.

The creep compliance function of the SLS model can be derived by solving the differential equation, Eq.(2.34), for a constant stress input. However, it can be obtained more easily by summing up (the two units are in series) the creep compliance functions of the spring

$$\epsilon_1(t) = \varphi_{c,1}(t) \sigma_0 = \frac{\sigma_0}{E_f}, \quad (2.35)$$

and of the Kelvin-Voigt model in Eq.(2.29)

$$\epsilon_2(t) = \varphi_{c,2}(t) \sigma_0 = \frac{\sigma_0}{E_s} (1 - e^{-t/\tau}), \quad (2.36)$$

resulting:

$$\varphi_c(t) = \varphi_{c,1}(t) + \varphi_{c,2}(t) = \frac{1}{E_f} [1 + R_e (1 - e^{-t/\tau})], \quad (2.37)$$

where $\tau = \eta_s / E_s$ and $R_e = E_f / E_s$. Again, the corresponding relaxation modulus can be derived by solving the differential equation, Eq.(2.34), with a constant strain input, which is

$$\psi_r(t) = \frac{E_f E_s}{E_f + E_s} (1 + R_e e^{-t/\tau}), \quad (2.38)$$

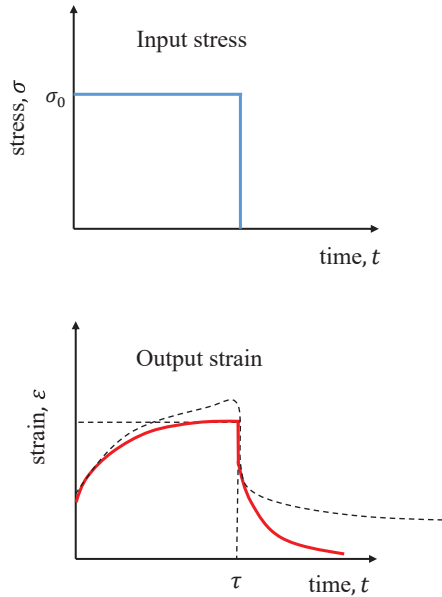


Figure 2.11: Creep behavior of viscoelastic materials characterized by the SLS model. The dashed line in the figure represents the response of a real viscoelastic behavior as given in Fig.2.2.

where $\tau_2 = \eta_s / (E_f + E_s)$.

The full creep-recovery response of the SLS model is shown in Fig.2.11. Compared to the response of realistic viscoelastic materials shown by the dashed line in the figure, it seems to be fairly close to almost all features of responses, although there is no permanent strain left.

From the above analysis, it can be seen that the creep compliance and relaxation modulus can be derived from the corresponding differential constitutive equations by: (a) assuming that the stress is constant and solving for the differential equation in strain, leading to the creep compliance function, and (b) assuming that the strain is constant and solving for the differential equation in stress, leading to the relaxation modulus function. The differential equations relating stress and strain of spring-dashpot models take the form of a linear ordinary differential equation with constant coefficients. Both relaxation modulus and creep compliance including exponential functions are summarized in Fig.2.12.

The expressions of the complex modulus in Fig.2.12 can be obtained with Eq.(2.12) by substituting Eqs.(2.10) and (2.11) into the constitutive equations of the viscoelastic rheological models. For details of the derivation processes, interested readers are referred to [119].


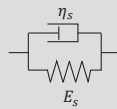
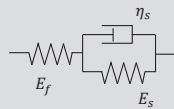
Model			
	The Maxwell model	The Kelvin-Voigt model	The SLS model in Kelvin representation
Constitutive equation	$\sigma + \eta_s \frac{\dot{\sigma}}{E_s} = \eta_s \dot{\epsilon}$	$\sigma = E_s \epsilon + \eta_s \dot{\epsilon}$	$E_f (\epsilon + \tau \dot{\epsilon}) = (1 + R_e) \sigma + \tau \dot{\sigma}$ $R_e = E_f/E_s$
Creep compliance	$\varphi_c(t) = \frac{1}{E_s} + \frac{t}{\eta_s}$	$\varphi_c(t) = \frac{1}{E_s} (1 - e^{-t/\tau})$	$\varphi_c(t) = \frac{1}{E_f} [1 + R_e (1 - e^{-t/\tau})]$
Relaxation modulus	$\psi_r(t) = E_s e^{-t/\tau}$ $\tau = \eta_s/E_s$	$\psi_r(t) = E_s + \eta_s \delta(t)$	$\psi_r(t) = \frac{E_f E_s}{E_f + E_s} (1 + R_e e^{-t/\tau_2})$ $\tau_2 = \eta_s/(E_f + E_s)$
Complex modulus	$E^* = \frac{E_s \tau^2 \omega^2}{1 + \tau^2 \omega^2} + i \frac{E_s \tau \omega}{1 + \tau^2 \omega^2}$	$E^* = E_s + i \eta_s \omega$	$E^* = E_R \frac{1 + \omega^2 \tau \beta}{1 + \beta^2 \omega^2} + i E_R \frac{\omega(\tau - \beta)}{1 + \beta^2 \omega^2}$ $E_R = \frac{E_f}{(1 + R_e)} \quad \beta = \frac{\tau}{(1 + R_e)}$

Figure 2.12: Viscoelastic material models and their rheological-mechanical properties.

It should be noted that the SLS model with a single relaxation time exhibits almost all generic aspects of viscoelastic material behavior; however, real viscoelastic materials can exhibit a spectrum of relaxation times [17, 21, 25]. In this thesis, the SLS model is used to understand fundamentals of dry and lubricated viscoelastic contact problems. The developed solvers can also be extended to consider multi-relaxation times of real materials, which will be demonstrated in Chapter 3.

2.3 Boltzmann Superposition Principle

In previous sections, the described relaxation and creep tests of viscoelastic materials are carried out at quasi-static conditions, i.e. using a constant strain and a constant stress respectively as input. However, most tribological problems are dynamic by nature in practical mechanical systems, for example a ball rolling on a viscoelastic substrate. This means that any point in the viscoelastic material experiences a varying stress/pressure input during its passage through the contact. To know the response of the linear viscoelastic material such as the output of strain/deformation, the Boltzmann superposition principle [17] is used, by which the stress-strain relation can be expressed in the form of an integral. The superposition principle is explained below.

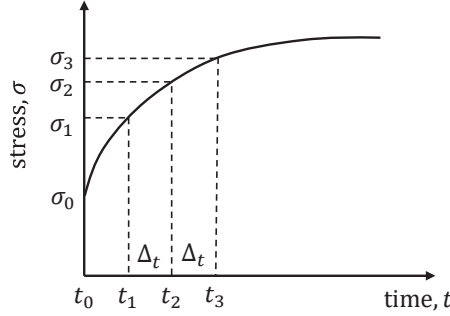


Figure 2.13: Varying stress as input

Proportionality: Firstly, decompose the varying stress input by a series of step inputs, each of which begins at different time as shown in Fig.2.13. Thus, the stress input can be expressed in the following form:

$$\sigma(t) = \sigma_0 + (\sigma_1 - \sigma_0) + (\sigma_2 - \sigma_1) + \dots + (\sigma_n - \sigma_{n-1}). \quad (2.39)$$

At each time instant, the strain response is proportional to the amplitude of the constant stress step applied at $t = t_i$ within the framework of linear viscoelasticity:

$$\epsilon_i(t) = \Delta\sigma_i\varphi_c(t - t_i). \quad (2.40)$$

Superposition: The strain response to two subsequently (at time $t = t_0$ and $t = t_1$) applied constant amplitude ($\Delta\sigma_0$ and $\Delta\sigma_1$) stress steps equals the sum of the separate response. For $t > t_1$

$$\epsilon(t) = \Delta\sigma_0\varphi_c(t - t_0) + \Delta\sigma_1\varphi_c(t - t_1). \quad (2.41)$$

Every excitation can now be seen as an infinite sequence of infinitesimal small stress steps. Superposition then leads to the so-called Boltzmann integrals. Assuming $t_0 = 0$ and taking the limit as n approaches infinity and Δt approaches zero, one obtains:

$$\epsilon(t) = \sigma_0\varphi_c(t) + \int_{0^+}^t \varphi_c(t - q) \frac{d\sigma(q)}{dq} dq. \quad (2.42)$$

For a relaxation test using a varying strain as input, the stress output can be expressed as:

$$\sigma(t) = \epsilon_0\psi_r(t) + \int_{0^+}^t \psi_r(t - q) \frac{d\epsilon(q)}{dq} dq. \quad (2.43)$$

2.4 Elastic-Viscoelastic Correspondence Principle

Due to the structural complexity of viscoelastic materials and their time-dependent properties, it is difficult to develop closed-form mathematical expressions/solutions in (contact) mechanics of viscoelastic materials. In 1944, Alfrey [3] proposed the elastic-viscoelastic

correspondence principle, which made it possible to use transform methods to convert viscoelastic problems into elastic problems in the transformed domain. The correspondence principle allows the wealth of elastic solutions to be used to solve viscoelastic problems. This is also true for the dry/lubricated contact problems in this thesis. Focusing on the point contact problem between a rigid ball and a viscoelastic half-space, the application of the correspondence principle in deriving the viscoelastic deformation equations is detailed in this section. For two elastic bodies in contacts, e.g. a standard Hertzian dry contact, deformation occurs instantaneously when an external load is applied. Therefore, static and frictionless rolling/sliding contact problems have identical governing equations as well as the same (numerical) solution regarding contact characteristics.

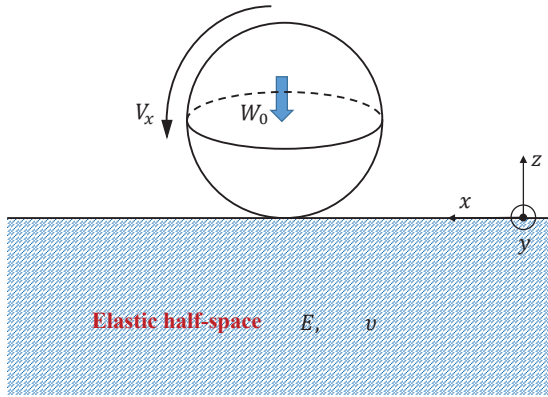


Figure 2.14: Schematic representation of a point contact between a rigid ball and an elastic half-space. (xoy is the coordinate system.)

Fig.2.14 schematically shows an elastic point contact between a rigid sphere of radius R_0 and an elastic half-space. The sphere is moving at a constant speed V_x under a constant load of W_0 . Based on the semi-infinite half-space approximation and the linear elasticity assumption, the Boussinesq double integral in Eq.(2.44) is widely used to determine the local normal displacement of the contact surfaces [75], as

$$u_e(x, y) = \frac{1-\nu^2}{\pi E} \iint \frac{p(x', y')}{\sqrt{(x-x')^2 + (y-y')^2}} dx' dy', \quad (2.44)$$

where E is the elastic modulus and ν is the Poisson ratio of the elastic substrate, and $p(x, y)$ is the generated pressure distribution in the contact zone. The benefit of using Eq.(2.44) is that the local elastic deformation of homogeneous and isotropic solids can be modeled and calculated in two dimensions (x and y directions) instead of fully solving the three-dimensional stress equilibrium equation, e.g. as in Ref. [153].

As a contrast, for viscoelastic contacts studied in this thesis, the time-dependent properties of the material have substantial effects on the process of surface deformation, such as the time-varying contact area under a constant step load of a static contact and the speed/frequency dependent deformation of a dynamic rolling/sliding contact. Proper

viscoelastic deformation equations are necessary to model and solve these viscoelastic contact problems for both dry and lubricated contacts. These are derived based on elastic expressions using the correspondence principle.

2

2.4.1 Viscoelastic Half-Space Deformation

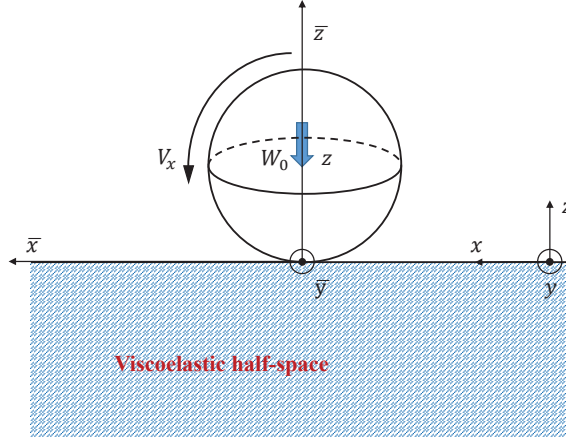


Figure 2.15: Dynamic rolling contact problem formed between a rigid ball with a viscoelastic half-space (xoy : fixed coordinate system; $\bar{x}o\bar{y}$: moving coordinate system).

For the viscoelastic contact problem, a rigid sphere rolling or sliding on a semi-infinite viscoelastic substrate at a constant speed V_x with the xoy coordinate system fixing on the substrate and the $\bar{x}o\bar{y}$ coordinate system moving with the rigid sphere, shown in Fig.2.15. A "viscoelastic Boussinesq equation" can be formulated in the fixed coordinate xoy following the correspondence principle [25] and the solution proposed in [23] for the normal deformation of isotropic viscoelastic half-space.

Similar to the derivation process of the stress-strain relationship for a varying stress as input in Sec.2.3:

- (1) Replacing the elastic compliance, $1/E$ in Eq.(2.44), with the creep compliance function, $\varphi_c(t)$, of the viscoelastic model;
- (2) Decomposing the pressure history into infinite sequence of infinitesimal small pressure steps in the time domain;
- (3) Calculating the response of every pressure excitation, $\Delta_p(p(x, y, t_n) - p(x, y, t_{n-1}))$, using the "viscoelastic Boussinesq equation":

$$\Delta_u(x, y, t) = \frac{1-\nu^2}{\pi} \varphi_c(t-t_n) \iint \frac{p(x', y', t_n) - p(x', y', t_{n-1})}{\sqrt{(x-x')^2 + (y-y')^2}} dx' dy'. \quad (2.45)$$

- (4) Superposition of all contributions based on the linear viscoelasticity assumption. The deformation of the surface of a viscoelastic material at time t due to a time varying

pressure can be obtained as

$$u(x, y, t) = \frac{1-\nu^2}{\pi} \varphi_c(t) \iint \frac{p(x', y', 0)}{\sqrt{(x-x')^2 + (y-y')^2}} dx' dy' + \frac{1-\nu^2}{\pi} \int_{0^+}^t \varphi_c(t-q) \iint \frac{1}{\sqrt{(x-x')^2 + (y-y')^2}} \frac{\partial p(x', y', q)}{\partial q} dx' dy' dq. \quad (2.46)$$

2

Compared to the elastic deformation equation, Eq.(2.44), an integration in time appears in order to take into account the effect of pressure history on the deformation at all instants q . Changing the order of integration for the second term on the right side, Eq.(2.46) can be expressed as

$$u(x, y, t) = \frac{1-\nu^2}{\pi} \varphi_c(t) \iint \frac{p(x', y', 0)}{\sqrt{(x-x')^2 + (y-y')^2}} dx' dy' + \frac{1-\nu^2}{\pi} \iint \frac{1}{\sqrt{(x-x')^2 + (y-y')^2}} \int_{0^+}^t \varphi_c(t-q) \frac{\partial p(x', y', q)}{\partial q} dq dx' dy'. \quad (2.47)$$

Integrating by parts for the integral with respect to the time variable t in Eq.(2.47) gives

$$\int_{0^+}^t \varphi_c(t-q) \frac{\partial p(x', y', q)}{\partial q} dq = [\varphi_c(t-q)p(x', y', q)]_{0^+}^t - \int_{0^+}^t p(x', y', q) d\varphi_c(t-q) = \varphi_c(0)p(x', y', t) - \varphi_c(t)p(x', y', 0) - \int_{0^+}^t p(x', y', q) \frac{d\varphi_c(t-q)}{dq} dq. \quad (2.48)$$

Substituting Eq.(2.48) into Eq.(2.47), the viscoelastic deformation equation can be written as

$$u(x, y, t) = \varphi_c(0)w_e(x, y, t) + \int_{0^+}^t \frac{d\varphi_c(q)}{dq} w_e(x, y, t-q) dq, \quad (2.49)$$

where $w_e(x, y, t) = \frac{1-\nu^2}{\pi} \iint \frac{p(x', y', t)}{\sqrt{(x-x')^2 + (y-y')^2}} dx' dy'$. Compared to Eq.(2.46), the local deformation at each instant now is expressed as the multiplication of the derivative of the creep compliance function and the corresponding "elastic deformation", $w_e(x, y, t)$ related to momentary pressure.

2.4.2 Deformation in Steady-State Rolling Contacts

The relations between the fixed xoy and the moving $\bar{x}\bar{o}\bar{y}$ coordinate systems in Fig.2.15 are

$$\begin{aligned} \bar{x} &= x - V_x t \\ \bar{y} &= y \end{aligned} \quad (2.50)$$

Eq.(2.49) can be written as

$$u(x, y, t) = \frac{1-v^2}{\pi} \varphi_c(0) \iint \frac{p(x', y', t)}{\sqrt{(x-x')^2 + (y-y')^2}} dx' dy' + \frac{1-v^2}{\pi} \int_{0^+}^t \frac{d\varphi_c(q)}{dq} \iint \frac{p(x', y', t-q)}{\sqrt{(x-x')^2 + (y-y')^2}} dx' dy' dq. \quad (2.51)$$

Restricting the analysis to be in the steady state regime and using the relations in Eq.(2.50), Eq.(2.51) can be represented in the moving coordinate, $\bar{x}o\bar{y}$, as

$$u(\bar{x} + V_x t, \bar{y}) = \frac{1-v^2}{\pi} \varphi_c(0) \iint \frac{p(\bar{x}' + V_x t, \bar{y}')}{\sqrt{(\bar{x} + V_x t - (\bar{x}' + V_x t))^2 + (\bar{y} - \bar{y}')^2}} d\bar{x}' d\bar{y}' + \frac{1-v^2}{\pi} \int_0^\infty \frac{d\varphi_c(q)}{dq} \iint \frac{p(\bar{x}' + V_x(t-q), \bar{y}')}{\sqrt{(\bar{x} + V_x t - (\bar{x}' + V_x t))^2 + (\bar{y} - \bar{y}')^2}} d\bar{x}' d\bar{y}' dq. \quad (2.52)$$

Let \bar{x} represent $\bar{x} + V_x t$ in Eq.(2.52), we get

$$u(\bar{x}, \bar{y}) = \frac{1-v^2}{\pi} \varphi_c(0) \iint \frac{p(\bar{x}', \bar{y}')}{\sqrt{(\bar{x} - \bar{x}')^2 + (\bar{y} - \bar{y}')^2}} d\bar{x}' d\bar{y}' + \frac{1-v^2}{\pi} \int_0^\infty \frac{d\varphi_c(q)}{dq} \iint \frac{p(\bar{x}' - V_x q, \bar{y}')}{\sqrt{(\bar{x} - \bar{x}')^2 + (\bar{y} - \bar{y}')^2}} d\bar{x}' d\bar{y}' dq. \quad (2.53)$$

Define $s = \bar{x}' - V_x q$, Eq.(2.53) can be represented as

$$u(\bar{x}, \bar{y}) = \frac{1-v^2}{\pi} \varphi_c(0) \iint \frac{p(\bar{x}', \bar{y}')}{\sqrt{(\bar{x} - \bar{x}')^2 + (\bar{y} - \bar{y}')^2}} d\bar{x}' d\bar{y}' + \frac{1-v^2}{\pi} \int_0^\infty \frac{d\varphi_c(q)}{dq} \iint \frac{p(s, \bar{y}')}{\sqrt{(\bar{x} - V_x q - s)^2 + (\bar{y} - \bar{y}')^2}} ds d\bar{y}' dq. \quad (2.54)$$

The double integral in the equation, $\iint \frac{p(\bar{x}', \bar{y}')}{\sqrt{(\bar{x} - \bar{x}')^2 + (\bar{y} - \bar{y}')^2}} d\bar{x}' d\bar{y}'$ means that the deformation at a location, (\bar{x}, \bar{y}) , depends on the pressure distribution at all points, (\bar{x}', \bar{y}') , in the domain. Then, $p(\bar{x}', \bar{y}')$ and $p(s, \bar{y}')$ in Eq.(2.54) both indicate the pressures at different points in the computational domain, and Eq.(2.54) can be rewritten in a standard form,

$$u(\bar{x}, \bar{y}) = \frac{1-v^2}{\pi} \varphi_c(0) \iint \frac{p(\bar{x}', \bar{y}')}{\sqrt{(\bar{x} - \bar{x}')^2 + (\bar{y} - \bar{y}')^2}} d\bar{x}' d\bar{y}' + \frac{1-v^2}{\pi} \int_0^\infty \frac{d\varphi_c(q)}{dq} \iint \frac{p(\bar{x}', \bar{y}')}{\sqrt{(\bar{x} - V_x q - \bar{x}')^2 + (\bar{y} - \bar{y}')^2}} d\bar{x}' d\bar{y}' dq. \quad (2.55)$$

Hunter [72] derived the same equation as Eq.(2.55) for viscoelastic half-space deformation by using the Fourier transform method. A common feature of these two derivation methods

is to convert the viscoelastic deformation from the time domain to the spatial domain for the dynamic rolling viscoelastic contact problems. As a result, the integration at different instants in the time domain in Eq.(2.46) or Eq.(2.49) is transformed into an integration over points in the spatial domain in Eq.(2.55).

Substituting the creep compliance function of a specific viscoelastic model in Eq.(2.55) gives the deformation equation of the corresponding viscoelastic material. For the SLS model used in this thesis, the deformation equation is

$$u(\bar{x}, \bar{y}) = u_e(\bar{x}, \bar{y}) + R_e \frac{1}{\tau} \int_0^{\infty} e^{-\frac{q}{\tau}} u_e(\bar{x} - V_x q, \bar{y}) dq, \quad (2.56)$$

where $u_e(\bar{x} - V_x q, \bar{y})$ in Eq.(2.56) is the instantaneous elastic deformation at location of $(\bar{x} - V_x q, \bar{y})$:

$$u_e(\bar{x} - V_x q, \bar{y}) = \frac{1 - \nu^2}{\pi} \frac{1}{E_f} \iint \frac{p(\bar{x}', \bar{y}')}{\sqrt{(\bar{x} - V_x q - \bar{x}')^2 + (\bar{y} - \bar{y}')^2}} d\bar{x}' d\bar{y}'. \quad (2.57)$$

Chapter 3

Viscoelastic Dry Contact

3

In this chapter, the viscoelastic concentrated contact modeling is studied, first considering the problem of a viscoelastic half-space and a rigid sphere, both in static (squeeze) as well as (frictionless) rolling/sliding conditions. In particular modeling aspects are discussed so that the efficiency of computation of the viscoelastic deformation remains close to the efficiency of (numerical) computation of an elastic deformation. This is achieved by rewriting Hunter's [72] deformation equation from an integral form into a differential form by applying the Leibniz integral theorem, even for complex materials with multiple relaxation times to represent complex viscoelastic properties of materials. The approach can be straightforwardly implemented in any elastic dry and lubricated (EHL) contact solver regardless of the numerical method. Results are discussed in detail, such as the effect of the Deborah number and the relation between the extreme cases of the rolling problem and the static problem. In addition to the case of a rigid sphere against a viscoelastic half-space, also the case of two viscoelastic bodies is considered.

The work in this chapter has been published as: Y. Zhao, G.E. Morales-Espejel, C.H. Venner. Aspects of modeling and numerical simulation of dry point contacts between viscoelastic solids. Tribology International, 165: 107245, 2022.

DOI: <https://doi.org/10.1016/j.triboint.2021.107245>.

3.1 Introduction

Modeling of linear viscoelastic material behavior is often based on the so-called correspondence principle proposed by Alfrey [3] in 1944, in which the solution to a viscoelastic problem was derived from the corresponding elastic solution in a Laplace or Fourier transformed domain [25]. The solution of static contact problems of viscoelastic materials dates back to the 1950s [3, 83, 84]. Lee and Radok [85] applied the correspondence principle and derived an analytical solution to the contact problem between a spherical indenter and a linear viscoelastic half-space. They proposed a generalized method to solve viscoelastic contact problems by replacing the elastic compliance in an elastic solution by a time-dependent viscoelastic creep function. However, the solution fails for the unloading process because negative pressures would appear with a decreasing contact radius. Several approaches [48, 49, 71, 130, 131] have been proposed to overcome this issue. Most studies are limited to idealized viscoelastic material with a single relaxation time. However, recently, Chen et al. [23] summarized Lee and Radok's method and presented a three-dimensional (3D) semi-analytical solution which is capable of simulating the creep behavior of a viscoelastic

material with multi-relaxation times coupled with Fast Fourier Transform (FFT) based algorithms. Koumi and Nelias et al. [82] extended this semi-analytical solution to contact problems between a rigid indenter and a heterogeneous viscoelastic material also using FFT based numerical methods.

Dynamic contact problems between viscoelastic bodies, including frictionless rolling and sliding motion, have been studied extensively. Hunter [72] and Goriacheva [44] proposed analytical solutions for the 2D contact problems between a rigid cylinder and a viscoelastic half-space. Panek and Kalker [106] extended Hunter's 2D line model [72] to a non-trivial 3D point contact case by enforcing the line integral approximation. Hooke and Huang [67] investigated a lubricated 2D EHL line contact problem between bodies of linear viscoelastic materials, and analyzed the influence of the viscoelastic material behavior on the EHL film thickness and pressure. Aleksandrov et al. [2] presented numerical solutions for a 3D sliding problem between a smooth sphere and a viscoelastic half-space. The above listed analyses are limited to ideal viscoelastic materials with one relaxation time. However, a real viscoelastic material presents a wide spectrum of relaxation times, and a single relaxation time is insufficient to represent the phenomenological viscoelastic behavior. For this purpose, viscoelastic models considering multi-relaxation times have been proposed [21, 81, 107, 112, 114]. In 2010, Persson [107] presented a new approach to estimate the apparent friction coefficient for the rolling contact of a rigid cylinder or a sphere on a viscoelastic solid. More recently, Carbone and Putignano [21] developed a novel model, which was validated through experiments later [115], to investigate rolling/sliding contact problems between viscoelastic bodies in the steady-state regime using boundary element method. Based on the model proposed in [21], Putignano and Dini [112, 114] further investigated the influence of solid viscoelastic rheology on a lubricated contact of soft materials. Koumi et al. [81] introduced elastic inhomogeneties in a viscoelastic substrate and solved the frictionless rolling contact problem using FFT methods based on the model in [23].

In principle, both the static and the dynamic contact problems of linear viscoelastic materials can be solved based on the well-established elastic deformation equation, i.e. the Boussinesq deformation equation for an elastic half-space. For the former, a time integral should be added to the elastic Boussinesq equation (Eq.(2.44)) after applying the time integral operation according to the Boltzmann superposition principle (Sec.2.3). For dynamic contact problems, a simplified treatment is to represent the time-dependent deformation equation of viscoelastic materials in a moving coordinate [21, 67, 82] so that the deformation can be converted into an influence coefficient in the elastic Boussinesq deformation equation [21, 72]. In this way, the viscoelastic deformation in a rolling/sliding contact can also be obtained based on existing elastic deformation solutions. However, the challenge is that solving a viscoelastic contact problem is more demanding in terms of computational time. In the literature of EHL study, it has been reported that the elastic deformation or the double integral in the Boussinesq equation can be solved efficiently by numerical methods such as discrete convolution, fast Fourier transform (DC-FFT) [88, 126], and multilevel multi-integration (MLMI) [16, 141]. In viscoelastic contact mechanics, while FFT related methods have been widely used in deformation calculation, MLMI and multigrid techniques have been rarely reported.

In this work, multigrid and MLMI methods [141] have been used to analyze dry contact

problems of a viscoelastic half-space at both static and dynamic contact conditions. The standard linear solid (SLS) model, either with a single relaxation time or with multi-relaxation times, is used to characterize the viscoelastic property of the half-space. A detailed description is given on how to introduce the effect of viscoelasticity into an existing elastic solution for the numerical solution of linear viscoelastic contact problems. Firstly, for static contacts, a new expression of the deformation equation is proposed which can be further used to derive the deformation equation for dynamic rolling/sliding contacts in the spatial domain. Secondly, for solving dynamic viscoelastic contact problems, a novel and efficient numerical approach is proposed allowing the considerations of multi-relaxation times while keeping almost the same computational time as that for an elastic solution. The validation of the developed model and multigrid solver is carried out by comparing the numerical results with Lee and Radok's [85] analytical solution and Carbone's [21] numerical results. After validation, the proposed model is applied to investigate the influence of types of motion, i.e. rolling and sliding, on the pressure distribution and on the contact footprint of viscoelastic materials. The correlation between the static contact problem and the dynamic contact problem at extreme velocity conditions is shown in detail.

Studies regarding viscoelastic modeling, the use of different models and equations, and the information regarding numerical solution are quite scattered in the literature. This work revisits modeling and numerical simulation aspects of viscoelastic behavior for modeling and simulation of concentrated contacts, i.e. contact problems between a sphere and a viscoelastic half-space of single relaxation time and of multi-relaxation times at both static and frictionless dynamic rolling/sliding conditions.

3.2 Viscoelastic Modeling

In this study, the three element SLS model, see Fig.2.10, and its multi-branch generalized version in Fig.3.1 are used to characterize the viscoelastic behavior of the contacting bodies. The SLS model consists of two units (a spring and a Kelvin model) in series, for which the creep compliance function can be obtained from the creep compliance functions of the units, see Sec.2.2.4.

Even though the SLS model with a single relaxation time exhibits the generic aspects of viscoelastic material behavior, it will not accurately cover viscoelastic behavior of specific real materials which can exhibit a spectrum of relaxation times [17, 21, 25] over the length of the contact, since the material properties of both the film and the solids may spatially vary. Multiple relaxation times can be modeled by constructing a model in which each of the units is an SLS model by itself, see Fig.2.10, and the units are in a parallel configuration, see Fig.3.1. This is referred to as the multi-branch generalized SLS model.

In this case, the constitutive relations form a set of n equations, where n is the number of branches considered.

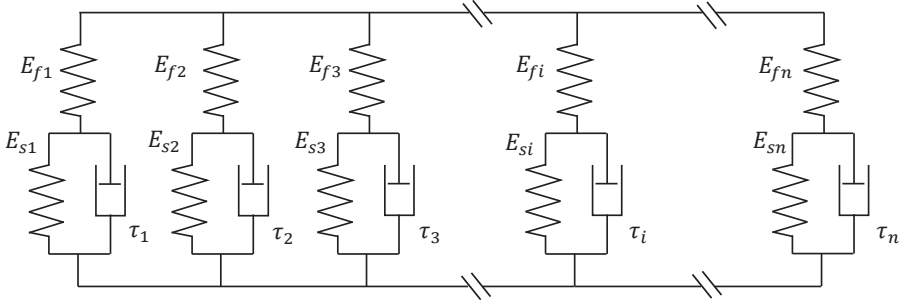


Figure 3.1: Schematic of the multi-branch generalized SLS model describing viscoelastic behavior with multiple relaxation times.

$$\left\{ \begin{array}{l} E_{f1}[\epsilon(t) + \tau_1 \frac{\partial \epsilon(t)}{\partial t}] = (1 + R_{e1})\sigma_1(t) + \tau_1 \frac{\partial \sigma_1}{\partial t} \\ E_{f2}[\epsilon(t) + \tau_2 \frac{\partial \epsilon(t)}{\partial t}] = (1 + R_{e2})\sigma_2(t) + \tau_2 \frac{\partial \sigma_2}{\partial t} \\ \dots \\ E_{fn}[\epsilon(t) + \tau_n \frac{\partial \epsilon(t)}{\partial t}] = (1 + R_{en})\sigma_n(t) + \tau_n \frac{\partial \sigma_n}{\partial t} \end{array} \right. \quad (3.1)$$

where $\tau_i = \eta_{si}/E_{si}$ and $R_{ei} = E_{fi}/E_{si}$. The closure relation of the system is the expression that the overall stress equals the sum of the stresses in the branches (units):

$$\sigma = \sum_{i=1}^n \sigma_i(t). \quad (3.2)$$

Concentrated point contact problems are considered under both static (zero speed) and rolling (and frictionless sliding) condition involving viscoelastic material. The governing equations, in particular the viscoelastic deformation modeling equations, are presented below.

3.2.1 Static Contact

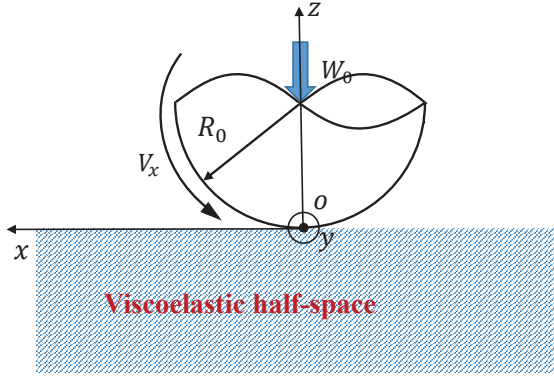


Figure 3.2: Static viscoelastic contact formed between a rigid spherical indenter and a viscoelastic half-space with an applied constant normal load.

The static contact problem between a rigid sphere and a viscoelastic half-space, schematically shown in Fig.3.2, is firstly analyzed. A normal load W_0 is instantaneously applied to the viscoelastic half-space through a spherical indenter of radius R_0 . Subsequently the load is kept constant. The objective is to obtain the variation of the local deformation, the contact region, and the pressure distribution with time.

The static dry contact problem of viscoelastic material can be modeled, like the elastic dry contact (Hertzian) problem [141], by two equations, and a complementary condition. First the gap height equation, Eq.(3.3), consists of the undeformed gap shape approximating the surfaces of the contacting elements as parabolas, and their normal deformation. Next, the load balance equation, Eq.(3.4), stating that, neglecting the contact dynamics, the integral over the pressure should equal the externally applied load at all times. Finally, the actual complementary problem to be solved, is stated in Eq.(3.5). The gap is closed and the pressure is positive; or when the gap is open, neglecting adhesion, the pressure is zero (ambient). This is the Hertz-Signorini-Moreau condition.

$$h(x, y, t) = h_0(t) + \frac{(x - V_x t)^2}{2R_0} + \frac{y^2}{2R_0} + u(x, y, t), \quad (3.3)$$

$$W_0(t) = \iint p(x, y, t) dx dy, \quad (3.4)$$

$$\begin{aligned} h(x, y, t) &= 0, p(x, y, t) > 0, \text{ in contact area} \\ h(x, y, t) &> 0, p(x, y, t) = 0, \text{ out contact area.} \end{aligned} \quad (3.5)$$

Note that Eqs.(3.3)~(3.5) are given in a fixed coordinate system xoy . The variables gap height h , the pressure p , and the normal deformation u , are varying in time, due to the viscoelasticity only as the load is assumed to be constant. For the static problem, the moving velocity V_x is 0. The normal deformation u for viscoelastic materials can be expressed as

(Eq.(2.47), Chapter 2):

$$u(x, y, t) = \varphi_c(t)w_e(x, y, 0) + \int_{0^+}^t \varphi_c(t-q)\Delta_p w_e(x, y, q)dq, \quad (3.6)$$

where $w_e(x, y, t) = \frac{1-\nu^2}{\pi} \iint \frac{p(x', y', t)}{\sqrt{(x-x')^2+(y-y')^2}} dx' dy'$ is the elastic deformation integral transform with the pressure distribution as input, and

$$\Delta_p w_e(x, y, q) = \frac{1-\nu^2}{\pi} \iint \frac{1}{\sqrt{(x-x')^2+(y-y')^2}} \frac{\partial p(x', y', q)}{\partial q} dx' dy' \quad (3.7)$$

is the same integral transform but with the time derivative of the pressure as input. Eq.(3.6) is based on the Boussinesq solution for an elastic infinite half-space [75] and the correspondence principle [25]. The derivation is given in Sec.2.4.1, see Eq.(2.47). The equation has also been used in e.g. [23, 81].

According to the derivation process detailed in Sec.2.4.1, Eq.(3.6) can be rewritten as,

$$u(x, y, t) = \varphi_c(0)w_e(x, y, t) + \int_{0^+}^t \frac{d\varphi_c(q)}{dq} w_e(x, y, t-q)dq. \quad (3.8)$$

Note that Eq.(3.8) uses the derivative of the creep compliance function, rather than the derivative of the pressure in Eq.(3.6) to obtain the static viscoelastic deformation. Both equations should of course lead to the same result. However, Eq.(3.8) has an advantage from the numerical solution point of view. When a given solver for elastic material contact problems is available the extension to viscoelastic behavior is rather straightforward as the computation of the time derivative of the pressure is not needed. Also, when large derivatives occur in the pressure distribution, numerical approximation via Eq.(3.8) may be more accurate as the derivative of the compliance function can often be determined analytically. Implementation in a numerical solver is discussed in Sec.3.3.

3.2.2 Rolling Contact Problem

The second problem, where the surfaces are in motion, is illustrated in Fig.3.3. For simplicity, we restrict ourselves to a rigid sphere rolling on a stationary viscoelastic half-space with a constant surface speed V_x under a constant normal load W_0 . However, the methods presented here can also be used for the case where both surfaces are moving, and for the case of two viscoelastic half-spaces. Some of these aspects will be discussed in the results of Sec.3.4.

For the rolling contact, relative to the contact location the situation is steady state. The (time-dependent) governing equations, Eqs.(3.3)~(3.5), in the inertial coordinate system can be transformed to a reference frame fixed to the contact location. In that reference the governing equations for the dynamic contact problems are the same as Eqs.(3.3)~(3.5), with the variable x , in the deformation integral for the viscoelastic body replaced by the transformed speed-dependent variable $x + V_x t$, to account for the motion of the viscoelastic material relative to the contact location. Note that when the surface is non-smooth also in the terms for the undeformed shape one needs to account for the motion relative to the contact location in this way.

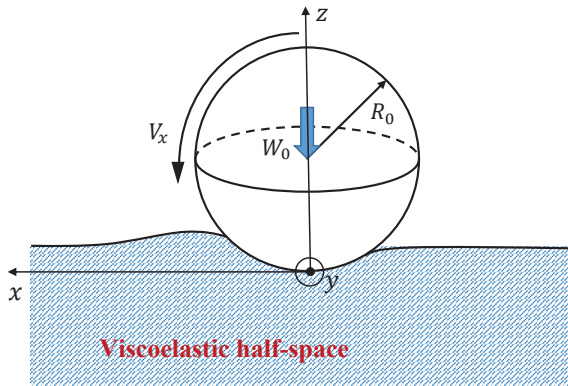


Figure 3.3: Dynamic rolling viscoelastic point contact problems formed between a rigid sphere with a viscoelastic half-space.

In the new reference frame, Eq.(3.8) for the deformation can be expressed as (see also Eq.(2.55) in Sec.2.4.2):

$$u(x, y) = \varphi_c(0)w_e(x, y) + \int_0^\infty \frac{d\varphi_c(q)}{dq} w_e(x - V_x q, y) dq. \tag{3.9}$$

where $w_e(x - V_x q, y) = \frac{1-\nu^2}{\pi} \iint \frac{p(x', y')}{\sqrt{(x - V_x q - x')^2 + (y - y')^2}} dx' dy'$. For the EHL line contact between viscoelastic bodies, Eq.(3.9) was also used by Hooke and Huang [67].

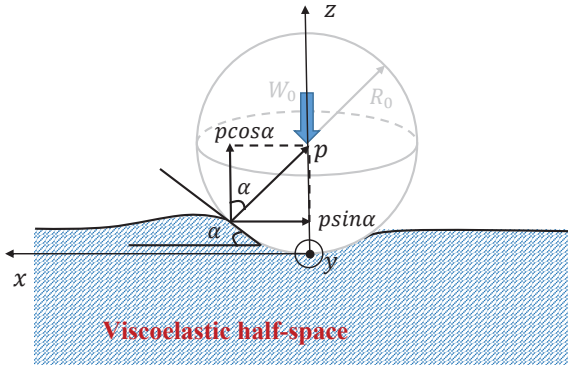


Figure 3.4: Pressure projection for friction calculation.

Finally, two approaches were used to calculate the tangential force (rolling resistance of friction) generated in the contact between a rigid sphere and viscoelastic half-space through the moment equilibrium or projecting pressure along the deformed surface.

(1) *Friction deduced from moment equilibrium*: the friction force, F_r , can be deduced by calculating the moment which prevents the sphere from rotating.

$$F_r R_0 = \iint x p(x, y) dx dy. \quad (3.10)$$

(2) *Friction deduced from pressure projection*: the friction force, F_r , can also be obtained by projecting pressure along the axis ox , as shown in Fig.3.4. The friction force reads:

$$F_r = \iint p(x, y) \sin \alpha dx dy. \quad (3.11)$$

where $\tan \alpha = \frac{\partial u(x, y)}{\partial x}$. This method allows equivalent interfacial shear stress representation of the friction to be defined at each point of the surface $\tau_{\text{interface}} = p(x, y) \sin \alpha$. Once the rolling friction is obtained with either Eq.(3.10) or Eq.(3.11), the friction coefficient can be simply calculated with

$$\mu = \frac{F_r}{W_0}. \quad (3.12)$$

3.3 Numerical Solution

To achieve numerical solutions for the two contact problems as given in Sec.3.2, Eqs.(3.3)~(3.5) must be solved with the viscoelastic deformation given by Eq.(3.6) or Eq.(3.8) for the static contact problem, and by Eq.(3.9) for rolling contact problem. A spatial domain $x_{\text{in}} \leq x \leq x_{\text{out}}$ and $y_{\text{in}} \leq y \leq y_{\text{out}}$ is used where $x_{\text{in}} = y_{\text{in}} = -3a_0$ and $x_{\text{out}} = y_{\text{out}} = 3a_0$ is taken, with a_0 the contact radius corresponding to the instantaneous elastic response of the viscoelastic material, i.e. with the instantaneous modulus E_f of the free spring in the SLS model (Fig.2.10). The resulting non-dimensional variables are:

$$a_0 = \sqrt[3]{\frac{3W_0 R_0 (1 - \nu^2)}{4E_f}}, p_H = \frac{3W_0}{2\pi a_0^2}, \delta = \frac{a_0^2}{R_0}, \bar{\tau} = \frac{\tau V_x}{a_0}, \bar{a} = \frac{a}{a_0}, H = \frac{h}{\delta}, P = \frac{p}{p_H}, \quad (3.13)$$

$$U = \frac{u}{\delta}, H_0 = \frac{h_0}{\delta}, T = \frac{t}{\tau}, X = \frac{x}{a_0}, Y = \frac{y}{a_0}.$$

The domain in dimensionless space is thus $-3 \leq X \leq 3$ and $-3 \leq Y \leq 3$. For the static surface problem a time domain, $0 \leq T \leq 5$, is taken and divided into $N_t = 200$ (uniform) steps in time.

Various methods exist for the discretization of the problem, e.g. finite difference and Finite Element Methods [54], and for the numerical solution, e.g. conjugate gradient method [109], local iterative methods, local iterative methods using Multilevel/Multigrid techniques for convergence acceleration [141], and global iterative methods (Newton Raphson), each with their own merits. As part of solving the equation, evaluating the integral transforms is a computationally expensive task, which can be accelerated using FFT methods [88, 126, 148], Fast Multipole Methods [13], or MLMI methods [16, 141]. For the present study the elastic (Hertzian) dry contact numerical solver published in [141] was taken as a starting point.

A second order finite difference method was used on a uniform grid for the spatial discretization of the equations. The numerical solution of the equations (at each time step)

was done using a distributive relaxation process as used for the elastic dry contact problem augmented with coarser grids in a multigrid cycle to accelerate convergence to a grid independent rate [141]. The force balance equation can be treated as a global constraint in this cycle. For the fast evaluation of the spatial integral transforms in Eq.(3.6) or Eq.(3.9), the MLMI method was used, see [16, 141]. This serves as a good example to see the increase in computational complexity when changing an existing numerical solution algorithm from an elastic to a viscoelastic contact problem. Since the modifications are mainly related to the computation of the viscoelastic deformation, the following description focuses on these aspects.

3.3.1 Static Contact

The discretization of the spatial integral transforms in Eq.(3.6) or Eq.(3.8) for the viscoelastic deformation was done in the same way as for the elastic contact problem [141]. Assuming a piecewise constant pressure on integration intervals e.g. of the size of a gridcell around a grid point, the deformation in each grid point can be approximated by a summation over all contributions from the integration intervals. This yields a multi-summation (full matrix multiplication) with influence coefficients that can be determined analytically [141]. The discretization is of second order as mentioned above. To account for the viscoelastic effect of the pressure history, the time integral in Eq.(3.6) or Eq.(3.8) needs to be discretized too. Assuming a uniform timestep Δ_t a first order backward (in time) discretization of the pressure derivative in Eq.(3.7) can be used:

$$\frac{\partial p(x', y', q)}{\partial q} = \frac{p(x', y', q) - p(x', y', q - \Delta_t)}{\Delta_t} + O(\Delta_t). \quad (3.14)$$

Let $u(x, y, k\Delta_t)$ and $p(x, y, k\Delta_t)$ represent the total deformation and the pressure at a location (x, y) at time $t = k\Delta_t$, with k ($0 \leq k \leq N_t$) indicating the (uniform) timestep. The resulting discretization in time of Eq.(3.6) can then be written as:

$$u(x, y, k\Delta_t) = \varphi_c(k\Delta_t)w_e(x, y, 0) + \sum_{n=1}^k \varphi_c((k-n)\Delta_t)\Delta_p^n w_e(x, y, n\Delta_t)\Delta_t, \quad (3.15)$$

where $w_e(x, y, 0)$ is as defined in Eq.(3.6), and

$$\Delta_p^n w_e(x, y, n\Delta_t) = \frac{1-v^2}{\pi} \iint \frac{1}{\sqrt{(x-x')^2 + (y-y')^2}} \frac{p(x', y', n\Delta_t) - p(x', y', (n-1)\Delta_t)}{\Delta_t} dx' dy' \quad (3.16)$$

is the discrete equivalent in time of Eq.(3.7). Even though the discretization in time is strictly first order, it should be noted that the derivatives in time of the compliance are generally quite smooth so that at a timestep comparable to the mesh size effectively the second order discretization error in space will dominate. Note that the evaluation of the viscoelastic deformation in time is not a one step incremental procedure. At a particular time (step) its summation of integral transforms at each previous timesteps multiplied with a creep contribution which depends on both the previous timestep(s) ($1 \dots n$) as well as the time (step) at which the result is required (k). This is most efficiently achieved by storing the integral transforms (Eq.(3.16)) at each timestep, so they can be used again

at later timesteps but then multiplied e.g. with the creep function of a different time delay $(k - n)$. Assuming that the convergence is grid independent, as is achieved using Multigrid/Multilevel techniques, the total computational effort of the algorithm is then of the order of $N_t(N_t + 1)/2 * O(N \log N)$, where N is the number of points on the spatial grid, and $O(N \log N)$ the amount of work of the evaluation of the discrete spatial integral transform when done using e.g. FFT or MLMI methods.

The discretization of Eq.(3.8) in time can be done also by approximating the integral over time by a summation:

3

$$u(x, y, k\Delta_t) = \varphi_c(0)w_e(x, y, n\Delta_t) + \sum_{n=1}^k \frac{d\varphi_c(q)}{dq} \Big|_{q=n\Delta_t} w_e(x, y, (k-n)\Delta_t) \Delta_t, \quad (3.17)$$

where $w_e(x, y, t)$ is as defined in Eq.(3.6) or the (instantaneous) "elastic" response to the pressure, $p(x, y, n\Delta_t)$ ($0 \leq n \leq k$), at time $t = n\Delta_t$, which discretized on the spatial grid gives the already explained multi-summation.

Two numerical approaches can now be used to calculate the total viscoelastic deformation at the k^{th} time step:

Numerical Method 1 (NM1): using the derivative of pressure (Eq.(3.6) or Eq.(3.15)): substitution of Eq.(2.37), the creep compliance function of the SLS viscoelastic model, in Eq.(3.15), gives:

$$u(x, y, k\Delta_t) = \frac{1}{E_f} [1 + R_e(1 - e^{-\frac{k\Delta_t}{\tau}})] w_e(x, y, 0) + \sum_{n=1}^k \frac{1}{E_f} [1 + R_e(1 - e^{-\frac{(k-n)\Delta_t}{\tau}})] \Delta_p^n w_e(x, y, n\Delta_t) \Delta_t. \quad (3.18)$$

Numerical Method 2 (NM2): using the derivative of creep function (Eq.(3.8), Eq.(3.17)): substitution of Eq.(2.37), the creep compliance function of the SLS viscoelastic model, in Eq.(3.17), the following equation is obtained:

$$u(x, y, k\Delta_t) = \frac{1}{E_f} w_e(x, y, k\Delta_t) + R_e \frac{1}{E_f} \frac{1}{\tau} \sum_{n=1}^k e^{-\frac{n\Delta_t}{\tau}} w_e(x, y, (k-n)\Delta_t) \Delta_t. \quad (3.19)$$

The continuous expressions for the spatial integral transfers are approximated by multi-summations, see [141] and the governing equations given in Sec.3.2 solved using either Eq.(3.18) or Eq.(3.19) for the viscoelastic deformation. The procedure starts with the Hertzian pressure for the instantaneous elastic response of the material as initial approximation at $T = 0$. Subsequently for each timestep the equations are solved to obtain the time evolution of pressure and gap height. For the multigrid method, without additional description, a uniform grid with $513 * 513$ points has been used on the finest level of grid (level 5). The discrete equations of each timestep were solved until the pressure distribution satisfies the load balance equation with an absolute error smaller than 10^{-4} .

3.3.2 Rolling Contact

To determine the viscoelastic deformation in the coordinate system relative to the contact, the creep compliance function of the SLS model can be substituted in Eq.(3.9) giving

$$u(x, y) = u_e(x, y) + R_e \frac{1}{\tau} \int_0^\infty e^{-\frac{q}{\tau}} u_e(x - V_x q, y) dq, \quad (3.20)$$

where $u_e(x - V_x q, y)$ in Eq.(3.20) is the instantaneous elastic deformation at location of $(x - V_x q, y)$:

$$u_e(x - V_x q, y) = \frac{1 - \nu^2}{\pi} \frac{1}{E_f} \iint \frac{p(x', y')}{\sqrt{(x - V_x q - x')^2 + (y - y')^2}} dx' dy'. \quad (3.21)$$

Substitution of the integration variable with $s = x - V_x q$ in Eq.(3.20) gives:

$$u(x, y) = u_e(x, y) + R_e \frac{1}{V_x \tau} \int_{-\infty}^x e^{\frac{s-x}{V_x \tau}} u_e(s, y) ds. \quad (3.22)$$

The spatial domain is taken to extend over $x_{in} \leq x \leq x_{out}$ and $y_{in} \leq y \leq y_{out}$, where $x_{in} = y_{in} = -3a_0$ and $x_{out} = y_{out} = 3a_0$. Assuming that the computational domain is taken sufficiently large so that all points (s, y) are inside the domain, and that the gridpoints (s, y) with $x_{in} \leq s \leq x$ coincide with the meshed grid points (x, y) by setting that the $V_x \Delta_t$ equals to the mesh size Δ_x in the x direction. The discretization of the spatial integral transform $u_e(s, y)$ and its evaluation, can be done in exactly the same way as that of $u_e(x, y)$. When evaluating the deformation at a point (x, y) , the effect of the deformation at all previous points (s, y) $x_{in} \leq s \leq x$ on the deformation of the current point is equivalent to the result of multiplying its elastic deformation by the exponential decay function, $e^{\frac{s-x}{V_x \tau}}$, and summing up as equivalent of the continuous integration over s in Eq.(3.22). As the elastic deformation is evaluated for all locations on the grid simultaneously, this multiplication can easily be done. However, while this evaluation is straightforward, the resulting discrete deformation has a larger discretization error than made in the standard elastic deformation because of the division by the velocity, $dq = ds/V_x$, and gives a grid (mesh size h_x) dependent solution, see Sec.3.4.2. This implies that to maintain comparable accuracy when decreasing the speed, a more dense grid should be used, at least in the velocity direction. This point is also noted by Hooke and Huang [67]. However, this problem can be overcome in a different, grid (mesh size) independent way.

Defining:

$$\mathfrak{R}(x, y) = \frac{1}{V_x \tau} \int_{-\infty}^x e^{\frac{s-x}{V_x \tau}} u_e(s, y) ds, \quad (3.23)$$

and taking its derivative with respect to x using the Leibniz integral theorem:

$$\frac{\partial \mathfrak{R}}{\partial x} = \frac{1}{V_x \tau} e^{\frac{s-x}{V_x \tau}} u_e(s, y) \Big|_{s=x} - \left(\frac{1}{V_x \tau}\right)^2 \int_{-\infty}^x e^{\frac{s-x}{V_x \tau}} u_e(s, y) ds, \quad (3.24)$$

one obtains

$$V_x \tau \frac{\partial \mathfrak{R}}{\partial x} = u_e(x, y) - \mathfrak{R}. \quad (3.25)$$

From the original definition of \mathfrak{R} in Eq.(3.23), the following relation can be obtained

$$\mathfrak{R}(x, y) = \frac{u(x, y) - u_e(x, y)}{R_e}. \quad (3.26)$$

Substituting of Eq.(3.26) in Eq.(3.25), one obtains a new form of the "viscoelastic Boussinesq equation" with a single relaxation time

$$u(x, y) + V_x \tau \frac{\partial u(x, y)}{\partial x} = (1 + R_e) u_e(x, y) + V_x \tau \frac{\partial u_e(x, y)}{\partial x}. \quad (3.27)$$

This equation can now be discretized in space, e.g. assume for simplicity the use of a first order backward scheme, $\frac{\partial u(x,y)}{\partial x} \approx \frac{u(x,y)-u(x-h_x,y)}{h_x}$ and $\frac{\partial u_e(x,y)}{\partial x} \approx \frac{u_e(x,y)-u_e(x-h_x,y)}{h_x}$. Substitution in Eq.(3.27) gives an equation from which $u(x,y)$ can be solved in each point for a given y , by marching in the positive x direction, with $u_e(x,y)$ known. Once the elastic contribution is known, the extra work to obtain the viscoelastic deformation is then just one pass over the grid at each point involving only a few multiplications and additions. This is a major advantage over direct simulation via Eq.(3.20) and also computationally cheaper and more accurate especially for low velocities as detailed in Sec.3.4.2.

3

3.3.3 Multi-Relaxation Times

Finally, the use of a more complex viscoelastic model with multiple relaxation times is considered. The "viscoelastic Boussinesq equation", Eq.(3.27) for the SLS model with a single relaxation time, can be extended to consider multiple relaxation times using the generalized viscoelastic model shown in Fig.3.1 (the parallel-connected multi-branch SLS model).

$$\left\{ \begin{array}{l} u + V_x \tau_1 \frac{\partial u}{\partial x} = \frac{(1+R_{e1})}{E_{f1}} u_{e1} + \frac{V_x \tau_1}{E_{f1}} \frac{\partial u_{e1}}{\partial x} \\ u + V_x \tau_2 \frac{\partial u}{\partial x} = \frac{(1+R_{e2})}{E_{f2}} u_{e2} + \frac{V_x \tau_2}{E_{f2}} \frac{\partial u_{e2}}{\partial x} \\ \dots \\ u + V_x \tau_i \frac{\partial u}{\partial x} = \frac{(1+R_{ei})}{E_{fi}} u_{ei} + \frac{V_x \tau_i}{E_{fi}} \frac{\partial u_{ei}}{\partial x} \\ \dots \\ u + V_x \tau_n \frac{\partial u}{\partial x} = \frac{(1+R_{en})}{E_{fn}} u_{en} + \frac{V_x \tau_n}{E_{fn}} \frac{\partial u_{en}}{\partial x} \end{array} \right. \quad (3.28)$$

where $u_{ei}(x,y) = \frac{1-v^2}{\pi} \iint \frac{p_i(x',y')}{\sqrt{(x-x')^2+(y-y')^2}} dx' dy'$, while the total pressure which is applied on the surface is

$$p(x,y) = \sum_i p_i(x,y). \quad (3.29)$$

The definition of the surface displacement in each branch calls for the calculation of a surface double integral, u_{ei} . A direct calculation is time consuming when large numbers of mesh points and relaxation times are considered. Thus, a numerical approach is proposed which allows the consideration of multi-relaxation times while keeping the same level of computational time as that for an elastic solution. The differential equation for each branch

is developed using backward first order discrete operators as follows

$$\left\{ \begin{array}{l} a_1 u_{l,m} - b_1 u_{l-1,m} = u_{e1l,m} - c_1 u_{e1l-1,m} \\ a_2 u_{l,m} - b_2 u_{l-1,m} = u_{e2l,m} - c_2 u_{e2l-1,m} \\ \dots \\ a_i u_{l,m} - b_i u_{l-1,m} = u_{eil,m} - c_i u_{eil-1,m} \\ \dots \\ a_n u_{l,m} - b_n u_{l-1,m} = u_{enl,m} - c_n u_{enl-1,m} \end{array} \right. \quad (3.30)$$

The indices, l and m correspond to the position of the mesh point in the ox and oy directions. The index i indicates the branch of the model that is considered. The coefficient a_i , b_i , and c_i are defined as below

$$\begin{aligned} a_i &= \frac{1 + \frac{V_x \tau_i}{h_x}}{\frac{1+R_e}{E_{fi}} + \frac{\frac{V_x \tau_i}{h_x}}{E_{fi}}} \\ b_i &= \frac{\frac{V_x \tau_i}{h_x}}{\frac{1+R_e}{E_{fi}} + \frac{\frac{V_x \tau_i}{h_x}}{E_{fi}}} \\ c_i &= \frac{\frac{V_x \tau_i}{h_x}}{1 + R_e + \frac{V_x \tau_i}{h_x}} \end{aligned} \quad (3.31)$$

where h_x is the mesh size in the ox direction. Summing all the equations in Eq.(3.30) leads to the following relation, which enables the determination of the surface displacement

$$u_{l,m} = \frac{1}{\sum_i a_i} (u_{e(l,m)} - \sum_i c_i u_{ei(l-1,m)} + u_{l-1,m} \sum_i b_i). \quad (3.32)$$

The first term in the bracket corresponds to the "elastic displacement"

$$u'_e(x, y) = \frac{1 - \nu^2}{\pi} \iint \frac{p(x', y')}{\sqrt{(x - x')^2 + (y - y')^2}} dx' dy'. \quad (3.33)$$

To obtain the surface displacement, the mesh is visited in a lexicographic order along the rolling direction. First, the elastic deformation, $u_{e(l,m)}$, is calculated. All the other terms, $u_{ei(l-1,m)}$ and $u_{l-1,m}$, in the bracket are known from previous calculations. Once the surface displacement, $u_{l,m}$, is calculated, the surface displacement for each individual branch can then be found using the following relation

$$u_{ei(l,m)} = a_i u_{l,m} - b_i u_{l-1,m} + c_i u_{ei(l-1,m)}. \quad (3.34)$$

Only the terms calculated in the previous mesh points need to be kept in memory. The method only requires the surface displacement and the total pressure to be restored for the determination of the surface displacement regardless of the number of the relaxation times. The integral transform to be calculated is the same as the one used for an elastic problem.

3.4 Results and Discussion

Numerical results are presented for the contact problems described before, and the different ways of evaluating the viscoelastic deformation. In Sec.3.4.1, results are presented for the static contact problem computing the compliance in time subject to a fixed load. These results are validated with analytical solutions. In Sec.3.4.2 results are presented for the dynamic rolling/sliding contact. First for a rigid indenter rolling over a viscoelastic surface the method is verified against results published in the literature. Next, detailed results are presented showing the influence of various model parameters for a rolling contact such as the Deborah number, and the ratios of the elastic springs in the SLS model.

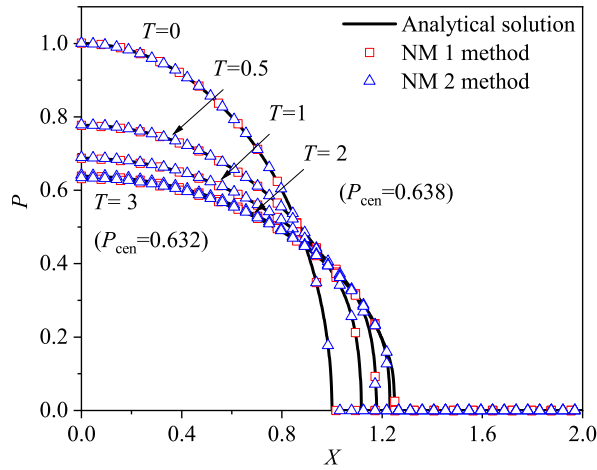
3

3.4.1 Static Contact Results

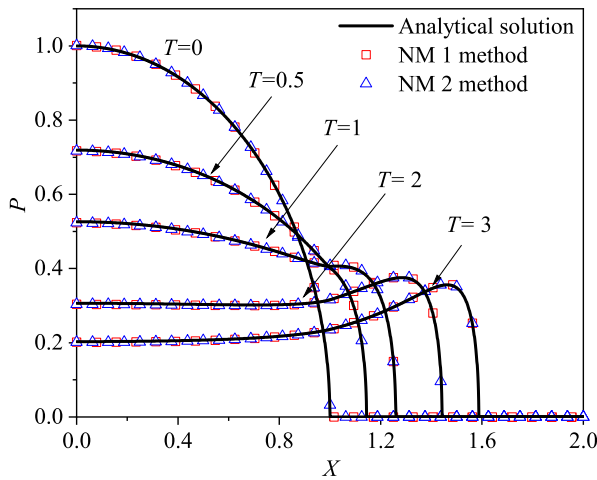
The results obtained with the two different numerical approaches are validated by comparing with the analytic solution given by Lee and Radok [85] for static contact problems under an instantaneously applied load (see in Sec.3.2.1). All results are presented in dimensionless forms using the dimensionless parameters shown in Eq.(3.13), based on the instantaneous response of the viscoelastic half-space, the modulus E_f in the SLS model, see Fig.2.10.

Fig.3.5 shows the (dimensionless) pressure profile at the centerline of the contact as a function of the dimensionless coordinate X at different times relative to the relaxation time. Owing to radial symmetry, only half of the profile is shown. Fig.3.5 (a) shows the results for the SLS model and Fig.3.5 (b) shows the results for the Maxwell model. In both figures the analytic solution is shown, as well as the results obtained using the NM1 formulation (with pressure derivative) and the NM2 formulation (with derivative of the creep function). Firstly, the numerical results show excellent agreement with the analytic solution. The excellent agreement of both computational approaches NM1 and NM2 with the analytic solution also shows the effectiveness of the newly derived viscoelastic deformation equation, Eq.(3.8) used in the NM2, by adopting the derivative of the creep compliance function to replace the derivative of the pressure in Eq.(3.6) (NM1).

Fig.3.6 shows the variation of the central pressure and the contact radius with (dimensionless) time T in a creep process for the SLS viscoelastic material. Initially the material responds purely elastically to the instantaneous load applied. Only the free spring, see Fig.2.10, in the SLS model responds, giving a Hertzian pressure distribution with dimensionless central pressure P_{cen} and dimensionless contact radius \bar{a} of unity, because the scaling used is based on these Hertzian contact parameters. As time increases, the material creeps under the applied constant load. The contact radius \bar{a} increases and as the load is fixed, with increasing contact area the central pressure P_{cen} decrease, see Fig.3.6. The time rate of change of the contact radius and the maximum pressure decreases in time, which are consistent with the viscoelastic model used. As anticipated for $T \geq 3$, i.e. at a time larger than three times of the relaxation time of the material, the contact pressure and contact radius are close to their asymptotic values which are determined by the two springs in series. According to the analytical solution of Lee and Radok [85], the maximum contact radius is $\bar{a}_{max} = (1 + R_e)^{\frac{1}{3}}|_{R_e=1} = 1.2599$.



(a) The SLS model



(b) The Maxwell model

Figure 3.5: Dimensionless pressure as a function of the (dimensionless) coordinate at different times during creep for a static contact problem under an instantaneously applied load: Comparison of the results of two numerical solution approximations, and the analytical solution of Lee and Radok [85]. The results are for the case of (a) SLS model with $R_e = 1$, and (b) Maxwell model.

In the current simulation when $T = 5$, the dimensionless radius has reached a value 1.25, which is very close to this maximum analytical value. The maximum contact pressure is $P_{cen} = (1 + R_e)^{-\frac{2}{3}}|_{R_e=1} = 0.63$. With increasing time, the numerical result approximates this value. As indicated in the figure at $t = 2\tau$ the value is 0.638, and at $t = 3\tau$ it is 0.632, see Fig.3.5 (a).

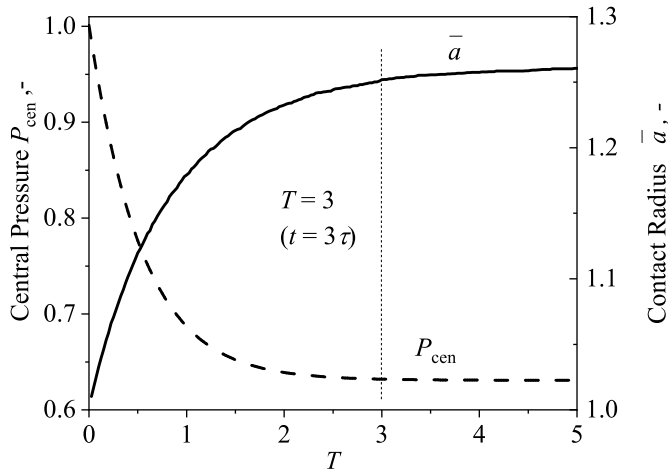


Figure 3.6: Variations of the dimensionless central pressure and the contact radius with dimensionless time during the creep process. Static contact with an instantaneous load (SLS viscoelastic model, $R_e = 1$, $NM 2$ for surface deformation).

Whereas the results for the SLS model in time converge to the steady Hertzian contact for the elastic modulus representative of the sum of the two springs, the results for the Maxwell model in Fig.3.5 (b) show a continuous creep in time. The contact region continuously extends and the pressure lowers, as is consistent with the fact that initially both springs accommodate the load completely, after which the viscous damper relaxes the load.

3.4.2 Rolling Contact Results

To avoid the grid dependent solution with the deformation equation Eq.(3.20) as explained in Sec.3.3.2, all the results shown in the following parts are obtained by solving Eq.(3.27). Eq.(3.20) gives a straightforward way to calculate the viscoelastic deformation, but there is large discretization error especially at small velocities. This can be clearly seen from Fig.3.7, which shows the pressure distributions obtained by solving the Eq.(3.20) and Eq.(3.27) respectively for a small dimensionless velocity, $\bar{v} = 0.01$. With increasing number of grid points from 257 to 1025 in each of the computational direction, Eq.(3.20) results in a grid dependent solution (GDS) with the maximum pressure increasing from 0.484 to 0.59, while Eq.(3.27) gives a grid independent solution (GIDS) with the maximum pressure being stable at a value of 0.63. When increasing grid points to $4097 * 4097$ for the GDS using Eq.(3.20), the maximum pressure is just close to that of the GIDS using Eq.(3.27). Therefore, Eq.(3.27) is more accurate and computationally inexpensive.

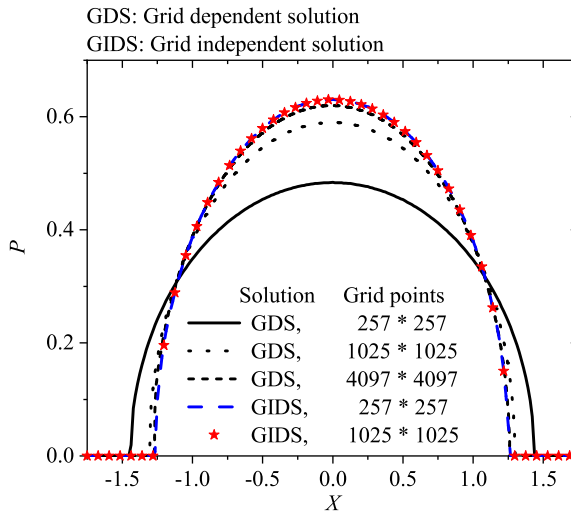
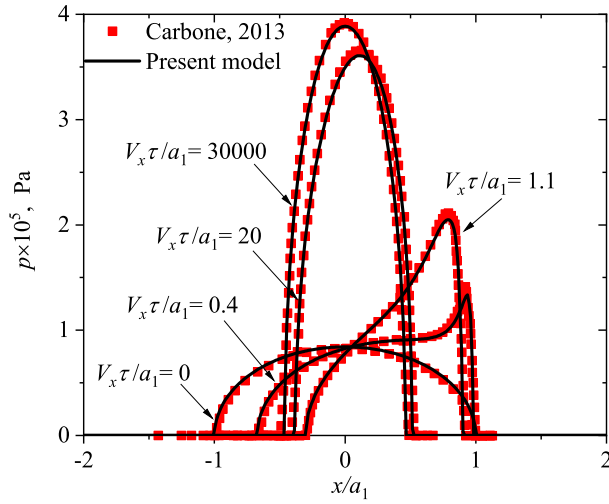


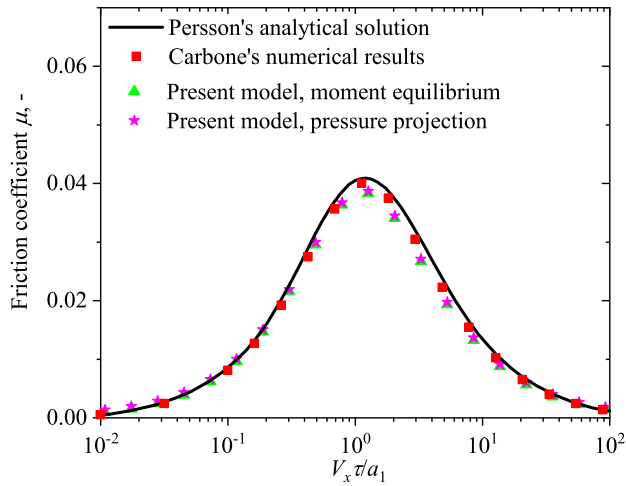
Figure 3.7: The Grid Dependent Solution (GDS) and the Grid Independent Solution (GIDS) of pressure distributions along the central line of the contact with different grid points for a small rolling velocity, $\bar{\tau} = 0.01$ (SLS viscoelastic model, $R_e = 1$).

For the dynamic rolling contact problem, (see Sec.3.2.2), an analytical solution is not available. Instead, the numerical results are verified with numerical results obtained by Carbone and Putignano with a boundary element method [21], also using an SLS viscoelastic model. The operating conditions in [21] are $E_f = 10\text{MPa}$, $E_f/E_0 = 10$ with E_0 the effective elastic modulus of the two springs in series at an extremely low velocity: $E_0 = 1/(1/E_s + 1/E_f)$, $R_0 = 10\text{mm}$, $W_0 = 0.15\text{N}$ and $\tau = 0.01\text{s}$. The dimensionless velocity $\bar{\tau}$ was varied over a wide range $0 \leq \bar{\tau} \leq 3 \times 10^4$, where a_1 is the Hertzian contact radius at an extremely low velocity with a modulus of E_0 [21]. Fig.3.8 shows the centerline profiles of the results for pressure distribution for a range of rolling velocities, as well as the variation of the coefficient of friction with rolling velocity obtained using the two approaches indicated in Sec.3.2.2, friction derived either by the moment equilibrium or by the pressure projection. The friction coefficients obtained using the present model were validated by comparing with Persson's [107] analytical solution and Carbone's [21] numerical results. Obviously the agreement is very good for both the pressure distribution and the friction coefficient in Fig.3.8.

Furthermore, Fig.3.9 shows the contour plots of the dimensionless pressure at different rolling velocities. The loading conditions and material properties are the same as these in Fig.3.8. The scaling parameter p_H used in the figure is calculated with the Hertzian contact radius a_1 . When the rolling velocity increases, the size of the contact zone gradually decreases with a sharp shrinkage at the outlet at first and then return to circular finally.



(a) Pressure distribution



(b) Friction coefficient

Figure 3.8: Comparison of numerical results from the present model (lines) with those from Carbone and Putignano [21] at a wide range of rolling velocities: (a) pressure distribution (rolling to the right side), (b) friction coefficient.

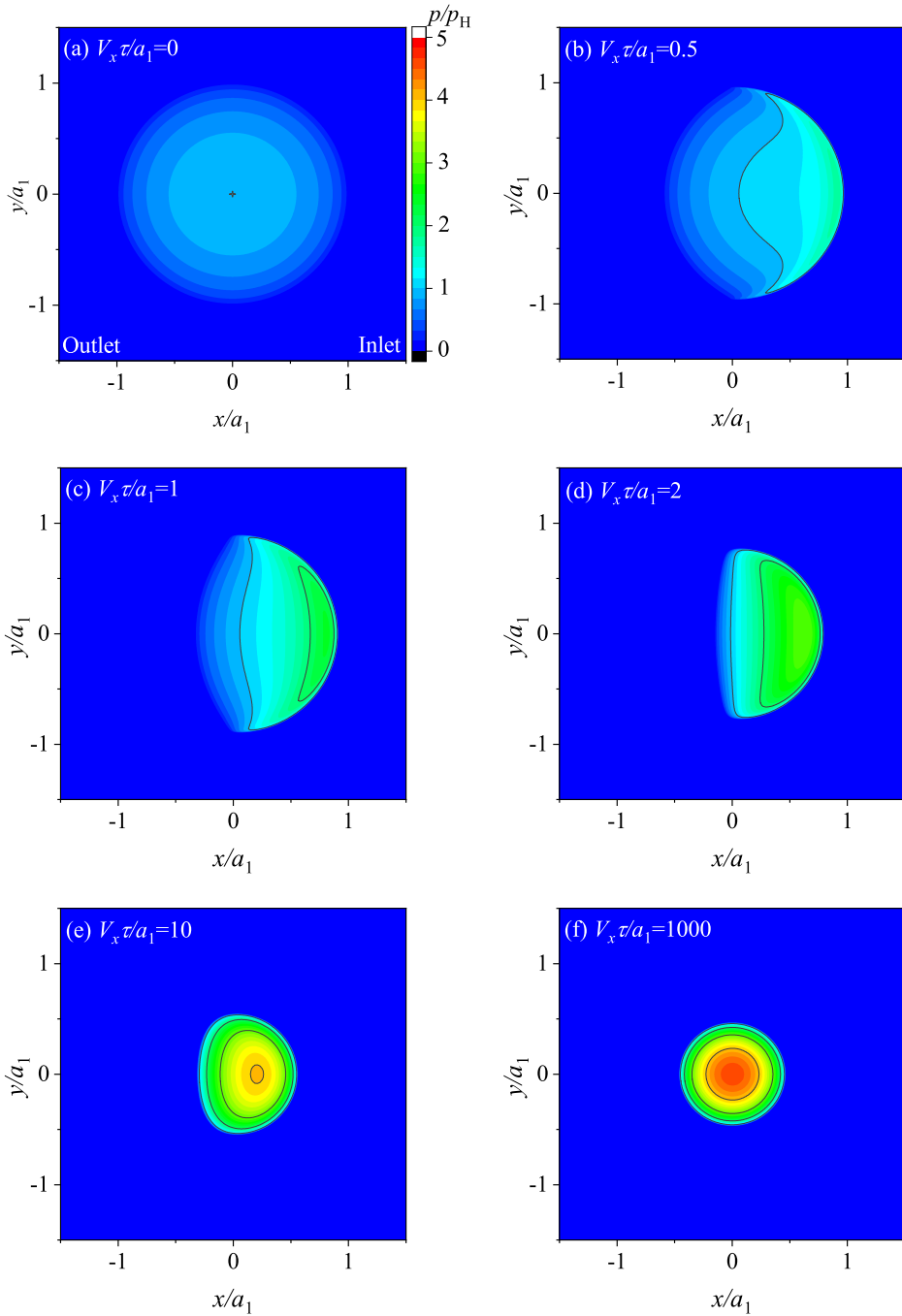


Figure 3.9: Contour plots of dimensionless pressure at different rolling velocities. The operating conditions and material properties are same as these in Fig.3.8. (The scaling parameter p_H in the figure is obtained based on the Hertzian contact radius a_1 .)

In the remaining part of this section the speed dependent viscoelastic behavior that has been shown in Fig.3.8 (a) is further analyzed. In the dimensionless equations expressed in the coordinate system relative to the contact, the influence of the velocity in the integral transform kernel function (Green's function) in Eq.(3.21) appears as in the dimensionless number $\bar{\tau} = \tau V_x / a_0$. The Deborah number is the ratio of two timescales, i.e. the material timescale which is the relaxation time τ and an exposure time during which a load acts, i.e. the exposure time in the contact a_0 / V_x . In this sense Fig.3.8 (a) in fact shows results for different values of the Deborah number ranging from 0 to 30000.

3

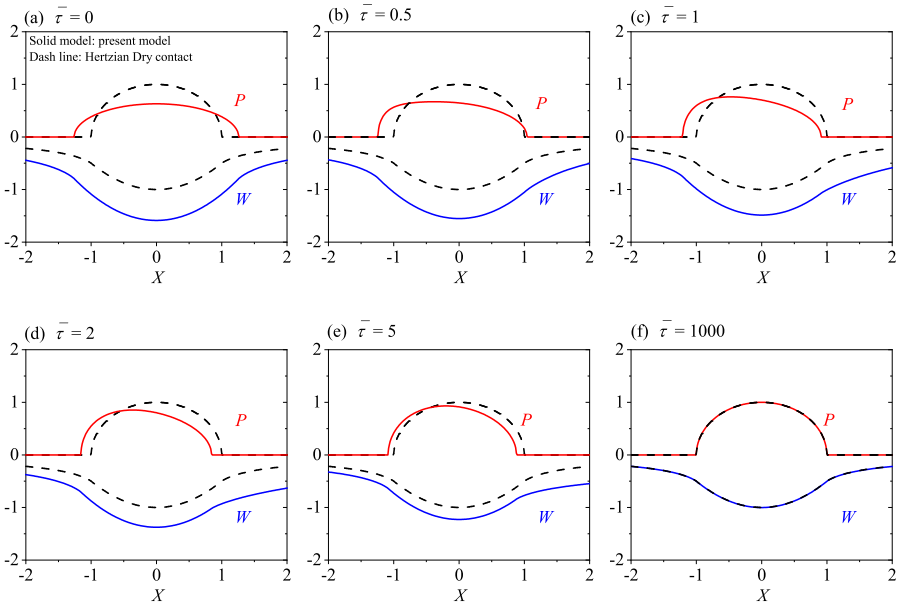


Figure 3.10: Pressure and deformation distribution at different rolling velocities for a frictionless rolling contact between a rigid sphere and a viscoelastic half-space. The sphere is rolling forwards in the negative x -axis direction, and the corresponding Hertzian elastic solution of pressure and deformation with only the modulus E_f in the SLS model in reaction is drawn in dashed line for comparison. ($R_e = E_f / E_s = 1$)

In Fig.3.10 the centerline profiles of the dimensionless pressure P and the dimensionless deformation W are shown for the case of a smaller elasticity modulus ratio of $R_e = E_f / E_s = 1$, and values of the Deborah number ranging from 0 to 1000. Also shown in the figure as dashed line are the pressure and deformation for the reference case used for scaling, i.e. based on the modulus E_f in the SLS model.

At a very low or very high Deborah number the pressure distribution is Hertzian and thus symmetric (Fig.3.10 (a) and Fig.3.10 (f)). These are the solutions characterized by the springs in the SLS model. At a low velocity, the dashpot does not play any role and the material behaves as a pure elastic material with a rigidity of E_0 . At a high velocity, the dashpot does not have enough time to respond and becomes exceedingly rigid. The material

response is then governed by the free spring of modulus, E_f . Hence, the deformation and pressure distribution in a rolling contact at the low and high extreme speed conditions are exactly the same as the solutions to the static contact problem at the time $T \rightarrow \infty$ and $T = 0$ respectively. This is illustrated in Fig.3.11.

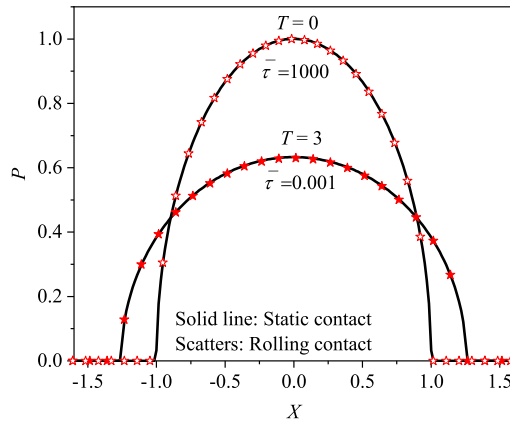


Figure 3.11: Comparison of the pressure distribution between static and rolling viscoelastic contact at two extreme conditions when the responses are purely elastic: $T = 0$ and $T = 3$ ($t = 3\tau$) for static contact, $\bar{\tau} = 0.001$ and $\bar{\tau} = 1000$ for rolling contact. ($R_e = E_f/E_s = 1$).

Solutions for other $\bar{\tau}$ (e.g., Fig.3.10 (b)~(e)), show the transition between the two extreme cases. The pressure distributions are asymmetric, skewed towards the inlet side of the contact. The pressure becomes steeper in the inlet region compared to the low Deborah number Hertzian solution as the material behaves increasingly rigid when it enters the contact at a higher velocity. The contact area is shifted towards the entrance of the contact and there is a distinct difference between the front and the rear semi-length of the contact area, as reported in [21, 112]. At the trailing edge of the contact, unlike elastic material of instantaneous response, the viscoelastic material needs more time to recover to its original state. These variations in pressure between the front and the rear of the contact lead to a rolling resistance (friction). With varying Deborah number (speed) the friction coefficient exhibits a bell shape as shown in Fig.3.8 (b). The maximum friction coefficient occurs at a Deborah number close to $\bar{\tau} = 1$. Referring to the graphs in Fig.3.10, this is the situation where the asymmetry in the pressure is the largest which coincides with the largest off center shift of the contact zone, see Fig.3.9.

The effect of the elasticity ratio $R_e = E_f/E_s$ on the asymmetrical pressure distribution is shown in Fig.3.12 for $\bar{\tau} = 1$. With increasing R_e the asymmetry increases as the contact edge moves further to the inlet side. The solution even has a local maximum close to the edge of the contact for $R_e = 6$, $R_e = 8$ and $R_e = 10$. These results imply that with increasing R_e in the numerical simulation the computational domain must be increased accordingly. This is also explained by the larger rigidity of the material entering the contact. As can be expected, the pressure peak in the inlet and the pressure asymmetry lead to a higher rolling resistance and a higher friction coefficient. This trend can be clearly seen from

Fig.3.13, which plots the variation of the dimensionless friction force with Deborah number at different elasticity ratios as used in Fig.3.12.

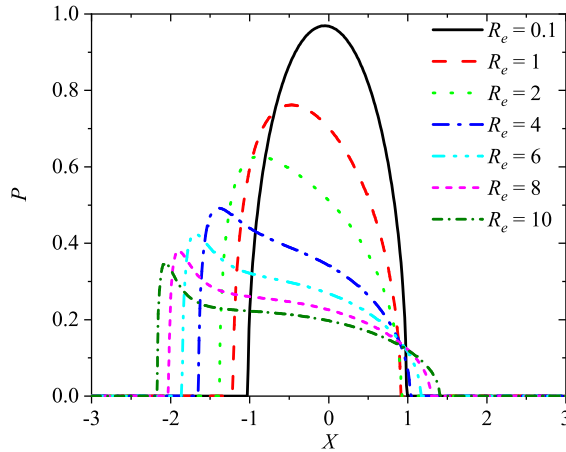


Figure 3.12: Pressure distributions at different elasticity ratios for Deborah number $\bar{\tau} = 1$. (SLS viscoelastic model; the left side is the rolling entrance)

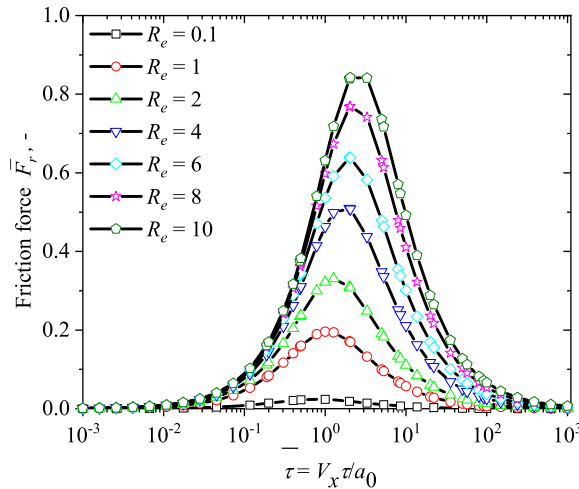


Figure 3.13: Dimensionless friction force with different elasticity ratios varied over Deborah number, $\bar{\tau}$. (SLS viscoelastic model, calculated with moment equilibrium method, R_e values are the same as in Fig.3.12)

3.4.3 Rolling/Sliding Viscoelastic-on-Viscoelastic Contacts

So far the case of a rolling contact between a rigid ball and a viscoelastic half-space was considered. In this case, the rolling problem is equivalent to a frictionless sliding problem

(rigid ball sliding on viscoelastic substrate) regarding the pressure distribution and surface deformation. This is similar to the behavior of an elastic contact, where in practice for the calculation of elastic deformation, an elastic-elastic contact is usually equivalent to a rigid-elastic contact by introducing a reduced elastic modulus. In this section the case of two viscoelastic bodies is considered. Because of the viscoelasticity of the material, pure rolling and sliding are now fundamentally different. This effect is studied here by assuming that the two bodies are made of identical viscoelastic material and have identical mechanical properties.

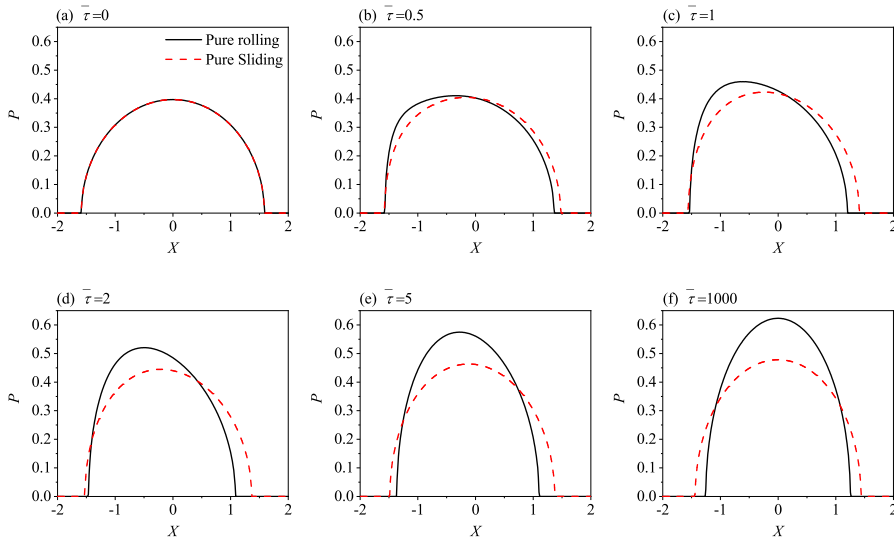


Figure 3.14: Comparison of pressure distributions between rolling and sliding conditions for a viscoelastic contact with identical material of the two bodies. (SLS viscoelastic model with $R_e = E_f/E_s = 1$; the left side is the rolling/sliding entrance)

For the pure rolling case, the two contact bodies have the same creep and deformation behavior, and the combined deformation can be obtained by summing up their individual contributions according to Eq.(3.27). While for the pure sliding case, only the moving body (the viscoelastic sphere or the viscoelastic half-space) shows the viscoelastic effect during the deformation process, the fixed one behaves elastically and deforms with a fixed modulus of E_0 as its speed is zero; this is also reported in [112]. Fig.3.14 compares the calculated pressure distribution for these two cases at different speeds. At the lowest speed of $\bar{\tau} = 0$, the rolling case and the sliding case have identical pressure distribution since the two bodies show both elastic response of modulus E_0 . As velocity increases, the pure rolling condition would bring more new material into the contact than the sliding contact with a surface in stationary. Therefore, pure rolling condition leads to a smaller contact radius and a larger contact pressure. At the highest speed of $\bar{\tau} = 1000$, the two bodies behave elastically in both the pure rolling case and the pure sliding case, and the rigidity of the rolling contact (each body is characterized by a modulus of E_f) is larger than that

of the sliding contact (one body is E_f , while the other is E_0). As a result, the final contact radius is smaller, and the maximum pressure is larger for the pure rolling case.

3.4.4 Multiple-Relaxation Times

Here, one example is given for viscoelastic materials of multiple relaxation times to show the efficiency of the developed method by carrying out pressure calculation for a dynamic rolling contact problem described in Sec.3.3.3. For the generalized SLS model, different number of branches n has been used, ranging from 1 to 300. To make the simulation results being comparable to one another, the effective viscoelastic properties of the material as a whole are set to be identical on purpose among different cases. This could be achieved by setting $E_{f1} = E_{f2} = \dots = E_{fn} = E_f/n$, $E_{s1} = E_{s2} = \dots = E_{sn} = E_s/n$, $R_{e1} = R_{e2} = \dots = R_{en} = 1$ and $\tau_1 = \tau_2 = \dots = \tau_n = \tau$. Fig.3.15 shows identical pressure distributions along the central line of the contact for the multi-branch SLS model with different number of branches. Table 3.1 compares the computation time and the maximum contact pressure for different numbers of branches in the generalized SLS model using a laptop (CPU at 1.9GHz). It can be found that with increasing numbers of branches, there is no significant increase in computational time, especially when the material can be described with less than 100 relaxation times.

Table 3.1: Computational time for different number of branches of generalized SLS model to consider multi-relaxation times of viscoelastic materials. (Parameters: $R_e = E_{fi}/E_{si} = 1$; $513 * 513$ grid points and the computational domain is $8a_0$ in both x direction and y direction)

Number of branches, n	Computational time, s	Maximum pressure, -
1	72.9	0.76
10	73.4	0.76
30	78	0.76
50	90	0.76
100	96	0.76
300	161	0.76

Finally, another example of multi-branch SLS model is given for $\bar{\tau} = 1$ with different elastic ratios, $R_{en} = nR_e$, and relaxation times, $\tau_n = n\tau$, on each branch. In this case, the increase of branch numbers causes an increase in the rigidity of the viscoelastic material and thus leads to a higher pressure and a narrower contact width as shown in Fig.3.16. The pressure distribution with $n = 1$ coincides with the pressure obtained with a single relaxation time, see Fig.3.10 (c).

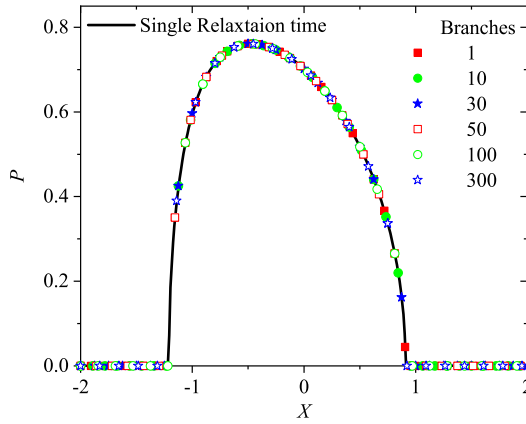


Figure 3.15: Dimensionless pressure distribution along the central line of the contact for the multi-branch SLS model with different number of branches.(Deborah number $\bar{\tau} = 1, R_{e1} = R_{e2} = \dots = R_{en} = 1,$ where n is the number of branches.)

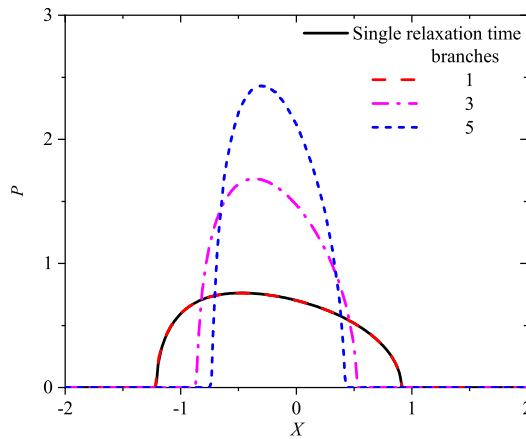


Figure 3.16: Pressure distributions with different elasticity ratios and relaxation times on each branch for Deborah number $\bar{\tau} = 1.$ (multi-branch SLS viscoelastic model with $R_{e1} = R_e, R_{e2} = 2R_e, \dots, R_{en} = nR_e,$ and $\tau_1 = \tau, \tau_2 = 2\tau, \dots, \tau_n = n\tau,$ where n is the number of branch.)

3.5 Conclusion

Several aspects of modeling and numerical simulation of viscoelastic point contact problems have been discussed in detail. Firstly, different ways to model the viscoelastic deformation were discussed for both static and rolling point contact problems. For the static problem the presented approach using the derivative of the creep compliance function of the material, Eq.(3.8), is most efficient. This approach was also used by Hooke and Huang [67] for the EHL dynamic rolling line contact problem. However, as it is sensitive to a low speed

increased discretization error, for a rolling problem this approach is less suited, unless very fine grids can be used as is easily the case in a line contact. For the point contact an alternative approach is presented here. The viscoelastic deformation expression can be cast in an easy way to evaluate differential equation. This new equation, Eq.(3.27) allows accurate evaluation in an amount of computational time equivalent to that of the elastic deformation, also for complex models with multiple relaxation times. The methodology can be integrated straightforwardly in an existing contact solver, e.g. the Multigrid/Multilevel solution method presented in [141] which was used here.

3

Results have been presented for static and rolling dry point contacts. For the rigid indenter viscoelastic half-space static contact the results were validated with analytical solutions of Lee and Radok [85]. For the same configuration in rolling contact the results were compared with results from Carbone and Putignano [21], demonstrating the importance to use a sufficiently large domain. For this problem using the SLS viscoelastic material model results of a parameter study are presented of variation of contact size, the pressure distribution. And the rolling friction has been analyzed over a wide range of values of the Deborah number. The condition where the asymmetry in pressure is maximal is associated with the highest value of friction coefficient, which is around a value of unity of the Deborah number. Also the correlation between the static (creep) contact and the rolling contact solutions is shown, i.e. the initial (time $t = 0$) and the asymptotic ($t \rightarrow \infty$) solution for the static problem are identical to the high speed $V_x \rightarrow \infty$ and the $V_x = 0$ for the rolling contact problem. When considering two viscoelastic bodies in contact the viscoelasticity causes big differences between rolling and sliding running conditions of viscoelastic-to-viscoelastic contacts. Only one surface shows viscoelastic response and the other responses elastically under sliding condition, while the two moving surfaces response both viscoelastically in a pure rolling contact. This leads to differences in the pressure distribution and in the contact radius. Finally the approach proposed here is also shown to work for a multiple relaxation time problem.

Chapter 4

Viscoelastic Lubricated Contact

In this chapter, the lubricated viscoelastic point contact problem has been studied theoretically and experimentally. An efficient visco-elastohydrodynamic lubrication (VEHL) numerical algorithm has been developed by implementing the novel viscoelastic deformation equation proposed in Chapter 3. The relevant dimensionless parameters of the VEHL problem are identified and a parameter study is presented showing the effect of solid viscoelasticity on the pressure and film thickness in the conjunction. In addition experimental results are presented for film thickness measurements in configurations of a PMMA ball rolling against a glass disc, and a steel ball rolling against a glass disc using optical interferometry. Finally the scaling of the pressure and film profiles in the inlet and outlet regions to the contact has been studied, investigating self similarity of the pressure and film solution in these regions. The results presented provide clear reference for the understanding and interpretation of viscoelastic solid effects on the film and pressure in highly deformed (soft) lubricated contacts.

The work in this chapter has been published as: Y. Zhao, H.C. Liu, G.E. Morales-Espejel, C.H. Venner. Effects of solid viscoelasticity on elastohydrodynamic lubrication of point contacts. Tribology International, 171: 107562, 2022.

DOI: <https://doi.org/10.1016/j.triboint.2022.107562>.

4.1 Introduction

Detailed understanding and prediction of the forces in dry and/or thin layer of fluid lubricated contact mechanics is of high relevance for many applications in science and engineering like seals, physics of flow with colloidal particle interaction, bio-(fluid)mechanics, and soft matter. Mostly soft materials behave viscoelastically rather than purely elastically, which means that they exhibit time-dependent deformation behavior and dissipate energy under dynamic contact conditions [17, 25, 110]. Although some soft materials with good self-lubricating properties can be used in engineering in unlubricated contacts, lubricants even though sometimes in minute quantities, are used to enhance their tribological performance by reducing adhesion and wear, and to prolong the service life in soft contacts [58].

Lubricated soft contacts with viscoelastic materials exhibit phenomena that cannot be described by the classical elastohydrodynamic lubrication (EHL) theory, e.g. inlet film collapse, inlet pressure peak and abnormal Stribeck curve [96, 114, 123]. This work studies the soft lubrication of point contacts, including viscoelastic solid behavior, in short, the

visco-elastohydrodynamic lubrication (VEHL) of point contact problems [137]. The main difference between EHL and VEHL is in their different deformation response to an external load in static and/or dynamic rolling/sliding contacts, as a result of the different rheological behavior of elastic and viscoelastic materials. Elastic materials deform instantaneously in response to an applied load. For dry contact problems, the contact parameters, e.g. the deformation depth, the contact area and the contact pressure, can be calculated analytically according to the Hertzian contact theory without showing any time, speed, or type of motion dependent deformation behavior. While for lubricated EHL contacts without an available analytical solution, the solution can be obtained numerically by solving the elastic deformation with efficient numerical methods such as the discrete convolution fast Fourier transform (DC-FFT) method [88] and the multilevel multi-integration (MLMI) method [141]. The knowledge of EHL nowadays is very mature. Adequate models and efficient numerical methods are available for simulation, however, this is not yet the case for contacts between bodies that deform viscoelastically.

4

The most challenging aspect of solving a VEHL point/line contact problem is the computation of the viscoelastic deformation. Viscoelastic materials show a time-dependent deformation in static contacts [23, 82, 85] and a speed-dependent deformation in dynamic rolling/sliding contacts [21, 33, 44, 49, 72, 81, 107]. This time delayed viscoelastic response results in hysteresis friction, asymmetric deformation and also a pressure distribution that may exhibit a strong asymmetry with a significant inlet pressure rise, as is also seen in dry rolling contacts [21, 72, 81]. These features are quite different from the phenomena in a purely elastic dry contact and cannot be described by elastic contact mechanics. For the modeling of linear viscoelastic contact problems, the deformation equations proposed by Hunter in 1961 [72] have laid the foundation for both 2D and 3D viscoelastic contact mechanics.

A VEHL numerical solution can be achieved by replacing the elastic deformation function in an EHL model by a viscoelastic one. In literature, several numerical methods have been developed to solve both VEHL line and point contact problems, such as the fast Fourier transform (FFT) method [60, 61, 81, 82], the boundary element method (BEM) [21, 112, 114], the finite difference method (FDM), and the finite element method (FEM) [82, 125]. Elsharkawy [34] solved VEHL line contact problems using an iterative Newton-Raphson method for a linear viscoelastic material. Hooke and Huang [67] investigated the effect of viscoelasticity in soft EHL line contacts with multigrid techniques. Putignano and Dini [114] solved the VEHL point contact problem with BEM methods to analyze the viscoelastic effect on the lubrication between a rigid sphere and a viscoelastic half-space. Based on the model in [114], Putignano [112] further investigated the effect of viscoelasticity on VEHL at different contact configurations, e.g. hard-on-soft, soft-on-hard, and soft-on-soft. More recently, based on the FFT numerical methods, He et al. developed a VEHL model [61] for a layered viscoelastic point contact problem, as well as a thermo-VEHL model [60] to consider the thermal effect on VEHL. For the VEHL models mentioned above, one more time integrals have been added to the elastic Boussinesq equation [75] to evaluate the viscoelastic deformation based on the correspondence principle [25]. This is significantly demanding in computational time compared to the EHL problem. To overcome this difficulty, a viscoelastic deformation equation in a novel differential form was proposed in Chapter 3. This equation maintains a similar computational efficiency as that for an

elastic solution and can be implemented in any EHL solver regardless of the numerical methods.

Experimentally, much work has been carried out on friction measurements of soft EHL contacts see for examples in [107, 123], while less work has been reported on the film thickness measurements. The optical interferometry technique has been widely used to measure the "hard" EHL film thickness on ball-on-disc test rigs since 1950s owing to its high precision (as high as 1 nm) and the visualization of the complete map of the dynamic lubricating film. The local EHL film thickness can be obtained by detecting the coherent wavelength [76], or by matching the color [20, 59], or by analyzing the intensity of the interference fringes/patterns [53, 92] depending on the used light source and hardware. However, the above-mentioned interterometry techniques have rarely been applied to the study of soft EHL. The reason may be that it is difficult to coat a soft transparent disc with a semi-reflective coating [38], e.g. the widely used chromium coating, which is needed to achieve high quality interferograms. As a first attempt, Marx et al. [96] successfully prepared Cr-coated discs made of polymethylmethacrylate (PMMA) and polyurethane (PU) soft materials and measured the EHL film thickness on a ball-on-disc test rig. Later, Putignano and Dini [114] continued the film thickness measurements with PMMA materials and interpreted the contact area reduction behavior at the flow outlet with viscoelastic theory. Until now, very few studies have been carried out both experimentally and theoretically for VEHL point contact problems because of either difficulty in measuring the thin film thickness quantitatively or in solving viscoelastic deformation.

In this work, the novel viscoelastic deformation equation in Chapter 3 based on SLS rheological model is used to model the viscoelastic deformation in VEHL point contact problems. The efficient MLMI and multigrid techniques are used in solving the viscoelastic deformation equation and the Reynolds equation, respectively. Numerical results of VEHL are compared with the EHL and the VED results to show the effect of solid viscoelasticity on the lubrication of soft EHL point contact problems. Furthermore, film thickness measurements are carried out for soft EHL contacts on a ball-on-disc test rig with Cr-coated PMMA discs/balls using two optical interferometry methods with an updated RGB light source. Finally, scaling of soft EHL film and pressure results is discussed for both the EHL and VEHL regimes based on the numerical and experimental results.

4.2 Theory and Numerical Methods

Fig.4.1 shows a schematic representation of the generic problem considered: the contact between a rigid sphere of radius R_0 loaded against a viscoelastic half-space under a constant normal load W_0 . The surface velocities of the sphere and the viscoelastic half-space are v_1 and v_2 , respectively. We restrict ourselves to pure rolling $v_1 = v_2$ under steady state conditions. However, the methods presented here can also be used for the case where both surfaces are moving at different velocities, and for the case of two viscoelastic bodies in contact, see Chapter 3. In this section the viscoelastic rheological solid model is presented. The deformation equations for viscoelastic materials in contact mechanics, the governing equations for a VEHL point contact problem, and the numerical methods used to solve these equations are explained.

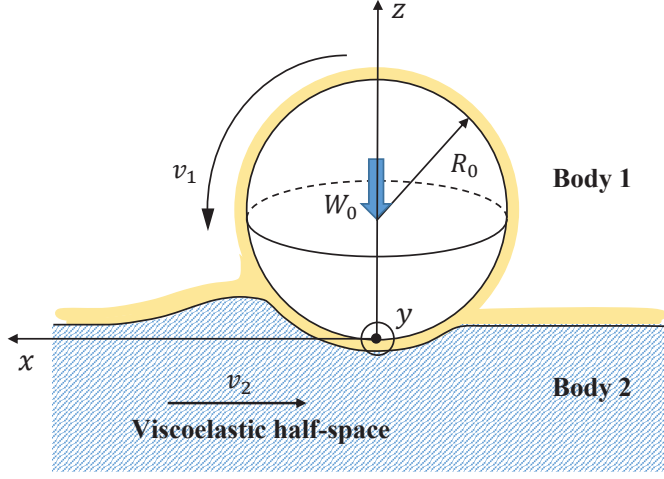


Figure 4.1: Schematic of a lubricated viscoelastic rolling contact formed between a rigid sphere of radius R_0 and a viscoelastic half-space at an applied constant load W_0 .

4.2.1 Viscoelastic Deformation

In this work, a three-element SLS model in the Kelvin representation is used, see Fig.2.10. The creep compliance function of the SLS model can be expressed as Eq.(2.37). For details of the derivation of the creep equation and an introduction to the correspondence principle, see Sec.2.2.4.

Assuming linear viscoelasticity, the deformation of a body of viscoelastic material in a VEHL/VED point contact can be determined by applying the correspondence principle [3] to the common point contact elastic deformation expression based on the semi-infinite half-space approximation:

$$u(x, y, t) = \frac{1 - \nu_2^2}{\pi} \int_{0^-}^t \varphi_c(t - q) \iint \frac{1}{\sqrt{(x - x')^2 + (y - y')^2}} \frac{\partial p(x', y', q)}{\partial q} dx' dy' dq, \quad (4.1)$$

where the integration over time with the compliance function φ_c accounts for the history effect which is characteristic for viscoelastic behavior.

Integrating by parts for the time integral in Eq.(4.1) gives

$$\begin{aligned} \int_{0^-}^t \varphi_c(t - q) \frac{\partial p(x', y', q)}{\partial q} dq &= \varphi_c(t) p(x', y', 0) + \int_{0^+}^t \varphi_c(t - q) \frac{\partial p(x', y', q)}{\partial q} dq \\ &= \varphi_c(t) p(x', y', 0) + [\varphi_c(t - q) p(x', y', q)]_{0^+}^t - \int_{0^+}^t p(x', y', q) d\varphi_c(t - q) \\ &= \varphi_c(0) p(x', y', t) - \int_{0^+}^t p(x', y', q) \frac{d\varphi_c(t - q)}{dq} dq, \end{aligned} \quad (4.2)$$

Eq.(4.2) can be further expressed as:

$$\int_{0^-}^t \varphi_c(t-q) \frac{\partial p(x', y', q)}{\partial q} dq = \varphi_c(0)p(x', y', t) + \int_{0^+}^t p(x', y', t-q) \frac{d\varphi_c(q)}{dq} dq. \quad (4.3)$$

Substituting Eq.(4.3) into Eq.(4.1), the viscoelastic deformation equation can be rephrased as

$$u(x, y, t) = \frac{1-v_2^2}{\pi} \int_{0^-}^t \frac{dq \varphi_c(q)}{dq} \iint \frac{p(x, y, t-q)}{\sqrt{(x-x')^2 + (y-y')^2}} dx' dy' dq. \quad (4.4)$$

In Eq.(4.4), the time-dependent viscoelastic deformation is represented in the inertial coordinate system. However, considering the case of a rolling contact that has achieved a steady state condition (constant operating conditions, perfectly smooth surfaces), Eq.(4.4) can be rewritten in a time-independent form in a reference coordinate system fixed to the contact location. This involves a coordinate transformation where the variable x in Eq.(4.4) should then be replaced by the speed-dependent variable $x + v_2 t$ to account for the motion of the viscoelastic material in the x direction relative to the contact location, where v_2 is the surface speed of the viscoelastic contacting element. The resulting expression for the deformation is:

$$u(x, y) = \varphi_c(0)w_e(x, y) + \int_0^\infty \frac{d\varphi_c(q)}{dq} w_e(x - v_2 q, y) dq, \quad (4.5)$$

$$\text{where } w_e(x, y) = \frac{1-v_2^2}{\pi} \iint \frac{p(x', y')}{\sqrt{(x-x')^2 + (y-y')^2}} dx' dy'.$$

The form of Eq.(4.5) for the viscoelastic deformation equation has also been used by Hooke and Huang [67] and by Wu et al. [152] in the study of VEHL line contact problems. For further details of the derivation of Eq.(4.5), see Sec.2.2.4. Substitution of the creep compliance function of the SLS model, Eq.(2.37), for φ_c in Eq.(4.5) gives

$$u(x, y) = u_e(x, y) + R_e \frac{1}{\tau} \int_0^\infty e^{-\frac{q}{\tau}} u_e(x - v_2 q, y) dq, \quad (4.6)$$

where $u_e(x, y)$ is the instantaneous elastic deformation defined by the standard Boussinesq equation [75] with only the spring E_f in effect in the SLS model:

$$u_e(x, y) = \frac{1-v_2^2}{\pi} \frac{1}{E_f} \iint \frac{p(x', y')}{\sqrt{(x-x')^2 + (y-y')^2}} dx' dy'. \quad (4.7)$$

$u_e(x - v_2 q, y)$ in Eq.(4.6) is the elastic deformation at location $(x - v_2 q, y)$. According to Eq.(4.6), the viscoelastic deformation $u(x, y)$ at a point (x, y) can be considered as the summation of the instantaneous elastic deformation at the current point and the accumulated (history) effect of the deformation at all previous points $(x - v_2 q, y)$ on the current point. The deformation at a single previous point is equivalent to the product of the elastic deformation $u_e(x - v_2 q, y)$ multiplied by the exponential decay $e^{-q/\tau}$. When tailoring the discretization of the equation for numerical solution such that the evaluation points $(x - v_2 q, y)$ coincide with the grid mesh points of the computational domain relative to the contact location (x, y) , this provides a straightforward way to evaluate the viscoelastic deformation. This

approach has been used for a VEHL line contact by Hooke and Huang [67]. A significant drawback of this formulation, as also noted in [67], is that this method leads to a large discretization error for low speeds v_2 and thus strongly grid-dependent results [159], see also in Chapter 3. Also, by definition Eq.(4.6) is computationally more demanding due to the time integration, so that solving a VEHL problem is computationally considerably more expensive than solving the equivalent EHL problem. This can be avoided by introducing an alternative equation in a differential form which is obtained by applying the Leibniz integration rule, see Chapter 3.

For the specific case of the SLS viscoelastic material model it reads:

$$u(x, y) + v_2 \tau \frac{\partial u(x, y)}{\partial x} = (1 + R_e) u_e(x, y) + v_2 \tau \frac{\partial u_e(x, y)}{\partial x}. \quad (4.8)$$

This equation has two advantages. Firstly, the computational complexity of the viscoelastic deformation is the same as for the elastic deformation, see Chapter 3. Secondly, it can straightforwardly be extended to a generalized multi-branch SLS model with multiple relaxation times to model more complex viscoelastic materials, as shown in Sec.3.3.3. For simplicity, but without loss of generality, the SLS model with a single relaxation time is used in this work.

4.2.2 EHL Equations

The governing equations for the VEHL point contact problem are almost the same as those in a classical “hard” EHL problem [141], except for the (visco-)elastic deformation in the film thickness equation. The equations can be non-dimensionalized with the following dimensionless variables:

$$\begin{aligned} X &= x/a_0, & Y &= y/a_0, & P &= p/p_H, & H &= h/\delta, & \delta &= a_0^2/R_0, \\ \bar{\eta} &= \eta/\eta_0, & \bar{\rho} &= \rho/\rho_0, & a_0 &= \sqrt[3]{\frac{3W_0 R_0 (1 - v_2^2)}{4E_0}}, & p_H &= \frac{3W_0}{2\pi a_0^2} \end{aligned} \quad (4.9)$$

where a_0 and p_H are the Hertzian contact parameters related to the elastic response of both springs (in series) in the SLS model, the low speed elastic limit mentioned in Sec.2.2.4. This leads to the following dimensionless Reynolds equation [141]:

$$\frac{\partial}{\partial X} \left(\frac{\bar{\rho} H^3}{\bar{\eta} \lambda} \frac{\partial P}{\partial X} \right) + \frac{\partial}{\partial Y} \left(\frac{\bar{\rho} H^3}{\bar{\eta} \lambda} \frac{\partial P}{\partial Y} \right) - \frac{\partial (\bar{\rho} H)}{\partial X} = 0, \quad (4.10)$$

where:

$$\lambda = 12 \frac{\eta_0 v_m R_0^2}{a_0^3 p_H} \quad (4.11)$$

is the dimensionless load/speed parameter, which for an elastic solid can also be seen as the ratio of the elastic force deforming the body and the viscous forces in the lubricant film in the inlet region, see Snoeijer et al. [124]. Note that Wu et al. [152] use parameter $\beta = 1/\lambda$ and refer to it as the inverse generalized Hersey number.

The second equation is the gap height equation which, approximating the undeformed body by a parabola, is given by:

$$H(X, Y) = H_0 + \frac{X^2}{2} + \frac{Y^2}{2} + U(X, Y), \quad (4.12)$$

where $U(X, Y)$ is the dimensionless viscoelastic deformation which follows Eq.(4.8):

$$U(X, Y) + D_{\text{Hertz}} \frac{\partial U(X, Y)}{\partial X} = (1 + R_e) U_e(X, Y) + D_{\text{Hertz}} \frac{\partial U_e(X, Y)}{\partial X}, \quad (4.13)$$

where

$$D_{\text{Hertz}} = \frac{v_2 \tau}{a_0} \quad (4.14)$$

is the Deborah number based on the Hertzian contact radius a_0 . $U_e(X, Y)$ in Eq.(4.13) represents the instantaneous dimensionless elastic deformation characterized by the upper spring, E_f , in the SLS model (see Fig.2.10), defined as:

$$U_e(X, Y) = \frac{2}{\pi^2} \frac{E_0}{E_\infty} \iint \frac{P(X', Y')}{\sqrt{(X - X')^2 + (Y - Y')^2}} dX' dY'. \quad (4.15)$$

H_0 in Eq.(4.12) is the mutual approach of two remote points in the solids and is determined by the contact dynamics equation, see Wijnant et al. [151]. Neglecting acceleration this equation reduces to the usual condition of force balance equation in dimensionless form:

$$\iint P(X, Y) dX dY = \frac{2\pi}{3}. \quad (4.16)$$

From Eqs.(4.10), (4.13), and (4.16), it can be seen that the VEHL problem is controlled by three dimensionless groups: λ in the Reynolds equation, Eq.(4.10), D_{Hertz} in the viscoelastic deformation equation, Eq.(4.13), and R_e , also in the deformation equation, Eq. (4.13). The effects of these three parameters on the (dimensionless) film thickness and solution will be analyzed in Sec.4.4.1.

At this point the constitutive behavior of the lubricant has not been considered yet. This introduces additional (dimensionless) parameters. Assuming an isothermal contact situation, equations of state $\bar{\eta}(P)$ and $\bar{\rho}(P)$ need to be known. For an isoviscous incompressible lubricant $\bar{\eta} = \bar{\rho} = 1$. For the simple case of an exponential Barus viscosity pressure relation [11], one has

$$\eta = \eta_0 \exp(\alpha p), \quad (4.17)$$

where α is the viscosity-pressure coefficient, which in dimensionless form:

$$\bar{\eta} = \exp(\bar{\alpha} P) \quad (4.18)$$

leads to the additional lubricant related dimensionless parameter i.e. $\bar{\alpha} = \alpha p_H$. So in that case the EHL problem is fully determined by two parameters λ and $\bar{\alpha}$. Any quantity in the dimensionless problem formulation, i.e. the dimensionless central film thickness $H_c = H(X = Y = 0)$, is a function of only two non-dimensional groups: $H_c = H_c(\lambda, \bar{\alpha})$ which allows the use of practical charts. The set $(\lambda, \bar{\alpha})$ can be replaced by any other set of two that can be (re)created from these two parameters which in fact represents an alternative appropriate way to non-dimensionalize the equations. Of course the underlying problem

remains the same. In the history of EHL, e.g. see [50, 94, 135] and references therein, there has been quite some discussion about which sets of dimensionless parameters to be used, with basically three groups distinguished. Firstly, Dowson and Higginson [30], who for the line contact used a (dimensionless) load parameter W , a speed parameter U , and a lubricant parameter G , suggesting that a dimensionless film thickness $H = H(W, G, U)$. This set was chosen as it apparently represents the variables as changed/controlled in real operating conditions, but this set is overcomplete, see [50, 98]. Moes [98, 99] demonstrated that the problem can fully be characterized by a dimensionless film thickness parameter H^M , a dimensionless load parameter M , and a lubricant parameter L , so that $H^M = H^M(M, L)$. Johnson [74] used an alternative dimensionless film thickness and two dimensionless parameters g_E , and g_V (line contact), which can of course be directly related to the other parameters. Parameters also used are $P = \bar{\alpha}$ and $S = 2^{-1/4}L$ [50, 140].

4

The dimensionless parameter set used partly as matter of preference, depends on the researcher. The major point is that it is recommended to use the minimum set, as it allows the most efficient representation of data in e.g. graphical charts for design. Moreover, when deriving predictive film thickness formulas it is desired that the set used allows a natural representation of the solutions in asymptotic regimes. A disadvantage of the Moes parameters (M, L) [99] is that for the line and point contact the M parameter is different which obscures that the inlet dominated nature of the problem in both cases is exactly the same. As shown in [124] for the isoviscous case, this is naturally achieved in terms of the λ parameter which is consistent for line and point contact [124]. Different sets of dimensionless parameters and their relations for the case of an EHL circular contact are given in Appendix A.

When the discussion is extended to more complex lubricant rheological equations the number of parameters related to the lubricant behavior will increase depending on the nature and complexity of the equations. Various empirical relations are widely used, such as the Roelands viscosity-pressure equation [118] which in a dimensionless form is

$$\bar{\eta} = \exp((\ln(\eta_0) + 9.67)(-1 + (1 + \frac{p_H}{p_0}P)^\zeta)), \quad (4.19)$$

and the Dowson-Higginson pressure-density relation [31] which in dimensionless form is,

$$\bar{\rho} = \frac{5.9 \times 10^8 + 1.34 p_H P}{5.9 \times 10^8 + p_H P}. \quad (4.20)$$

These two equations of state for lubricants are mainly used for "hard" EHL where the Hertzian pressures are large. The exact physically correct equations to model the piezoviscous/rheological behavior of the lubricant still are an ongoing topic, see [8]. For the accurate prediction of friction other rheological fluid models, such as free volume models are used, often involving many parameters which should then be determined for each fluid separately. In the present work the influence of the lubricant piezoviscosity is ignored.

For contacts between common viscoelastic materials the Hertzian pressures are often quite limited, and in that case the piezoviscous parameter will not be dominant. As in [67, 152] for the line contact, and in the numerical parameter study in the present work, see Sec.4.4.1, an isoviscous lubricant is assumed and the emphasis is on the analysis of the

viscoelastic effect of the solid on the pressure and film thickness in the lubricated contact, and to investigate the effect of the dimensionless parameters λ , D_{Hertz} , and R_e . However, when comparing with experimental results the piezoviscous parameter is considered.

4.2.3 Numerical Solution

The governing equations, Eqs.(4.10)~(4.16), must be solved numerically to obtain the pressure and film distribution in the VEHL point contact problem. In present study, the multigrid/multilevel EHL numerical solver published in [141] was taken as a starting point. The equations are discretized on a uniform grid with $(n_x + 1) \times (n_y + 1)$ gridpoints and mesh size $h_x = h_y$ in x and y direction respectively. A second order Finite Difference discretization is used. For the spatial discretization of the equations, see Appendix B. The discrete equations are solved using a Gauss-Seidel line relaxation in the outer regions and distributive Jacobi line relaxation in the high pressure region. This provides good smoothing of the error in the entire domain so that coarse grids can efficiently be used to solve smooth errors, and a multigrid coarse grid correction cycle is obtained with a grid independent rate of convergence [141]. For the fast evaluation of the elastic deformation multi-integrals, MLMI [16, 141] is used. Finally, the force balance equation in the algorithm is treated as a global constraint that is relaxed by adjusting the value of the mutual separation H_0 on the coarsest grid in the Multigrid coarse grid correction cycles, see [16].

This algorithm can straightforwardly be adapted to the VEHL problem. For the fast evaluation of the elastic deformation multi-integrals Eq.(4.15) Multilevel Multi-Integration can still be used. The additional step needed is the solution of the viscoelastic deformation. This is achieved by using an upstream first order operator to discretize Eq.(4.13):

$$U_{i,j} + D_{\text{Hertz}} \frac{U_{i,j} - U_{i-1,j}}{h_x} = (1 + R_e)U_{e(i,j)} + D_{\text{Hertz}} \frac{U_{e(i,j)} - U_{e(i-1,j)}}{h_x}, \quad (4.21)$$

which can be expressed as:

$$U_{i,j} = A1U_{i-1,j} + A2U_{e(i,j)} - A3U_{e(i-1,j)}, \quad (4.22)$$

where $A1$, $A2$ and $A3$ depend only on the operating conditions and the mesh size of the grid.

$$A1 = \frac{D_{\text{Hertz}}/h_x}{1 + D_{\text{Hertz}}/h_x}, \quad A2 = 1 + \frac{R_e}{1 + D_{\text{Hertz}}/h_x}, \quad A3 = \frac{D_{\text{Hertz}}/h_x}{1 + D_{\text{Hertz}}/h_x}. \quad (4.23)$$

Once the elastic contribution $U_{e(i,j)}$ has been determined from the discretized version of Eq.(4.15), Eq.(4.22) can be solved for $U_{i,j}$ by marching in the positive X direction on a given gridline of constant Y . Compared with an elastic deformation computation, the extra work is limited by only a few multiplications and additions. Moreover, the solution is more accurate than through direct discretization of Eq.(4.6) which suffers from the large errors for low velocities as mentioned in Sec.4.2.1. It is also noted that this approach of computing the viscoelastic deformation can be extended to calculate the deformation of complex viscoelastic materials with multi-relaxation times, see Chapter 3. Fig.4.2 gives a flow chart of the various steps in the relaxation process on a single grid.

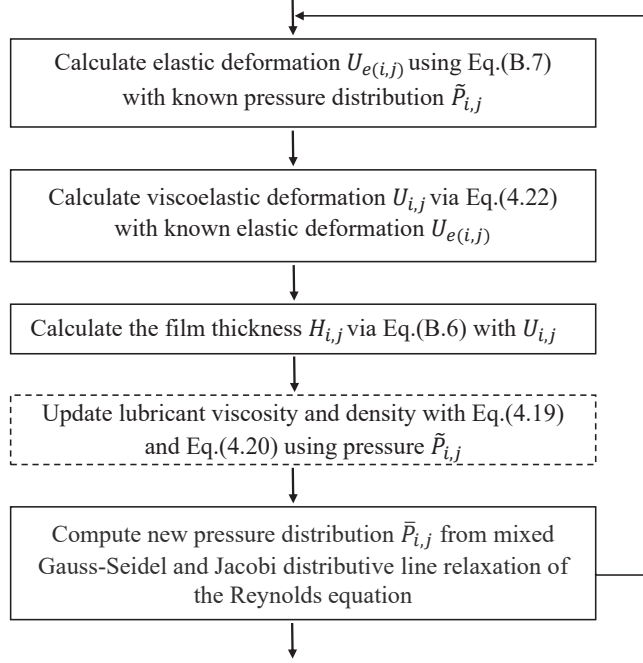


Figure 4.2: Flow chart of a single grid relaxation.

With a Full Multigrid algorithm, the equations are solved to an error that is small compared to the discretization error. Grid convergence of the results is demonstrated in the Appendix C. The results presented in this work were, unless specified otherwise, obtained using 513×513 grid points on the finest (target) grid in the Full Multigrid algorithm.

For larger values of λ (typically $\lambda > 10^{-3}$), as occur at low loads or large velocities, a spatial domain $-4.5 \leq X \leq 1.5$ and $-3 \leq Y \leq 3$ was used to ensure that the inlet region is sufficiently large to avoid so called computational starvation. For small values of λ , a smaller domain of $-1.5 \leq X \leq 1.5$ and $-1.5 \leq Y \leq 1.5$ was generally sufficient.

In the Appendix C, results are presented demonstrating domain (in)dependence of the solutions, and grid convergence, as well as verification of model predictions with results presented in the literature.

4.3 Experimental Approach

In addition to the theoretical/numerical study of the effect of different parameters in the model on the film thickness and the pressure in the VEHL point contact, for experimental validation, film thickness measurements have been carried out on a ball-on-disc apparatus (EHD2, PCS instruments, UK) with discs/balls made of polymethylmethacrylate (PMMA) which is much softer than steel and presumed to behave viscoelastically [114]. The film thickness is measured by optical interferometry. The transparent PMMA ball/disc

specimens were coated with a semi-reflective chromium (Cr) layer of 10~20nm to enable interference patterns. Two configurations of ball-on-disc contacts have been used in this work, see Fig.4.3: (a) Configuration-1 consisting of a PMMA disc against a steel ball, and (b) Configuration-2 a PMMA ball against a glass disc coated with Cr layer on top of which a SiO₂ spacer layer has been added. For each configuration, the film thickness was obtained from the interferometric data. The test rig, the materials and the specific optical methods are described below.

4.3.1 Test Setup and Materials

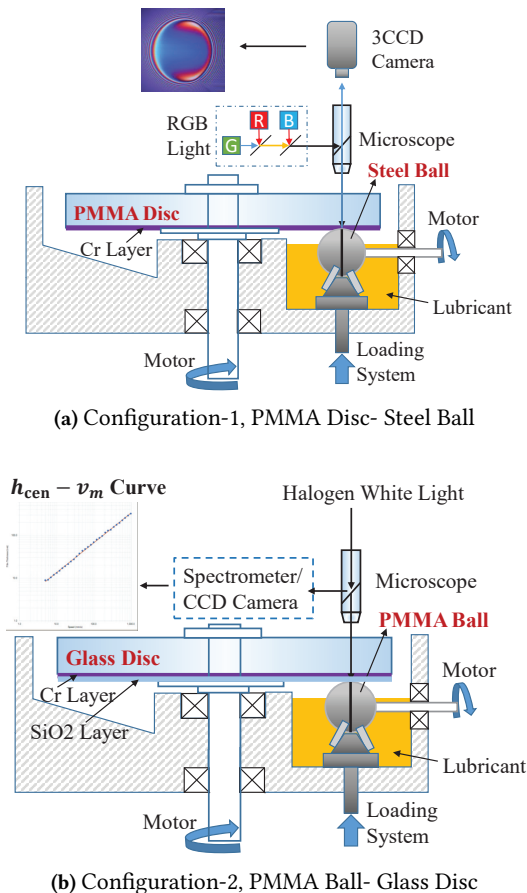


Figure 4.3: Schematic of the optical ball-on-disc test rig for soft EHL film thickness measurement. (a) Configuration-1: PMMA Disc-Steel Ball, an intensity-based method for EHL film mapping measurement with a RGB light source; (b) Configuration-2: Glass Disc-PMMA Ball, spectrometry-based method for central film thickness measurement.

Fig.4.3 schematically shows the setup used in the study of a "hard" EHL film problem, i.e. a transparent glass/sapphire disc and a steel ball. The ball and the disc are loaded and driven separately. The ball is supported by a bearing carriage partly immersed in the lubricant so as to ensure ample lubricant supply to the contact. Temperature control is achieved by the heating of the reservoir. To achieve interferograms of high contrast, the bottom surface of the glass disc is coated with a thin transparent semi-reflective layer Cr layer, as mentioned above. When light is shone into the contact zone, part of the light is reflected immediately from the Cr surface whereas the other part of the light passes through the layer, through the optional spacer layer, the lubricant film and is then reflected from the surface of the polished steel ball, back through spacer layer and film, the Cr layer and the glass disc.

Table 4.1: Test conditions for interferometry measurements.

Parameter	[unit]	value
radius of ball (R_0)	m	9.525×10^{-3}
rolling velocity (v_m)	m/s	0.01 ~ 1
load (W_0)	N	10
lubricant	-	HVI 60
temperature	°C	23

Table 4.2: Hertzian parameters at the nominal conditions for different contacts.

Contact	reduced modulus E' , [Pa]	Hertzian pressure p_H , [Pa]	Hertzian contact width a_0 , [m]
Steel ball-Glass disc	1.170×10^{11}	4.18×10^8	1.07×10^{-4}
Steel ball-PMMA disc	1.173×10^{10}	90.2×10^6	2.30×10^{-4}
PMMA ball-Glass disc	1.118×10^{10}	87.3×10^6	2.34×10^{-4}

Table 4.3: Properties of lubricant HVI 60.

Parameter	[unit]	value
dynamic viscosity at 23°C (η_0)	Pa·s	0.054
viscosity-pressure coefficient (α)	Pa ⁻¹	2.25×10^{-8}
refractive index	-	1.48

The resulting interference image is a map of the lubricant film thickness and optional spacer layer, where this spacer layer thickness can be subtracted from knowing its thickness through calibration. For the film thickness measurements in soft contacts, it was challenging to coat a soft and largely-deformable material (disc/ball) with the semi-refractive Cr layer. Marx et al. [96] succeeded in preparing Cr-coated transparent discs with two soft materials,

i.e. polymethylmethacrylate (PMMA) and polyurethane (PU). In this work, Cr-coated PMMA discs and balls were used. The elastic modulus of the PMMA used was determined to be about 5.1GPa by measuring the radius of the contact between a steel ball and the PMMA disc as a function of load, and Hertzian contact theory, see the Appendix D. The value obtained at room temperature (23°C) is in the expected range when compared to the value of 3.3GPa determined at 40°C reported in [96].

The film thickness was measured as a function of the entrainment speed at pure rolling conditions, room temperature (23°C), and at a fixed load of 10N. The rolling velocity was varied from 0.01m/s to 1m/s. The experimental conditions are summarized in Table4.1. The resulting Hertzian contact parameters for different types of soft contacts (Fig.4.3) are listed in Table4.2. The maximum Hertzian pressure is about 90.2MPa for the PMMA disc-steel ball contact and 87.3MPa for the glass disc-PMMA ball contact. The lubricant is a single grade hydraulic oil, HVI 60. Its properties are listed in Table4.3. The measurement at each rolling speed was repeated three times. The value of the dimensionless parameter $\bar{\alpha} \approx 1.5$ which indicates indeed a weak piezoviscous lubricant effect as is typical for soft contacts, compared to the value of $\bar{\alpha} \approx 9.4$ for the case of the steel ball vs. glass disc contact.

4.3.2 Optical Interferometry Methods

The film thickness can be obtained from the interferograms in three ways using suitable light sources and specific hardware:

- (1) Spectrometry
- (2) Interference fringe color
- (3) Intensity and order of interference fringes

The first approach uses a spectrometer to detect the wavelength at the maximum intensity in the interference pattern at a particular location (often the center of the contact). This method has been widely used in the thin film lubrication studies, and is a build-in function of PCS-Instruments EHD2 ball-on-disc test rig illuminated with a halogen light source. From this wavelength the film thickness either directly follows, or, after correction for the (known) spacer layer thickness. It is an absolute measurement method with a high accuracy of a few nanometers, see [76]. The second approach is based on colorimetry, which enables a high measurement efficiency for 3D reconstruction/mapping of the film shape. Usually, a white light source is used to generate abundant colors in the interferograms. Typically a reference calibration is used translating color information to film thickness, see [20]. Also here often a spacer layer is used to measure film thicknesses below the wavelength of visible light. In the third, intensity-based method, a monochromatic, a dichromatic, or a trichromatic light source with known wavelength(s) is used, e.g. using laser RGB (lineup Red-Green-Blue LED) or a light source with a narrow band wavelength, i.e. small full width at half maximum (FWHM), to avoid the problem of wavelength uncertainty. This method is usually applied to a partial map of the contact region. It has a wide measurement range, from nanometers to several micrometers, see for example [53, 87, 92].

In this work, the intensity based measurement is used for the PMMA disc-steel ball contact (Configuration 1) and the spectrometry based method for the glass disc with spacer

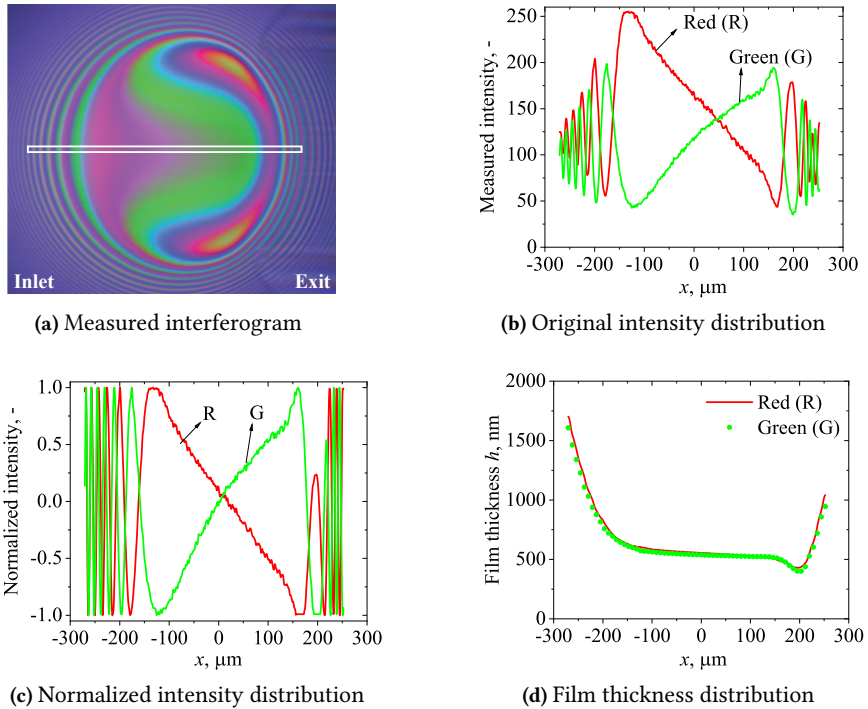


Figure 4.4: EHL film thickness analysis with intensity-based DIIM method for PMMA disc-steel ball configuration-1. (a) captured interference pattern with a RGB light source, square: zone of interest, 1m/s, 10N, HVI 60, pure rolling; (b) Original intensity distribution for both Red and Green light interferometry; (c) Normalized intensity distribution for Red and Green components; (d) Measured film thickness centerline profile with the R and G two-color interferometry.

layer-PMMA ball contact (Configuration 2), as shown in Fig.4.3. The second colorimetric method was not used here, because the SiO_2 spacer layer approach is likely to be too fragile to be on top of a soft PMMA disc and therefore it would be difficult to measure in the ultra-thin film regime with this method.

For Configuration-1 (PMMA disc- steel ball), the dichromatic interference intensity modulation (DIIM) approach, Ref. [87], has been used. Compared with monochromatic interferometry, this method can avoid counting the fringe order at the contact center, which is usually of low efficiency and shall be achieved by starting the test at a low speed and gradually increasing the rolling speed. With DIIM, for an interferogram captured at any speed, the fringe order at contact center can be known through the color of characteristic fringes (modulated intensity) out of the Hertzian contact zone. A RGB trichromatic LED light source (HLV3-3M-RGB-4, CCS Inc., Japan) has been used for this purpose. According to the spectrum provided by the manufacturer, the peak wavelengths are 465nm, 520nm, and 630nm, respectively, for the blue, green, and red single-color LED lights. The FWHM for each LED light is about 20nm, and a light source with narrow FWHM enables a good contrast of the interference fringes. The intensity of both the red (R) and green (G)

components in an interferogram has been analyzed to obtain the EHL film thickness. Fig.4.4 (a) shows the EHL interferogram obtained with the RGB light source for configuration-1, PMMA disc-steel ball. The centerline film thickness along the entrainment direction has been analyzed based on the intensity of the original (Fig.4.4 (b)) and on the normalized (on the difference between maximum and minimum intensity) (Fig.4.4 (c)) Red (R) and Green (G) components. Fig.4.4 (d) shows a typical film thickness centerline profile result obtained using the R and G intensities respectively. The results obtained based on the different colors show excellent agreement.

4.4 Results and Discussion

By numerical simulations the influence of the three dimensionless groups identified in Sec.4.2.2, i.e. the Deborah number D_{Hertz} , the elasticity ratio R_e and the load/speed parameter λ , on the (dimensionless) pressure and film thickness distribution, has been investigated. The results are presented in Sec.4.4.1. In Sect.4.4.2, the experimental results of (soft) EHL with PMMA material for the two configurations shown in Fig.4.3 are presented and compared with numerical results. Finally in Sec.4.4.3, the scaling and the self similarity in the film thickness and pressure results are investigated in perspective of the theoretical scaling found in [124].

4.4.1 Dimensionless Parameter Variation

It should be noted that, in reality, λ and D_{Hertz} are linked via load/speed operating parameters, see Eq.(4.11) and Eq.(4.14). Varying D_{Hertz} to investigate the effect of the Deborah number in Sec.4.4.1 means physically we vary the relaxation time via changing the viscosity of the dashpot η_s in the SLS model, while varying λ means that we vary the loading conditions.

Materials with low elastic modulus under lubricated point contact conditions are deformed significantly with high degree of local conformity, which results in relatively low contact pressures, typically 1~100MPa, so that often the effect of piezoviscosity of the lubricant is small. In the sections below, numerical results for $\bar{\alpha} = 0$ ($L = 0$) are therefore presented.

Effect of the Deborah Number D_{Hertz}

The influence of the Deborah number on the pressure and film thickness in VEHL is studied for pure rolling. The Deborah number D_{Hertz} is defined as Eq.(4.14), $D_{\text{Hertz}} = \tau/(a_0/v_2)$. It represents the ratio of the material relaxation time to the passage time of a point of the surface of the viscoelastic body through the contact. Fig.4.6 shows the dimensionless pressure and the dimensionless film thickness contours for D_{Hertz} from 0 to 10 for the elasticity ratio $R_e = 9$ and $\lambda = 0.01$. When $D_{\text{Hertz}} = 0$, the (SLS) material behaves purely elastically (elastic rubbery regime).

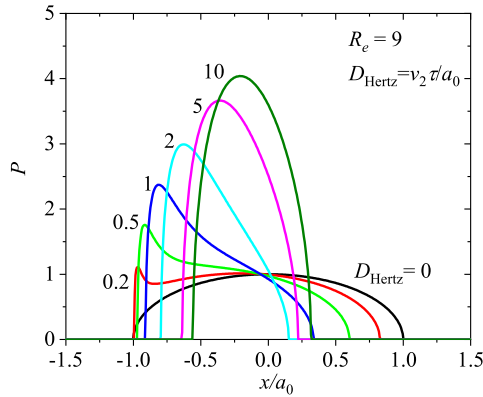
In this special case, the VEHL lubricated rolling contact problem is equivalent to an EHL problem, and shows a circular contact region, with the characteristic horseshoe shape of the film thickness on a contour plot. In the central region the film thickness is nearly uniform, with a restriction on the outlet side, with smoothly transitions to the so-called side lobes. The pressure distribution is nearly semi-elliptical, see Fig.4.6 (a) and Fig.4.5

(b). With an increase in D_{Hertz} , the shape of the contact area changes to non-circular as it shortens in the flow direction. This is due to the viscoelastic behavior as a result of which, in the region of decreasing pressure, the deformation can not quickly enough recover. The restriction at the outlet is less pronounced and the sidelobes are more separated. The pressurized region changes accordingly, most dominantly in the outlet half of the Hertzian contact region. From the film thickness contour plots it can be seen that the level of the central film thickness initially reduces quickly with increasing D_{Hertz} but then slowly settles. Fig.4.6 shows that the solid viscoelasticity has a significant influence on the film shape and pressure distribution in soft EHL contacts in particular in the range $D_{\text{Hertz}} < 2$. For larger values, a circular contact region returns in the limit of high velocities where the contact again exhibits elastic behavior but with elastic modulus E_{∞} .

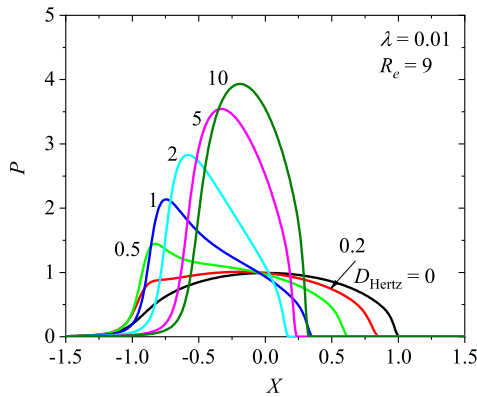
To further illustrate the effect of solid viscoelasticity on the VEHL, the results of centreline pressure distribution for both lubricated VEHL contacts and the corresponding viscoelastic dry contacts (VED) are given in Fig.4.5. The results of VED were calculated as shown in Chapter 3.

Comparing the lubricated and dry contact results, it can be seen that the VEHL pressure distribution and the length of the contact zone are almost identical for all Deborah numbers except for the short inlet pressure rise and the outlet region at a larger Deborah number. Similar to elastic contact problems, the lubricated contact is a singular perturbation on dry contact [124]. For both cases, the asymmetric pressure distribution originates from the same physical mechanism, i.e. the time delayed response of viscoelastic solids. With increasing Deborah number, the deformation at the trailing edge fails to recover in time so that the load-carrying zone shrinks. The leading edge experiences a larger pressure than the trailing edge, showing a pressure peak. For the lubricated contacts in Fig.4.5 (b), the extent of the inlet peak is reduced by the inlet pressure sweep resulting in a smoother inlet pressure rise. Note there is no (Petrusevich) pressure spike in the pressure profile on the outlet side. This is also not expected as the parameters are outside the range where this spike occurs, see [51, 142].

The dimensionless film thickness along the central line ($Y = 0$) is shown in Fig.4.7 for the same values of the Deborah number and operating conditions as in Figs.4.6 and 4.5 (b). The dimensionless film thickness profiles characterize the EHL behavior with a restriction at the outlet due to mass conservation. For $D_{\text{Hertz}} = 0$, the solution corresponds to the elastic solution with the low-speed modulus E_0 , and the EHL film thickness is the highest. With increasing Deborah number, the film thickness decreases rapidly up to $D_{\text{Hertz}} = 2$, followed by a slower approximation to the limit elastic solution for very high D_{Hertz} . The viscoelastic behavior of the solids causes a significant reduction in the film thickness. This effect increases with the Deborah number. Meanwhile, roughly in the range $0.2 \leq D_{\text{Hertz}} \leq 2$, a local minimum of the film thickness appears in the inlet region, as is marked by black circles in Fig.4.7 (bottom), responding to the an inlet pressure peak just prior to its location in Fig.4.5 (b). This inlet constriction (local minimum) is caused by the viscoelastic behavior of the solids, as the inlet pressure peak also appears in dry rolling contacts in Fig.4.5 (a). The mechanism causing the local minimum in the film thickness of this inlet is somewhat similar to the classical EHL film constriction close to the outlet. When the inlet constriction is present the depth of the exit restriction is reduced.



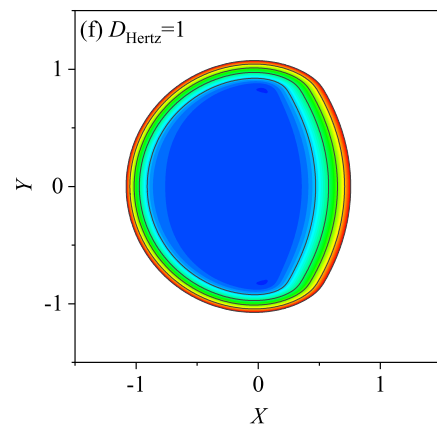
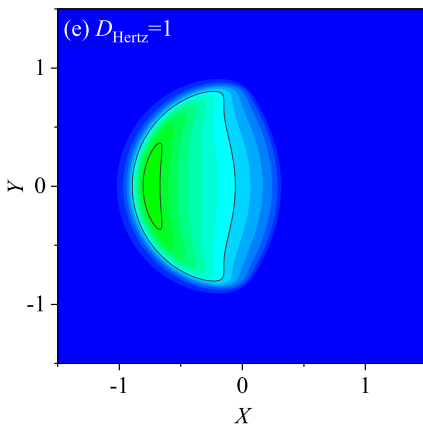
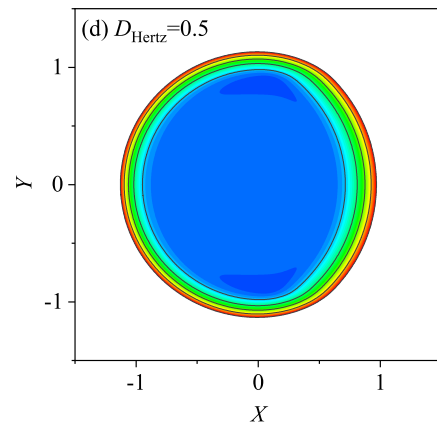
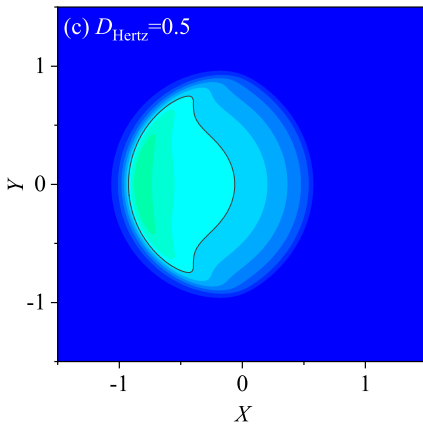
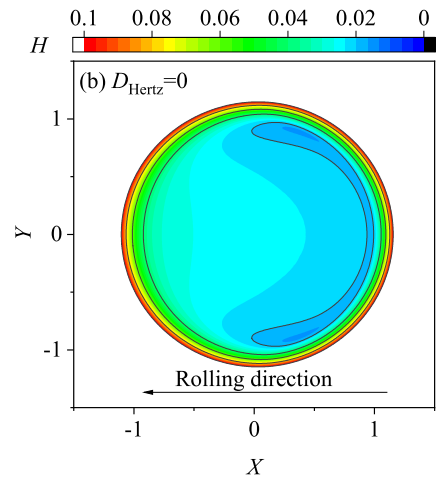
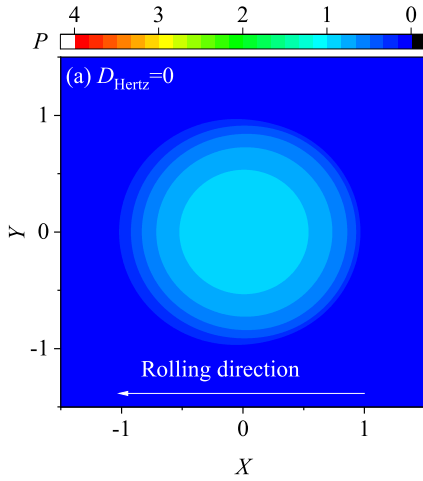
(a) VED contact



(b) VEHL contact

Figure 4.5: Dimensionless pressure distribution along the central line as a function of the Deborah number D_{Hertz} . (a) viscoelastic dry contact (VED), and (b) lubricated viscoelastic contact. The left side is the rolling entrance. (SLS viscoelastic solid, $R_e = 9$, pure rolling, $\lambda = 0.01$)

4



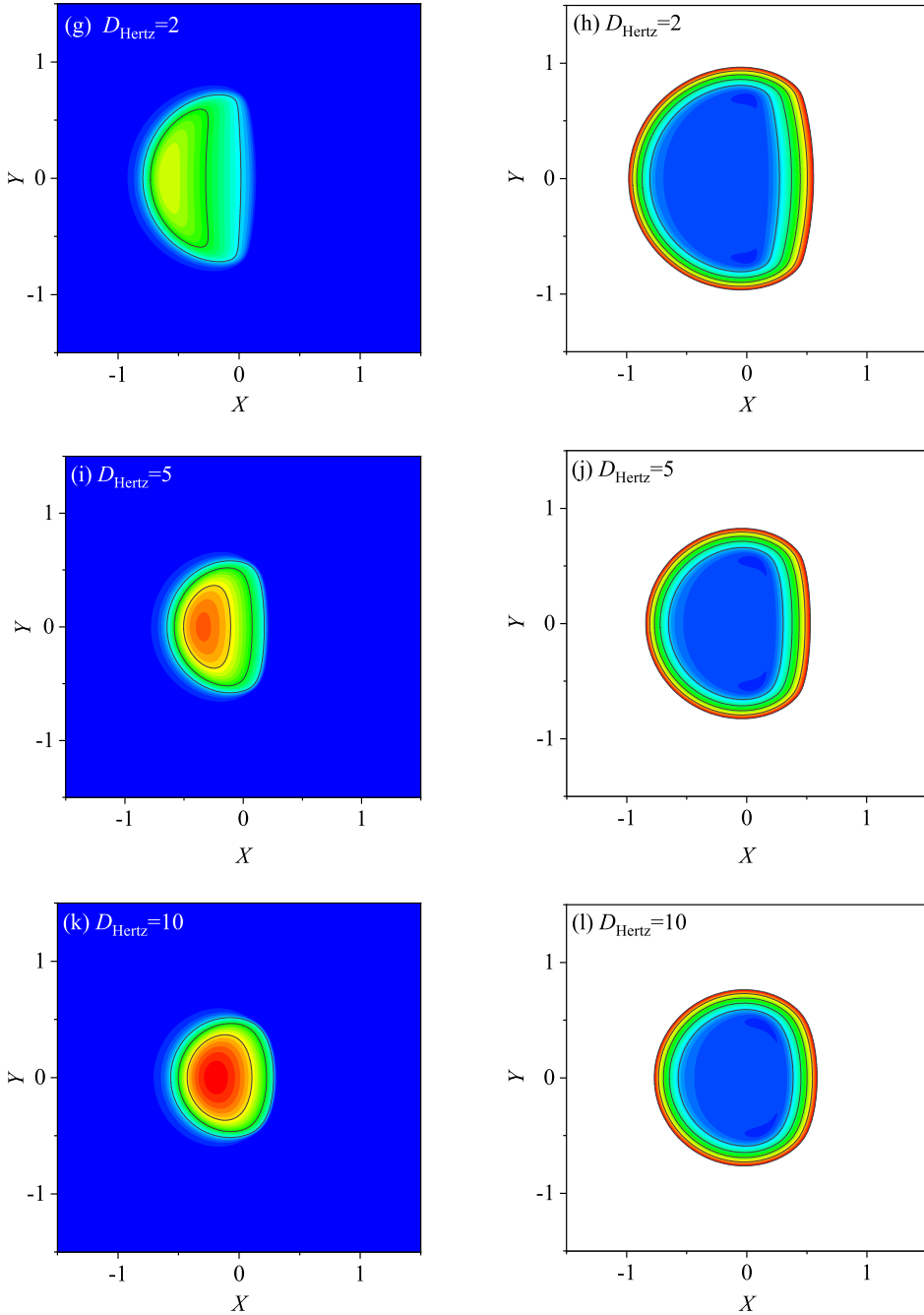


Figure 4.6: Contour plots of dimensionless pressure (left) and film thickness (right) in a VEHL contact at different values of Deborah number, D_{Hertz} . The left side is the entrance. (SLS viscoelastic solid, $R_e = 9$, $\lambda = 0.01$, pure rolling)

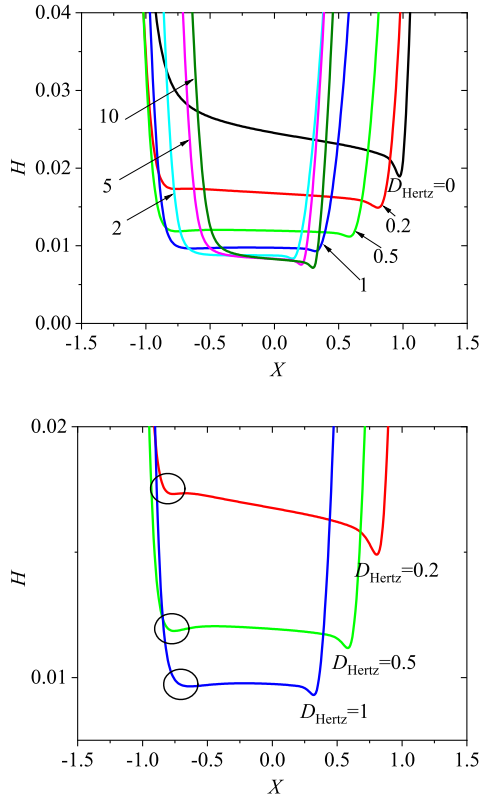


Figure 4.7: Variation of the dimensionless film thickness along the central line with D_{Hertz} in VEHL (top) the overall variation of the film thickness with Deborah number, (bottom) the film thickness with obvious inlet restriction in the top figure. The left side is the entrance. (SLS viscoelastic solid, $R_e = 9$, $\lambda = 0.01$, pure rolling)

Effects of the Elasticity Ratio R_e

Fig.4.8 shows the centreline pressure and film thickness profiles for different values of the elasticity ratio R_e at fixed values: $D_{\text{Hertz}} = 0.2$ and $\lambda = 0.01$. The increase in elasticity ratio causes a significant reduction in the film thickness and leads to a pressure peak at the inlet side. Larger elasticity ratios, e.g. $R_e = 9$ or even $R_e = 99$, result in an inlet film constriction and an increasingly flat film thickness profile. The variation of the maximum pressure P_{max} and the film thickness at the location of the maximum pressure H_{pmax} as a function of D_{Hertz} is given in Fig.4.9. All curves start at unity since the low-speed elastic modulus E_0 has been used in the calculation of the Hertzian parameters which have been used to define dimensionless variables in Sec.4.2.2. The curves end at the associated elastic solution with the high-speed elastic modulus $E_\infty = E_0(1 + R_e)$. The curve with a larger R_e , thus, ends at a higher maximum pressure P_{max} . The limit $D_{\text{Hertz}} \rightarrow \infty$ for the dry contact follows from the definition of the Hertzian contact parameters as $P_{\text{max},\infty} = (1 + R_e)^{(2/3)}$ which gives 4.64 for $R_e = 9$.

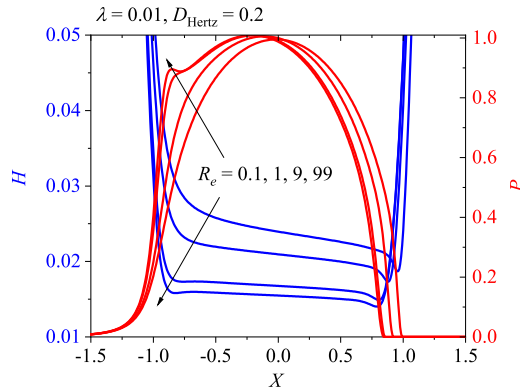


Figure 4.8: Influence of elasticity ratio R_e on centreline pressure and film thickness profiles in VEHL. The left side is the rolling entrance. (SLS viscoelastic solid, $D_{\text{Hertz}} = 0.2$, $\lambda = 0.01$, pure rolling)

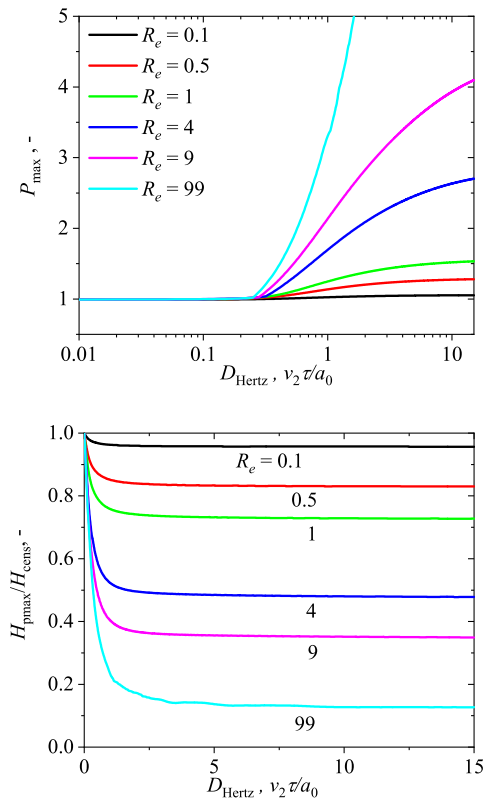


Figure 4.9: Dimensionless maximum pressure P_{max} (top) and film thickness at the maximum pressure H_{pmax} (bottom) as a function of the Deborah number D_{Hertz} , for different R_e . (SLS viscoelastic solid, $\lambda = 0.01$, pure rolling)

For fixed values of D_{Hertz} and λ , varying R_e implies varying the elastic modulus of the upper spring E_f in the SLS model because $R_e = E_\infty/E_0 - 1 = E_f/E_0 - 1$, see the definition of E_∞ and E_0 in Nomenclature. In Fig.4.9 (bottom), the variation of the film thickness H_{pmax} is presented relative to the corresponding elastic solution H_{cens} obtained at zero speed conditions. As D_{Hertz} is increased, all curves drop rapidly to the elastic solution corresponding to the effective modulus E_f . Similar to elastic contacts, the curve with a larger elasticity ratio and correspondingly a larger effective modulus results in a smaller film thickness in Fig.4.9 (bottom) and a higher maximum pressure in Fig.4.9 (top).

Effect of the Dimensionless Parameter λ

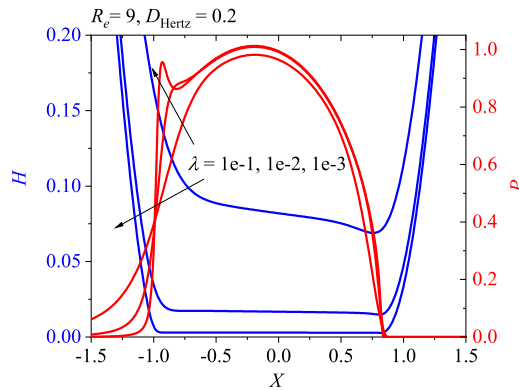


Figure 4.10: Influence of λ on the centreline pressure and film thickness profiles. The left side is the rolling entrance. (SLS viscoelastic solid, $D_{\text{Hertz}} = 0.2$, $R_e = 9$, pure rolling)

Fig.4.10 shows the effect of the dimensionless parameter λ on the pressure and film thickness distribution at a constant value of $R_e = 9$ and $D_{\text{Hertz}} = 0.2$. A smaller value of λ represents a heavier loading condition for a fixed speed condition. It can be seen from the figure that a small λ results in a shorter inlet region and a higher pressure peak at the inlet. The additional local minimum occurs at inlet in the fluid film as a response to the inlet pressure peak, as was seen in Fig.4.7 (b).

Fig.4.11 shows the variations of the dimensionless maximum pressure P_{max} and the dimensionless film thickness at the maximum pressure H_{pmax} as a function of D_{Hertz} . Again, all plots start from unity as a result of the chosen scaling and end with the elastic state governed by the high-speed elastic modulus E_∞ . In between, the solid shows viscoelastic transition. As a reference, the variation of the P_{max} in the corresponding dry contact has also been given in Fig.4.11 (top) with a black line. Note that the pressure in the lubricated contact closely resembles the pressure in dry contact. However, the dry contact has a larger P_{max} because a lubricated contact introduces an entrainment pressure sweep in the inlet and a continuous decay to ambient pressure in the outlet. As the integral over the pressure in both cases should be the same due to force balance Eq.(4.16), this implies that the maximum pressure in the lubricated contact is somewhat lower.

The variation of the film thickness $H_{\text{pmax}}/H_{\text{cens}}$ at the maximum pressure with the Deborah number is shown in Fig.4.11 (bottom). Within a certain range of D_{Hertz} , all curves

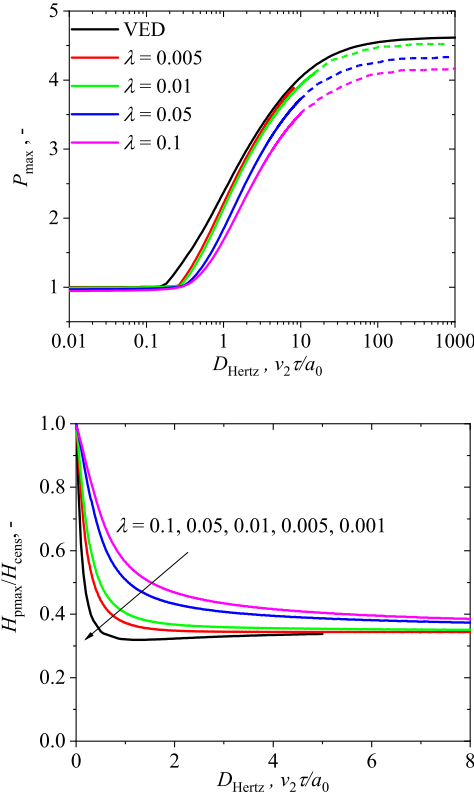


Figure 4.11: Variation of the dimensionless maximum pressure P_{\max} (top) and film thickness at the maximum pressure H_{pmax} (bottom) as a function of the Deborah number D_{Hertz} for a series of loading cases, λ . (SLS viscoelastic solid, $R_e = 9$, pure rolling)

fall rapidly indicating that the solid viscoelasticity has a negative effect on the EHL film thickness. This range is referred to as viscoelastic transition in [67]. After the viscoelastic transition, the relative film thickness for all loading cases varies little and reaches a final value which corresponds to the elastic solution with the effective high-speed modulus of E_{∞} .

Summarizing the results of Sec.4.4.1, the VEHL point contact problem is governed by the above three dimensionless parameters, and their individual influence on the VEHL film thickness and pressure has been discussed separately. From the above analysis, the pressure distribution in VEHL point contacts is determined by the solid deformation inside the contact zone characterized by D_{Hertz} , while the film thickness is determined in the inlet region which is shown later in Sec.4.4.3. It should be pointed out that in a "real" VEHL contact problem with a specified viscoelastic material, only the elasticity ratio R_e is fixed, while the other two speed-related parameters, D_{Hertz} and λ , vary simultaneously. In the following section, film thickness experiments are carried out with PMMA soft materials to further analyze the film behavior in a real EHL/VEHL contact.

4.4.2 Experimental Results

Most experimental results for viscoelastic material concern friction measurements. Film thickness measurements of highly deformed (nearly) isoviscous (V)EHL point contacts showing film profiles are relatively rare, e.g. see [95, 114] using optical interferometry, and [41] using ultrasonic reflection techniques. In this work (V)EHL film thickness interferograms and centerline film thickness profiles obtained with the intensity-based method for configuration-1 (Fig.4.3 (a)), and central film thickness values obtained from spectrometry-based measurements for configuration-2 (Fig.4.3 (b)), are compared with numerical simulation results of EHL and VEHL models. For completeness in the simulations for all cases, the pressure dependence of the viscosity and density of the lubricant are taken into account using Eq.(4.19) and Eq.(4.20).

4

Spectrometry-Based Measurements

Spectrometry-based measurements have been carried out to obtain the variation of the central film thicknesses with rolling entrainment speeds ($h_{cen}-v_m$ curve) for the glass disc-PMMA ball contact (Configuration-2). The operating conditions are listed in Table4.1. The lubricant is HVI60, and the load is 10N. Fig.4.12 shows the measured central film thickness on a double-log scale. Two numerical results are also given. The first is the simulation result from a conventional EHL solution using the elastic modulus determined for the PMMA ball, of 5.1GPa. This EHL simulation was achieved with the VEHL model by setting the damper viscosity η_s in the SLS model to zero, and it was verified that the conventional EHL solver [141] gives exactly the same result. The second theoretical result is from the simulation with the VEHL model with a single relaxation time $\tau = 0.01s$ and an elasticity ratio of $R_e = 1$ in the SLS model. This value of τ was taken from [114] for the same material PMMA. However it should be noted that these two parameters for the PMMA material used are not exactly known.

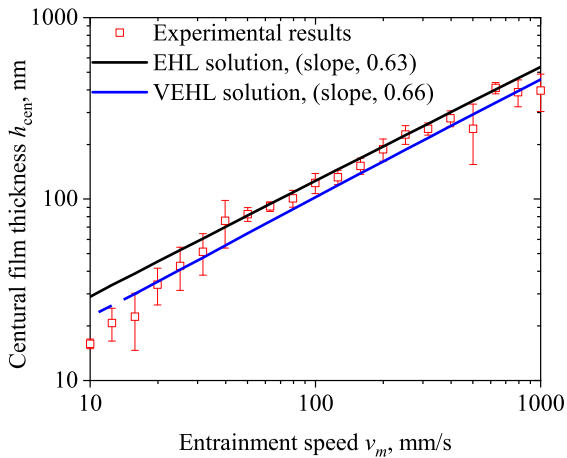


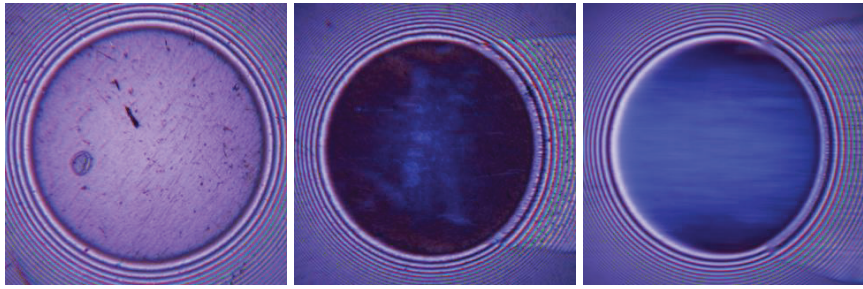
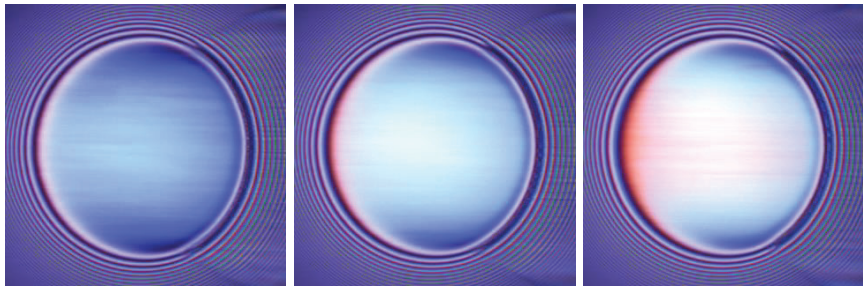
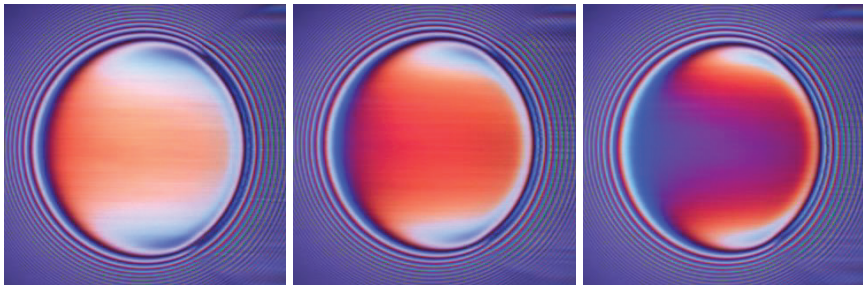
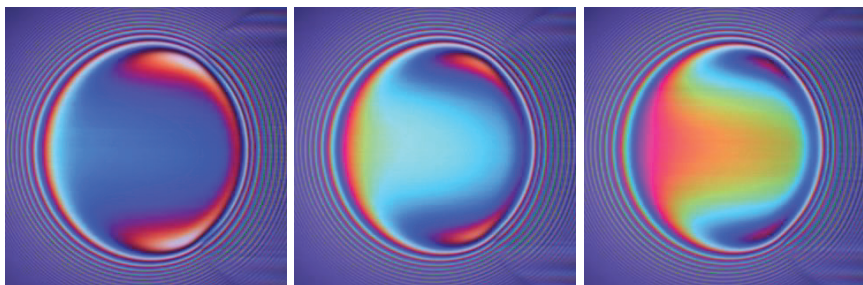
Figure 4.12: Central film thicknesses comparison between purely soft EHL and VEHL with $h_{cen}-v_m$ curves. (HVI60 oil, 10N, 23°C, pure rolling. Measurements:glass disc-PMMA ball. VEHL simulation: SLS model with a single relaxation time, $\tau = 0.01s$ and an elasticity ratio of $R_e = 1$)

Fig.4.12 shows that the experimental film thickness on log scale increases linearly with increasing rolling speed with an overall slope of 0.63. The theoretical EHL result taking into account the piezoviscosity has a slightly higher film thickness with a slope of 0.63 as in the experiments. The theoretically predicted VEHL results show a reduction of the central film thickness compared to the EHL results and a somewhat steeper slope of 0.66. The agreement between the experimental and the theoretical results is quite good in the speed range from 0.04m/s to 1m/s. The EHL prediction lies slightly above the experimental values, the VEHL prediction slightly below. For lower speeds, the film thickness decays more rapidly with speed. This phenomenon has also been shown in the following section measured with the second optical methods, see Fig.4.15. The possible reasons will be discussed later.

Regarding the viscoelastic parameters, for $\tau = 0.01$ s the value of D_{Hertz} ranges from 0.43 ~ 43 for the range of 0.1 ~ 1m/s. Even though this is a relatively large value of the Deborah number, for $R_e = 1$ the effect of viscoelasticity on the central film thickness is relatively small, see Fig.4.9 (b), and regarding the film thickness a reduction of about 20% could be expected. Even when the real relaxation time of the PMMA is much larger than assumed, this will not change much of this maximum reduction as it is mostly determined by R_e . More detailed validation therefore requires additional material testing e.g. to validate the viscoelastic model and in this case the value of R_e .

Intensity-Based Measurements

Experiments were also carried out with a PMMA disc against a steel ball (configuration-1). The test conditions are identical, see Table4.1. Fig.4.13 shows a series of interferograms for a fixed load of 10N and a rolling speed ranging from 0.01 ~ 1m/s. Putignano and Dini [114] used basically the same setup but with speeds ranging from 1 ~ 3m/s and a load of 15N. In the present study high quality interference images are obtained also for lower speeds with the updated RGB light source. The figure shows that, similar to a typical "hard" EHL film, a horse-shoe shaped film occurs for almost all speeds. However, there are two features in this group of interferograms that do not exist in classical "hard" EHL. Firstly, the size of the contact zone at zero speed is larger than that at a rolling speed. This could be due to adhesion, or to viscoelastic creep of the PMMA at a fixed load. Secondly, as the entrainment speed is increased to about 0.2m/s, the EHL zone looks no longer circular in shape, as the outlet length reduces. This phenomenon has also been observed by Marx et al. [96] and Putignano and Dini [114]. This behavior may be caused by tangential deformation of the disc due to a slight slip in the experiments, see [86]. One may also attribute it to effects of viscoelasticity [114].

 $v_m = 0$ m/s $v_m = 0.02$ $v_m = 0.04$  $v_m = 0.06$ $v_m = 0.1$ $v_m = 0.13$  $v_m = 0.16$ $v_m = 0.2$ $v_m = 0.25$  $v_m = 0.32$ $v_m = 0.4$ $v_m = 0.5$

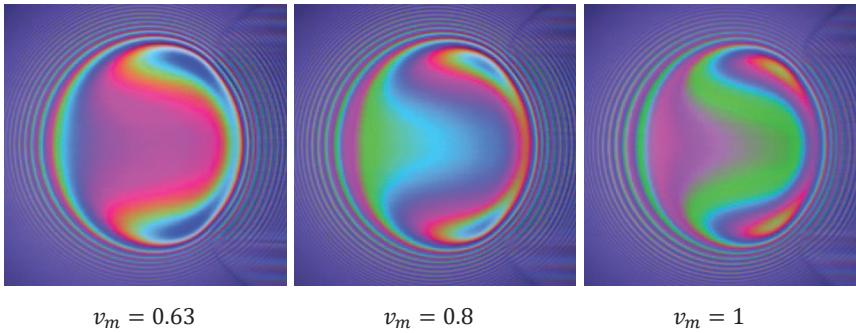


Figure 4.13: Interferograms of soft EHL formed between PMMA disc-steel ball (Configuration-1) at different rolling speeds. The inlet is at the left side. (HVI60 oil, 10 N, 23 °C, pure rolling)

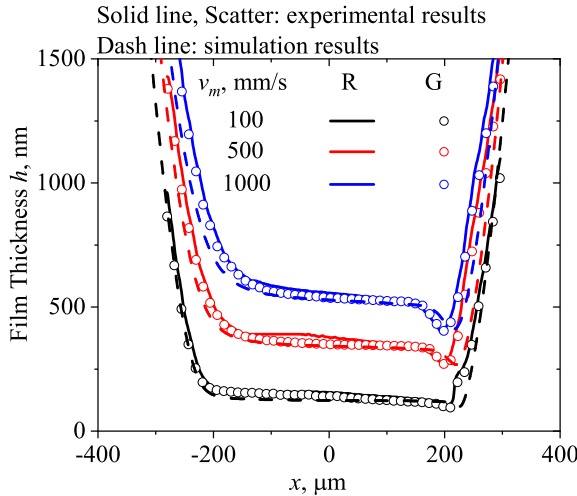


Figure 4.14: Centreline film thickness profiles at rolling speeds of 100, 500 and 1000mm/s obtained by analyzing the corresponding interferograms given in Fig.4.13 with the dichromatic interference intensity modulation (DIIM) approach [87]. Elastic simulation results in dash lines are obtained by the degenerated VEHL model with the operating conditions listed in Table4.1. The left side is the inlet side.

As mentioned before, based on a relaxation time, $\tau = 0.01s$, the Deborah number in the experimental conditions ranges from $D_{\text{Hertz}} = 0.43$ for $v_m = 0.01m/s$ to $D_{\text{Hertz}} = 43$ for $v_m = 1m/s$. Comparing the images in Fig.4.13 with the contour plots in Fig.4.6, the viscoelastic effects in terms of the shape change of the contact region by outlet length reduction in the experiment are small. This was also noted in [114]. This can be explained from the parameter study as mentioned above. Even though D_{Hertz} reaches quite large values, the magnitude of the viscoelastic effects more strongly depends on the value of R_e , see Fig.4.9. For Fig.4.6, $R_e = 9$ was used whereas $R_e = 1$ in the present calculations and

comparison. Finally, one may argue that the value of the relaxation time used in reality could be much different but, exploiting the result of the numerical parameter study that would not alter the agreement between experimental and theoretical results as this would mainly change the value of D_{Hertz} , whereas, which following the same reasoning would not give much different results for the given value of Re .

Fig.4.14 compares the film thickness distribution along the central line obtained from measurements and simulations for three speeds, 0.1, 0.5 and 1m/s. The experimental film was evaluated with both green and red light intensity for the interferograms using the DIIM [87] and labeled as 'R' and 'G', respectively. It can be seen from the figure that the two experimental results agree well. The numerical results from the VEHL model with elastic solid assumption are given in dashed lines in Fig.4.14. A good agreement is achieved. The main deviation appears to occur in the exit region, which may be caused by the shrinkage of the film shape and the cavitation zone as shown by the interferograms in Fig.4.13.

4

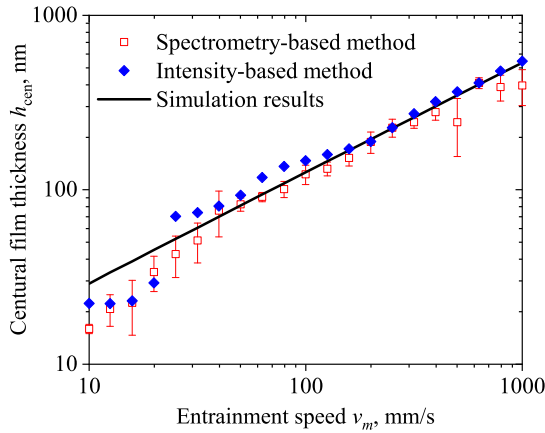


Figure 4.15: Comparison of the measured film thickness between two kinds of configurations and two interferometry methods shown in Fig.4.3. Open square: spectrometry-based method for Configuration-2, glass disc-PMMA ball; Filled square: intensity-based method for Configuration-1, PMMA disc-steel ball; Solid line: EHL simulation results.

The $h_{cen}-v_m$ curve measured for Configuration-1 using the intensity-based method is compared with the curve measured in Configuration-2 using the spectrometry-based method in Fig.4.15. Even though the two test configurations look different, the operating conditions are comparable in terms of effective material and contact parameters, e.g. the effective elastic modulus of solids, the Hertzian pressure, and the contact width, see Table 4.2. As a result, the three dimensionless governing parameters discussed in Sec.4.4.1 are also similar for these two cases and indeed, as seen in Fig.4.15, the two configurations result in a film thickness that is nearly the same. However, at low speeds the measured film thickness is smaller than the simulations for both optical methods. There can be various reasons among which as the influence of surface roughness and micro-EHL, slightly viscoelastic effect, or other interfacial influence factors due to relatively low affinity of Cr layer. However, above a film thickness of 40nm, the $h_{cen}-v_m$ curves shows a clear power-law relation.

4.4.3 Film Thickness Scaling and Self Similarity

For the highly deformed isoviscous regime with ($\bar{\alpha} = 0$), Snoeijer et al. [124] showed that the EHL problem is a singular perturbation on the Hertz dry contact problem. For both line and point contact the film profiles in the inlet and outlet exhibit self similarity. The self similar solution for the inlet (and central) film thickness, the film scaling is $H^* = \frac{\pi}{4} H \lambda^{-3/5}$. The power of 0.6 for the velocity was also found by Herrebrug [62] for line contact by numerical solution, and by Hooke [66, 68]. As shown by Snoeijer et al., the length scaling is $X^* = (X + 1)\lambda^{-2/5}$, the scaled distance to the Hertzian contact radius, the inlet length, also referred to as the length of the inlet pressure sweep. Physically it represents the length over which the pressure flow terms lose their importance and shear flow starts to dominate. So far there has not been much experimental validation in film thickness measurements showing this inlet scaling. For highly deformed (soft) contacts considered in this chapter the piezoviscosity parameter is low enough to expect that the results should closely agree with the scaling for the isoviscous case. This is investigated in the following subsection. Next the deviation induced by the viscoelasticity is investigated using numerical results.

Scaling Results for Isoviscous Soft (Highly Deformed) EHL

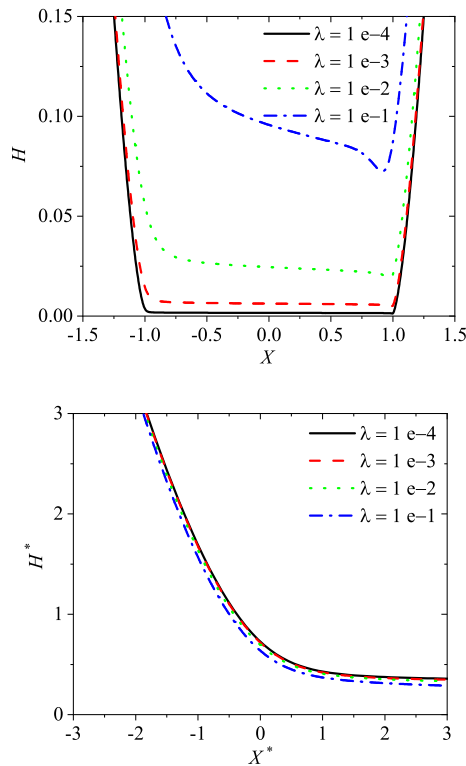
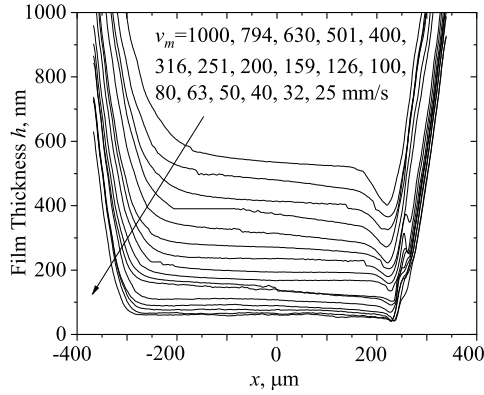
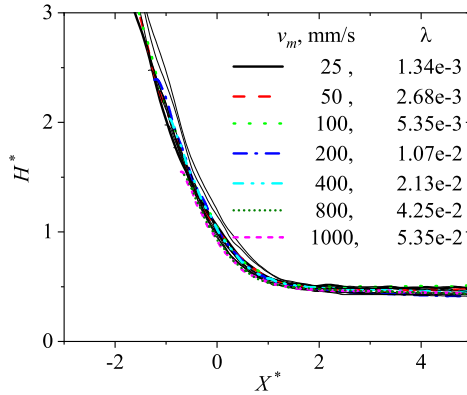


Figure 4.16: Simulated dimensionless centreline film thickness H at different λ , isoviscous condition (top). Scaled film thickness $H^* = \frac{\pi}{4} H \lambda^{-3/5}$ as a function of scaled coordinate $X^* = (X + 1)\lambda^{-2/5}$ in the inlet region (bottom).

Fig.4.16 (top) shows the dimensionless centerline film thickness profile computed numerically for the isoviscous EHL case for four values of λ . Fig.4.16 (bottom) shows the same result scaled as $H^* = \frac{\pi}{4}H\lambda^{-3/5}$ as a function of $X^* = (X+1)\lambda^{-2/5}$. Clearly with decreasing λ the results converge to a single curve which is the self similar solution. The scaling for the outlet film works in the same way but with $X^* = (X-1)\lambda^{-2/5}$. These results are shown in Sec.4.4.3.



(a) Experimental results



(b) Scaled experimental results

Figure 4.17: (a) Measured centreline film thickness profiles at different entrainment speeds for interferograms given in Fig.4.13. (b) Scaled film thickness $H^* = \frac{\pi}{4}H\lambda^{-3/5}$ as a function of scaled coordinate $X^* = (X+1)\lambda^{-2/5}$ for the inlet region.

The experimentally obtained centerline film profiles measured for different rolling velocities for Configuration-1 obtained using the DIIM intensity based approach are presented in Fig.4.17 (a) for the captured interferograms in Fig.4.13. The rolling speed in the experiments ranges from 25mm/s to 1000mm/s, and value of λ from 1.34×10^{-3} to 5.35×10^{-2} . With the same scaling parameter for the inlet region, $H^* = \frac{\pi}{4}H\lambda^{-3/5}$ as a func-

tion of $X^* = (X + 1)\lambda^{-2/5}$, the measured film thickness profiles at different rolling speeds closely collapse to a single curve, see Fig.4.17 (b). Even though the scaling parameters strictly apply to the isoviscous case it also works for the experimental conditions with the PMMA disc. This is due to the fact that piezoviscous effects are almost absent, and apparently also the viscoelastic effects are small. The results here provide experimental evidence, for the first time, for the scaling parameter and the similarity theory.

Inlet and Outlet Scaling Results for VEHL

The film thickness in EHL contacts is dominated by the inlet region, see [124] and [65]. In Fig.4.11 (b), the viscoelastic transition starts earlier for a lower Deborah number and the film thickness drops more rapidly with smaller values of λ . According to Hooke and Huang [67], this transition behavior from initially elastic to viscoelastic is controlled by a new Deborah number based on the inlet length $D_{\text{inlet}} = v_2\tau/e$ where e is the entrainment length representing the length of the pressure sweep from the point of pressure inflection to the root of the dry contact. D_{inlet} can also be understood as the ratio of the relaxation time of the viscoelastic material τ to the transit time of the material through the inlet e/v_2 . For soft EHL line contact problems, the hydrodynamic inlet length e may be expressed as a function of the semi-contact width a_0 and Johnson's elasticity parameter g_3 [67], that is $e = 3.264a_0g_3^{-0.8}$. For point contacts used in this study, the inlet length of elastic contacts may be proposed as following based on the similarity solutions by Snoeijer et al. [139],

$$e = a_0\lambda^{\frac{2}{5}} \quad (4.24)$$

where a_0 is the Hertzian radius at a very small Deborah number (elastic solution with E_0). A smaller λ gives a shorter inlet length and thus a thinner fluid film, which is in line with the simulation results of the entrainment sweep and the film thickness shown in Fig.4.10. The relative film thickness in Fig.4.11 (b) is re-plotted as a function of the inlet Deborah number D_{inlet} in Fig.4.18. It shows that all results at different λ collapse on a single curve up to $D_{\text{inlet}} = 0.5$, but differ increasingly for larger D_{inlet} where the film thickness is largely influenced by the viscoelastic property of the material. Note that these results apply to the case $R_e = 9$ so as to have stronger viscoelastic effects.

For very low values of D_{inlet} , the transit time e/v_2 is larger than the relaxation time τ , and the material behaves mainly elastically with an effective modulus close to E_0 . This means that the damper in the SLS model (Fig.2.10) is almost fully compressed, and mainly the two springs, E_f and E_s in series support the applied load. As the Deborah number D_{inlet} is increased, the transit time through the inlet becomes shorter, and thus, the damper does not have enough time to fully respond, showing increasingly viscoelastic effects at inlet. These viscoelastic effects cause a significant reduction in the film thickness H_{pmax} , as shown in Fig.4.11 (b), since the variation of the film thickness mainly depends on the inlet behavior. Next the degree to which the film thickness profiles in the inlet and outlet start to deviate from this scaling is considered.

The scaling parameters proposed in [124] for the film thickness and pressure for the isoviscous soft EHL case are further used to explore the behavior for VEHL contacts. The original parameters are $P^* = P\lambda^{-1/5}$ and $H^* = \frac{\pi}{4}H\lambda^{-3/5}$ as a function $X^* = (X \pm 1)\lambda^{-2/5}$ for the inlet and the outlet region, respectively. This scaling will be used but instead of taking the inlet and outlet length defined as the distance to the edge of the Hertzian contact region,

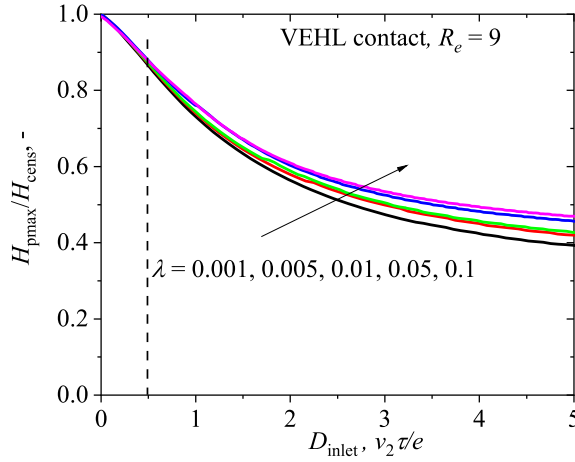


Figure 4.18: Variation of the film thickness with the Deborah number based on the inlet length $D_{\text{inlet}} = v_2 \tau / e$. Data from Fig.4.11 (b). (SLS viscoelastic solid, $R_e = 9$, pure rolling)

the X in X^* are taken as the dimensionless entry and exit contact radius determined from the numerical solution of the corresponding viscoelastic dry contact (VED), $X_1 = x_1/a$ for the inlet and $X_2 = x_2/a$ for outlet, respectively.

Firstly, Fig.4.19 shows the dimensionless centreline pressure P and film thickness H distributions calculated at different Deborah numbers D_{Hertz} for four values of λ obtained with the VEHL model. The effects of λ and D_{Hertz} on the film thickness and the inlet pressure sweep are discussed in Sec.4.4.1. With decreasing λ , the inlet length decreases, and the film thickness decreased. And in both the inlet and the outlet, pressure and film approximate the dry contact solution which for $D_{\text{Hertz}} = 0$ is the Hertzian solution, but which already for $D_{\text{Hertz}} = 0.1$ significantly deviates from this profile particularly in the inlet due to the occurrence of the pressure maximum which has a significantly steeper slope than the Hertzian solution. The scaled results are shown in Fig.4.20 for both the inlet and the outlet. As a reminder, $X^* = 0$ refers to the contact edge of the viscoelastic dry contact. For each $D_{\text{Hertz}} < 0.01$ all solutions converge to a single curve in both the inlet and the outlet regions as shown in Figs.4.20 (a)~(f). The material responds mainly elastically at these small Deborah numbers. With increasing D_{Hertz} , e.g. $D_{\text{Hertz}} = 0.1$ in Figs.4.20 (g) and (h), the scaling rule still gives quite a good approximation to a "single" curve, particularly so for the film thickness in the inlet, and the pressure in the outlet. However, the scaling does not fit the pressure in the inlet, and the film thickness in the outlet, quite well. The length scaling appears to be correct, but the height scaling needs correction.

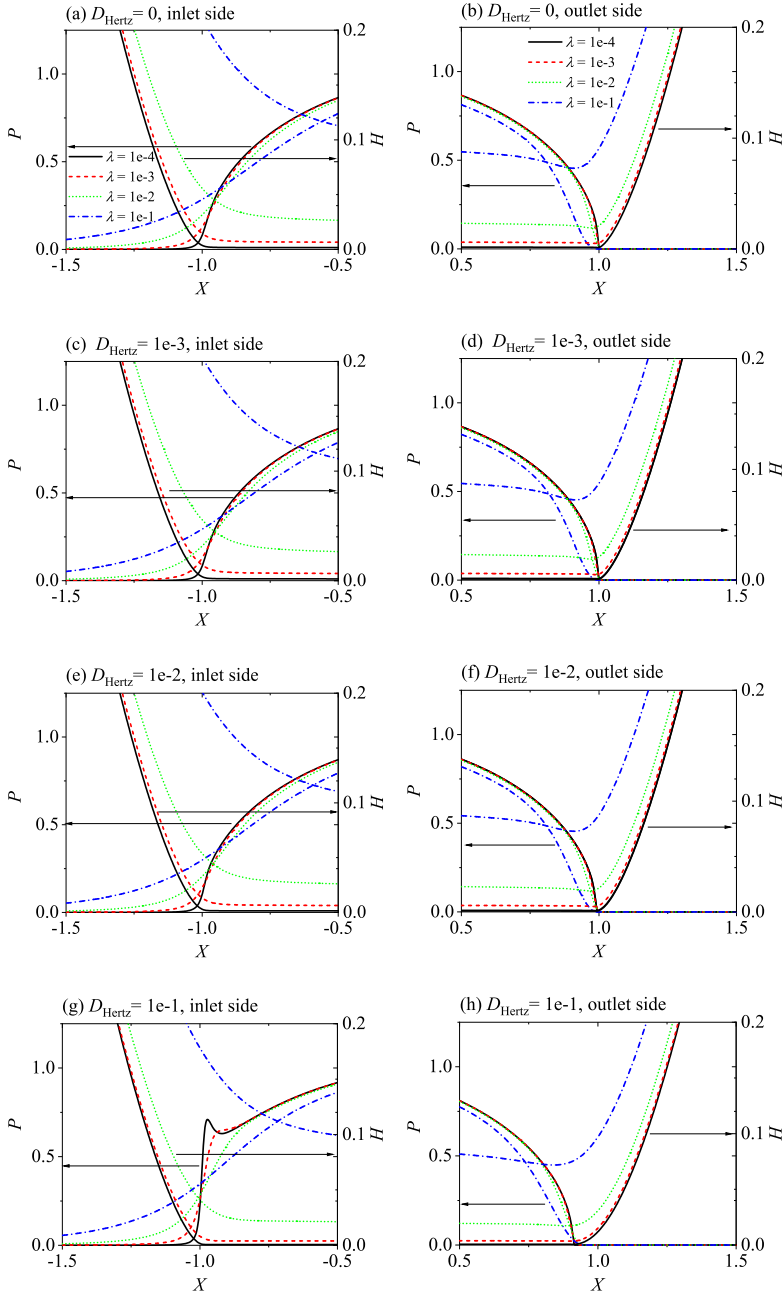


Figure 4.19: Distribution of originally calculated dimensionless centreline pressure P and film thickness H at different Deborah numbers D_{Hertz} for a series of λ using the developed VEHL model. Left: inlet region; right: outlet region. (SLS viscoelastic solid, $R_e = 9$, pure rolling)

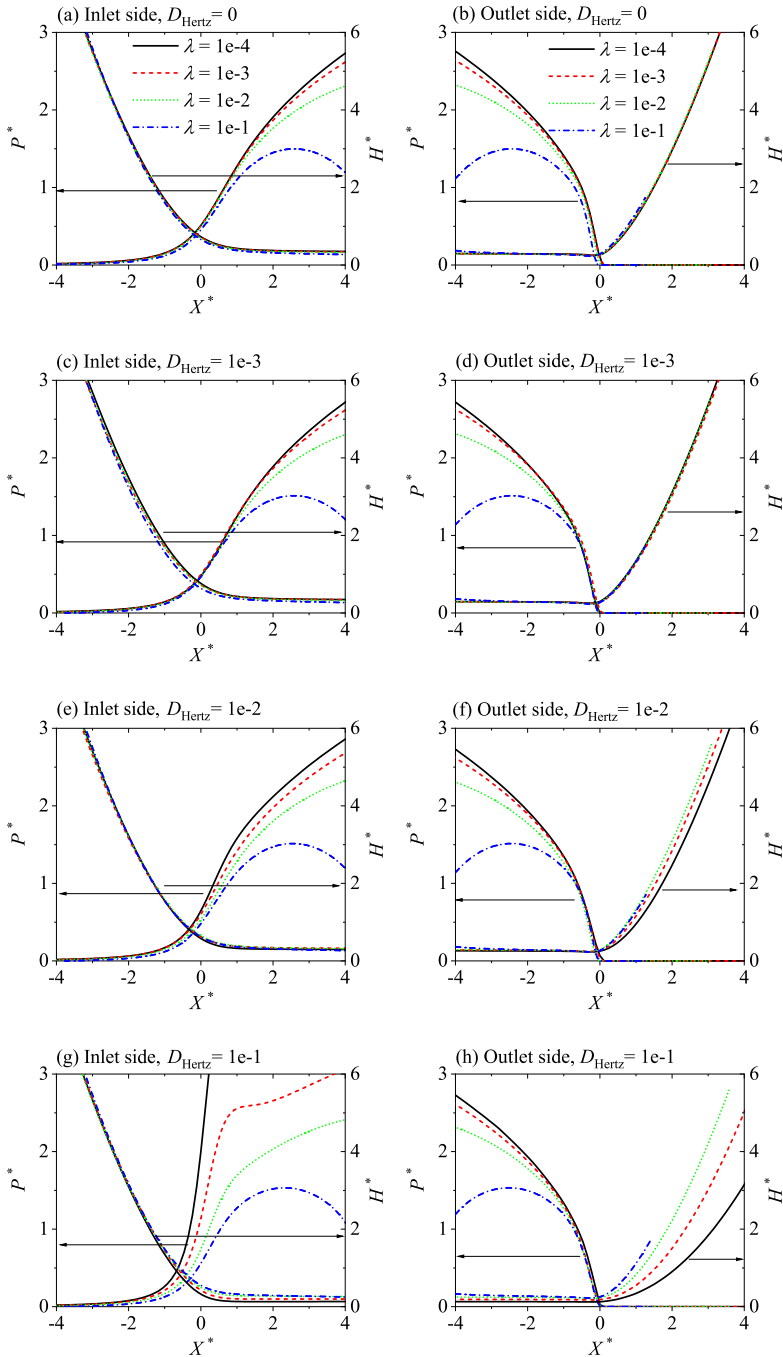


Figure 4.20: Results of inlet pressure and film thickness scaling for VEHL results in Fig.4.19 using parameters from soft EHL, i.e. centreline pressure $P^* = P\lambda^{-1/5}$ and film thickness $H^* = \frac{\pi}{4}H\lambda^{-3/5}$ as a function of scaled coordinate $X^* = (X + X_1)\lambda^{-2/5}$ and $X^* = (X - X_2)\lambda^{-2/5}$ for the inlet and outlet region, respectively. X_1 and X_2 are the contact limits in VED dry rolling contacts.

4.5 Conclusion

A visco-elastohydrodynamic lubrication (VEHL) model has been developed for point contact problems by implementing a novel viscoelastic deformation equation proposed in Chapter 3 into an existing EHL multigrid solver. The SLS model with a single relaxation time was used to characterize the viscoelastic solids behavior. The developed VEHL solver yields the pressure and film thickness solution with a computational efficiency of the same order as for solving a classical EHL problem. The approach allows straightforward extension of existing EHL algorithms to VEHL. Also the proposed equation does not suffer from accuracy loss at low surface speeds.

Three dominant dimensionless parameters are identified for VEHL problems, the dimensionless parameter λ , the elasticity ratio R_e and the Deborah number D_{Hertz} . By numerical simulations the effects of these parameters on the pressure and film thickness solution have been analyzed. The time-delayed response of the viscoelastic material can have a profound influence on the contact pressure and the film shape through effects of the elasticity ratio R_e and the Deborah number D_{Hertz} . Generally the viscoelastic solid behavior leads to a reduced film thickness compared to the purely elastic case. For the SLS viscoelastic material model the VEHL solution clearly exhibits two extreme elastic solutions, one for low and one for high surface speeds. In the transitional regime, the size of the contact zone on the exit side can reduce significantly leading to a non-circular contact region. The VEHL pressure distribution inherits features of the viscoelastic dry contact problem and may exhibit a steep local maximum in the pressure as well as a local film minimum on the inlet side. The results of the parameter study provide a clear frame of reference for the interpretation and understanding of solid viscoelastic body effects on the pressure and film thickness in highly deformed lubricated contacts.

Film thickness measurements have been carried out on a ball-on-disc test rig with two configurations, a PMMA ball rolling against a glass disc, and a steel ball rolling against a PMMA disc. High quality interferograms were captured for PMMA-steel contact with a new RGB light source. The experimental results agree well with the numerical solutions. However, the used PMMA shows only very weak viscoelastic behavior within the range of operating conditions. This is explained using the knowledge obtained from the numerical parameter study.

Finally the scaling of film thickness and pressure in the inlet and outlet region has been studied in relation to the known scaling for isoviscous elastic contacts in [124] from which self similar solutions are known. The experimentally obtained film profiles results provide excellent validation for this scaling and self similarity. It is shown that the isoviscous elastic scaling to a first approximation also holds quite well for the viscoelastic solid case for small values of the Deborah number mapping the film thickness and pressure solutions for different speeds on single curves. However, with increasing viscoelastic effects the outlet size reduction and the occurrence of the inlet local pressure maximum cause the scaling for the pressure in the inlet and for the film thickness in the outlet to be less accurate, whereas the film thickness in the inlet, and the pressure in the outlet are on the other hand still scaled quite well.

4.6 Appendixes to Chapter 4

A Relations between Dimensionless Parameters for EHL Point Contact

For convenience of the reader, some sets of commonly used dimensionless parameters and their relations are given in this section. This overview is restricted to the case of a circular contact.

Hamrock-Dowson

The dimensionless parameters for circular contact as defined by Hamrock and Dowson [56, 57] are:

$$H^{dh} = \frac{h}{R_0} \quad (\text{A.1})$$

$$W^{dh} = \frac{W_0}{E'R_0^2} \quad (\text{A.2})$$

$$G = \alpha E' \quad (\text{A.3})$$

$$U = \left(\frac{\eta_0 v_m}{E'R_0} \right) \quad (\text{A.4})$$

where v_m is the entrainment speed or average speed of the surfaces, $v_m = v_s/2$.

Moes Parameters

The Blok-Moes [99] parameters for a circular contact are:

$$H^M = \frac{h}{R_0} \left(\frac{E'R_0}{\eta_0 v_s} \right)^{1/2} = H^{dh} (2U)^{-1/2} \quad (\text{A.5})$$

$$M = \frac{W_0}{E'R_0^2} \left(\frac{E'R_0}{\eta_0 v_s} \right)^{3/4} = W^{dh} (2U)^{-3/4} \quad (\text{A.6})$$

$$L = \alpha E' \left(\frac{E'R_0}{\eta_0 v_s} \right)^{-1/4} = G (2U)^{-1/4} \quad (\text{A.7})$$

Hertzian Contact Scaling Based Parameters

Circular contact

$$H = \frac{hR_0}{a_0^2} \quad (\text{A.8})$$

$$\lambda = 6 \frac{\eta_0 v_s R_0^2}{a_0^3 p_H} = \left(\frac{128\pi^3}{3M^4} \right)^{1/3} \quad (\text{A.9})$$

$$\bar{\alpha} = \alpha p_h = \frac{L}{\pi} \left(\frac{3M}{2} \right)^{1/3} \quad (\text{A.10})$$

$$H^M = H \sqrt{\frac{6\pi}{\lambda}} \quad (\text{A.11})$$

Greenwood, Hooke

Dimensionless parameters used by e.g. Greenwood [50] and Hooke [65, 69] are

$$P = \alpha p_H \quad (\text{A.12})$$

$$S = \alpha E' \left(\frac{\eta_0 v_m}{E' R_0} \right)^{1/4} \quad (\text{A.13})$$

Obviously

$$P = \bar{\alpha} \quad (\text{A.14})$$

and

$$S = 2^{-1/4} L \quad (\text{A.15})$$

B Discrete Equations

The governing equations shown in Sec.4.2.2 are discretized on a uniform grid using finite differences. The indices i, j are used to indicate the x and y direction respectively. The mesh size for each dimension is h_x, h_y , with $h_x = h_y$. The discrete Reynolds equation with a second order accuracy for the point (i, j) of the grid can be expressed in the following way:

$$\begin{aligned} & \frac{\xi_{i-1/2,j} P_{i-1,j} - (\xi_{i-1/2,j} + \xi_{i+1/2,j}) P_{i,j} + \xi_{i+1/2,j} P_{i+1,j}}{h_x^2} + \\ & \frac{\xi_{i,j-1/2} P_{i,j-1} - (\xi_{i,j-1/2} + \xi_{i,j+1/2}) P_{i,j} + \xi_{i,j+1/2} P_{i,j+1}}{h_y^2} - \\ & (\bar{\rho}H)_x = 0 \end{aligned} \quad (\text{B.1})$$

where $P_{i,j} = 0$ for the points on the boundary, and the cavitation condition $P_{i,j} \geq 0$. The coefficients $\xi_{i\pm 1/2,j}$ and $\xi_{i,j\pm 1/2}$ are defined by:

$$\begin{aligned} \xi_{i\pm 1/2,j} &= (\xi_{i,j} + \xi_{i\pm 1,j})/2 \\ \xi_{i,j\pm 1/2} &= (\xi_{i,j} + \xi_{i,j\pm 1})/2 \end{aligned} \quad (\text{B.2})$$

with:

$$\xi_{i,j} = \frac{\bar{\rho}(P_{i,j}) H_{i,j}^3}{\bar{\eta}(P_{i,j}) \lambda} \quad (\text{B.3})$$

$(\bar{\rho}H)_x$ in Eq.(B.1) represents the discrete ‘wedge’ term. For all points $i \geq 2$, a second order upstream discretization is given by:

$$(\bar{\rho}H)_x = \frac{1.5\bar{\rho}_{i,j} H_{i,j} - 2\bar{\rho}_{i-1,j} H_{i-1,j} + 0.5\bar{\rho}_{i-2,j} H_{i-2,j}}{h_x} \quad (\text{B.4})$$

At the first line near the boundary ($i = 1$) it can be replaced by a first order discretization:

$$(\bar{\rho}H)_x = \frac{\bar{\rho}_{i,j} H_{i,j} - \bar{\rho}_{i-1,j} H_{i-1,j}}{h_x} \quad (\text{B.5})$$

The discrete form of the film thickness equation, Eq.(4.12), reads:

$$H_{i,j} = H_0 + \frac{X_i^2}{2} + \frac{Y_j^2}{2} + U_{i,j} \quad (\text{B.6})$$

where $U_{i,j}$ is the viscoelastic deformation which can be obtained with Eq.(4.22), once the elastic deformation is known. The discrete form of the elastic deformation equation, Eq.(4.15), reads:

$$U_{e(i,j)} = \sum_{i'} \sum_{j'} K_{i,i',j,j'} P_{i',j'} \quad (\text{B.7})$$

where, for a second order discretization based on an approximation of the pressure by a piecewise constant function on a square $h_x \times h_y$ around at $X_{i'}, Y_{j'}$ the coefficients $K_{i,i',j,j'}$ are given by:

$$K_{i,i',j,j'} = \frac{2}{\pi^2} \int_{Y_j-h/2}^{Y_j+h/2} \int_{X_i-h/2}^{X_i+h/2} \frac{dX' dY'}{\sqrt{(X_i - X')^2 + (Y_j - Y')^2}} \quad (\text{B.8})$$

and can be calculated analytically:

$$\begin{aligned} K_{i,i',j,j'} = \frac{2}{\pi^2} \{ & |X_p| \operatorname{arcsinh} \left(\frac{Y_p}{X_p} \right) + |Y_p| \operatorname{arcsinh} \left(\frac{X_p}{Y_p} \right) \\ & - |X_m| \operatorname{arcsinh} \left(\frac{Y_p}{X_m} \right) - |Y_p| \operatorname{arcsinh} \left(\frac{X_m}{Y_p} \right) \\ & - |X_p| \operatorname{arcsinh} \left(\frac{Y_m}{X_p} \right) - |Y_m| \operatorname{arcsinh} \left(\frac{X_p}{Y_m} \right) \\ & \left. + |X_m| \operatorname{arcsinh} \left(\frac{Y_m}{X_m} \right) + |Y_m| \operatorname{arcsinh} \left(\frac{X_m}{Y_m} \right) \right\} \quad (\text{B.9}) \end{aligned}$$

with:

$$\begin{aligned} X_p &= X_i - X_{i'} + h/2 \\ X_m &= X_i - X_{i'} - h/2 \\ Y_p &= Y_j - Y_{j'} + h/2 \\ Y_m &= Y_j - Y_{j'} - h/2 \end{aligned} \quad (\text{B.10})$$

Notice that on a uniform grid the coefficients $K_{i,i',j,j'}$ are a function of $|i - i'|$ and $|j - j'|$ only.

Finally, the force balance equation, Eq.(4.16), can be discretized as:

$$h_x h_y \sum_i \sum_j P_{i,j} = \frac{2\pi}{3} \quad (\text{B.11})$$

C VEHL Model Validation

In a numerical simulation, it is crucial to have grid-independent results. For the developed VEHL model, spatial grid convergence tests, including the preliminary confirmation of the size of the domain, the mesh size tests and the computational domain tests, have been done firstly. And then the numerical results of the EHL film thickness and pressure distribution are compared with the results in [112]. In this section, the same group of VEHL working parameters at pure-sliding as those in [112] has been used. They are: a normal load of $W_0 = 34\text{N}$, a rigid sphere radius of $R_0 = 20\text{mm}$, velocities of $v_2 = 0.42\text{m/s}$ and $v_1 = 0$ respectively, a modulus $E_\infty = 10^8\text{Pa}$, a ratio of $E_\infty/E_0 = 100$ in the SLS model with a single relaxation time $\tau = 0.01\text{s}$, and an isoviscous lubricant with $\eta_0 = 1\text{Pa}\cdot\text{s}$. The centreline pressure and film thickness distributions are used in the grid convergence tests and in the validation.

Table C.1: Influence of computational domain in the X direction on the calculated value of the central pressure, the maximum pressure, the central film thickness and the minimum film thickness. 5 levels of grids with 513 grid points in each direction on the finest level of grid.

Computational domain in X direction	P_{cen}	P_{max}	H_{cen}	H_{min}
(-1.5, 1.5)	0.939	2.23	6.81×10^{-3}	6.53×10^{-3}
(-2.5, 1.5)	0.929	2.10	7.24×10^{-3}	6.96×10^{-3}
(-4.5, 1.5)	0.928	2.10	7.28×10^{-3}	6.99×10^{-3}
(-6.5, 1.5)	0.927	2.09	7.26×10^{-3}	7.00×10^{-3}

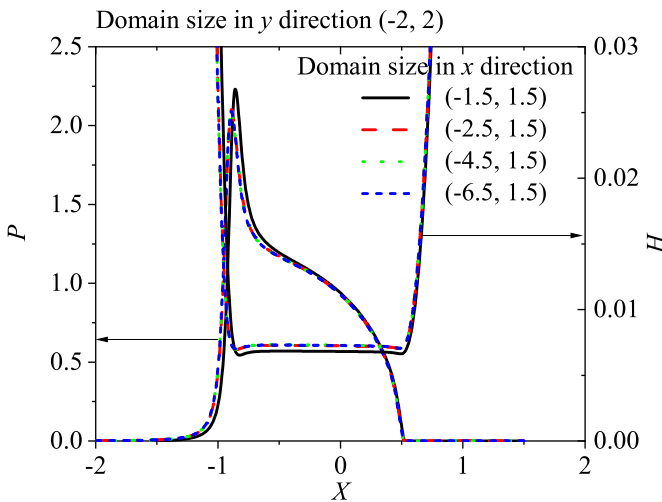


Figure C.1: Preliminary confirmation of the computational domain based on the centreline pressure and film thickness distribution. The left side is rolling entrance.

Fig.C.1 shows the preliminary confirmation of the domain size with 5 levels of grids and $513 * 513$ points on the finest level of grid. TableC.1 compares the calculated values of the central pressure, the maximum pressure, the central film thickness and the minimum film thickness for each case. The variation of the computational domain is mainly in the entrainment direction, while the domain in the Y direction is fixed at $(-2, 2)$. The results indicate that a domain size of $(-2.5, 1.5)$ in the X direction is sufficient. Therefore, the computational domain of $(-2.5, 1.5)$ in the X direction and $(-2, 2)$ in the Y direction has been used for the mesh size and domain size tests in the following part.

For mesh size tests, $257 * 257$, $513 * 513$ and $1025 * 1025$ grid points have been used on the finest level of grid (level 5). Through the results of P_{cen} , P_{max} , H_{cen} and H_{min} listed in TableC.2, it shows that the number of grid points of $513 * 513$ is sufficient for 5 levels of grids.

Table C.2: The influence of the mesh size on the central pressure, the maximum pressure, the central film thickness and the minimum film thickness with the same calculation condition for Fig.C.1. 5 levels of grids with the calculation domain $(-2.5, 1.5)$ in X direction and $(-2, 2)$ in Y direction.

Number of grid points	P_{cen}	P_{max}	H_{cen}	H_{min}
257*257	0.936	2.06	7.06×10^{-3}	6.84×10^{-3}
513*513	0.929	2.10	7.24×10^{-3}	6.96×10^{-3}
1025*1025	0.928	2.11	7.23×10^{-3}	6.95×10^{-3}

Finally, the influence of the size of the computational domain on the calculated values of the pressure and film thickness is given in TableC.3. The number of grid points used in each calculation on the finest level are $513 * 513$, $1025 * 1025$ and $2049 * 2049$ respectively on the finest grid to keep the same mesh size. The results show that the computational domain of $-2.5 \leq X \leq 1.5$ and $-2 \leq Y \leq 2$ and 5 levels of grids with $513 * 513$ grid points on the top level are sufficient for the numerical simulation under the operating conditions.

Table C.3: Influence of the size of the computational domain on the centreline pressure and film thickness distributions with the same calculation condition for Fig.C.1.

Computational domain	P_{cen}	P_{max}	H_{cen}	H_{min}
$(-2.5, 1.5) * (-2, 2)$	0.929	2.10	7.24×10^{-3}	6.96×10^{-3}
$(-5.0, 3.0) * (-4, 4)$	0.928	2.09	7.25×10^{-3}	7.01×10^{-3}
$(-10, 6.0) * (-8, 8)$	0.927	2.09	7.25×10^{-3}	7.01×10^{-3}

After the grid convergence tests, the verification of the developed VEHL model is performed by comparing with the numerical results in [112]. Fig.C.2 shows the centreline profiles of the pressure and film thickness distribution for the same calculation conditions listed above. Basically, the results are quite similar. But some deviations can be seen in the inlet region for both the pressure and the film thickness distribution. The deviation for

the pressure distribution is mainly around the inlet pressure peak, which has also been reported in [19]. The reason for this deviation is not clear. It may be caused by the size of the computational domain, see for example the effect of the domain on the pressure distribution in Fig.C.1. A smaller computational domain causes a higher inlet pressure peak and correspondingly a smaller film thickness. Note that the developed VEHL model can go back to a pure elastic EHL model, and the simulation results of the film thickness and pressure distribution are identical to that from a classical EHL solver.

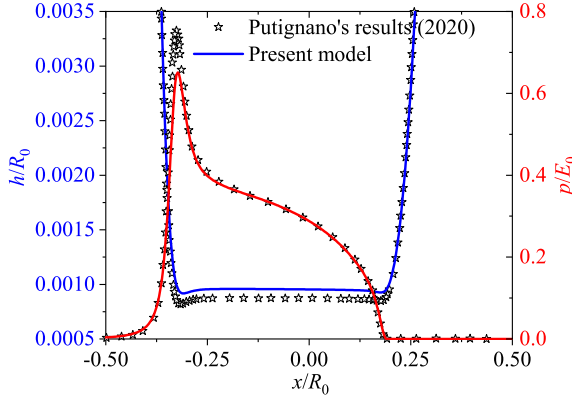


Figure C.2: Pressure and film thickness distributions of the present model and those from Putignano [112] under a pure sliding condition with a velocity of $v_1 = 0.42\text{m/s}$. The operating conditions are $W_0 = 34\text{N}$, $R_0 = 20\text{mm}$, $E_\infty = 10^8\text{Pa}$ and $E_\infty/E_0 = 100$ for the SLS model and an isoviscous lubricant with $\eta_0 = 1\text{Pa}\cdot\text{s}$. The SLS model with a single relaxation time $\tau = 0.01\text{s}$ is used to characterize the viscoelastic behavior. The rigid ball is stationary and the viscoelastic half space is moving to the right hand side.

D Elastic Modulus Determination of PMMA

Following the method used to determine the elastic modulus of the materials in [96], the contact diameter formed in a static contact between a PMMA disc and a steel ball was measured firstly at several loads at a room temperature (23°C). Based on the Hertzian contact theory, the relationship between the contact width and the applied load can be expressed as:

$$a^3 = \frac{3R_0}{2E'}W \quad (\text{D.1})$$

where E' is the reduced modulus of the PMMA-steel combination,

$$\frac{2}{E'} = \frac{1 - \nu_{\text{steel}}^2}{E_{\text{steel}}} + \frac{1 - \nu_{\text{PMMA}}^2}{E_{\text{PMMA}}} \quad (\text{D.2})$$

According to Eq.(D.1), the measured radius in the form of a^3 against W is shown in Fig.D.1. Then, the reduced modulus E' can be obtained from the slope of the plots. Using some known material parameters of $E_{\text{steel}} = 211\text{GPa}$, $\nu_{\text{steel}} = 0.3$ and $\nu_{\text{PMMA}} = 0.39$ [96], the elastic modulus of the PMMA material can be calculated according to Eq.(D.2). It is 5.1GPa here.

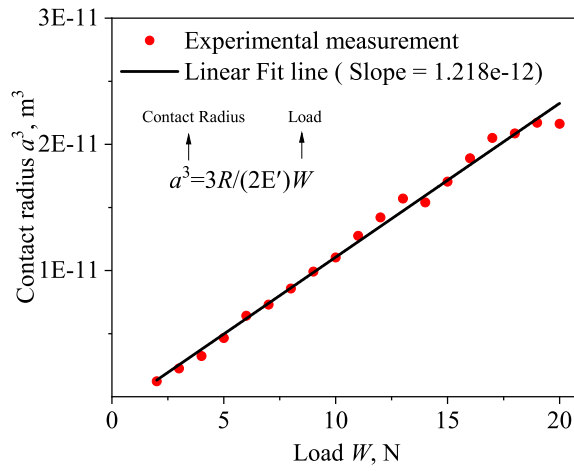


Figure D.1: Contact width varied with applied loads for PMMA disc-steel ball contacts.

With the measured elastic modulus of the PMMA material, the Hertzian dry contact parameters in different contacts at nominal test conditions of $W = 10\text{N}$ are given in Table 4.2.

Chapter 5

Viscoelastic Layer Modeling

In this chapter, the 3D quasi-static layered contact problem is studied for a rigid sphere rolling on a viscoelastic/elastic layered elastic half-space. The standard linear solid (SLS) model with a single relaxation time is used to characterize the viscoelastic properties of the layer. Two types of modeling, i.e. the foundation approach and the Papkovitch-Neuber (PN) approach based on the Navier-Cauchy stress analysis, are used to investigate the effect of a thin viscoelastic layer in rolling contacts. The developed numerical solvers have been validated by comparing with the results in literature for different contact problems, such as (visco-)elastic layered contacts, viscoelastic half-space contacts. Having studied the effect of solid viscoelasticity on dry and lubricated contact in Chapter 3 and 4 as well as developed the numerical methods, to analyze layered contacts now herein to the question if and when (visco)elastic layer model can replace the continuum fluid equation for EHL.

The work in this chapter is planned to be submitted to Tribology International or Friction as: Y. Zhao, H.C. Liu, G.E. Morales-Espejel, C.H. Venner, Behavior of thin elastic/viscoelastic layer on an elastic half-space in rolling contacts: towards a new modeling approach for EHL lubrication.

5.1 Introduction

In the previous two chapters, the effect of solid viscoelasticity on the contacts of homogeneous solids has been studied under both dry and lubricated conditions. The studies are based on the viscoelastic half-space approximation. However, a large variety of systems operate with coatings (e.g. DLC, TiAlN, PTFE), thin films (e.g. grease thickener rich layer [26, 39], anti-wear additives induced tribofilms [29]) and/or material inhomogeneities (e.g. inclusions, anisotropic grains [155]) with the mechanical properties of the close-to-surfaces material being different from the bulk. This is in particular of interest in bio-mechanics, such as soft layered contact problems regarding joint cartilage and human skin. In this chapter, 3D viscoelastic layered contact problems are studied.

In addition to the relevance for soft (layered) contacts in biomechanical applications, viscoelastic layer modeling might also be interesting to the studies of the thin film lubrication in concentrated "hard" contacts. In general lubricated contacts are working under increasingly severe operating conditions by using low viscosity lubricants, reduced lubricant supply, and higher temperatures and/or loads, which all lead to thinner and intermittent films. In these circumstances small scale effects such as local high pressure rheology of lubricants and/or the particular composition/topology of the material may

play an important role for lubricant film formation and surface failure. In particular cases contacts are operating close to, or even in the mixed lubrication regime. In this respect the lubrication modeling ability of the continuum Reynolds based solution is quite limited in terms of intermittent contacts and complex fluid rheology. Inspired by the work of van Emden et al. [35], these lubrication problems may be modeled as layered dry contact problems, i.e. not from the viewpoint of a (continuous) thin fluid film but from the viewpoint of a viscoelastic interface layer forming a local support.

The concept of viscoelastic layer modeling for EHL or even mixed lubrication may be supported by the following physical-rheological features of a thin confined film. First, both pressure-induced bulk glass transition [4, 7] and confinement-induced nano-rheological solidification [70, 116] have been recognized in highly-loaded EHL contacts. The lubricant film behaves as a viscoelastic material with a long relaxation time or a "soft" deformable elastic solid with a yield stress when it is far into the glassy state [7, 103, 105], e.g. with the viscosity in the order of 10^{12} Pa·s for inorganic liquids and about 10^7 Pa·s for organic liquids [7]. In such cases, a pressure gradient may exist across the thin lubricating film [9], which may break the classical lubrication assumption (i.e. a constant pressure across the thin film) and thus limit the application of the Reynolds equation in modeling such problems. Second, in case that the contact pressure is not high enough to induce glass transition, the lubricant in an EHL lubricated contact, owing to the high viscosity, hardly exhibits any pressure driven flow and behaves as a near solid layer passing through the contact. Therefore, viscoelastic layer modeling may provide a new approach to model EHL and/or mixed lubrication by taking account of the complex mechanical-rheological properties of the lubricants. Note that viscoelastic layered (dry) contact problems are relatively easier to solve compared to the classical governing equations of "hard" EHL including (fluid-structure) coupling between the Reynolds equation and the solid deformation equation [141].

Regarding viscoelastic layer modeling, much work has been done in the field of contact mechanics, such as problems of a viscoelastic layer on a rigid substrate [1, 5, 6, 37, 97, 101, 113, 127], on an elastic [12, 14, 35, 45–47, 61, 78, 158] or on a viscoelastic half-space [145, 146], even though the aim of these studies was not to model EHL. Here, some work on the modeling of viscoelastic layered elastic half-space in rolling contacts is introduced. In 1967, Batra and Ling [12], using a Fourier transform method, firstly analyzed the stress-strain state for contact problems of a viscoelastic layer on an elastic half-space under a moving load. Later, Kalker et al. [14, 78] studied the contact of cylinders coated with viscoelastic layers under conditions of dry rolling friction both theoretically and experimentally. They proposed an efficient numerical model with the Airy stress functions for the displacements and stresses, and validated their results in experiments with laser Doppler anemometry. Based on the work of Kalker, Goryacheva et al. [45, 47] performed an analytical analysis of contact problems of a cylinder rolling/sliding on an elastic base coated with a viscoelastic layer. Recently, they extended this two-dimensional (2D) line contact analysis to 3D [46] using the strip method to calculate the contact pressure distribution and the internal stresses. Zhang and He et al. proposed a new semi-analytical model to investigate the response of a viscoelastic layer-elastic substrate system under both dry [158] and lubricated [61] conditions, including the pressure distribution, displacements, viscoelastic dissipation and subsurface stresses.

The published modeling and numerical methods for the study of the viscoelastic layered contacts can be classified into two main categories: (1) calculating the deformation of the viscoelastic layer and the elastic half-space separately [35, 46]; (2) determining the viscoelastic layer deformation by solving the displacement field of the integrated layered system [61, 158]. For the first method, different models of varying accuracy and complexity have been developed, among which the simplest case calculates the layer deformation using the constitutive equation of the viscoelastic layer based on a prescribed pressure distribution of the elastic half-space. For the second method, analogous to the numerical solution of an elastic contact problem [10], Papkovitch-Neuber (PN) potentials have been used to construct the solution in the frequency domain for viscoelastic layered contacts. In this thesis, these two approaches are used. A foundation approach based layer model and a PN potential based model have been developed for thin viscoelastic layered contact problems. The results of the simplified foundation approach will be compared with the physically more sound PN approach in the analysis of the deformation behavior of layered contacts with different mechanical-rheological properties, e.g. a rigid, elastic or viscoelastic layer on top of a rigid, elastic or viscoelastic half-space. The PN model can be reduced to the Green's function based model developed by Carbone and Putignano et al. [113] when the substrate is rigid.

To address the question if the viscoelastic layer modeling can indeed work towards EHL and mixed lubrication, the present study is carried out in the thin layer regime with layer thickness in the order of $a_0 \times O(10^{-3})$ where a_0 is the Hertzian contact width, whereas previous studies mainly focused on contact problems with relatively thick viscoelastic layers, i.e. usually larger than a quarter of the contact width. The main result is in the pressure distribution and the stress and displacement fields. The developed layered contact models in this chapter are verified with the simulation results published in the literature for both viscoelastic and elastic layered rolling contacts, as well as for a viscoelastic half-space in contact. In addition to the contact pressure and the stress distribution, the deformation behavior of the viscoelastic layer and the resulting layer profile are analyzed in a parametric study using the PN approach. Finally, to answer the question if and when a viscoelastic layer exhibits EHL film characteristics, the piezoviscous effect of the viscoelastic layer is studied with the foundation approach for the layer modeling. Strictly, this is outside the scope of the linear viscoelasticity assumption. The simulation results show typical EHL film shapes.

5.2 Viscoelastic Modeling and Formulation

Fig.5.1 schematically shows the layered contact problem of a rigid sphere of radius R_0 rolling on a viscoelastic layered elastic half-space. As mentioned above, it is interesting for soft contacts, e.g. in bio-mechanical engineering and for "hard" EHL contacts in which the viscoelastic layer may be used to represent the thickener rich layer in grease lubrication. The rigid sphere and the layered substrate move at constant surface velocities v_1 and v_2 , respectively, under a constant normal load W_0 . The mean velocity of the two moving bodies is v_m , $v_m = (v_1 + v_2)/2$. The viscoelastic layer has a constant thickness of l_0 and it is assumed to be perfectly bonded to the elastic half-space. The mechanical properties of the elastic half-space are characterized by the elastic modulus E^s and the Poisson ratio

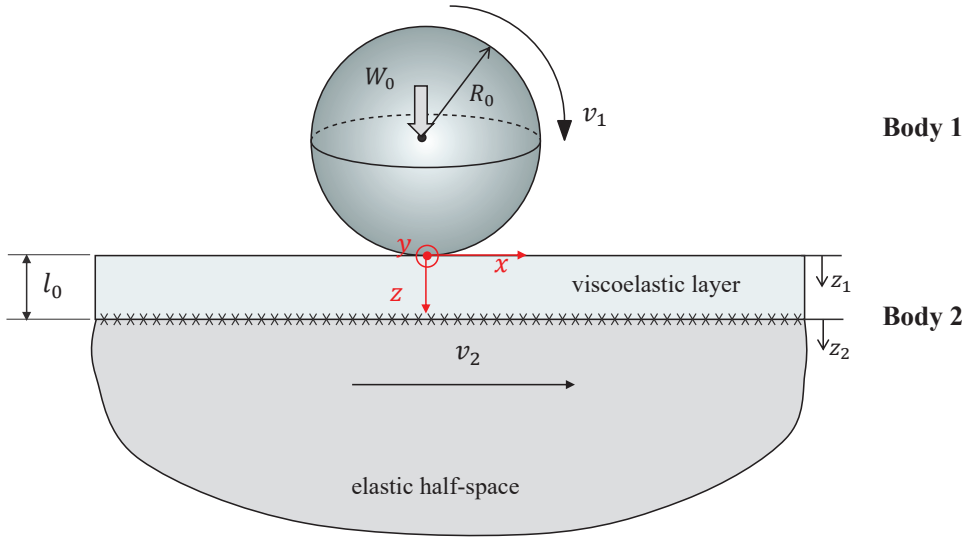


Figure 5.1: Schematic of a rolling contact formed between a rigid sphere of radius R_0 and a layered elastic half-space at an applied constant load W_0 .

v^s . The mechanical-rheological properties of the viscoelastic layer and the mathematical formulations of the contact problem are introduced in the following two sections.

5.2.1 Viscoelastic Rheological Model

A three-element SLS model is used to represent the viscoelastic behavior of the layer. The SLS model in the Kelvin representation with a single relaxation time is shown in Fig.2.10. It is well suited to explore the main features of viscoelasticity [21, 46, 158]. A detailed description was given in Chapter 2. However, some key points are repeated here for completeness.

The constitutive equation relating stress and strain is

$$\sigma + \beta \frac{\partial \sigma}{\partial t} = E_0^c \left[\epsilon + \tau \frac{\partial \epsilon}{\partial t} \right] \quad (5.1)$$

where τ is the constant (single) relaxation time $\tau = \eta_s / E_s$ and $\beta = \tau / (1 + R_e)$ with $R_e = E_f / E_s$. Analogous to the definition of the compliance (the reciprocal of the elastic modulus) in the theory of linear elasticity, the creep compliance function of the SLS model can be derived by solving Eq.(5.1), for a constant stress input, which gives,

$$\varphi_c(t) = \frac{1}{E_0^c} + \left(\frac{1}{E_\infty^c} - \frac{1}{E_0^c} \right) e^{-\frac{t}{\tau}} \quad (5.2)$$

where E_0^c is the effective modulus in the long time limit (e.g. in a steady rolling contact at extremely low speeds): $E_0^c = 1 / (1/E_s + 1/E_f)$. E_∞^c is the elastic response at short times (e.g. in a steady rolling contact at extremely high speeds): $E_\infty^c = E_f$.

The relation between the creep compliance function and the relaxation function of viscoelastic materials in the frequency domain is given in Appendix A: $\hat{\psi}_r(\omega) = [i\omega\hat{\phi}_c(\omega)]^{-1}$. The relaxation modulus function of the SLS model can be obtained by Fourier transform of Eq.(5.2):

$$\hat{\psi}_r(\omega) = 1 / \left[\frac{1}{E_0^c} + \left(\frac{1}{E_\infty^c} - \frac{1}{E_0^c} \right) \frac{i\omega}{1 + i\omega\tau} \right], \quad (5.3)$$

where ω is the frequency, i the imaginary unit, and the hat $\hat{}$ means the Fourier transform with respect to time t .

5.2.2 Modeling Formulation

In the same way as a classical Hertzian (elastic dry) contact problem [141], the viscoelastic layered rolling contact problem in Fig.5.1 can be mathematically modeled by two equations concerning the gap height and the load balance with a complementary condition at the interface $z_1 = 0$.

- The gap height equation:

$$h(x, y, t) = h_0(t) + \frac{(x - v_m t)^2}{2R_0} + \frac{y^2}{2R_0} + u(x, y, t) \quad (5.4)$$

where $h_0(t)$ is an indentation constant determined by force balance, Eq.(5.5).

- The load balance equation:

$$W_0(t) = \iint p(x, y, t) dx dy \quad (5.5)$$

- The complementary condition:

$$\begin{aligned} h(x, y, t) = 0, p(x, y, t) > 0, & \text{ in contact area} \\ h(x, y, t) > 0, p(x, y, t) = 0, & \text{ out contact area} \end{aligned} \quad (5.6)$$

The gap height equation, Eq.(5.4), consists of the undeformed gap shape approximating the surfaces of the contacting elements as parabolas and their normal deformation. The load balance equation, Eq.(5.5), states that, neglecting the contact dynamics, the integral of the pressure should equal the externally applied load at any time. Finally, the actual problem to be solved is stated in Eq.(5.6) by the Hertz-Signorini-Moreau complementary condition, i.e. $ph = 0$ here. This means that when the gap is closed the pressure is positive, and when the gap is open, neglecting adhesion, the pressure is zero (ambient).

The gap height h , the pressure p , and the normal deformation u in Eqs.(5.4)~(5.6) are functions of time t , which allows the present model to solve the dynamic response of the contact problem in a transient manner. The studied pure rolling contact, relative to the contact location, is steady-state (quasi-static) intrinsically. The time-dependent governing equations, Eqs.(5.4)~(5.6), in the inertial coordinate system can be transformed to a reference frame fixed to the contact location. In the reference system, the governing equations for the layered contact problem are the same as those for an elastic dry (Hertzian)

contact problem [141] with the variable x replaced by the transformed speed-dependent variable $x + v_m t$ to account for the motion of the moving bodies relative to the contact location.

Compared to the Hertzian contact of an elastic half-space, the most challenging aspect of solving the viscoelastic layered contact problem is the evaluation of the deformation of the layered half-space. The deformation term $u(x, y, t)$ in Eq.(5.4) includes two portions: the deformation of the viscoelastic layer and the elastic half-space. In literature, two approaches have been used to evaluate the deformation of a viscoelastic layered half-space. The first is the foundation approach and the second the Papkovitch-Neuber (PN) approach. Since the modifications of the contact problem equations are mainly related to the deformation calculation of the layered substrate by one of these methods, the following description focuses only on this aspect.

5.3 Foundation Approach

5

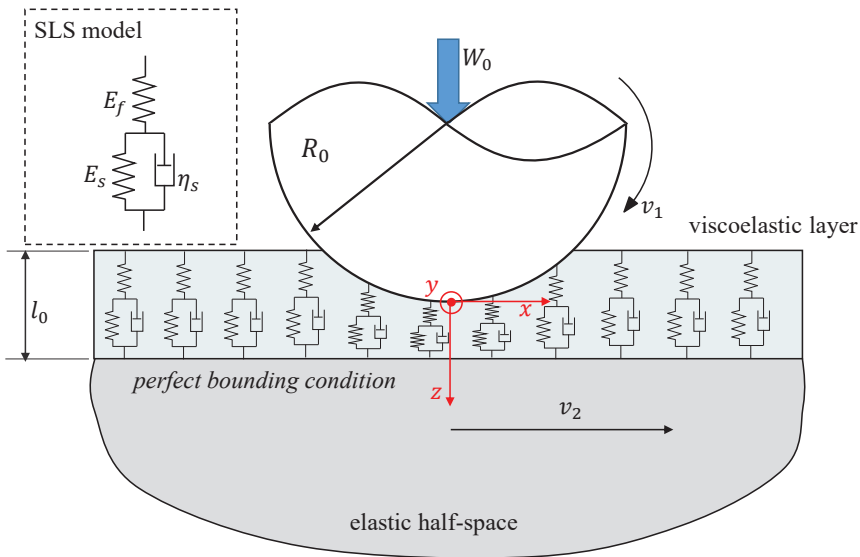


Figure 5.2: Schematic representation of using foundation approach to model the deformation of the viscoelastic layer for the layered contact problem shown in Fig.5.1.

In the foundation approach, the deformations of the layer and the substrate are calculated separately. The contact stresses/pressures at the interfaces of the layer-substrate and of the ball-layer are assumed to be the same (thin layer approximation, which is the equivalent of the lubrication assumption in fluid mechanics).

The viscoelastic layer is represented by a discrete set of columns in the SLS representations with a constant initial thickness l_0 . Upon loading see Fig.5.2, the displacement of each SLS column is assumed to be limited to the vertical direction (oedometric layer assumption),

satisfying the constitutive equation of the SLS model, Eq.(5.1). This means that at a local spot/element the deformation at neighboring locations (local support) is neglected. The deformation of the elastic substrate is calculated using the Boussinesq equation Eq.(5.9) based on the half-space assumption. The total deformation $u(x, y, t)$ is obtained by adding the deformation of the viscoelastic layer u^c and of the elastic half-space u^s .

5.3.1 Deformation Equation

The viscoelastic layer deformation u^c is obtained by replacing ϵ and σ in the SLS constitutive equation Eq.(5.1) by u^c/l_0 and p , giving:

$$p(x, y, t) + \beta \frac{\partial p(x, y, t)}{\partial t} = \frac{E_0^c}{l_0} [u^c(x, y, t) + \tau \frac{\partial u^c(x, y, t)}{\partial t}]. \quad (5.7)$$

For a pure rolling contact in steady-state, Eq.(5.7) can be represented in the time-independent form by replacing x with $x + v_m t$. Afterwards, with the same notation, it is simplified to

$$p(x, y) + v_m \beta \frac{\partial p(x, y)}{\partial x} = \frac{E_0^c}{l_0} [u^c(x, y) + v_m \tau \frac{\partial u^c(x, y)}{\partial x}] \quad (5.8)$$

It should be noted that Eq.(5.7) in the limit of long time and Eq.(5.8) give the same steady solution for the contact problem. Eq.(5.7) evolves in time to the steady-state problem by showing the deformation process of the layer. It was used by van Emden et al. [35]. Eq.(5.8) directly describes the steady-state solution in space and has the advantage of saving computational time of marching in time. It will be used in the current study.

The pressures at the top surface of the layer $z_1 = 0$ and the normal stresses at the interface of the viscoelastic layer and the elastic half-space $z_1 = l_0$ are assumed to be equal in steady state in the foundation approach [35, 46]. Hence, the deformation of the elastic substrate is

$$u^s(x, y) = \frac{1 - (v^s)^2}{\pi E^s} \iint \frac{p(x', y')}{\sqrt{(x - x')^2 + (y - y')^2}} dx' dy' \quad (5.9)$$

The total deformation $u(x, y)$ is the sum of the two contributions

$$u(x, y) = u^s(x, y) + u^c(x, y) \quad (5.10)$$

With the foundation approach, the layer thickness after deformation can be obtained by

$$l(x, y) = l_0 - u^c(x, y) \quad (5.11)$$

5.3.2 Numerical Methods

To achieve a numerical solution of the viscoelastic layered contact problem given in Sec.5.2 based on the foundation approach, the governing equations Eqs.(5.4)~(5.6) with Eqs.(5.8)~(5.10), must be solved. Compared to the solution of the classical Hertzian dry contact problem in [141], an additional procedure is needed to calculate the deformation of the viscoelastic layer.

Taking the multigrid/multilevel elastic numerical method published in [141] as a starting point, the equations can be non-dimensionalized with the dimensionless variables:

$$\begin{aligned} X &= x/a_0, & Y &= y/a_0, & P &= p/p_H, & U &= u/\delta, & \bar{l}_0 &= l_0/\delta, & \delta &= a_0^2/R_0 \\ a_0 &= \sqrt[3]{\frac{3W_0R_0(1-(\nu^s)^2)}{4E^s}}, & p_H &= \frac{3W_0}{2\pi a_0^2}, & \bar{E}_0 &= E_0/p_H \end{aligned} \quad (5.12)$$

where a_0 and p_H are the Hertzian contact parameters of the elastic half-space with modulus E^s . The dimensionless form of Eq.(5.8) is expressed as

$$P(X,Y) + \frac{De}{1+Re} \frac{\partial P(X,Y)}{\partial X} = \frac{\bar{E}_0^c}{\bar{l}_0} [U^c(X,Y) + De \frac{\partial U^c(X,Y)}{\partial X}] \quad (5.13)$$

where $De = v_m \tau / a_0$ a dimensionless rolling velocity as well the ratio of the relaxation time to the passage time of surface point through the Hertzian contact zone, referred as the Deborah number in viscoelasticity. For the dimensionless form of the other governing equations, see [141].

Accounting for the additional complexity of the viscoelastic deformation equation, a second order finite difference method is used on a uniform grid for the spatial discretization of the equations. For the numerical solution of the equations, Eqs.(5.4)~(5.6), a distributive relaxation process was developed as used for the elastic dry contact problem, see Chapter 3. Coarser grids were used in a multigrid cycle to accelerate convergence to a grid independent rate [141]. The force balance equation is treated as a global constraint that is relaxed by adjusting the value of the mutual separation h_0 in this cycle. For the fast evaluation of the spatial integral transforms in Eq.(5.9), the MLMI method is used [141]. With the full Multigrid algorithm the equations are solved to an error smaller than the discretization error.

In this process, the calculation of the layer deformation is only performed on the finest grid level. In the foundation approach, neighboring points are not linked at all. In a MG cycle, this leads to an instability (nonphysical behavior) of high frequency components. This can be solved by requiring a smoothness on the scale of the coarse grid. The mean pressure values of four surrounding grid points are used to calculate the local deformation of the layer. u^c is then obtained in the intermediate grid points by solving Eq.(5.8) numerically with the mean pressure values.

In the MG calculation, five grid levels with $513 * 513$ equidistant grid points on the finest level are used. The computational domain is set to $(-8a_0, 4a_0)$ in the x direction to consider the delayed viscoelastic layer deformation at the outlet, while in the y direction the range of $(-4a_0, 4a_0)$ is large enough.

5.4 Papkovitch-Neuber (PN) Approach

The proposed PN approach does not rely on the assumptions in the foundation approach, i.e. the thin layer assumption and the oedometric layer assumption. A local element deformation in the layer is influenced by the entire pressure distribution rather than only

having a local support. This leads to a general and precise solution to the studied problem. The PN approach can also be solved based on the solution for elastic layered problems. In the following, the elastic solver is introduced at first followed by an illustration of application of the correspondence principle to the elastic solution to achieve the viscoelastic formulation.

5.4.1 3D Elastic Half-Space and Elastic Layered Solution

To obtain a 3D solution of the stress and displacement fields of an elastic contact problem, the Navier equation of elasticity [10] should be solved with the governing equations and the complementary boundary conditions. Without considering the acceleration and body forces, the Navier equation reads

$$(\lambda + \mu)\nabla(\nabla \cdot \mathbf{u}) + \mu\nabla^2 \mathbf{u} = 0 \quad (5.14)$$

where $\mu = \frac{E}{2(1+\nu)}$ and $\lambda = \frac{E\nu}{(1+\nu)(1-2\nu)}$ are the Lamé constants with E and ν the elastic modulus and the Poisson ratio of the material. Whereby variations of λ and μ in the half-space domain, the heterogeneous e.g. layered material could be modeled [155].

To reduce the complexity of the computation when solving Eq.(5.14) in a 3D domain, potential functions are often used to represent the displacement. Define the displacement function \mathbf{u} in Eq.(5.14) as [10]

$$2\mu\mathbf{u} = -4(1-\nu)\boldsymbol{\psi} + \nabla(\mathbf{r} \cdot \boldsymbol{\psi} + \phi) \quad (5.15)$$

where ϕ and ψ_k ($k = 1, 2, 3$) are the Papkovitch-Neuber elastic potentials with $\boldsymbol{\psi} = (\psi_1, \psi_2, \psi_3)$ and $\mathbf{r} = r(x, y, z)$. From substituting Eq.(5.15) in strain-displacement relations

$$\epsilon_{ij} = \frac{1}{2} \left(\frac{\partial u_i}{\partial x_j} + \frac{\partial u_j}{\partial x_i} \right), \quad (5.16)$$

and the result in generalized Hooke's law:

$$\sigma_{ij} = \lambda \delta_{ij} \epsilon_{kk} + 2\mu \epsilon_{ij}, \quad (5.17)$$

the displacements and stresses for both the elastic layer and the elastic substrate are obtained as:

$$\begin{aligned} u_i^k &= \frac{1}{2\mu^k} \left[\phi_{,i}^k + x\psi_{1,i}^k + z\psi_{3,i}^k - (3-4\nu^k)\psi_i^k \right], \\ \sigma_{ij}^k &= \phi_{,ij}^k - 2\nu^k(\psi_{1,1}^k + \psi_{3,3}^k)\delta_{ij} - (1-2\nu^k)(\psi_{i,j}^k + \psi_{j,i}^k) + x\psi_{1,ij}^k + z\psi_{3,ij}^k. \end{aligned} \quad (5.18)$$

where the indices i and j have values of 1, 2, and 3 which correspond to x , y , and z , respectively. δ_{ij} is the Kronecker delta. The superscript $k = c$ or $k = s$ indicates the coating or the substrate. The comma "," in Eq.(5.18) indicates the differentiation with respect to the coordinate with the index following. The stresses and displacements, σ_{ij}^c and u_i^c , in the layer are taken as functions of (x, y, z_1) , while in the half-space they are functions of (x, y, z_2) , as shown in Fig.5.1.

For the present layered contact problem given in Fig.5.1, regardless of elastic or viscoelastic layer, the boundary conditions can be divided into two categories:

- On the top surface of the layer $z_1 = 0$, the pressure and shear stresses for frictionless rolling/sliding contacts are prescribed as following:

$$\begin{aligned}\sigma_{33}^c(x, y, 0) &= -p(x, y) \\ \sigma_{31}^c(x, y, 0) &= 0 \\ \sigma_{32}^c(x, y, 0) &= 0\end{aligned}\quad (5.19)$$

- Assuming perfect bonding, at the interface between the layer and the substrate $z_1 = l_0$, continuity of the tangential stresses and displacements is required:

$$\begin{aligned}u_1^s(x, y, 0) &= u_1^c(x, y, l_0) \\ u_2^s(x, y, 0) &= u_2^c(x, y, l_0) \\ u_3^s(x, y, 0) &= u_3^c(x, y, l_0) \\ \sigma_{31}^s(x, y, 0) &= \sigma_{31}^c(x, y, l_0) \\ \sigma_{32}^s(x, y, 0) &= \sigma_{32}^c(x, y, l_0) \\ \sigma_{33}^s(x, y, 0) &= \sigma_{33}^c(x, y, l_0)\end{aligned}\quad (5.20)$$

5

Now this completes the governing equations and boundary conditions for the 3D elastic layered contact problem. Various numerical methods exist to solve these 3D equations, e.g. Multigrid (MG) methods [153], Fast Fourier Transform (FFT) methods [149, 150] and Finite Element Methods (FEM) [144], each with their own merits. In this work, the FFT method has been used, because in the Fourier transform domain the viscoelastic equations are equivalent to the elastic equations for contact problems according to the elastic-viscoelastic correspondence principle [3, 158]. The deformation and stress equations in the frequency domain are as follows.

Fourier transform of the Papkovitch-Neuber potentials ϕ and ψ_k ($k = 1, 2, 3$) with respect to x and y gives:

$$\begin{aligned}\tilde{\phi}^k &= A^k e^{-\alpha z_k} + \bar{A}^k e^{\alpha z_k} \\ \tilde{\psi}_1^k &= B^k e^{-\alpha z_k} + \bar{B}^k e^{\alpha z_k} \\ \tilde{\psi}_3^k &= C^k e^{-\alpha z_k} + \bar{C}^k e^{\alpha z_k}\end{aligned}\quad (5.21)$$

where the symbol \approx indicates double Fourier transform in x and y , and $\alpha = \sqrt{m^2 + n^2}$ with m and n the Fourier transform variables corresponding to x and y , respectively. Note that ψ_2 vanishes when body forces are ignored [93]. Based on the linear elasticity assumption, the deformation and stress components in Eq.(5.18) can be represented in the Fourier domain as

$$\begin{aligned}\tilde{u}_i^k &= \frac{1}{2\mu^k} \left[\tilde{\psi}_{,i}^k + FT_{xy}(x\psi_{1,i}^k) + z\tilde{\psi}_{3,i}^k - (3 - 4\nu^k) \tilde{\psi}_i^k \right] \\ \tilde{\sigma}_{ij}^k &= \tilde{\phi}_{,ij}^k - 2\nu^k (\tilde{\psi}_{1,1}^k + \tilde{\psi}_{3,3}^k) \delta_{ij} - (1 - 2\nu^k) (\tilde{\psi}_{i,j}^k + \psi_{j,i}^k) + FT_{xy}(x\psi_{1,ij}^k) + z\tilde{\psi}_{3,ij}^k\end{aligned}\quad (5.22)$$

where FT_{xy} indicates the double Fourier transform with respect to x and y . The detailed expression of Eq.(5.22) of all displacement and stress components are given in Appendix B.

Eq.(5.21) shows that 12 unknown coefficients $A^k, B^k, C^k, \bar{A}^k, \bar{B}^k$ and \bar{C}^k with $k = c$ or $k = s$ need to be determined in order to solve the problem. The condition that the displacements and stresses should vanish at infinity in z direction of the substrate leads to $\bar{A}^s = \bar{B}^s = \bar{C}^s = 0$. The other nine unknown coefficients can be solved from the nine boundary conditions, as given in Eqs.(5.19) and (5.20). The detailed expressions are given in Appendix B.

5.4.2 Correspondence Principle and Viscoelastic Layered Solution

Green's functions are the solution of the potential response of the studied system when subjected to a unit force. It is also referred as influence coefficient and has been widely used to calculate the deformation of an elastic half-space also in this thesis in the previous chapters. According to the elastic-viscoelastic correspondence principle, the Green's function for a viscoelastic half-space can be obtained from the corresponding elastic one. The analysis and derivation process is given in Appendix C for point contact problems. The main points for homogeneous half-space are summarized as:

- (1) In the spatial domain: the time-dependent viscoelastic Green's function can be derived from the elastic Green's function by replacing the compliance, $1/E$, with the compliance function of the viscoelastic model, $\varphi_c(t)$.
- (2) In the Fourier domain: the steady-state viscoelastic Green's function can be directly obtained from the transformed elastic Green's function by replacing the elastic modulus E with the relaxation function $\psi_r(w = mv_m)$.

For describing the deformation of elastic layered contact problems no Green's function is available in the spatial domain, while it exists in the frequency domain. Wang et al. [149, 150] proposed that the stress and displacement components given by Eq.(5.22) can be regarded as the transform of the Green's functions referred as the Frequency Response Functions (FRFs) obtained from a Dirac delta function as pressure excitation in Eq.(5.19). Hence, the transformed viscoelastic Green's functions or FRFs in steady-state can be obtained by replacing the elastic modulus $\frac{1}{2\mu^k}$ in Eq.(5.22) with the relaxation function of the viscoelastic model $\hat{\psi}_r^k(w = mv_m)$. For the present layered contact under frictionless rolling conditions, the FRF of normal displacement of the viscoelastic layer can be derived from Eq.(B.3)

$$\begin{aligned} \tilde{u}_3^c(m, n, mv_m) = & \hat{\psi}_r^c(mv_m) \left\{ -\alpha(A^c e^{-\alpha z^c} - \bar{A}^c e^{\alpha z^c}) \right. \\ & \left. -(3 - 4\nu^c)(C^c e^{-\alpha z^c} + \bar{C}^c e^{\alpha z^c}) - \alpha z^c(C^c e^{-\alpha z^c} - \bar{C}^c e^{\alpha z^c}) \right\} \end{aligned} \quad (5.23)$$

The obtained transformed elastic/viscoelastic Green's functions (FRFs) are used to calculate the continuous Fourier transform Influence Coefficients (ICs), \tilde{C}_{sub}^{sup} with the subscript representing the excitation, and the superscript indicating the response. For example, the influence coefficient linking the pressure excitation p and the normal displacement u_3^c of the viscoelastic layer is

$$\tilde{C}_p^{u_3^c}(m, n, mv_m) = \tilde{u}_3^c(m, n, mv_m) \tilde{Y}(m, n) \quad (5.24)$$

where \tilde{u}_3^c is the viscoelastic FRF given by Eq.(5.23) and \tilde{Y} is the Fourier transformed shape function [149]. A discrete convolution and fast Fourier transform (DC-FFT) algorithm

can be used to translate the continuous \tilde{C} to the discrete forms \hat{C} to account for arbitrary pressure shape at the top boundary in Eq.(5.19). For the procedure of this translation from \tilde{C} to \hat{C} and the shape function, see [149, 150].

By applying the Inverse Fast Fourier Transform (IFFT), the steady-state response of the normal displacement is obtained

$$u_3^c(x, y) = IFFT \left[\hat{C}_p^{u_3^c}(m, n, mv_m) \cdot \hat{p}(m, n) \right] \quad (5.25)$$

By substituting $u_3^c(x, y)$ in the gap height equation Eq.(5.4), the problem can be fully solved by coupling the stresses and displacements with the governing equations. Correspondingly, in a steady-state regime, the layer thickness after deformation is

$$l(x, y) = l_0 + u_3^s(x, y) - u_3^c(x, y) \quad (5.26)$$

5

In the literature, the 3D contact problem of an elastic layer perfectly bonded to an elastic substrate has first been solved by O'Sullivan and King [104] with the FFT methods in 1988. Based on this work, Wang et al. [149, 150] extended the solution to imperfectly bonded interfaces between the elastic layer and the substrate, e.g. dislocation-like and force-like interface discontinuities. More recently, Zhang et al. [158] extended the elastic layered model to a viscoelastic one.

In the present study, the models proposed in [149, 150] are taken as references to investigate the thin viscoelastic layer behavior in rolling contacts. A schematic overview of the different steps in the solution of the problem is given in Fig.5.3. The main difference lies in the layer deformation calculation, in which the modulus of the elastic layer needs to be replaced by the relaxation function of the viscoelastic layer. Taking the Hertzian contact radius a_0 and the maximum pressure p_H given in Eq.(5.12) as the dimensionless parameters, the dimensionless form of the steady-state relaxation function in the frequency domain can be obtained from Eq.(5.3) by setting $\omega = mv_m$, resulting in:

$$\tilde{\psi}_r(\bar{m}v_m) = 1 / \left[\frac{1}{\bar{E}_\infty^c} + \left(\frac{1}{\bar{E}_0^c} - \frac{1}{\bar{E}_\infty^c} \right) \frac{1}{1 + i\bar{m}De} \right] \quad (5.27)$$

where the symbol $-$ represents the dimensionless form, $De = v_m\tau/a_0$ and \bar{m} is the dimensionless frequency variable corresponding to the variable $X(= x/a_0)$ in the spatial domain.

The pressure distribution is solved with a computational domain of $(-8a_0, 4a_0)$ and $(-4a_0, 4a_0)$ with 513×513 grid points in the x and y direction, respectively. A relevant convergence criteria is used regarding the calculated pressures,

$$ERR_p = \sum \sum \left| P_{i,j}^{new} - P_{i,j}^{old} \right| / \sum \sum \left| P_{i,j}^{new} \right| \leq 10^{-6} \quad (5.28)$$

In the subsequent stress calculations, there are 80 equidistant grid points in the layer in z direction. The flow chart for the PN based calculation is given in Fig.5.3.

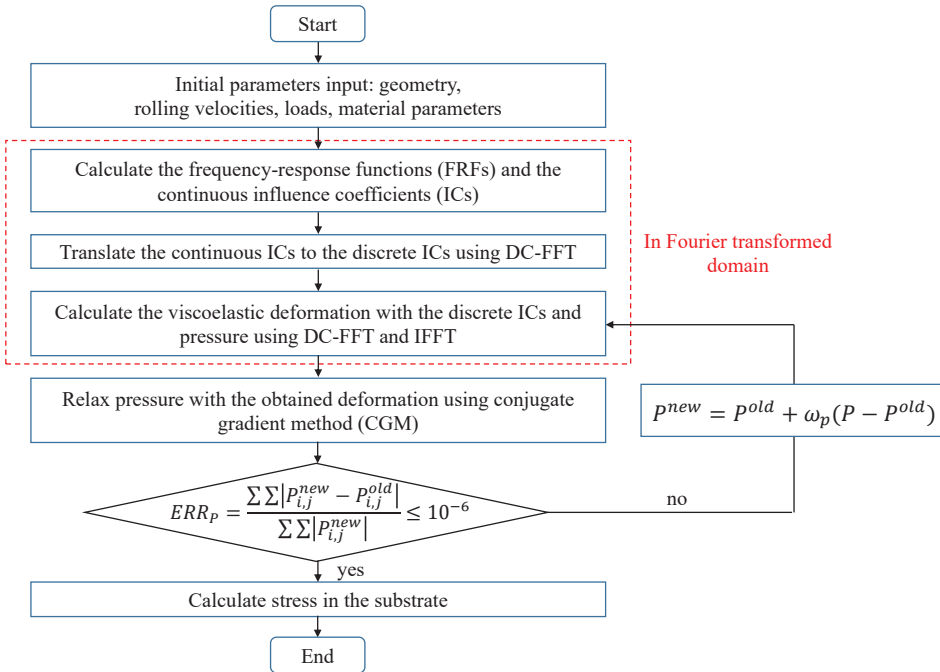


Figure 5.3: Flow chart of the PN approach based viscoelastic layered model. The DC-FFT algorithm is used for the surface deformation and material stress calculations.

5.5 Model Verification

The verification of the two approaches for viscoelastic layered contact problems, i.e. the foundation approach and the PN approach, is presented in this section. The PN approach is validated with three types of contact problems using reduced versions of the model. The first is the elastic layer-elastic substrate system, the second the viscoelastic half-space (no layer), and the third the viscoelastic layer-elastic substrate system. Subsequently, the calculated layer thickness results obtained with the foundation approach are compared with the PN results.

5.5.1 Elastic Layer-Elastic Substrate System

The pressure profiles in an elastic layer elastic half-space contact are compared with the results published in [104]. The developed viscoelastic layer model can easily be degenerated to the elastic case with a layer modulus of E_0^c by setting $E_\infty^c = E_0^c$ in the creep compliance function of the SLS model, Eq.(5.2). The same parameters as in [104] have been used: an elastic layer with thickness of $l_0 = a_0$ where a_0 is the Hertzian contact radius calculated with the properties of the elastic substrate as given in Eq.(5.12). A Poisson ratio of $\nu^c = \nu^s = 0.3$ is assumed, and varying ratios of E_0^c/E^s are considered by using different values of E_0^c at a fixed E^s as input. The pressure distribution along the central line in the x direction is

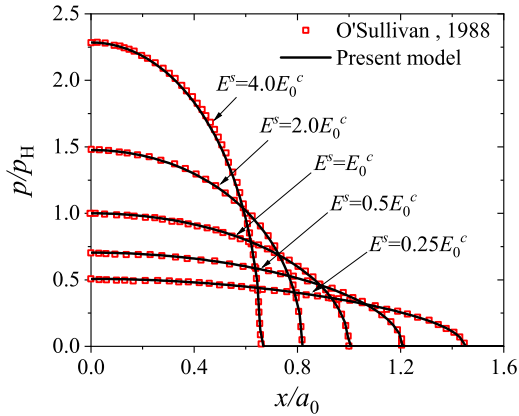


Figure 5.4: Comparison of the normalized pressure profiles with the data in [104] for the contact between a rigid sphere and an elastic layered half-space with layer thickness of a_0 . a_0 and p_H are Hertzian solution calculated with the elastic properties of the substrate.

5

compared in Fig.5.4. The markers indicate the solution in [104] and the solid lines are the results obtained from the developed solver. A good agreement is observed between the two solutions. When the substrate modulus is larger than the coating, the contact width becomes smaller.

5.5.2 Viscoelastic Half-Space

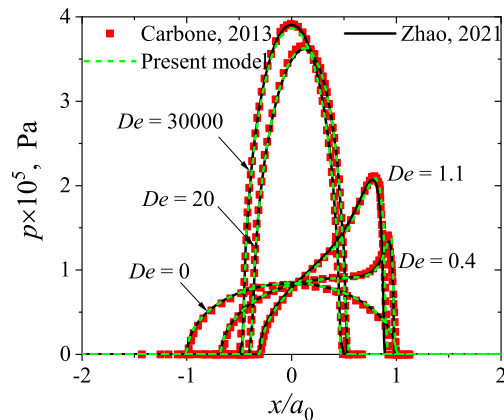


Figure 5.5: Comparison of pressure distribution from the present model (lines) with results of Carbone and Putignano [21] and our previous work [159] (also Chapter 3) for a viscoelastic half-space at a wide range of rolling velocities. (The right side is the rolling entrance)

Next the developed PN layer model is reduced to a viscoelastic half-space contact by setting the thickness of the viscoelastic layer to a very large value ($1000a_0$). The results

are compared with numerical results of [21] and of our previous work [159] as shown in Chapter 3. The operating conditions are $E_\infty^c = 10\text{MPa}$, $E_\infty^c/E_0^c = 10$, $R_0 = 10\text{mm}$, $W_0 = 0.15\text{N}$ and $\tau = 0.01\text{s}$. Note that these previous solutions in Chapter 3 were from a MG solver of the equations in the spatial domain. The contact pressure is calculated at a range of dimensionless velocities (Deborah number) $De = \tau/(a_0/v_m)$ with $0 \leq De \leq 3 \times 10^4$, where a_0 is the Hertzian contact radius at an extremely low velocity with a modulus of E_0^c [21]. Fig.5.5 shows the pressure distribution along the centerline. Obviously, the agreement is very good for all numerical models and values of De .

5.5.3 Viscoelastic Layer-Elastic Substrate System

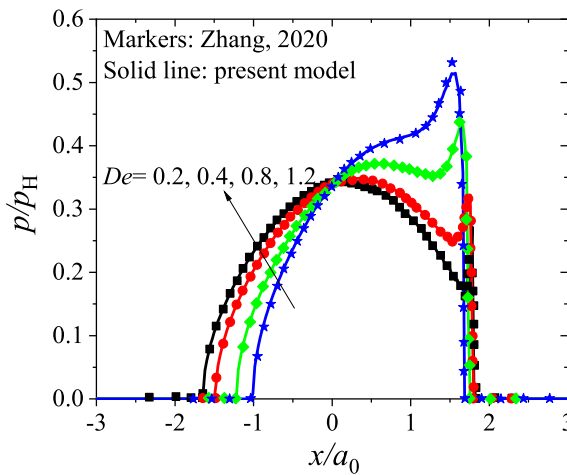


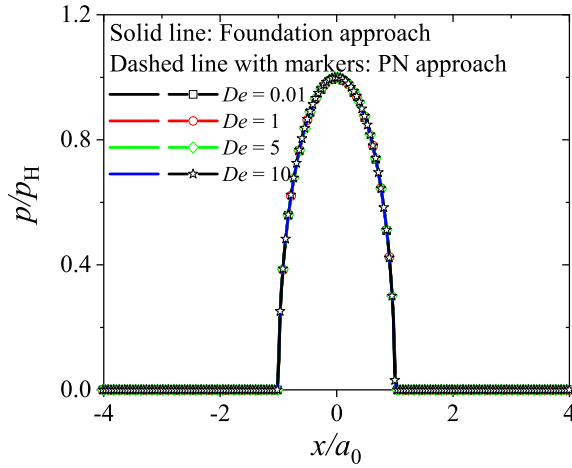
Figure 5.6: Comparison of pressure distribution from the present model (lines) with those from Zhang et al. [158] for a viscoelastic layered contact problem at different De . (layer thickness of $l_0 = a_0$; the right side is the rolling entrance)

The developed PN approach is validated by comparing with the simulation results presented in [158] for a viscoelastic layered rolling contact problem, see Fig.5.6. The parameters are identical as in [158]: a layer thickness of $l_0 = a_0$ where a_0 is the Hertzian contact radius in terms of the properties of the elastic substrate, a normal load of $W_0 = 1.48\text{N}$, a rigid sphere of radius $R_0 = 10\text{mm}$, Poisson ratio of $\nu^c = \nu^s = 0.3$, modulus $E_\infty^c = 10^8\text{Pa}$, $E_\infty^c/E_0^c = 10$ in the SLS model, a single relaxation time $\tau = 0.01\text{s}$ and the elastic modulus of the substrate $E^s = 2E_\infty^c$. Fig.5.6 shows that a good agreement is achieved for the pressure distribution at different values of De .

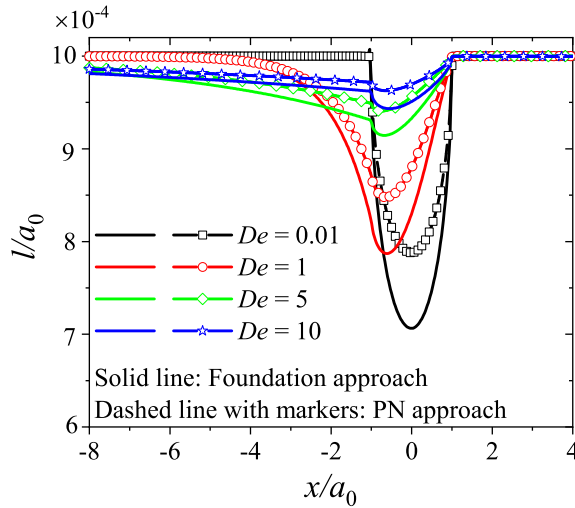
5.5.4 Foundation Approach vs PN Approach

The PN layer model solution has been validated thoroughly, and it may serve as a reference in the investigation of the accuracy of the foundation approach. In this section, the pressure distribution and the deformed layer thickness predicted by these two approaches are compared for a viscoelastic layered rolling contact (elastic substrate) at different speeds.

The common input parameters are: a sphere radius $R_0 = 9.525\text{mm}$, an applied load $W_0 = 10\text{N}$, a substrate elastic modulus $E^s = 1\text{GPa}$, Poisson ratio $\nu^c = \nu^s = 0.3$, and for the viscoelastic layer a modulus $E_0^c = 0.1\text{GPa}$ with a ratio $E_\infty^c/E_0^c = 10$. In this case, the layer thickness is as thin as $l_0 = 1 \times 10^{-3}a_0$, which is in a typical range of an EHL film.



(a) Dimensionless centerline pressure distribution



(b) Dimensionless centerline deformed layer thickness

Figure 5.7: Dimensionless pressure (a) and layer thickness (b) distribution along the central line for both foundation approach and PN approach at different rolling velocities. (The right side is the rolling entrance.)

Fig.5.7 compares the dimensionless pressure distribution (a) and the layer thickness (b) calculated from the two approaches at different values of De , $0.01 \leq De \leq 10$ corresponding to rolling speeds from 4×10^{-4} to 0.4m/s assuming the relaxation time of the layer is $\tau = 0.01$ s. The pressure distribution is for all cases identical to the Hertzian profile associated with the substrate elastic modulus. The effect of the viscoelastic layer on the pressure distribution is negligible. A similar phenomenon has also been reported for elastic layered contact problems by Chen [22] and O'sullivan [104]. For the layer thickness in Fig.5.7 (b), the results from the foundation approach show similar trends of variation compared to the results from the PN approach, even though quantitatively the resulting layer thickness is smaller. This is caused by the oedometric layer assumption in the foundation approach, which neglects the compatibility relation of deformation with surrounding non-local points. This leads to a larger deformation in the normal direction and hence a smaller layer thickness. The results imply that the relatively simple foundation approach can predict the layer deformation behavior qualitatively quite well even though it is not as accurate as the PN solution.

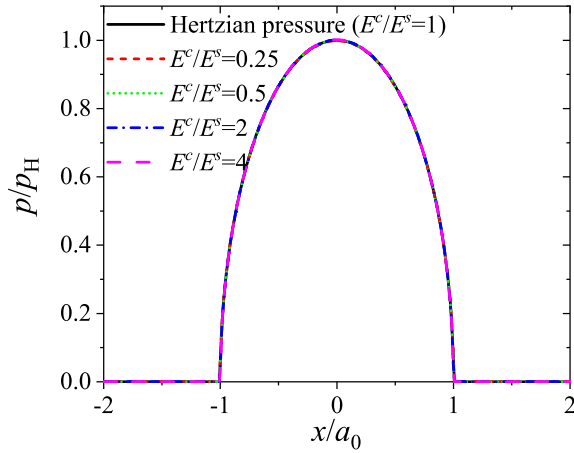
5.6 Results and Discussion

Before showing the main characteristics of the deformed viscoelastic layer at various contact conditions in Sec.5.6.2, some typical results for elastic layered contact problems are shown in Sec.5.6.1 as a reference. The results in these two sections have been obtained using the PN based solution method verified in the previous section.

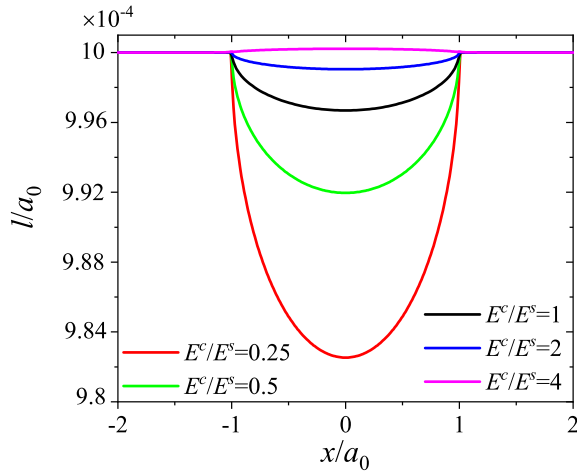
In literature, the output of viscoelastic layered contact problems is mainly the pressure distribution, the stress field and the total deformation, whereas the layer thickness after deformation rarely gains attention. However, to investigate the possibility of using a viscoelastic layer to represent an EHL film behavior, the layer thickness after deformation is a key parameter. To ensure that the thickness of the layer is comparable to an EHL film, the layer thickness relative to the contact radius is taken as $l_0/a_0 = 10^{-3}$ in the following analysis. Note that the deformation behavior of such a thin layer has rarely been studied in the literature. The Poisson ratio is taken as 0.3 for both the layer and the substrate, $\nu^c = \nu^s = 0.3$. The Hertzian parameters calculated with the mechanical properties of the substrate, a_0 and p_H in Eq.(5.12), are used for the non-dimensionalization of the layer thicknesses and stresses, respectively.

5.6.1 Elastic Layered Elastic Half-Space

The response of an elastic layered contact problem is dominated by two dimensionless parameters, the relative layer thickness l_0/a_0 and the relative stiffness E^c/E^s . An elastic layered solution can be obtained with the developed PN approach by simply setting $E_\infty^c = E_0^c$ in Eq.(5.2) so that the resulting elastic modulus of the layer is $E^c = E_0^c$. In this section, the effect of the ratio of the elastic modulus of the layer relative to the substrate E^c/E^s (layer stiffness) is studied at a constant layer thickness of $l_0/a_0 = 0.001$. The input values for E^c/E^s are the same as used in [104]. They are achieved by fixing the elastic modulus E^s of the substrate and varying E^c .



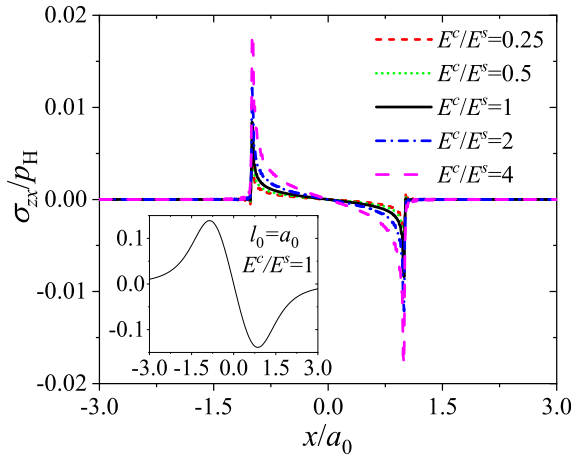
(a) Dimensionless pressure distribution



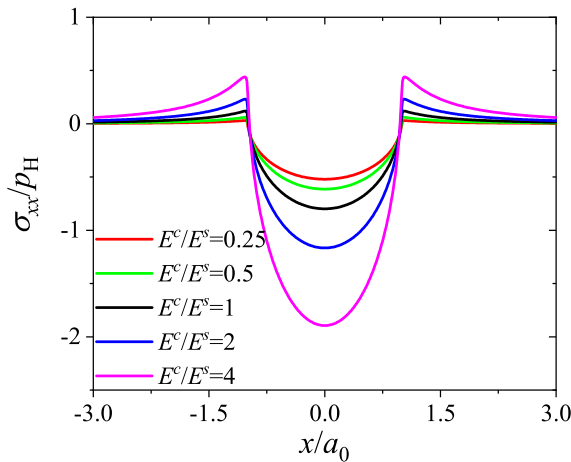
(b) Dimensionless deformed layer thickness distribution

Figure 5.8: Dimensionless pressure (a) and layer thickness (b) profiles along the central line for a thin elastic layer coated elastic half-space at different E^c/E^s . ($l_0 = 0.001a_0$)

Fig.5.8 shows the pressure profile and the deformed layer thickness at different elasticity ratios E^c/E^s . When $E^c/E^s = 1$, the layered elastic contact problem returns to an elastic half-space one, which serves as a reference for other cases of $E^c/E^s < 1$ (soft compliant layer) and $E^c/E^s > 1$ (hard stiff layer). It can be seen in Fig.5.8 (a) that for such a thin layer the pressure distribution remains close to the Hertzian pressure for all cases regardless of the elastic modulus ratios. The corresponding layer thicknesses given in Fig.5.8 (b) shows that the more compliant layer with a smaller elasticity ratio E^c/E^s has a larger change in thickness. For the stiffest layer of $E^c/E^s = 4$ in this study, the layer thickness is even larger than its initial value, see Fig.5.8 (b). When the layer is stiffer than the substrate, the stiffer



(a) Dimensionless layer/substrate interface stress σ_{zx}



(b) Dimensionless layer/substrate interface stress σ_{xx}

Figure 5.9: Dimensionless stress components (a) σ_{zx} , (b) σ_{xx} at the layer/substrate interface for different values of E^s/E^c in elastic layered contacts.

layer behaves as a beam attached to the elastic half-space resulting in bending stresses in the layer [22, 104], which may cause the increase in its thickness. Note that in all cases the deformation of the substrate is many times larger than the thickness of the layer.

The interfacial stresses, σ_{zx} and σ_{xx} , at $z_1 = l_0$ are plotted in Fig.5.9 for different layer stiffness. The profiles of σ_{zx} in Fig.5.9 (a) show that a compression zone occurs in front of the rolling contact and a traction zone behind. The interfacial shear stress becomes larger when the elastic modulus of the layer increases relative to the substrate. Compared to the relative thick layer of $l_0 = a_0$ in the inset in Fig.5.9 (a), the thin layer causes that the shear stresses σ_{zx} concentrates at the edges of the contact zone with a local maximum. For this

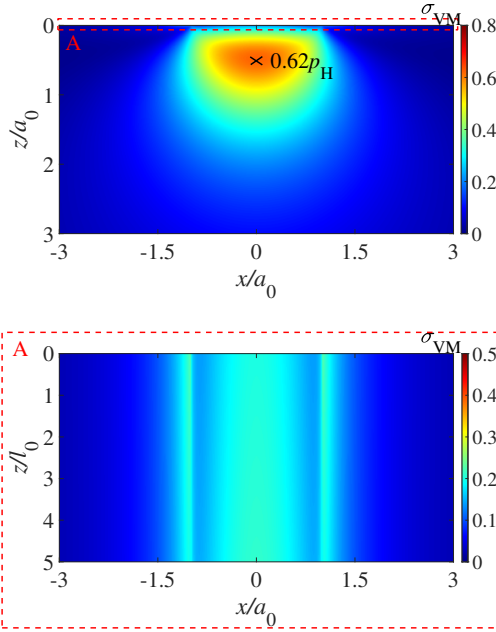


Figure 5.10: Dimensionless von Mises stresses on the plane $y = 0$ for homogeneous elastic half-space $E^s/E^c = 1$.

thin layer case of $l_0 = 0.001a_0$, the curves of σ_{xx} in Fig.5.9 (b) show that the stiffer layer further increases both the maximum tensile and compressive stresses at the interface. The rate of increase is becoming larger with increasing elasticity ratio.

To have an overall representation of the stresses, the corresponding dimensionless von Mises stresses (the second invariant of the stress deviator tensor) are given in Fig.5.10 and Fig.5.11 according to the Eq.(5.29)

$$\sigma_{VM} = \sqrt{\frac{1}{2} [(\sigma_{xx} - \sigma_{yy})^2 + (\sigma_{yy} - \sigma_{zz})^2 + (\sigma_{zz} - \sigma_{xx})^2 + 6(\sigma_{xy}^2 + \sigma_{xz}^2 + \sigma_{yz}^2)]}. \quad (5.29)$$

The results are presented in a cross sectional view of the central plane $y = 0$. The elastic homogeneous case of $E^c/E^s = 1$ in Fig.5.10 is exactly a regular contact with the maximum $0.62p_H$ at approximately $0.47a_0$ below the surface. The von Mises stress fields in the elastic substrate remain almost the same for all cases. The von Mises stress shows significant discontinuities at the interface between the layer and the substrate for all cases in Fig.5.11 as expected. The discontinuity increases when the layer becomes either harder or softer. For the soft compliant layer in Fig.5.11 (a) and (b), the von Mises stress concentrates in the Hertzian zone, spanning roughly from -1 to 1 in the x direction and increases mainly in the center of the contact. As a contrast, the hard stiffer layer in Fig.5.11 (d) and (e) has a wider stress distribution area, and the von Mises stress in the film first concentrates on the edge of the contact area and then increases inside the contact area with increasing elastic modulus.

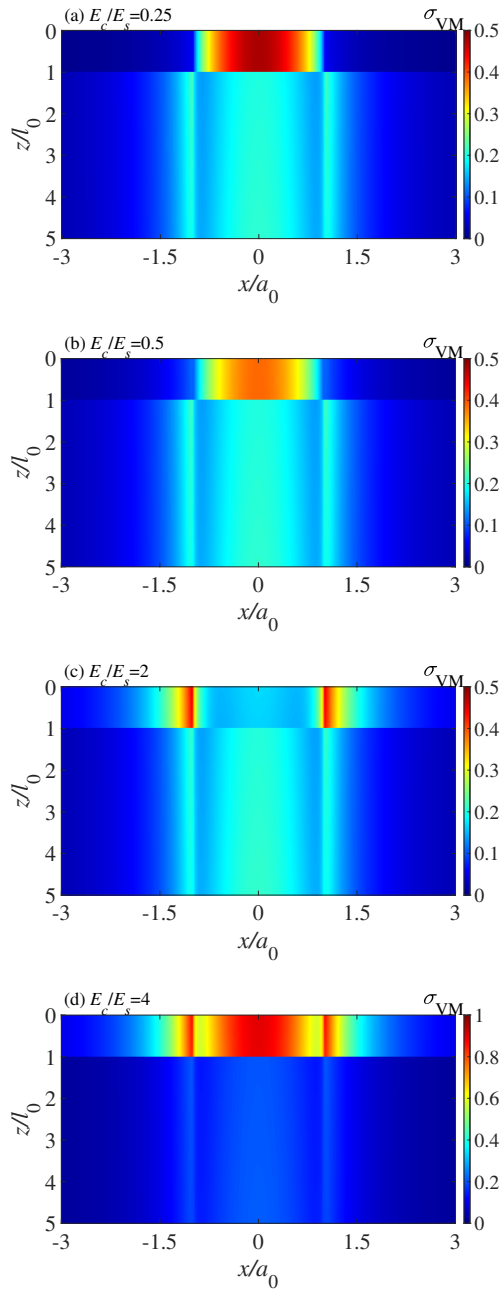


Figure 5.11: Dimensionless von Mises stresses in the plane $y = 0$ for different values of E^s/E^c in elastic layered contacts. (The layer thickness is $l_0 = 0.001a_0$). Note that the color scale bar in Fig.5.11 (d) is different from the rest for a better view of the stress field in the layer.

As a short summary, the layer elastic modulus relative to the substrate E^c/E^s has a strong effect on the layer deformation and the stress discontinuities at the layer/substrate interface. However, it has only negligible influence on the pressure response of the elastic layer-elastic substrate system when the layer thickness is much smaller than the contact radius $l_0 \ll a_0$. In such cases, the substrate dominates the pressure distribution. This is a demonstration of thin layer behavior where $dp/dz \approx 0$, in mechanics problems and equivalently in hydrodynamic/aerodynamic boundary layers (lubrication assumption).

5.6.2 Viscoelastic Layer on Elastic Half-Space

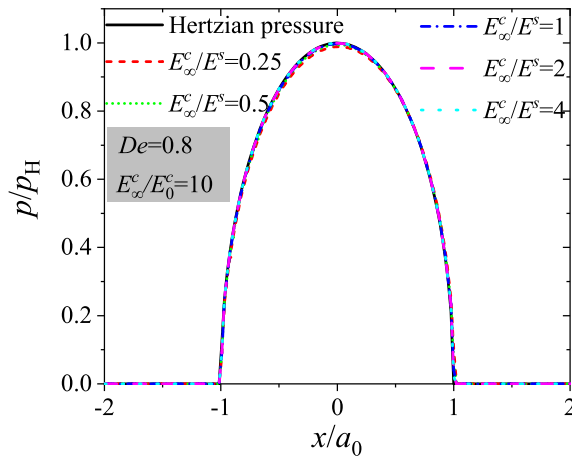
Compared to the elastic layered contact problem in the previous section, the viscoelastic layer-elastic substrate system introduces two additional dimensionless parameters: E_∞^c/E_0^c the ratio of the two elastic limits of the SLS viscoelastic layer, and the Deborah number De which relates the relaxation time of the viscoelastic material τ to the characteristic time of the material passing through the contact a_0/v_m . As a result, the studied viscoelastic layered contact problem with a specific layer thickness l_0/a_0 is governed by three dimensionless parameters: (1) the ratio of the elastic modulus E_∞^c/E^s , (2) the dimensionless velocity or the Deborah number $De = v_m\tau/a_0$ and (3) the ratio of the two elastic limits of the SLS model $E_\infty^c/E_0^c = 1 + R_e$. In this section, a parametric study is carried out with the PN approach. The influence of these parameters on the contact pressure distribution and the deformed layer thickness are investigated under thin-layer rolling contact conditions.

5

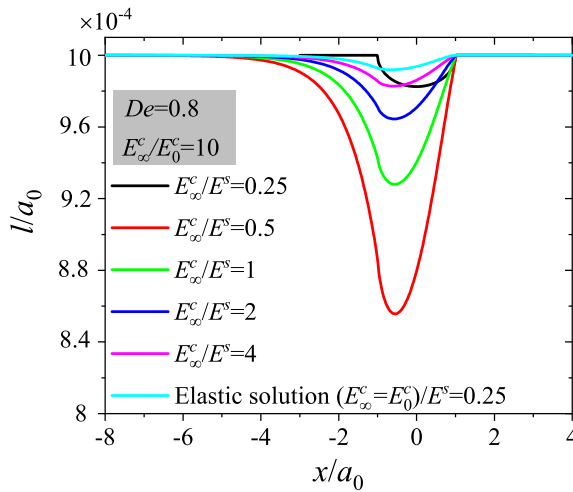
Effect of the Ratio of Elastic Modulus, E_∞^c/E^s

The effect of the elastic modulus ratio E_∞^c/E^s on the pressure distribution, layer deformation and stresses is investigated in the thin layer regime of $l_0 = 0.001a_0$. As before, the elastic modulus of the elastic substrate E^s is fixed and the layer modulus E_∞^c is varied to achieve different ratios of E_∞^c/E^s . The Deborah number De and the ratio of the two elastic modulus of the SLS model E_∞^c/E_0^c are prescribed as 0.8 and 10, respectively.

Fig.5.12(a) and (b) show the centerline dimensionless pressure distribution and the layer thickness after deformation, respectively, for different ratios of E_∞^c/E^s from 0.25 to 4. Similar to the elastic solution that has been shown in Fig.5.8 (a), the pressure profiles in Fig.5.12 (a) are all nearly identical to Hertzian solution, but are quite different from the case of a thick viscoelastic layer of $l_0 = a_0$ shown in Fig.5.6. This is the consequence of the studied very thin layer. The pressure can not vary over the layer thickness, hence, it is completely dictated by the substrate. Fig.5.12 (b) shows that a more compliant layer (smaller elastic modulus ratio E_∞^c/E^s) gives a larger layer deformation. The solid black line in the figure represents an elastic layered half-space solution as a reference to the viscoelastic layered cases. Compared to the elastic layered case, an asymmetric layer thickness distributions are observed for all the viscoelastic layered cases, which is caused by the time-delayed response of the viscoelastic material. Unlike the instantaneous response to an external load for an elastic layer, it takes time for a viscoelastic layer to return to its original state at the outlet side in Fig.5.12 (b) and thus results in an asymmetric layer deformation.



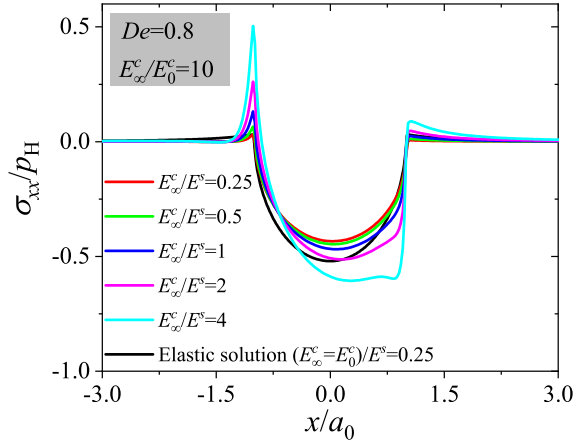
(a) Dimensionless pressure distribution



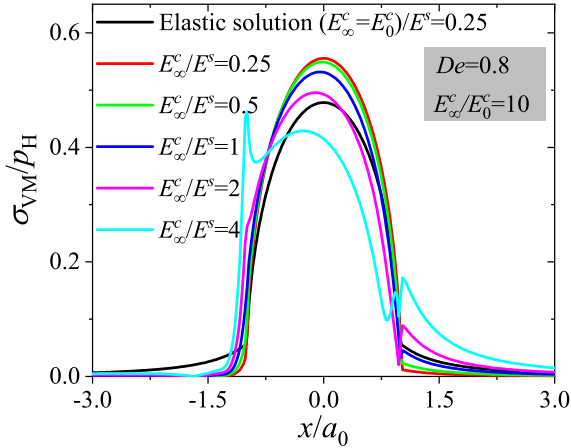
(b) Dimensionless layer thickness

Figure 5.12: Centerline profiles of pressure distribution (a) and layer thickness after deformation (b) for different values of E_∞^c/E^s in viscoelastic layered contacts. (SLS viscoelastic model with $E_\infty^c/E_0^c = 10$, at a fixed viscoelastic layer thickness of $l_0 = 0.001a_0$ and $De = 0.8$; the right side is the rolling entrance.)

Fig.5.13 shows the interfacial stress σ_{xx} and the von Mises stress at the interface for different elasticity ratios E_∞^c/E^s . In Fig.5.13 (a), the maximum tensile stress at the outlet side of the contact edge when the layer is more compliant than the substrate. Compared to the elastic layered solution, the interfacial stress component σ_{xx} is asymmetric and inclined towards the inlet side. For the soft layer cases, $E_\infty^c/E^s = 0.25$ and $E_\infty^c/E^s = 0.5$, there are only slight differences in the profiles of σ_{xx} in the interface. For the hard layer case of $E_\infty^c/E^s = 4$, a local minimum occurs on the inlet side for the interfacial stress



(a) Dimensionless layer/substrate interface stress σ_{xx}



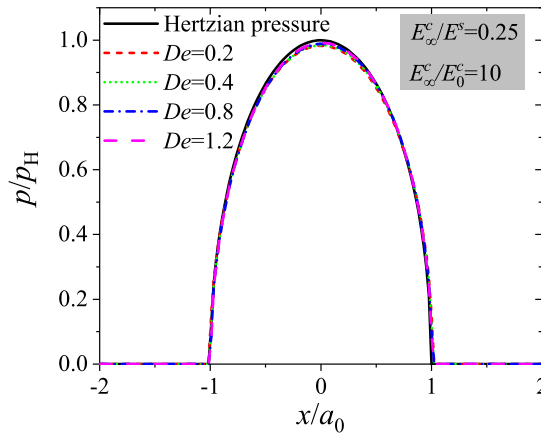
(b) Dimensionless von Mises stress σ_{VM}

Figure 5.13: Dimensionless layer/substrate interface stress (a) σ_{xx} , and the corresponding von Mises stress (b) for different elasticity ratios E_{∞}^c/E^s in viscoelastic layered contacts. (SLS viscoelastic model with $E_{\infty}^c/E_0^c = 10$, at a fixed viscoelastic layer thickness of $l_0 = 0.001a_0$ and $De = 0.8$; the right side is the rolling entrance.)

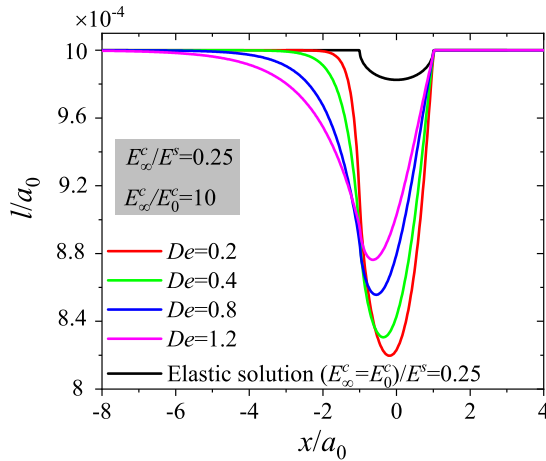
σ_{xx} . While for the von Mises stress given in Fig.5.13 (b), the viscoelastic solutions skew to the outlet side. For the hard layer case, $E_{\infty}^c/E^s = 4$, a local maximum appears at the outlet side and fluctuations occur at the inlet side.

Effect of the Deborah number, De

This section studies the influence of the Deborah number $De = v_m\tau/a_0$, while keeping the other parameters constant: $E_{\infty}^c/E^s = 0.25$ and $E_{\infty}^c/E_0^c = 10$. Fig.5.14 shows the centerline pressure (a) and the deformed layer thickness (b) profiles for different dimensionless rolling



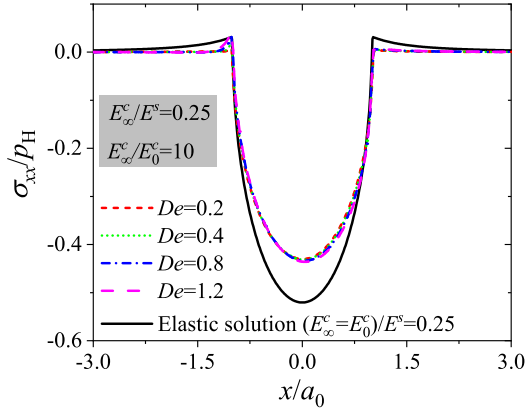
(a) Dimensionless pressure distribution



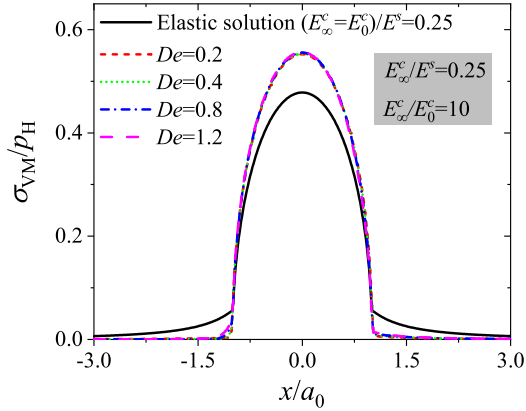
(b) Dimensionless layer thickness

Figure 5.14: Centerline profiles of pressure distribution (a) and layer thickness after deformation (b) for different values of speed De in viscoelastic layered contacts. (SLS viscoelastic model with $E_\infty^c/E_0^c = 10$, at fixed values of $l_0 = 0.001a_0$ and $E_\infty^c/E_s = 0.25$; the right side is the rolling entrance).

velocities De of 0.2, 0.4, 0.8 and 1.2. As shown in Fig.5.14 (a), the pressure distribution at different values of De coincides with the elastic Hertzian pressure because of the thin layer thickness, $l_0 = 0.001a_0$. For the deformed layer thickness shown in Fig.5.14 (b), the viscoelastic property of the layer results in an asymmetric layer thickness profile for all cases. When the velocity is high (large De) the viscoelastic layer has less time to deform resulting in a larger thickness. The trend is in line with the behavior of the EHL films in classical lubrication theory, even though the shape/profile does not look the same. Also the outlet sweep of the deformed layer thickness increases with the velocity, needing more time to recover to its original state.



(a) Dimensionless stress σ_{xx}



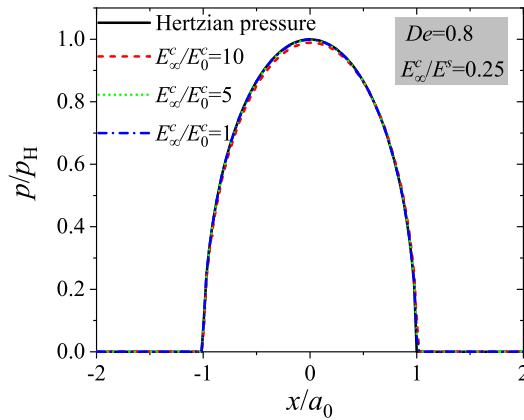
(b) Dimensionless von Mises stress σ_{VM}

Figure 5.15: Dimensionless layer/substrate interface stress (a) σ_{xx} , and the corresponding von Mises stress (b) for different values of speed De in viscoelastic layered contacts. (SLS viscoelastic model with $E_{\infty}^c/E_0^c = 10$, at fixed values of $l_0 = 0.001a_0$ and $E_{\infty}^c/E_s = 0.25$; the right side is the rolling entrance).

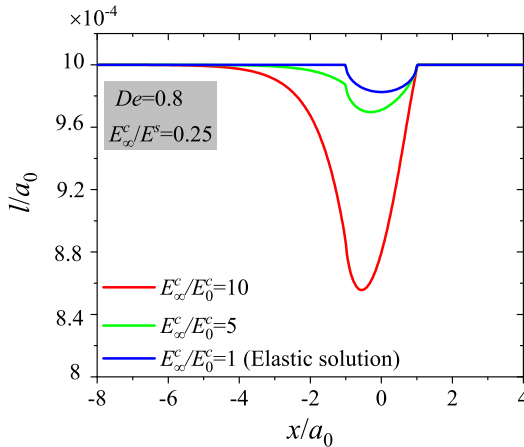
The layer/substrate interfacial stresses are plotted in Fig.5.15. The elastic layered solution represented by the black solid line is given in the figure as a reference. The central line profiles of σ_{xx} in Fig.5.15 (a) shows that the viscoelasticity of the layer induces smaller stress values than the elastic solution, while the increase in the rolling velocity from 0.2 to 1.2 causes almost no change to the stresses. Regarding the von Mises stresses at the layer/substrate interface in Fig.5.15 (b), an increase is observed for the viscoelastic solution compared to the elastic solution. The central line profiles of the von Mises stress show a smaller sweep zone at both the inlet and outlet sides than for the elastic case. Nevertheless, the values of the viscoelastic von Mises stresses remain similar to each other with the set of speeds applied at frictionless and thin layer conditions.

Effect of the Ratio of the Two Elastic Limits of the SLS Model, E_∞^c/E_0^c

In this section, the effect of the ratio of the two elastic limits in the SLS model for the viscoelastic layer, E_∞^c/E_0^c , is studied. These two elastic limits correspond to the rubbery and glassy states of viscoelastic materials at extremely low or high frequencies, as shown in Fig.A.1. We keep the other parameters constant: $l_0 = 0.001a_0$, $De = 0.8$ and $E_\infty^c/E^s = 0.25$. Fig.5.16 shows the dimensionless pressure distribution and the deformed layer thickness for various ratios of $E_\infty^c/E_0^c = 1, 5$ and 10 . For $E_\infty^c/E_0^c = 1$, the viscoelastic layered solution reduces to the elastic layered solution, according to Eq.(5.3). Note that $E_\infty^c/E_0^c = (1 + R_e)$ cannot be smaller than one as $R_e = E_f/E_s \geq 0$.

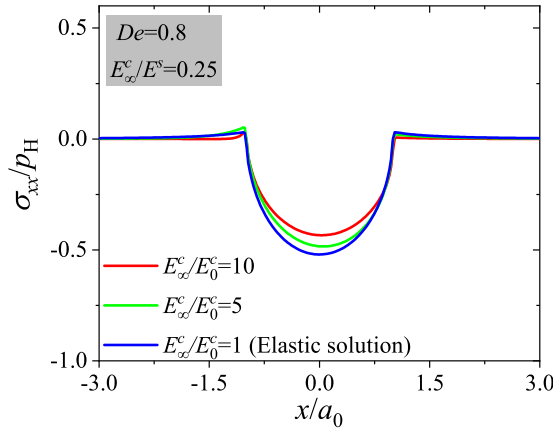
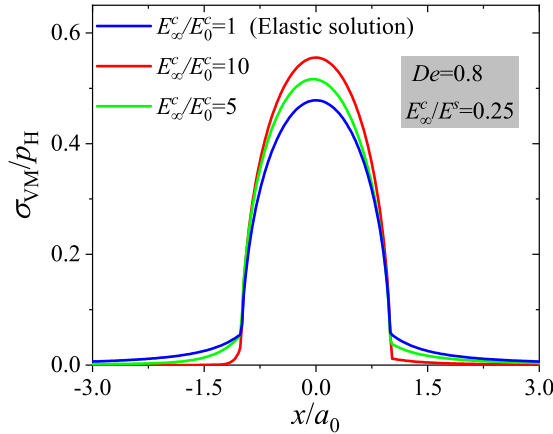


(a) Dimensionless pressure distribution



(b) Dimensionless layer thickness

Figure 5.16: Centerline profiles of pressure distribution (a) and layer thickness after deformation (b) for different values of E_∞^c/E_0^c in viscoelastic layered contacts. (SLS viscoelastic model a single relaxation time, at fixed values of $l_0 = 0.001a_0$ and $De = 0.8$; the right side is the rolling entrance).

(a) Dimensionless stress σ_{xx} 

(b) Dimensionless von Mises stress

Figure 5.17: Dimensionless layer/substrate interface stress (a) σ_{xx} , and the corresponding Von Mises stress (b) for different ratio values of E_{∞}^c/E_0^c in viscoelastic layered contacts. (SLS viscoelastic model a single relaxation time, at fixed values of $l_0 = 0.001a_0$ and $De = 0.8$; the right side is the rolling entrance).

The graphs in Fig.5.16 (a) show that the effect of the ratio of the two elastic limits of the SLS model on the pressure distributions is negligible for the studied thin layer regime, while it has considerable effect on the layer deformation as shown in Fig.5.17 (b). The layer with a larger ratio of E_{∞}^c/E_0^c gives a larger layer deformation.

Fig.5.17 shows the corresponding dimensionless stresses, i.e. the σ_{xx} and the von Mises stress, at the layer/substrate interface. The viscoelasticity of the layer causes the stress distribution to be skewed slightly to the inlet side for all cases. The hard layer cases, e.g. $E_{\infty}^c/E_0^c = 5$ and $E_{\infty}^c/E_0^c = 10$, give a larger σ_{xx} and smaller von Mises stresses compared to the elastic layered solution when $E_{\infty}^c/E_0^c = 1$.

From the above analysis in Sec.5.6.2, it can be seen that the properties of the elastic substrate dominate the pressure response of the system in the thin layer regime so that an elastic Hertzian pressure distribution remains for all the studied cases. We may say that the pressure distribution of the viscoelastic layer in dry contacts is similar to that of the classical EHL in particular at high contact pressure. The variation of the dimensionless parameters has significant effect on the layer deformation and the stress components at the layer/substrate interface, even though their effect on the pressure is negligible.

The viscoelasticity of the layer leads to the asymmetric distribution of the deformation, since the layer needs time to recover to its original status giving a larger deformation at the outlet. However, the deformed layer thickness in the layered contacts hardly shows EHL lubricant film behavior, lacking of the rather flat parallel film in the contact and the film constriction at the outlet. One possible reason for the difference relies on the constant viscosity and thus the constant relaxation time used in the SLS model for the viscoelastic layer. At a high Hertzian contact pressure in the order of GPa, the viscosity of the viscoelastic layer and thus the relaxation time in the SLS model may increase with pressure, which would be beyond the scope of linear viscoelasticity. In the following section, the foundation approach is used to consider the effect of the pressure-dependent viscosity on the deformation of the thin viscoelastic layer in a simple manner. Some interesting results are obtained, and the possibility to model the EHL lubricant film behavior is further explored.

5.7 Towards EHL Film Behavior Modeling

In the foundation approach, the layer deformation is simply evaluated with the constitutive equation of the oedometric layer. In the previous section it has been shown that fully bonded viscoelastic layer with isotropic homogeneous behavior do not show lubricant/fluid like behavior in a contact. Next we return to the foundation approach. This may provide an easier framework to consider the piezoviscous effect of the thin viscoelastic layer in contact problems, even though it is out of the scope of linear viscoelasticity.

As a preliminary study, the pressure-viscosity relation proposed by Roelands is modified by multiplying a constant C_0 to model the viscosity of the dashpot in the SLS layer.

$$\eta_s = C_0 \eta_{s0} \exp \left[(\ln(\eta_{s0}) + 9.67) \left(-1 + \left(1 + \frac{p}{p_0} \right)^z \right) \right] \quad (5.30)$$

where η_{s0} is the viscosity of the dashpot at ambient pressure p_0 , and z is the pressure viscosity index.

The input parameters for the viscoelastic layered model based on the foundation approach are: a loading force of $W_0 = 10\text{N}$, a sphere radius of $R_0 = 9.525\text{mm}$, a rolling velocity of $v_m = 0.1\text{m/s}$, an SLS viscoelastic layer thickness of $l_0 = 0.001a_0$, modulus of $E_0^c = 1\text{GPa}$, ratio of $E_\infty^c/E_0^c = 1000$, viscosity of $\eta_{s0} = 0.0447\text{Pa}\cdot\text{s}$, $C_0 = 1.0 \times 10^6$, pressure constant of $p_0 = 0.196\text{GPa}$, viscosity pressure index of $z = 0.67$, and reduced modulus of $E' = 117\text{GPa}$.

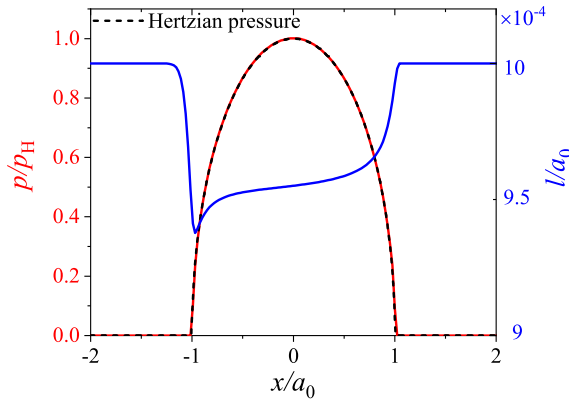


Figure 5.18: Pressure and layer thickness distribution along the central line predicted by foundation approach of viscoelastic layer modeling by considering the piezoviscous effect of the dashpot in the SLS model. ($v_m = 0.1\text{m/s}$, SLS viscoelastic model with $E_\infty^c/E_0^c = 1000$; the right side is the rolling entrance)

5

Fig.5.18 shows the resulting pressure and layer thickness distribution along the central line with the input parameters listed above. For the pressure distribution, as reported in the last section Sec.5.6.2, it coincides with the Hertzian pressure because of the thin layer thickness and the dominating effect of the elastic substrate. Interestingly, with consideration of the piezoviscous effect of the SLS viscoelastic layer, the layer behaves as an EHL film showing a relatively constant film thickness in the contact zone and a local minimum at the exit side. In the contact zone, the viscosity of the dashpot and thus the relaxation time of the viscoelastic layer increase locally depending on the contact pressure. In the contact center the viscosity becomes extremely large in the SLS model, which delays the deformation and hence results in a relatively constant film thickness in the contact zone. Close to the exit boundary of $x/a_0 = -1$, the low pressure there deforms the viscoelastic layer at a high rate giving a rapid decrease in the film thickness as happened in the inlet region when the layer just came into the pressurized zone. At the position of $x/a_0 = -1$, the contact pressure becomes zero as a result of the complementary dry contact boundary condition and since then the viscoelastic layer has fully past the pressurized contact zone and recovers quickly. This kind of compression and recovery effects lead to the local constriction in the film at the outlet. The position of the minimum film thickness corresponds to the position of zero pressure at $x/a_0 = -1$ for the low speed used in this case.

A higher rolling velocity (higher Deborah number), there is less time for the layer to deform, which results in a thicker film thickness as well as a reduced minimum film thickness peak at $x/a_0 = -1$, see Fig.5.19. At extreme speed conditions, e.g. $v_m = 0$ and 1000m/s , the viscoelastic layered model gives elastic solutions due to the nature of viscoelastic materials. In the intermediate values of speeds corresponding to the transition regime of viscoelastic materials, typical EHL film behaviors can be obtained.

The entire shape of the thin viscoelastic layer after deformation is shown in Fig.5.20 (a) on a contour plot for the case in Fig.5.18. A typical horse-shoe shaped film is obtained,

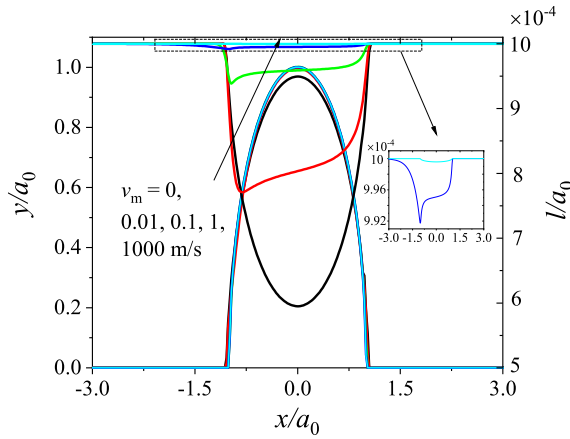


Figure 5.19: Pressure and layer thickness distribution along the central line predicted by foundation approach of viscoelastic layer modeling at different rolling velocities. (The ratio of the elastic limits is $E_{\infty}^c/E_0^c = 1000$ for the SLS layer; the right side is the rolling entrance.)

5

which looks quite similar to a classical EHL film as well as the experimental observations in the PDMS viscoelastic layer experiments, see Fig.5.20 (b) and (c) respectively. Even though the comparison is not quantitative, the current results obtained with the SLS model of a single relaxation time represent the typical features of the EHL film behavior. From the above analysis, the concept of modeling EHL via viscoelasticity may work when the piezoviscosity property of the viscoelastic layer is taken into account in a foundation model. For future work, nonlinear viscoelasticity layered model needs to be developed for a better description of the EHL behavior or even modeling mixed lubrication with discontinuous heterogeneous layers.

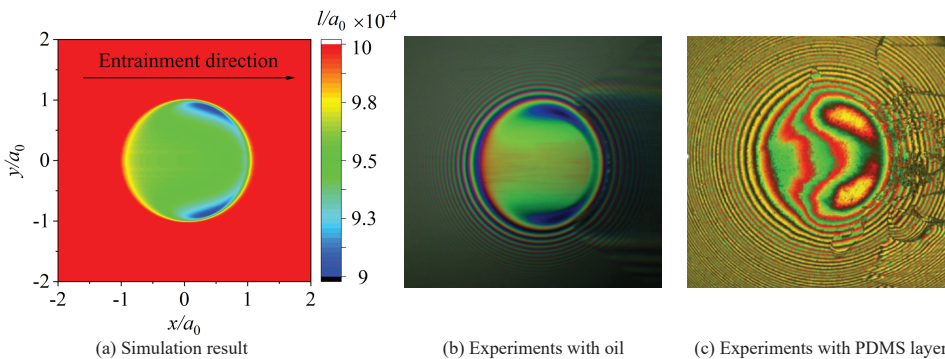


Figure 5.20: Qualitative comparison between simulation and experimental results: (a) simulated film shape with the foundation viscoelastic layered model, (b) measured film shape with oil HVI60 by optical interferometry, (c) measured deformed layer shape with a PDMS layer of initial thickness of 20 μ m, no oil.

5.8 Conclusion

In this work, two different modeling approaches, i.e. the foundation approach and the PN approach, have been presented to study the deformation behavior of a thin viscoelastic/elastic layer in dry rolling contacts. The PN approach can deal with different kinds of 3D layered contact problems, including the most complex system of a viscoelastic layer on a viscoelastic half-space. The foundation approach solves viscoelastic layered contact problems in a relative simple way regarding the layer deformation based on the oedometric layer assumption and the thin layer assumption. The developed PN approach has been validated by comparing with results of degenerated contact problems in literature as well as results of the viscoelastic half-space of our previous work. With the developed two approaches, the possibility to model the EHL film behavior using the concept of viscoelastic layered dry contact modeling is studied.

A parametric study has been carried out for the viscoelastic layered elastic half-space contact problem. Effects of the mechanical rheological properties of the SLS viscoelastic layer and the elastic substrate, e.g. the elasticity ratio of the layer and substrate, the Deborah number, and the elastic limits of the SLS model, on the contact pressure, layer deformation and contact stresses have been studied within thin viscoelastic layer regime. These parameters have negligible effect on the pressure distribution, while its effect on the stress components and layer deformation is significant. With the thin viscoelastic layer in contacts, the pressure response of the system is dominated by the substrate. However, the resulting film shape is hard to represent an EHL film for all studied cases with the linear viscoelasticity assumption.

The prediction results from the foundation approach are compared with the PN approach, which shows that the foundation approach can be used to model the layered contact problem qualitatively. By considering the piezoviscous effect of the viscoelastic layer in the foundation approach, the typical features of an EHL film can be represented with the viscoelastic layer concept and modeling. Therefore, non-linear viscoelastic layer modeling with a proper consideration of the piezoviscous effect may provide a new solution to "hard" EHL and even mixed lubrication problems.

5.9 Appendixes to Chapter 5

A Viscoelastic Properties

Fundamentals of Viscoelasticity

Viscoelastic materials show significant time-delayed response due to their time-dependent physical-mechanical properties, thus, the current state, e.g. the stress or the strain, of a viscoelastic material is the result of the entire history. Similar to the definition of the compliance and the elastic modulus in the theory of linear elasticity, two time-dependent functions, the creep compliance function $\varphi_c(t)$ and the relaxation modulus function $\psi_r(t)$, are defined to characterize the response of viscoelastic materials [18, 25] in viscoelasticity. The creep test with a constant stress as input and the relaxation test with a constant strain as input are usually carried out to determine the creep compliance function $\varphi_c(t)$ and the relaxation modulus function $\psi_r(t)$, respectively.

For constant strain and stress inputs, the stress and the strain response of a specific viscoelastic material can be expressed with $\sigma(t) = \psi_r(t)\epsilon_0$ and $\epsilon(t) = \varphi_c(t)\sigma_0$, respectively. While for a time-varying stress input to linear viscoelastic materials, the strain response can be obtained by applying the Boltzmann superposition principle [18]:

$$\epsilon(t) = \int_{0^-}^t \varphi_c(t-q) \frac{d\sigma(q)}{dq} dq \quad (\text{A.1})$$

Similarly, the stress response to a time-varying strain input can be expressed as:

$$\sigma(t) = \int_{0^-}^t \psi_r(t-q) \frac{d\epsilon(q)}{dq} dq \quad (\text{A.2})$$

The lower limit 0^- of the integration in Eqs.(A.1) and (A.2) indicates that the discontinuity of applications of the stress and the strain at time $t = 0$ also should be taken into account. For details of the derivation of the compliance and relaxation modulus functions, interested readers can refer to [18, 25, 159].

Applying the Laplace transform to Eqs.(A.1) and (A.2), one obtains

$$\hat{\varphi}_c(s)\hat{\psi}_r(s) = \frac{1}{s^2} \quad (\text{A.3})$$

where s is the variable in the Laplace transform domain. Using the convolution theorem yields,

$$\int_0^t \varphi_c(q)\psi_r(t-q)dq = t \quad (\text{A.4})$$

Note that the relationship of mutual reciprocal in elasticity between the compliance and the elastic modulus is not valid in the time domain for viscoelasticity; instead, it is only valid in the transform domain [18].

Taking Fourier transform of Eq. (A.1), one obtains

$$\hat{\epsilon}(\omega) = i\omega\hat{\varphi}_c(\omega)\hat{\sigma}(\omega) \quad (\text{A.5})$$

where ω is the time-related variable in the Fourier frequency domain. According to the correspondence principle, the relation of the stress and strain in the frequency domain

is $\hat{\epsilon}(\omega) = \hat{\sigma}(\omega)/\hat{\psi}_r(\omega)$, which is equivalent to the corresponding elastic one. Hence, the relation of relaxation modulus function $\psi(t)$ and the creep compliance function $\varphi(t)$ of viscoelastic materials in frequency domain is

$$\hat{\psi}_r(\omega) = [i\omega\hat{\varphi}_c(\omega)]^{-1} \quad (\text{A.6})$$

Frequency Response of the SLS Model

The frequency response of the material model is obtained by applying the Fourier transform to the differential constitutive equation, Eq.(5.1):

$$\frac{1}{2\pi} \int_{t=-\infty}^{+\infty} \left[\sigma + \beta \frac{\partial \sigma}{\partial t} \right] e^{i\omega t} dt = \frac{1}{2\pi} \int_{t=-\infty}^{+\infty} \left[E_0 \left(\epsilon + \tau \frac{\partial \epsilon}{\partial t} \right) \right] e^{i\omega t} dt \quad (\text{A.7})$$

Introducing the following functions in both frequency and time space:

$$\begin{aligned} \sigma(t) &= \int_{\omega=-\infty}^{+\infty} \hat{\sigma}(\omega) e^{-i\omega t} d\omega, & \hat{\sigma}(\omega) &= \frac{1}{2\pi} \int_{t=-\infty}^{+\infty} \sigma(t) e^{i\omega t} dt \\ \epsilon(t) &= \int_{\omega=-\infty}^{+\infty} \hat{\epsilon}(\omega) e^{-i\omega t} d\omega, & \hat{\epsilon}(\omega) &= \frac{1}{2\pi} \int_{t=-\infty}^{+\infty} \epsilon(t) e^{i\omega t} dt \end{aligned} \quad (\text{A.8})$$

the material response in frequency is then:

$$\hat{\sigma}(\omega) = E_0 \frac{1 - i\omega\tau}{1 - i\omega\beta} \hat{\epsilon}(\omega) \quad (\text{A.9})$$

Using this relation, the complex modulus is given as:

$$\hat{E}(\omega) = E_0 \frac{1 - i\omega\tau}{1 - i\omega\beta} \quad (\text{A.10})$$

which can be decomposed in real and imaginary parts

$$\hat{E}(\omega) = \hat{E}'(\omega) + i\hat{E}''(\omega) \quad (\text{A.11})$$

Using this definition, the following expressions are obtained:

$$\begin{aligned} \hat{E}'(\omega) &= E_0 \frac{1 + \omega^2\tau\beta}{1 + \omega^2\beta^2} \\ \hat{E}''(\omega) &= E_0 \frac{\omega(\tau - \beta)}{1 + \omega^2\beta^2} \\ \tan(\delta) &= \frac{\hat{E}''(\omega)}{\hat{E}'(\omega)} = \frac{\omega(\tau - \beta)}{1 + \omega^2\tau\beta} \end{aligned} \quad (\text{A.12})$$

The evolution of $\hat{E}'(\omega)$, $\hat{E}''(\omega)$ and $\tan(\delta)$ as a function of $\omega\tau$ for $\tau/\beta = 10$ ($R_e = 9$) is given in Fig. A.1. It shows that the material exhibits changes in behavior with frequency. At a low frequency, the dashpot does not play any role and the material behaves as a pure elastic material with a rigidity equals to E_0 , $\hat{E}'(\omega = 0)/E_0 = 1$. At a high frequency, the dashpot becomes exceedingly rigid and the material response is governed by the modulus

$E_\infty, \hat{E}'(\omega = \infty)/E_0 = 1 + R_e = 10$. In these two extreme conditions, the viscoelastic dissipation is related to the imaginary part $\hat{E}''(\omega)$, which become negligible and correspondingly the loss angel is close to 0. While, the loss angel $\tan(\delta)$ is very large in the intermediate frequency range, and it is mainly this region determines the energy dissipation during rolling or sliding contacts, as reported in [21],

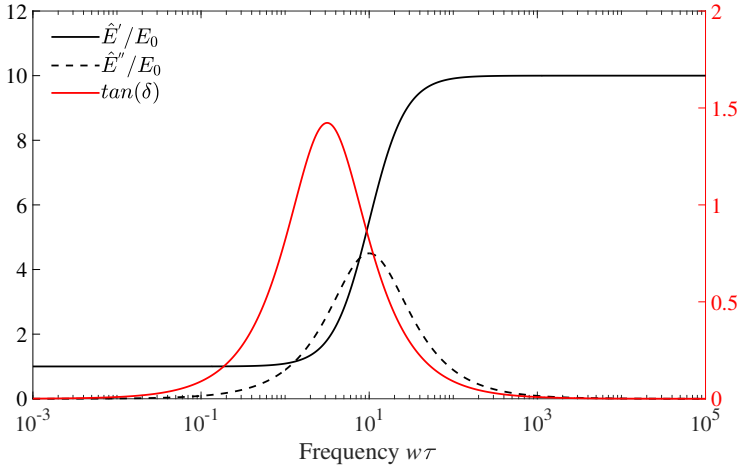


Figure A.1: Evolution of $\hat{E}'(\omega)/E_0$, $\hat{E}''(\omega)/E_0$ and $\tan(\delta)$ for an SLS model with $\tau/\beta = 10$ ($R_e = 9$).

In viscoelasticity, the real part $\hat{E}'(\omega)$ and the imaginary part $\hat{E}''(\omega)$ in Eq.(A.11) are defined as storage modulus and loss modulus, separately. And their ratio $\tan(\delta)$ is named as loss angel, which are usually used to characterize the dynamic response of the viscoelastic materials [18]. The dynamic response indicates the response in a dynamic test, in which the stress (or strain) resulting from a sinusoidal strain (or stress) is measured [18, 119].

B Frequency Response of Elastic Layered Half-Space

Displacement and Stress Components

The elastic displacement and stress components in the frequency domain can be derived from Eq.(5.22) as following:

The displacement components are,

$$\tilde{u}_1^k = \frac{1}{2\mu^k} \left\{ \begin{aligned} &im(A^k e^{-\alpha z^k} + \bar{A}^k e^{\alpha z^k}) - 4(1 - \nu^k)(B^k e^{-\alpha z^k} + \bar{B}^k e^{\alpha z^k}) + m^2 \alpha^{-1} z^k \\ &(B^k e^{-\alpha z^k} - \bar{B}^k e^{\alpha z^k}) + imz^k(C^k e^{-\alpha z^k} + \bar{C}^k e^{\alpha z^k}) - m(B_{,m}^k e^{-\alpha z^k} + \bar{B}_{,m}^k e^{\alpha z^k}) \end{aligned} \right\} \quad (\text{B.1})$$

$$\tilde{u}_2^k = \frac{1}{2\mu^k} \left\{ \begin{aligned} &in(A^k e^{-\alpha z^k} + \bar{A}^k e^{\alpha z^k}) + mn\alpha^{-1} z^k (B^k e^{-\alpha z^k} - \bar{B}^k e^{\alpha z^k}) \\ &+ inz^k (C^k e^{-\alpha z^k} + \bar{C}^k e^{\alpha z^k}) - n(B_{,m}^k e^{-\alpha z^k} + \bar{B}_{,m}^k e^{\alpha z^k}) \end{aligned} \right\} \quad (\text{B.2})$$

$$\begin{aligned} \tilde{u}_3^k = \frac{1}{2\mu^k} \left\{ -\alpha(A^k e^{-\alpha z^k} - \bar{A}^k e^{\alpha z^k}) + imz^k(B^k e^{-\alpha z^k} + \bar{B}^k e^{\alpha z^k}) - im\alpha^{-1}(B^k e^{-\alpha z^k} - \bar{B}^k e^{\alpha z^k}) \right. \\ \left. - (3 - 4\nu^k)(C^k e^{-\alpha z^k} + \bar{C}^k e^{\alpha z^k}) - \alpha z^k(C^k e^{-\alpha z^k} - \bar{C}^k e^{\alpha z^k}) - i\alpha(B_{,m}^k e^{-\alpha z^k} - \bar{B}_{,m}^k e^{\alpha z^k}) \right\} \end{aligned} \quad (\text{B.3})$$

The stress components are,

$$\begin{aligned} \tilde{\sigma}_{11}^k = -m^2(A^k e^{-\alpha z^k} + \bar{A}^k e^{\alpha z^k}) + 2im(v^k - 2)(B^k e^{-\alpha z^k} + \bar{B}^k e^{\alpha z^k}) \\ + im^3\alpha^{-1}z^k(B^k e^{-\alpha z^k} - \bar{B}^k e^{\alpha z^k}) - m^2z^k(C^k e^{-\alpha z^k} + \bar{C}^k e^{\alpha z^k}) \\ + 2\alpha v^k(C^k e^{-\alpha z^k} - \bar{C}^k e^{\alpha z^k}) - im^2(B_{,m}^k e^{-\alpha z^k} + \bar{B}_{,m}^k e^{\alpha z^k}) \end{aligned} \quad (\text{B.4})$$

$$\begin{aligned} \tilde{\sigma}_{22}^k = -n^2(A^k e^{-\alpha z^k} + \bar{A}^k e^{\alpha z^k}) - 2imv^k(B^k e^{-\alpha z^k} + \bar{B}^k e^{\alpha z^k}) \\ + imn^2\alpha^{-1}z^k(B^k e^{-\alpha z^k} - \bar{B}^k e^{\alpha z^k}) - n^2z^k(C^k e^{-\alpha z^k} + \bar{C}^k e^{\alpha z^k}) \\ + 2\alpha v^k(C^k e^{-\alpha z^k} - \bar{C}^k e^{\alpha z^k}) - in^2(B_{,m}^k e^{-\alpha z^k} + \bar{B}_{,m}^k e^{\alpha z^k}) \end{aligned} \quad (\text{B.5})$$

$$\begin{aligned} \tilde{\sigma}_{33}^k = \alpha^2(A^k e^{-\alpha z^k} + \bar{A}^k e^{\alpha z^k}) + 2im(1 - v^k)(B^k e^{-\alpha z^k} + \bar{B}^k e^{\alpha z^k}) \\ - im\alpha z^k(B^k e^{-\alpha z^k} - \bar{B}^k e^{\alpha z^k}) + \alpha^2z^k(C^k e^{-\alpha z^k} + \bar{C}^k e^{\alpha z^k}) \\ + 2\alpha(1 - v^k)(C^k e^{-\alpha z^k} - \bar{C}^k e^{\alpha z^k}) + i\alpha^2(B_{,m}^k e^{-\alpha z^k} + \bar{B}_{,m}^k e^{\alpha z^k}) \end{aligned} \quad (\text{B.6})$$

$$\begin{aligned} \tilde{\sigma}_{12}^k = -mn(A^k e^{-\alpha z^k} + \bar{A}^k e^{\alpha z^k}) - 2in(1 - v^k)(B^k e^{-\alpha z^k} + \bar{B}^k e^{\alpha z^k}) \\ + im^2n\alpha^{-1}z^k(B^k e^{-\alpha z^k} - \bar{B}^k e^{\alpha z^k}) - mnz^k(C^k e^{-\alpha z^k} + \bar{C}^k e^{\alpha z^k}) \\ - imn(B_{,m}^k e^{-\alpha z^k} + \bar{B}_{,m}^k e^{\alpha z^k}) \end{aligned} \quad (\text{B.7})$$

$$\begin{aligned} \tilde{\sigma}_{31}^k = -im\alpha(A^k e^{-\alpha z^k} + \bar{A}^k e^{\alpha z^k}) - m^2z^k(B^k e^{-\alpha z^k} + \bar{B}^k e^{\alpha z^k}) \\ + [2\alpha(1 - v^k) + m^2\alpha^{-1}](B^k e^{-\alpha z^k} - \bar{B}^k e^{\alpha z^k}) \\ - im(1 - 2v^k)(C^k e^{-\alpha z^k} + \bar{C}^k e^{\alpha z^k}) - im\alpha z^k(C^k e^{-\alpha z^k} - \bar{C}^k e^{\alpha z^k}) \\ + m\alpha(B_{,m}^k e^{-\alpha z^k} - \bar{B}_{,m}^k e^{\alpha z^k}) \end{aligned} \quad (\text{B.8})$$

$$\begin{aligned} \tilde{\sigma}_{32}^k = -in\alpha(A^k e^{-\alpha z^k} - \bar{A}^k e^{\alpha z^k}) - mnz^k(B^k e^{-\alpha z^k} + \bar{B}^k e^{\alpha z^k}) \\ + mn\alpha^{-1}(B^k e^{-\alpha z^k} - \bar{B}^k e^{\alpha z^k}) - in(1 - 2v^k)(C^k e^{-\alpha z^k} + \bar{C}^k e^{\alpha z^k}) \\ - in\alpha z^k(C^k e^{-\alpha z^k} - \bar{C}^k e^{\alpha z^k}) + n\alpha(B_{,m}^k e^{-\alpha z^k} - \bar{B}_{,m}^k e^{\alpha z^k}) \end{aligned} \quad (\text{B.9})$$

where $\alpha = \sqrt{m^2 + n^2}$ with m and n being the Fourier transform variables corresponding to x and y , respectively. The letter i in the above equations is the imaginary unit.

Coefficients in Papkovitch-Neuber Potentials

The Fourier transform of Papkovitch-Neuber potentials, Eq.(5.21), shows that 12 unknown coefficients A^k , B^k , C^k , \bar{A}^k , \bar{B}^k and \bar{C}^k with $k = c$ or $k = s$ need to be determined in order to solve the problem. Following the description in [149, 150], the analytical expressions of the coefficients are given in this section. The condition that the displacements and stresses should vanish at infinite in z direction in the substrate indicates that $\bar{A}^s = \bar{B}^s = \bar{C}^s = 0$. And the rest nine coefficients in Eq.(5.21) can be obtained by solving the boundary conditions given by Eqs.(5.19) and (5.20).

With the following definition,

$$\begin{aligned}\alpha &= \sqrt{m^2 + n^2} \\ \theta &= e^{-2\alpha l_0} \\ \mu_{cs} &= \frac{\mu^c}{\mu^s}\end{aligned}\tag{B.10}$$

the B components and its related derivatives are

$$\bar{B}^c = -\frac{\tilde{q}_x \theta (t_4 \mu_{cs} - t_1)}{2\alpha(1 - \mu^c) [(t_4 \mu_{cs} + t_1) - \theta(t_4 \mu_{cs} - t_1)]}\tag{B.11}$$

$$\bar{B}_{,m}^c = \frac{\tilde{q}_x m \theta (t_4 \mu_{cs} - t_1) [(1 + 2\alpha l_0)(t_4 \mu_{cs} + t_1) - \theta(t_4 \mu_{cs} - t_1)]}{2\alpha^3(1 - \mu^c) [(t_4 \mu_{cs} + t_1) - \theta(t_4 \mu_{cs} - t_1)]^2}\tag{B.12}$$

$$B^c = \bar{B}^c - \frac{\tilde{q}_x}{2\alpha(1 - \mu^c)}\tag{B.13}$$

$$B_{,m}^c = \bar{B}_{,m}^c + \frac{\tilde{q}_x m}{2\alpha^3(1 - \mu^c)}\tag{B.14}$$

$$B^s = \frac{t_4(1 - \mu^c)(\theta - 1)}{1 - \mu^s} \bar{B}^c e^{\alpha l_0} - \frac{\tilde{q}_x t_4 e^{-\alpha l_0}}{2\alpha(1 - \mu^s)}\tag{B.15}$$

$$B_{,m}^s = -\frac{t_4(1 - \mu^c)}{(1 - \mu^s)} \frac{m l_0(1 + \theta)}{\alpha} \bar{B}^c e^{\alpha l_0} + \frac{t_4(1 - \mu^c)(\theta - 1)}{(1 - \mu^s)} \bar{B}_{,m}^c e^{\alpha l_0} + \frac{\tilde{q}_x(1 + \alpha l_0)t_4 m e^{-\alpha l_0}}{2\alpha^3(1 - \mu^s)}\tag{B.16}$$

where \tilde{q}_x is the Fourier transforms of shear traction with respect to x and y . Note that all B items will be zero for frictionless rolling contact, as reported in [158].

The A and C components are

$$A^c = \frac{S_2 + \alpha \bar{A}^c - (1 - 2\nu^c)C^c - (1 - 2\nu^c)\bar{C}^c}{\alpha}\tag{B.17}$$

$$\bar{A}^c = \frac{1}{2\alpha} [(S_1 - S_2) - C^c - (4\mu^c - 3)\bar{C}^c] \quad (\text{B.18})$$

$$C^c = \frac{S_c - k_{16}\bar{C}^c}{k_{15}} \quad (\text{B.19})$$

$$\bar{C}^c = \frac{k_{15}S_d - k_{17}S_c}{k_{15}k_{18} - k_{16}k_{17}} \quad (\text{B.20})$$

$$A^s = \frac{t_1}{\mu_{cs}} (e^{-\alpha l_0} A^c + e^{\alpha l_0} \bar{A}^c + l_0 e^{-\alpha l_0} C^c + l_0 e^{\alpha l_0} \bar{C}^c - \frac{\mu^c S_3}{t_1}) \quad (\text{B.21})$$

$$C^s = \frac{1}{2(1 - \mu^s)} \left\{ t_6 \alpha e^{-\alpha l_0} A^c + t_6 \alpha e^{\alpha l_0} \bar{A}^c + t_6 [2(1 - \mu^c) + \alpha l_0] e^{-\alpha l_0} C^c \right. \\ \left. - t_6 [2(1 - \mu^c) - \alpha l_0] e^{\alpha l_0} \bar{C}^c - \alpha A^s - S_6 \right\} \quad (\text{B.22})$$

where

$$k_{15}S_d - k_{17}S_c = \left(k_{10} - \frac{k_9}{2\alpha} \right) \left(S_b - \frac{k_5}{\alpha} S_2 - \frac{k_{12}}{2\alpha} (S_1 - S_2) \right) \\ - \left(k_{13} - \frac{k_{12}}{2\alpha} \right) \left(S_a - \frac{k_1}{\alpha} S_2 - \frac{k_9}{2\alpha} (S_1 - S_2) \right) \quad (\text{B.23})$$

The S components are

$$S_1 = \frac{i}{\alpha} \left[i\tilde{p} - 2m(1 - \mu^c)(B^c + \bar{B}^c) - \alpha^2 (B_{,m}^c + \bar{B}_{,m}^c) \right] \quad (\text{B.24})$$

where \tilde{p} is the Fourier transforms of pressure.

$$S_2 = \frac{i}{\alpha} \left[-m(B^c - \bar{B}^c) - \alpha^2 (B_{,m}^c + \bar{B}_{,m}^c) \right] \quad (\text{B.25})$$

$$S_3 = \frac{i}{\alpha} \left[\frac{t_1 m l_0}{\mu^c} (B^c e^{-\alpha l_0} - \bar{B}^c e^{\alpha l_0}) - \frac{t_1 \alpha}{\mu^c} (B_{,m}^c e^{-\alpha l_0} + \bar{B}_{,m}^c e^{\alpha l_0}) + \frac{\alpha}{\mu^s} B_{,m}^s \right] \quad (\text{B.26})$$

$$S_4 = \frac{i}{\alpha} \left[-\frac{t_3 m \alpha l_0}{\mu^c} (B^c e^{-\alpha l_0} + \bar{B}^c e^{\alpha l_0}) + \frac{t_3 m}{\mu^c} (B^c e^{-\alpha l_0} - \bar{B}^c e^{\alpha l_0}) \right. \\ \left. + \frac{t_3 \alpha^2}{\mu^c} (B_{,m}^c e^{-\alpha l_0} - \bar{B}_{,m}^c e^{\alpha l_0}) - \frac{m}{\mu^s} B^s - \frac{\alpha^2}{\mu^s} B_{,m}^s \right] \quad (\text{B.27})$$

$$S_5 = \frac{i}{\alpha} \left[-(1 - \alpha l_0) t_4 m B^c e^{-\alpha l_0} + (1 + \alpha l_0) t_4 m \bar{B}^c e^{\alpha l_0} \right. \\ \left. - t_4 \alpha^2 (B_{,m}^c e^{-\alpha l_0} - \bar{B}_{,m}^c e^{\alpha l_0}) + m B^s + \alpha^2 B_{,m}^s \right] \quad (\text{B.28})$$

$$S_6 = \frac{i}{\alpha} \left[-2t_6 m(1 - \mu^c)(B^c e^{-\alpha l_0} + \bar{B}^c e^{\alpha l_0}) + t_6 m \alpha l_0 (B^c e^{-\alpha l_0} - \bar{B}^c e^{\alpha l_0}) \right. \\ \left. - t_6 \alpha^2 (B_{,m}^c e^{-\alpha l_0} + \bar{B}_{,m}^c e^{\alpha l_0}) + 2m(1 - \mu^s) B^s + \alpha^2 B_{,m}^s \right] \quad (\text{B.29})$$

$$S_a = \frac{\mu^c}{2(1 - \mu^s)t_3} S_4 e^{-\alpha l_0} - \frac{(1 - 2\mu^s)\mu_{cs}}{2(1 - \mu^s)t_3} S_5 e^{-\alpha l_0} + \frac{\mu_{cs}}{t_3} S_6 e^{-\alpha l_0} \quad (\text{B.30})$$

$$S_b = \frac{\alpha \mu^c}{t_1} S_3 e^{-\alpha l_0} - \frac{(1 - 2\mu^s)\mu_{cs}}{t_1} S_5 e^{-\alpha l_0} + \frac{2(1 - \mu^s)\mu_{cs}}{t_1} S_6 e^{-\alpha l_0} \quad (\text{B.31})$$

$$S_c = S_a - \frac{k_1}{\alpha} S_2 - \frac{k_9}{2\alpha} (S_1 - S_2) \quad (\text{B.32})$$

$$S_d = S_b - \frac{k_5}{\alpha} S_2 - \frac{k_{12}}{2\alpha} (S_1 - S_2) \quad (\text{B.33})$$

The intermediate variables are

$$k_1 = \left(\frac{t_6 \mu_{cs}}{t_3} - 1 \right) \alpha \theta - \frac{1 - 2\mu^s}{2 - 2\mu^s} \left(\frac{t_4 \mu_{cs}}{t_3} - 1 \right) \alpha \theta \quad (\text{B.34})$$

$$k_2 = \left(\frac{t_6 \mu_{cs}}{t_3} + 1 \right) \alpha + \frac{1 - 2\mu^s}{2 - 2\mu^s} \left(\frac{t_4 \mu_{cs}}{t_3} - 1 \right) \alpha \quad (\text{B.35})$$

$$k_3 = [2(1 - \mu^c) + \alpha l_0] \frac{t_6 \mu_{cs} \theta}{t_3} - (3 - 4\mu^c + \alpha l_0) \theta \\ - \frac{(1 - 2\mu^s)\theta}{2 - 2\mu^s} \left((1 - 2\mu^c + \alpha l_0) \frac{t_4 \mu_{cs}}{t_3} - (3 - 4\mu^c + \alpha l_0) \right) \quad (\text{B.36})$$

$$k_4 = -[2(1 - \mu^c) - \alpha l_0] \frac{t_6 \mu_{cs}}{t_3} - (3 - 4\mu^c - \alpha l_0) \\ - \frac{1 - 2\mu^s}{2 - 2\mu^s} \left((1 - 2\mu^c + \alpha l_0) \frac{t_4 \mu_{cs}}{t_3} - (3 - 4\mu^c - \alpha l_0) \right) \quad (\text{B.37})$$

$$k_5 = \alpha \theta + \frac{\mu_{cs} \alpha \theta}{t_1} [(1 - 2\mu^s)t_6 - 2(1 - \mu^s)t_4] \quad (\text{B.38})$$

$$k_6 = \alpha + \frac{\mu_{cs} \alpha}{t_1} [(1 - 2\mu^s)t_6 + 2(1 - \mu^s)t_4] \quad (\text{B.39})$$

$$k_7 = \alpha l_0 \theta + \frac{(1 - 2\mu^s)\mu_{cs} \theta}{t_1} \left\{ [2(1 - \mu^c) + \alpha l_0] t_6 - \frac{2(1 - \mu^s)(1 - 2\mu^c + \alpha l_0)t_4}{1 - 2\mu^s} \right\} \quad (\text{B.40})$$

$$k_8 = \alpha l_0 - \frac{(1-2\mu^s)\mu_{cs}}{t_1} \left\{ [2(1-\mu^c) - \alpha l_0] t_6 + \frac{2(1-\mu^s)(1-2\mu^c - \alpha l_0) t_4}{1-2\mu^s} \right\} \quad (\text{B.41})$$

$$k_9 = k_1 + k_2 \quad (\text{B.42})$$

$$k_{10} = k_3 - \frac{k_1}{\alpha} (1-2\mu^c) \quad (\text{B.43})$$

$$k_{11} = k_4 - \frac{k_1}{\alpha} (1-2\mu^c) \quad (\text{B.44})$$

$$k_{12} = k_5 + k_6 \quad (\text{B.45})$$

$$k_{13} = k_7 - \frac{k_5}{\alpha} (1-2\mu^c) \quad (\text{B.46})$$

$$k_{14} = k_8 - \frac{k_5}{\alpha} (1-2\mu^c) \quad (\text{B.47})$$

$$k_{15} = k_{10} - \frac{k_9}{2\alpha} \quad (\text{B.48})$$

$$k_{16} = k_{11} - \frac{k_9}{2\alpha} (4\mu^c - 3) \quad (\text{B.49})$$

$$k_{17} = k_{13} - \frac{k_{12}}{2\alpha} \quad (\text{B.50})$$

$$k_{18} = k_{14} - \frac{k_{12}}{2\alpha} (4\mu^c - 3) \quad (\text{B.51})$$

C Green's Function Analysis

The correspondence principle proposed by Alfrey [3] implies that the viscoelastic solution to a problem can be derived from an appropriate elastic solution. Taking the point contact problem on a half-space as an example, the elastic deformation equation can be calculated by the Boussinesq equation,

$$u(x, y) = \iint G_E(x - x', y - y') p(x', y') dx' dy' \quad (\text{C.1})$$

where $G_E(x, y) = \frac{1-\nu^2}{\pi E} \frac{1}{\sqrt{x^2+y^2}}$ is the elastic Green's function. As reported in [21, 23] and also our previous work [159] or Chapter 3, the deformation equation for a viscoelastic half-space can be derived from Eq.(C.1), which is

$$u(x, y, t) = \int_{-\infty}^t \iint G_{VE}(x-x', y-y', t-q) \frac{\partial p(x', y', q)}{\partial q} dx' dy' dq \quad (C.2)$$

where $G_{VE}(x, y, t) = \frac{(1-\nu^2)\varphi_c(t)}{\pi} \frac{1}{\sqrt{x^2+y^2}}$ is the viscoelastic Green's function. The above two equations, Eqs.(C.1) and (C.2), show that the time-dependent viscoelastic Green's function G_{VE} can be easily derived from elastic Green's function by replacing the compliance, $1/E$, with compliance function, $\varphi_c(t)$, in G_E . Furthermore, the time-dependent viscoelastic deformation equation, Eq.(C.2), can be used to describe the steady-state response under rolling/sliding conditions with the following relations

$$u(x, y, t) = u(x + v_m t, y) \quad (C.3)$$

$$p(x, y, t) = p(x + v_m t, y) \quad (C.4)$$

Applying double Fourier transform to Eq.(C.1), which gives

$$\tilde{\tilde{u}}(m, n) = \tilde{\tilde{G}}_E(m, n) \tilde{\tilde{p}}(m, n) \quad (C.5)$$

where $\tilde{\tilde{G}}_E(m, n) = \frac{1-\nu^2}{\pi E} \frac{1}{\sqrt{m^2+n^2}}$ is the Fourier transformed elastic Green's function, and m and n being the transformed variables with respect to x and y , respectively. Applying triple Fourier transforms to Eqs.(C.2) ~ (C.4) with respect to t , x and y , respectively, leads to the following

$$\tilde{\tilde{u}}(m, n, \omega) = \tilde{\tilde{G}}_{VE}^*(m, n, \omega) \tilde{\tilde{p}}(m, n, \omega) \quad (C.6)$$

$$\tilde{\tilde{u}}(m, n, \omega) = 2\pi\delta(\omega - mv_m) \tilde{\tilde{u}}(m, n) \quad (C.7)$$

$$\tilde{\tilde{p}}(m, n, \omega) = 2\pi\delta(\omega - mv_m) \tilde{\tilde{p}}(m, n) \quad (C.8)$$

where $\tilde{\tilde{G}}_{VE}^* = i\omega\tilde{\tilde{G}}_{VE}$ in Eq.(C.6) is Fourier transformed viscoelastic Green's function, $\delta(\omega - mv_m)$ in Eqs.(C.7) and (C.8) being the Dirac delta function and ω being the time-related variable in transformed domain.

Substituting Eqs.(C.7) and (C.8) into Eq.(C.6), the following equation is obtained

$$\tilde{\tilde{u}}(m, n) = \tilde{\tilde{G}}_{VE}^*(m, n, mv_m) \tilde{\tilde{p}}(m, n) \quad (C.9)$$

This equation shows that the time-dependent viscoelastic deformation can be transferred to a speed-dependent problem with the relation $\omega = mv_m$. And the viscoelastic problem can be readily solved by replacing $G_E(m, n)$ with $\tilde{\tilde{G}}_{VE}^*(m, n, mv_m)$ in the corresponding elastic solution. In addition, the steady-state viscoelastic Green's function in the transformed domain $\tilde{\tilde{G}}_{VE}^*(m, n, mv_m)$ can be directly obtained by replacing the elastic modulus E with relaxation function $\psi_r(\omega = mv_m)$ in elastic Green's function $\tilde{\tilde{G}}_E(m, n)$.

Chapter 6

Conclusion and Recommendations

6.1 Conclusion

Viscoelastic materials, e.g. polymers and polymer-based composites, are widely used in modern engineering and biomedical fields due to their outstanding performance such as low cost, ease of manufacture, lightweight and good recyclability. Being different from elastic materials which respond instantaneously to external loads, viscoelastic materials exhibit time-dependent deformation behaviour and dissipate energy under dynamic contact conditions. Fundamental knowledge and modeling methods are essential to increase predictability, reliability and for optimization of the tribological performance of these soft viscoelastic contacts under lubricated as well as dry conditions.

In this thesis, the effect of solid viscoelasticity on both dry and lubricated point contacts are investigated by carrying out numerical simulations and experimental investigations. A novel deformation equation is proposed allowing an accurate and efficient evaluation of the deformation of viscoelastic half-space in an amount of computational time equivalent to that of an elastic problem, also working for complex viscoelastic materials with multiple relaxation times. It can be integrated straightforwardly in any existing elastic solvers for dry and/or EHL lubricated contacts, e.g. the multigrid and multilevel multi-integration numerical methods used in this work.

Firstly, a viscoelastic dry (VED) contact model was presented based on the novel deformation equation for both static creep and dynamic rolling contact conditions. At extreme speed/time conditions, the static (creep) contact and the rolling contact give exactly the same elastic solution. For rolling contacts in steady-state regime, the VED contact problem is dominated by two dimensionless parameters: the Deborah number which relates the relaxation time of the viscoelastic material to the characteristic time of the material passing through the contact, and the ratio of the two elastic limits of the SLS viscoelastic material. Asymmetric pressure distributions skewing towards the inlet side of the contact are obtained as a result of the time-dependent deformation behaviour of viscoelastic materials. The condition where the asymmetry in pressure is maximal is associated with the highest value of friction coefficient, which is around a value of unity of the Deborah number. In addition, when considering two viscoelastic bodies in contact the viscoelasticity causes big differences between rolling and sliding running conditions. Only one surface shows viscoelastic response and the other responses elastically under sliding conditions, while the two moving surfaces response both viscoelastically in a pure rolling contact.

Secondly, an efficient visco-elastohydrodynamic lubrication (VEHL) model has been developed for point contact problems by implementing the novel viscoelastic deformation equation into an existing multigrid EHL solver. Three dominating dimensionless parameters are identified for VEHL problems, the dimensionless parameter λ , the two elastic limits of the SLS model, and the Deborah number. The time-delayed response of the viscoelastic material has a profound influence on the contact pressure and the film shape. The VEHL pressure distribution inherits features of the VED contact problem and may exhibit a steep local maximum in the pressure as well as a local film minimum on the inlet side. For the SLS viscoelastic material model the VEHL solution clearly exhibits two extreme elastic solutions, one for low and one for high surface speeds. In the transitional regime, the size of the contact zone can reduce significantly on the exit side leading to a non-circular contact region. Generally the viscoelasticity of solids leads to a reduced film thickness compared to the corresponding purely elastic case. The experimentally obtained film profiles results provide excellent validation of the scaling for isoviscous elastic contacts in [124] by showing self similarity.

Finally, 3D viscoelastic layered contact problems were studied using the simplified foundation approach and the Papkovich-Neuber (PN) full numerical approach. The comparison of these two approaches shows that the foundation can predict the layer deformation qualitatively even though it is not as accurate as the PN approach because of the used oedometric layer assumption. The parametric study with the PN approach shows that deformed viscoelastic layers hardly show EHL film behaviour within the linear viscoelasticity assumption. Considering the piezoviscosity effect of the dashpot in the SLS model using the foundation approach, the obtained layer shape after deformation is remarkably similar to the EHL film and also to the experimental results with a PDMS layer in ball-on-disc rolling contacts. This may provide a new way to model EHL and mixed lubrication without solving the Reynolds equation.

6.2 Recommendations for Future Work

Several recommendations for future research are made.

For experimental validation and further development of the VED and VEHL models:

- Carry out rolling friction and optical film thickness measurements with viscoelastic discs/balls, e.g. using characterized polydimethylsiloxane (PDMS) and/or rubber material, and compare quantitatively with the developed VED and VEHL models. Dynamic mechanical analysis (DMA) of the rheological properties of viscoelastic specimens should be performed. For the film measurements, the viscoelastic disc should be coated with a semi-reflective layer, and the feasibility of using the widely used Cr layer needs to be tested on highly-deformable surfaces. The EHD2 ball-on-disc test rig shown in Fig.1.4 can be used for this purpose.
- For the scaling of the VEHL film and pressure profiles, with increasing viscoelastic effects, the outlet size reduction and the occurrence of the inlet local pressure maximum cause the scaling for the pressure in the inlet and for the film thickness in the outlet to be less accurate, whereas the film thickness in the inlet, and the pressure in the outlet are on the other hand still scaled quite well. The scaling behavior and

self similarity of the film thickness and pressure in the inlet and outlet in relation to the viscoelastic solid behavior need to be studied in more detail. This will not only benefit the physical understanding of the problem, but also provide easy-to-use equations for engineering practice. It should be noted that these are all based on the viscoelastic half-space assumption, in which the deformation is relatively small compared to the curvature of the contact bodies.

For further development of the viscoelastic layered model towards EHL and mixed lubrication modeling:

- Extend the layer deformation model to non-linear viscoelastic contact mechanics so that the pressure-dependent viscosity and shear modulus of the layer could be considered. Surface roughness effect and the resulting discontinuous interfacial layer in mixed lubrication should be modeled properly .
- Experimentally, coat continuous PDMS viscoelastic layer on the glass disc with varying thicknesses using a spin-coater. The layer could be further manufactured into micro non-discontinuous patterns with LIGA technology. Carry out experiments with the coated glass disc on the optical ball-on-disc test rig to study the layer deformation behavior.
- Extend the model to rolling/sliding contacts by considering possible (partial) slip behaviour at the interface between the layer and the substrate.

Bibliography

References

- [1] Alblas, J. B. and Kuipers, M. [1970], 'The contact problem of a rigid cylinder rolling on a thin viscoelastic layer', *International Journal of Engineering Science* **8**(5), 363–380.
- [2] Aleksandrov, V. M., Goryacheva, I. G. and Torskaya, E. V. [2010], 'Sliding contact of a smooth indenter and a viscoelastic half-space (3D problem)', *Doklady Physics* **55**(2), 77–80.
- [3] Alfrey, T. [1944], 'Non-homogeneous stresses in visco-elastic media', *Quarterly of Applied Mathematics* **2**, 113–119.
- [4] Alsaad, M., Bair, S., Sanborn, D. M. and Winer, W. O. [1978], 'Glass transitions in lubricants: Its relation to elastohydrodynamic lubrication (EHD)', *Journal of Lubrication Technology* **100**(3), 404–416.
- [5] Altenbach, H., Goldstein, R. V. and Murashkin, E. [2017], *Mechanics for Materials and Technologies*, Vol. 46 of *Advanced Structured Materials*, Springer.
- [6] Argatov, I. and Mishuris, G. [2015], *Contact mechanics of articular cartilage layers*, Springer.
- [7] Bair, S. [2018], 'The viscosity at the glass transition of a liquid lubricant', *Friction* **7**(1), 86–91.
- [8] Bair, S. [2019], *High pressure rheology for quantitative elastohydrodynamics*, Elsevier.
- [9] Bair, S., Khonsari, M. and Winer, W. O. [1998], 'High-pressure rheology of lubricants and limitations of the reynolds equation', *Tribology International* **31**(10), 573–586.
- [10] Barber, J. R. [2002], *Elasticity*, Springer.
- [11] Barus, C. [1893], 'Isothermals, isopiestic and isometrics relative to viscosity', *American Journal of Science* **45**(266), 87–96.
- [12] Batra, S. K. and Ling, F. F. [1967], 'On deformation friction and interface shear stress in viscoelastic-elastic layered system under a moving load', *ASLE Transactions* **10**(3), 294–301.
- [13] Beatson, R. and Greengard, L. [1997], 'A short course on fast multipole methods', *Wavelets, Multilevel Methods and Elliptic PDEs* **1**, 1–37.

- [14] Braat, G. and Kalker, J. [1970], ‘Theoretical and experimental analysis of the rolling contact between two cylinders coated with multilayered, viscoelastic rubber’, *WIT Transactions on Engineering Sciences* **1**, 8.
- [15] Brandt, A. [1977], ‘Multi-level adaptive solutions to boundary-value problems’, *Mathematics of computation* **31**(138), 333–390.
- [16] Brandt, A. and Lubrecht, A. A. [1990], ‘Multilevel matrix multiplication and fast solution of integral equations’, *Journal of Computational Physics* **90**(2), 348–370.
- [17] Brinson, H. F. and Brinson, L. C. [2008], *Polymer Engineering Science and Viscoelasticity: An introduction*, Springer.
- [18] Brinson, H. F. and Brinson, L. C. [2015], *Polymer Engineering Science and Viscoelasticity*, Springer.
- [19] Bugnicourt, R., Sainsot, P., Lesaffre, N. and Lubrecht, A. A. [2017], ‘Transient frictionless contact of a rough rigid surface on a viscoelastic half-space’, *Tribology International* **113**, 279–285.
- [20] Cann, P. M., Spikes, H. A. and Hutchinson, J. [1996], ‘The development of a spacer layer imaging method (SLIM) for mapping elastohydrodynamic contacts’, *Tribology Transactions* **39**(4), 915–921.
- [21] Carbone, G. and Putignano, C. [2013], ‘A novel methodology to predict sliding and rolling friction of viscoelastic materials: Theory and experiments’, *Journal of the Mechanics and Physics of Solids* **61**(8), 1822–1834.
- [22] Chen, W. T. [1971], ‘Computation of stresses and displacements in a layered elastic medium’, *International Journal of Engineering Science* **9**(9), 775–800.
- [23] Chen, W. W., Wang, Q. J., Huan, Z. and Luo, X. [2011], ‘Semi-analytical viscoelastic contact modeling of polymer-based materials’, *Journal of Tribology Transactions* **133**(4).
- [24] Choo, J. W., Olver, A. V. and Spikes, H. A. [2007], ‘The influence of transverse roughness in thin film, mixed elastohydrodynamic lubrication’, *Tribology International* **40**(2), 220–232.
- [25] Christensen, R. M. [1982], *Theory of Viscoelasticity: An introduction*, Elsevier.
- [26] Cyriac, F., Lugt, P. M., Bosman, R., Padberg, C. J. and Venner, C. H. [2016], ‘Effect of thickener particle geometry and concentration on the grease EHL film thickness at medium speeds’, *Tribology Letters* **61**(2), 1–13.
- [27] Damiens, B., Venner, C. H., Cann, P. M. E. and Lubrecht, A. A. [2004], ‘Starved lubrication of elliptical EHD contacts’, *Journal of Tribology* **126**(1), 105–111.

- [28] Degrange, J. M., Thomine, M., Kapsa, P., Pelletier, J. M., Chazeau, L., Vigier, G., Dudragne, G. and Guerbé, L. [2005], 'Influence of viscoelasticity on the tribological behaviour of carbon black filled nitrile rubber (NBR) for lip seal application', *Wear* **259**(1-6), 684–692.
- [29] Dorgham, A., Wang, C., Morina, A. and Neville, A. [2017], 'Local occupancy of viscoelastic interfaces: a new rheological respective on antiwear tribofilms', *44th Leeds-Lyon Symposium on Tribology*.
- [30] Dowson, D. and Higginson, G. [1959], 'A numerical solution to the elasto-hydrodynamic problem', *Journal of Mechanical Engineering Science* **1**(1), 6–15.
- [31] Dowson, D. and Higginson, G. R. [1966a], *Elasto-hydrodynamic lubrication : the fundamentals of roller and gear lubrication*, Pergamon Press, Oxford, Great Britain.
- [32] Dowson, D. and Higginson, G. R. [1966b], *Elasto-hydrodynamic lubrication: international series on materials science and technology*, Pergamon Press, Oxford, Great Britain.
- [33] Elsharkawy, A. A. [1996a], 'A numerical solution for dry contact between two viscoelastic rollers', *Tribology Transactions* **39**(3), 627–635.
- [34] Elsharkawy, A. A. [1996b], 'Visco-elastohydrodynamic lubrication of line contacts', *Wear* **199**(1), 45–53.
- [35] Emden, E. v., Venner, C. H. and Morales-Espejel, G. E. [2017], 'Investigation into the viscoelastic behaviour of a thin lubricant layer in an EHL contact', *Tribology International* **111**, 197–210.
- [36] Ertel, A. [1939], 'Hydrodynamic lubrication based on new principles', *Akad. Nauk SSSR Prikadnaya Matematika i Mekhanika* **3**(2), 41–52.
- [37] Essink, M. H., Pandey, A., Karpitschka, S., Venner, C. H. and Snoeijer, J. H. [2021], 'Regimes of soft lubrication', *Journal of Fluid Mechanics* **915**.
- [38] Foord, C. A., Wedeven, L. D., Westlake, F. J. and Cameron, A. [1969], 'Optical elastohydrodynamics', *Proceedings of the Institution of Mechanical Engineers* **184**(1), 487–505.
- [39] Fryza, J., Sperka, P., Krupka, I. and Hartl, M. [2021], 'Film thickness interrelationship of base oil and grease lubricated compliant and hard non-conformal contacts', *Proceedings of the Institution of Mechanical Engineers, Part J: Journal of Engineering Tribology* **235**(12), 2616–2625.
- [40] Gabelli, A. and Poll, G. [1992], 'Formation of lubricant film in rotary sealing contacts: Part I—lubricant film modeling', *Journal of Tribology* **114**, 280–287.
- [41] Gasni, D., Wan Ibrahim, M. K. and Dwyer-Joyce, R. S. [2011], 'Measurements of lubricant film thickness in the iso-viscous elastohydrodynamic regime', *Tribology International* **44**(7-8), 933–944.

- [42] Glovnea, R. P. and Spikes, H. A. [2002], 'Behavior of EHD films during reversal of entrainment in cyclically accelerated/decelerated motion', *Tribology Transactions* **45**(2), 177–184.
- [43] Gohar, R. and Cameron, A. [1963], 'Optical measurement of oil film thickness under elasto-hydrodynamic lubrication', *Nature* **200**(4905), 458–459.
- [44] Goriacheva, I. G. [1973], 'Contact problem of rolling of a viscoelastic cylinder on a base of the same material', *Journal of Applied Mathematics and Mechanics* **37**(5), 877–885.
- [45] Goryacheva, I. G., Goryachev, A. P. and Sadegi, F. [1995], 'Contact of elastic bodies with thin visco-elastic coatings under conditions of rolling or sliding friction', *Journal of Applied Mathematics and Mechanics* **59**(4), 607–614.
- [46] Goryacheva, I. G. and Miftakhova, A. [2019], 'Modelling of the viscoelastic layer effect in rolling contact', *Wear* **430**, 256–262.
- [47] Goryacheva, I. G. and Sadeghi, F. [1995], 'Contact characteristics of a rolling sliding cylinder and a viscoelastic layer bonded to an elastic substrate', *Wear* **184**(2), 125–132.
- [48] Graham, G. A. C. [1967], 'The contact problem in the linear theory of viscoelasticity when the time dependent contact area has any number of maxima and minima', *International Journal of Engineering Science* **5**(6), 495–514.
- [49] Greenwood, J. A. [2010], 'Contact between an axisymmetric indenter and a viscoelastic half-space', *International Journal of Mechanical Sciences* **52**(6), 829–835.
- [50] Greenwood, J. A. [2020], 'Elastohydrodynamic lubrication', *Lubricants* **8**(5), 51.
- [51] Greenwood, J. A. and Morales-Espejel, G. E. [1995], 'Pressure spikes in EHL', *In Lubricants and Lubrication, Proceedings of the 21st Leeds-Lyon Symposium on Tribology* **30**, 555–564.
- [52] Grubin, A. N. [1949], 'Fundamentals of the hydrodynamic theory of lubrication of heavily loaded cylindrical surfaces', *Investigation of the Contact Machine Components* **2**.
- [53] Guo, F. and Wong, P. L. [2005], 'A multi-beam intensity-based approach for lubricant film measurements in non-conformal contacts', *Proceedings of the Institution of Mechanical Engineers, Part J: Journal of Engineering Tribology* **216**(5), 281–291.
- [54] Habchi, W. [2018], *Finite element modeling of elastohydrodynamic lubrication problems*, Wiley Online Library.
- [55] Hamrock, B. J. and Dowson, D. [1976a], 'Isothermal elastohydrodynamic lubrication of point contacts: Part I—theoretical formulation', *Technical Report NASA USA* .
- [56] Hamrock, B. J. and Dowson, D. [1976b], 'Isothermal elastohydrodynamic lubrication of point contacts: Part I—theoretical formulation', *Journal of Lubrication Technology* **98**(2), 223–228.

- [57] Hamrock, B. J. and Dowson, D. [1977], 'Isothermal elastohydrodynamic lubrication of point contacts: Part III—fully flooded results', *Journal of Lubrication Technology* **99**(2), 264–275.
- [58] Hamrock, B. J., Schmid, B. J. and Jacobson, B. O. [2004], *Fundamentals of fluid film lubrication*, Vol. 169, CRC press.
- [59] Hartl, M., Krupka, I., Poliscuk, R., Liska, M., Molimard, J., Query, M. and Vergne, P. [2001], 'Thin film colorimetric interferometry', *Tribology Transactions* **44**(2), 270–276.
- [60] He, T., Wang, Q. J., Zhang, X., Liu, Y., Li, Z., Kim, H. J. and Pack, S. [2021a], 'Modeling thermal-visco-elastohydrodynamic lubrication (TVEHL) interfaces of polymer-based materials', *Tribology International* **154**.
- [61] He, T., Wang, Q. J., Zhang, X., Liu, Y., Li, Z., Kim, H. J. and Pack, S. [2021b], 'Visco-elastohydrodynamic lubrication of layered materials with imperfect layer-substrate interfaces', *International Journal of Mechanical Sciences* **189**.
- [62] Herrebrugh, K. [1968], 'Solving the incompressible and isothermal problem in elastohydrodynamic lubrication through an integral equation', *Journal of Lubrication Technology* **90**(1), 262–270.
- [63] Hertz, H. [1881], 'On the contact of elastic solids', *Z. Reine Angew. Mathematik* **92**, 156–171.
- [64] Holmberg, K. and Erdemir, A. [2017], 'Influence of tribology on global energy consumption, costs and emissions', *Friction* **5**(3), 263–284.
- [65] Hooke, C. J. [1977], 'The elastohydrodynamic lubrication of heavily loaded contacts', *Journal of Mechanical Engineering Science* **19**(4), 149–156.
- [66] Hooke, C. J. [1988], 'Calculation of clearances in soft point contacts', *Journal of Tribology* **110**(1), 167–173.
- [67] Hooke, C. J. and Huang, P. [1997], 'Elastohydrodynamic lubrication of soft viscoelastic materials in line contact', *Proceedings of the Institution of Mechanical Engineers, Part J: Journal of Engineering Tribology* **211**(J3), 185–194.
- [68] Hooke, C. J. and O'Donoghue, J. P. [2006], 'Elastohydrodynamic lubrication of soft, highly deformed contacts', *Journal of Mechanical Engineering Science* **14**(1), 34–48.
- [69] Hooke, C. J. and Venner, C. H. [2000], 'Surface roughness attenuation in line and point contacts', *Proceedings of the Institution of Mechanical Engineers, part J: Journal of Engineering Tribology* **214**(5), 439–444.
- [70] Hu, Y. Z. and Granick, S. [1998], 'Microscopic study of thin film lubrication and its contributions to macroscopic tribology', *Tribology Letters* **5**(1), 81–88.
- [71] Hunter, S. C. [1960], 'The Hertz problem for a rigid spherical indenter and a viscoelastic half-space', *Journal of the Mechanics and Physics of Solids* **8**(4), 219–234.

- [72] Hunter, S. C. [1961], 'The rolling contact of a rigid cylinder with a viscoelastic half space', *Journal of Applied Mechanics* **28**(4), 611–617.
- [73] Jeng, Y. R., Hamrock, B. J. and Brewe, D. E. [1986], 'Piezoviscous effects in nonconformal contacts lubricated hydrodynamically', *ASLE Transactions* **30**(4), 452–464.
- [74] Johnson, K. L. [1970], 'Regimes of elasto-hydrodynamic lubrication', *Journal of Mechanical Engineering Science* **12**(1), 9–16.
- [75] Johnson, K. L. [1985], *Contact mechanics*, Cambridge university press.
- [76] Johnston, G. J., Wayte, R. and Spikes, H. A. [1991], 'The measurement and study of very thin lubricant films in concentrated contacts', *Tribology Transactions* **34**(2), 187–194.
- [77] Jost, P. [1966], 'Lubrication (Tribology)-A report on the present position and industry's needs', *Department of Education and Science, HM Stationary Office, London, UK*.
- [78] Kalker, J. J. [1991], 'Viscoelastic multilayered cylinders rolling with dry friction', *Journal of Applied Mechanics* **58**(3), 666–679.
- [79] Kargar-Estahbanati, A. and Rallabandi, B. [2021], 'Lift forces on three-dimensional elastic and viscoelastic lubricated contacts', *Physical Review Fluids* **6**(3).
- [80] Kelly, P. [2013], 'Solid mechanics Part I: An introduction to solid mechanics', *Solid Mechanics Lecture Notes* pp. 241–324.
- [81] Koumi, K. E., Chaise, T. and Nelias, D. [2015], 'Rolling contact of a rigid sphere/sliding of a spherical indenter upon a viscoelastic half-space containing an ellipsoidal inhomogeneity', *Journal of the Mechanics and Physics of Solids* **80**, 1–25.
- [82] Koumi, K. E., Nelias, D., Chaise, T. and Duval, A. [2014], 'Modeling of the contact between a rigid indenter and a heterogeneous viscoelastic material', *Mechanics of Materials* **77**, 28–42.
- [83] Lee, E. H. [1955], 'Stress analysis in visco-elastic bodies', *Quarterly of Applied Mathematics* **13**(2), 183–190.
- [84] Lee, E. H. [1956], 'Stress analysis in viscoelastic materials', *Journal of Applied Physics* **27**(7), 665–672.
- [85] Lee, E. H. and Radok, J. R. M. [1960], 'The contact problem for viscoelastic bodies', *Journal of Applied Mechanics* **27**(3), 438–444.
- [86] Lengiewicz, J., de Souza, M., Lahmar, M. A., Courbon, C., Dalmas, D., Stupkiewicz, S. and Scheibert, J. [2020], 'Finite deformations govern the anisotropic shear-induced area reduction of soft elastic contacts', *Journal of the Mechanics and Physics of Solids* **143**.
- [87] Liu, H. C., Guo, F., Guo, L. and Wong, P. L. [2015], 'A dichromatic interference intensity modulation approach to measurement of lubricating film thickness', *Tribology Letters* **58**(1).

- [88] Liu, S. B., Wang, Q. and Liu, G. [2000], 'A versatile method of discrete convolution and FFT (DC-FFT) for contact analyses', *Wear* **243**(1-2), 101–111.
- [89] Liu, W., Gong, X., Ngai, T. and Wu, C. [2018], 'Near-surface microrheology reveals dynamics and viscoelasticity of soft matter', *Soft Matter* **14**(48), 9764–9776.
- [90] Lubrecht, A. A., ten Napel, W. E. and Bosma, R. [1986], 'Multigrid, an alternative method for calculating film thickness and pressure profiles in elastohydrodynamically lubricated line contacts', *ASME Journal of Tribology* **108**(4), 551–556.
- [91] Lubrecht, A. A., ten Napel, W. E. and Bosma, R. [1987], 'Multigrid, an alternative method of solution for two-dimensional elastohydrodynamically lubricated point contact calculations', *ASME Journal of Tribology* **109**(3), 437–443.
- [92] Luo, J., Wen, S. and Huang, P. [1996], 'Thin film lubrication. part i. study on the transition between EHL and thin film lubrication using a relative optical interference intensity technique', *Wear* **194**(1-2), 107–115.
- [93] Malvern, L. E. [1969], *Introduction to the mechanics of a continuous medium*, Springer Nature.
- [94] Marian, M., Bartz, M., Wartzack, S. and Rosenkranz, A. [2020], 'Non-dimensional groups, film thickness equations and correction factors for elastohydrodynamic lubrication: A review', *Lubricants* **8**(10), 95.
- [95] Martin, A., Clain, J., Buguin, A. and Brochard-Wyart, F. [2002], 'Wetting transitions at soft, sliding interfaces', *Physical Review E* **65**(3), 031605.
- [96] Marx, N., Guegan, J. and Spikes, H. A. [2016], 'Elastohydrodynamic film thickness of soft EHL contacts using optical interferometry', *Tribology International* **99**, 267–277.
- [97] Menga, N., Afferrante, L. and Carbone, G. [2016], 'Effect of thickness and boundary conditions on the behavior of viscoelastic layers in sliding contact with wavy profiles', *Journal of the Mechanics and Physics of Solids* **95**, 517–529.
- [98] Moes, H. [1965], 'Discussion on a paper by D. Dowson', *Proceedings of the Institution of Mechanical Engineers* **180**, 244–245.
- [99] Moes, H. [1992], 'Optimum similarity analysis with applications to elastohydrodynamic lubrication', *Wear* **159**(1), 57–66.
- [100] Moes, H. and Bosma, R. [1971], 'Design charts for optimum bearing configurations: I—the full journal bearing', *ASME Journal of Tribology* **93**(2), 302–306.
- [101] Naghieh, G. R., Jin, Z. M. and Rahnejat, H. [1998], 'Contact characteristics of viscoelastic bonded layers', *Applied Mathematical Modelling* **22**(8), 569–581.
- [102] Nijenbanning, G., Venner, C. H. and Moes, H. [1994], 'Film thickness in elastohydrodynamically lubricated elliptic contacts', *Wear* **176**(2), 217–229.

- [103] Ohno, N. [2007], ‘High-pressure behavior of toroidal CVT fluid for automobile’, *Tribology International* **40**(2), 233–238.
- [104] O’sullivan, T. C. and King, R. B. [1988], ‘Sliding contact stress field due to a spherical indenter on a layered elastic half-space’, *Journal of Tribology* **110**, 235–240.
- [105] Otsu, T. and Imado, K. [2018], ‘Study on changes in the rheologic properties of EHL film using fluorescence measurements’, *Tribology Letters* **66**(1), 1–10.
- [106] Panek, C. and Kalker, J. J. [1980], ‘Three-dimensional contact of a rigid roller traversing a viscoelastic half space’, *IMA Journal of Applied Mathematics* **26**(3), 299–313.
- [107] Persson, B. N. [2010], ‘Rolling friction for hard cylinder and sphere on viscoelastic solid’, *The European Physical Journal E* **33**(4), 327–33.
- [108] Petrusevich, A. I. [1951], ‘Fundamental conclusions from the contact-hydrodynamic theory of lubrication’, *Izv. Akad. Nauk. SSSR (OTN)* **2**, 209.
- [109] Polonsky, I. A. and Keer, L. M. [1999], ‘A numerical method for solving rough contact problems based on the multi-level multi-summation and conjugate gradient techniques’, *Wear* **231**(2), 206–219.
- [110] Popov, V. L., Heß, M. and Willert, E. [2019], *Handbook of contact mechanics: exact solutions of axisymmetric contact problems*, Springer Nature.
- [111] Popova, E. and Popov, V. L. [2015], ‘On the history of elastohydrodynamics: The dramatic destiny of Alexander Mohrenstein-Ertel and his contribution to the theory and practice of lubrication’, *ZAMM-Journal of Applied Mathematics and Mechanics/Zeitschrift für Angewandte Mathematik und Mechanik* **95**(7), 652–663.
- [112] Putignano, C. [2020], ‘Soft lubrication: A generalized numerical methodology’, *Journal of the Mechanics and Physics of Solids* **134**.
- [113] Putignano, C., Carbone, G. and Dini, D. [2015], ‘Mechanics of rough contacts in elastic and viscoelastic thin layers’, *International Journal of Solids and Structures* **69-70**, 507–517.
- [114] Putignano, C. and Dini, D. [2017], ‘Soft matter lubrication: Does solid viscoelasticity matter?’, *ACS Applied Materials Interfaces* **9**(48), 42287–42295.
- [115] Putignano, C., Reddyhoff, T., Carbone, G. and Dini, D. [2013], ‘Experimental investigation of viscoelastic rolling contacts: A comparison with theory’, *Tribology Letters* **51**(1), 105–113.
- [116] Reiter, G., Demirel, A. L. and Granick, S. [1994], ‘From static to kinetic friction in confined liquid films’, *Science* **263**(5154), 1741–1744.
- [117] Reynolds, O. [1886], ‘On the theory of lubrication and its application to mr. beauchamp tower’s experiments, including an experimental determination of the viscosity of olive oil’, *Philosophical Transactions of the Royal Society of London* (177), 157–234.

- [118] Roelands, C. J. A. [1966], *Correlational aspects of the viscosity-temperature-pressure relationship of lubricating oils*, PhD Thesis, Technische Hogeschool Delft, The Netherlands.
- [119] Roylance, D. [2001], 'Engineering viscoelasticity', *Department of Materials Science and Engineering-Massachusetts Institute of Technology, Cambridge MA* **2139**, 1–37.
- [120] Sakamoto, M., Nishikawa, H. and Kaneta, M. [2003], Behaviour of point contact EHL films under pulsating loads, in 'Tribology Series', Vol. 43, Elsevier, pp. 391–399.
- [121] Salant, R. F. [1999], 'Theory of lubrication of elastomeric rotary shaft seals', *Proceedings of the Institution of Mechanical Engineers, Part J: Journal of Engineering Tribology* **213**(3), 189–201.
- [122] Scaraggi, M. and Persson, B. N. J. [2014a], 'Theory of viscoelastic lubrication', *Tribology International* **72**, 118–130.
- [123] Scaraggi, M. and Persson, B. N. J. [2014b], 'Theory of viscoelastic lubrication', *Tribology International* **72**, 118–130.
- [124] Snoeijer, J. H., Eggers, J. and Venner, C. H. [2013], 'Similarity theory of lubricated Hertzian contacts', *Physics of Fluids* **25**(10), 1–6.
- [125] Stakenborg, M. J. L., van Leeuwen, H. J. and ten Hagen, E. A. M. [1990], 'Visco-elastohydrodynamic (VEHD) lubrication in radial lip seals: Part 1—steady-state dynamic viscoelastic seal behavior', *Journal of Tribology* **112**(4), 578–583.
- [126] Stanley, H. M. and Kato, T. [1997], 'An FFT-based method for rough surface contact', *Journal of Tribology* **119**(3), 481–485.
- [127] Stepanov, F. I. and Torskaya, E. V. [2018], 'Modeling of sliding of a smooth indenter over a viscoelastic layer coupled with a rigid base', *Mechanics of Solids* **53**(1), 60–67.
- [128] Stribeck, R. [1902], 'Die wesentlichen Eigenschaften der Gleit- und Rollenlager', *Zeitschrift des Vereines Deutscher Ingenieure* **46**, 1341–1348.
- [129] Svoboda, P., Kostal, D., Krupka, I. and Hartl, M. [2013], 'Experimental study of starved EHL contacts based on thickness of oil layer in the contact inlet', *Tribology International* **67**, 140–145.
- [130] Ting, T. C. T. [1966], 'The contact stresses between a rigid indenter and a viscoelastic half-space', *Journal of Applied Mechanics* **33**(4), 845–854.
- [131] Ting, T. C. T. [1968], 'Contact problems in the linear theory of viscoelasticity', *Journal of Applied Mechanics* **35**(2), 248–254.
- [132] Tower, B. [1883], 'First report on friction experiments', *Proceedings of the Institution of Mechanical Engineers* **34**(1), 632–659.
- [133] Trappe, V. V. and Weitz, D. A. [2000], 'Scaling of the viscoelasticity of weakly attractive particles', *Physical Review Letter* **85**(2), 449–52.

- [134] van Emden, E. [2017], *Aspects of flow and viscoelasticity in a model elastohydrodynamically lubricated contact*, PhD Thesis, University of Twente, The Netherlands.
- [135] van Leeuwen, H. J. [2018], The Delft EHL diagram from a historic perspective: righting a 50-year-old wrong, in '13. Arnold Tross Kolloquium, 15 May 2017, Hamburg, Germany', Shaker-Verlag, pp. 120–157.
- [136] van Leeuwen, H. J. and Stakenborg, M. J. L. [1990], 'Visco-elastohydrodynamic (VEHD) lubrication in radial lip seals: Part 2—fluid film formation', *Journal of Tribology* **112**(4), 584–592.
- [137] van Leeuwen, H. and Stakenborg, M. [1991], A new concept in rotary shaft seal lubrication: Viscoelastohydrodynamic (VEHD) lubrication, in 'Tribology Series', Vol. 18, Elsevier, pp. 373–380.
- [138] Venner, C. H. [1991], *Multilevel solution of the EHL line and point contact problems*, PhD Thesis, University of Twente, The Netherlands.
- [139] Venner, C. H., Biboulet, N. and Lubrecht, A. A. [2014], 'Boundary layer behaviour in circular EHL contacts in the elastic-piezoviscous regime', *Tribology Letters* **56**(2), 375–386.
- [140] Venner, C. H. and Hooke, C. J. [2006], *Surface roughness attenuation in EHL line and point contacts under conditions of starved lubrication*, IUTAM Symposium on Elastohydrodynamics and Micro-elastohydrodynamics, Springer.
- [141] Venner, C. H. and Lubrecht, A. A. [2000], *Multi-level methods in lubrication*, Vol. 37, Elsevier.
- [142] Venner, C. H. and Napel, W. T. [1990], 'Numerical calculations of the pressure spike in elastohydrodynamic lubrication', *Lubrication Science* **2**(4), 321–335.
- [143] Venner, C. H., van Zoelen, M. T. and Lugt, P. M. [2012], 'Thin layer flow and film decay modeling for grease lubricated rolling bearings', *Tribology International* **47**, 175–187.
- [144] Vijay, A. and Sadeghi, F. [2022], 'Rolling contact fatigue of coupled EHL and anisotropic polycrystalline materials', *Tribology International* **169**, 107479.
- [145] Wallace, E. R., Chaise, T. and Nelias, D. [2020], 'Three-dimensional rolling/sliding contact on a viscoelastic layered half-space', *Journal of the Mechanics and Physics of Solids* **143**.
- [146] Wallace, E. R., Chaise, T. and Nelias, D. [2022], 'Rolling contact on a viscoelastic multi-layered half-space', *International Journal of Solids and Structures* **239-240**.
- [147] Wang, J., Kaneta, M. and Yang, P. [2005], 'Numerical analysis of TEHL line contact problem under reciprocating motion', *Tribology International* **38**(2), 165–178.
- [148] Wang, Q. J., Sun, L. L., Zhang, X., Liu, S. B. and Zhu, D. [2020], 'FFT-based methods for computational contact mechanics', *Frontiers in Mechanical Engineering* **6**, 61.

- [149] Wang, Z., Yu, H. and Wang, Q. J. [2017a], 'Layer-substrate system with an imperfectly bonded interface: Coupled dislocation-like and force-like conditions', *International Journal of Solids and Structures* **122**, 91–109.
- [150] Wang, Z., Yu, H. and Wang, Q. J. [2017b], 'Layer-substrate system with an imperfectly bonded interface: spring-like condition', *International Journal of Mechanical Sciences* **134**, 315–335.
- [151] Wijnant, Y. H., Venner, C. H., Larsson, R. and Eriksson, P. [1999], 'Effects of structural vibrations on the film thickness in an EHL circular contact', *Journal of Tribology* **121**(2), 259–264.
- [152] Wu, H., Jagota, A. and Hui, C. Y. [2022], 'Lubricated sliding of a rigid cylinder on a viscoelastic half space', *Tribology Letters* **70**(1), 1–17.
- [153] Zhang, B. B., Boffy, H. and Venner, C. H. [2020], 'Multigrid solution of 2D and 3D stress fields in contact mechanics of anisotropic inhomogeneous materials', *Tribology International* **149**, 105636.
- [154] Zhang, B. B., Liu, H. C., Quiñonez, F. A. and Venner, C. H. [2020], 'Effects of 3D anisotropic heterogeneous subsurface topology on film thickness and subsurface stresses in elasto-hydrodynamically lubricated point contact', *Tribology International* **151**.
- [155] Zhang, B. B., Quiñonez, A. F. and Venner, C. H. [2020], 'Effect of material anisotropy on rolling contact fatigue life under dry and lubricated point contact conditions: A numerical study', *Tribology International* **152**, 106584.
- [156] Zhang, B., Minov, B., Venner, C. H. and Morales-Espejel, G. E. [2022], 'Effect of steel anisotropy on contact pressure and stress distribution in dry and lubricated point contacts: a case study with measured material properties', *Submitted to Tribology International*.
- [157] Zhang, J. and Spikes, H. [2020], 'Measurement of EHD friction at very high contact pressures', *Tribology Letters* **68**(1), 1–12.
- [158] Zhang, X., Wang, Q. J. and He, T. [2020], 'Transient and steady-state viscoelastic contact responses of layer-substrate systems with interfacial imperfections', *Journal of the Mechanics and Physics of Solids* **145**.
- [159] Zhao, Y., Morales-Espejel, G. E. and Venner, C. H. [2022], 'Aspects of modeling and numerical simulation of dry point contacts between viscoelastic solids', *Tribology International* **165**, 107245.

List of Publications

Journal Paper

1. **Y. Zhao**, G.E. Morales-Espejel, C.H. Venner. Aspects of modeling and numerical simulation of dry point contacts between viscoelastic solids. *Tribology International*, 165: 107245, 2022.
2. **Y. Zhao**, H.C. Liu, G.E. Morales-Espejel, C.H. Venner. Effects of solid viscoelasticity on elastohydrodynamic lubrication of point contacts. *Tribology International*, 171: 107562, 2022.
3. **Y. Zhao**, H.C. Liu, G.E. Morales-Espejel, C.H. Venner, Behavior of thin elastic/viscoelastic layer on an elastic half-space in rolling contacts: towards a new modeling approach for EHL lubrication. (Submitted to *Tribology International*)

Conference Presentation

1. **Y. Zhao**, C.H. Venner. Modeling EHL behavior via viscoelasticity. SKF UTC (University Technology Center) Info Day, June 15th, 2021, Online. (oral presentation)
2. **Y. Zhao**, C.H. Venner, Viscoelastic layers in elasto-hydrodynamic lubrication. Burgers Symposium, May 21st-22nd, 2019, Lunteren, The Netherlands. (oral presentation)
3. **Y. Zhao**, C.H. Venner, Viscoelastic layer modeling for contact mechanics. 3rd Young Tribological Researcher Symposium, May 9th-10th, 2019, Vienna. (oral presentation).

Acknowledgments

I gratefully acknowledge all people who have contributed in various ways to this work during the last four years.

First and foremost, I would like to express my deepest gratitude to my supervisor, Prof. C.H. (Kees) Venner: thank you for providing me the opportunity to carry out this project. Thank you for your guidance, support, enthusiasm and encouragement throughout the course of this research program. Thank you for your kindness and positive stimulation and inspiration in each step of my study and growth. I have learned a lot from your positive and energetic attitude, wise discussions and management arts. Your selfless knowledge sharing, attitude toward research, approach to mentoring students, and wise problem-solving skills all set great examples for me.

This research project was funded by the China Scholarship Council (CSC) and by SKF Research and Technology Development (RTD) in Houten, the Netherlands. From SKF, I would like to thank the former and the present managing director of SKF RTD Mr. Stefan Lammens and Mr. Bernie van Leeuwen for their permission to publish the results and their support of the long-term collaboration with the University of Twente of which this research has been a part. I would also like to thank Mr. Mark Verbakel (Head of Tribology & Prognostics Department) and Mr. Jeroen Bongaerts (Competence Team Leader Tribology & Life) for their support. Particularly, I would like to thank Prof. Guillermo Morales-Espejel for his cooperation, support, interest and valuable suggestions in project progress discussions.

I am also grateful to Dr. C.W. Visser of University of Twente for his valuable suggestions on my project in several meetings we had. I would like to thank Dr. Pascal Ehret for his helpful contribution on the methodology. I would also like to thank Dr. B.B. Zhang for helping me rewrite a Fortran code into Matlab, debugging programs and in particular for teaching me some details of multigrid techniques. Many thanks for his continuous support and enthusiasm.

Furthermore, I would like to thank the staff and colleagues of the EFD group and the TFE department, Faculty of Engineering Technology, University of Twente, for their cooperation and continuous support and for creating a very pleasant working atmosphere. In particular, I would like to thank colleagues Walter Lette, Bob Siemerink, Steven Wanrooij and Elise Leusink for their kind help on my experiments in the lab and Brenda Benders, Susan Janse-Godschalk, Sylvia Hodes-Laarhuis and Sally Kloost-Zimmerman van Woesik for offering me help in many aspects of my work and daily life. Special thanks to Prasansha Rastogi for sharing experimental experience, work-related tips, and interesting life moments with me. I would also like to thank Dr. J.K. Jiang for his explanation and valuable suggestions on preparing a thin PDMS coating on glass discs. I would like to thank Dr. G. Popovici for proof-reading and valuable suggestions for future work.

Many thanks to Robert Jan Meijer, Erik de Vries and Liangyong Chu in Surface Technology and Tribology group for their discussions and allowing me to use their experimental

instruments such as the spin-coater.

Many thanks to my committee members: Prof. P.M. Lugt of the group Surface Technology and Tribology of the faculty ET of University of Twente, Prof. A. Blume of the group Elastomer Technology and Engineering of the faculty ET of University of Twente, Prof. G. Poll of the IMKT of Leibniz Universität Hannover, Prof. J. Wang of the Mechanical Engineering department of Donghua University, and Dr. ir. R.A.J. van Ostayen of the PME department of Delft University of Technology. Thank you for your time and effort on my dissertation.

Special thanks to my boyfriend Dr. H.C. Liu for being my "daily life supervisor": gathering project-related information, assisting in revising my papers and thesis, answering my questions and providing valuable suggestions. Haichao, thank you for your love, support and endurance.

Finally, I would like to thank my parents, elder brothers and friends for their support, interest and encouragement.

Yan Zhao
Enschede, May 2022

